Numerical methods for the manufacture of optics using sub-aperture tools

A DISSERTATION PRESENTED
BY
WILHELMUS A. C. M. MESSELINK
TO
THE DEPARTMENT OF PHYSICS AND ASTRONONY

IN PARTIAL FULFILLMENT OF THE REQUIREMENTS
FOR THE DEGREE OF
DOCTOR OF PHILOSOPHY

UNIVERSITY COLLEGE LONDON
LONDON, UNITED KINGDOM
JULY 2015

Statement by the author

I, Wilhelmus A. C. M. Messelink, confirm that the work presented in this thesis is my own. Where information has been derived from other sources, I confirm that this has been indicated in the thesis.

The "Grolishing" experiments, to verify the numerical model developed by the author, were performed by Zheng Xiao, *Glyndŵr University*. The "Hexagonal to hexagonal tool-path" was developed by Dr. Anthony Beaucamp, *Zeeko Ltd./Chubu University*, and tested for the first time by the author. Some Fluid Jet Polishing experiments and numerical simulations were performed by Dr. Phillip Charlton of *Zeeko Ltd.* and Dr. Anthony Beaucamp of *Zeeko Ltd./Chubu University*, the results of which have been critically assessed and an alternative hypothesis developed by the author. All other experimental optimisation of parameters, data analysis, modelling and interpretation were conducted by the author.

Wilhelmus A. C. M. Messelink

September 8, 2015

Numerical methods for the manufacture of optics using sub-aperture tools

Abstract

Moore's law, predicting a doubling of transistor count per microprocessor every two years, remains valid, demonstrating exponential growth of computing power. This thesis examines the application of numerical methods to aid optical manufacturing for a number of case-studies related to the use of sub-aperture tools.

One class of sub-aperture tools consists of rigid tools which are well suited to smooth surfaces. Their rigidity leads to mismatch between the surfaces of tool and aspheric workpieces. A novel, numerical method is introduced to analyse the mismatch qualitatively and quantitatively, with the advantage that it can readily be applied to aspheric or free-form surfaces for which an analytical approach is difficult or impossible.

Furthermore, rigid tools exhibit an edge-effect due to the change in pressure between tool and workpiece when the tool hangs over the edge. An FEA model is introduced that simulates the tool and workpiece as separate entities, and models the contact between them; in contrast to the non-contact, single entity model reported in literature. This model is compared to experimental results.

Another class of sub-aperture processes does not use physical tools to press abrasives onto the surface. A numerical analysis of one such process, Fluid Jet Polishing, is presented - work in collaboration with Chubu University.

Numerical design of surfaces, required for generating tool-paths, is investigated, along with validation techniques for two test-cases, E-ELT mirror segments and IXO mirror segment slumping moulds.

Conformal tools are not well suited to correct surface-errors with dimensions smaller than the contact area between tool and workpiece. A method with considerable potential is developed to analyse spatial-frequency error-content, and used to change the size of the contact area during a process run, as opposed to the constant-sized contact area that is state-of-the-art.

These numerical methods reduce dependence on empirical data and operator experience, constituting important steps towards the ultimate and ambitious goal of fully-integrated process-automation.

Contents

Listing of figures

List of Tables

For Claudia.

Acknowledgments

The research described in this thesis would not have been possible without the strong support of *Zeeko*. The focus of my research was to better understand and optimise sub-aperture optical fabrication technologies which are used in *Zeeko*'s optical manufacturing machines. On their part, *Zeeko* supported my endeavours and professional development.

My sincere gratitude goes out to my primary doctoral supervisor, Professor David D. Walker, for our always fruitful and interesting discussions, his patience in reviewing my work and teaching me to be accurate in my expressions. I also would like to thank him for reviewing different versions of this manuscript and the many useful improvements he suggested. Similarly I would like to thank Doctors Christopher W. King and Oliver W. Fähnle for our interesting discussions and for reviewing parts of this manuscript.

During the four years of my research I have had help from many of my colleagues, both from *Zeeko* as from *OpTIC*. Too many to name them individually, I would like to take this opportunity to thank them all collectively. Without their support, collegiality and sense of humour my time working on my research would have been a much more difficult one. Special gratitude goes out to Doctors Anthony Beaucamp, Guoyu Yu and Hongyu Li and Mister Zheng Xiao for our fruitful cooperation. And last but not least I would like to thank my office mate and brother in arms, Mister Matt Bibby, for keeping me sane and not drinking all my coffee.

But most importantly, I would like to thank my wife, Claudia, who left home and country to support me in this enterprise.

There are, I understand many problems of economic, medical and sociological interest and importance awaiting study which at present cannot be undertaken because of the formidable load of computing involved.

Douglas Rayner Hartree

1 Introduction

Tools have been used to aid mathematical computation at least since the Sumer invented the abacus around 2700–2300 BC [1], but the rate with which the capacity of such machines improved has increased dramatically in the last century. Chances are that the reader has more processing power in their pocket than was used to send people into space. The IBM AP-101 avionics computer that has been used in the U.S. Space Shuttle was a 450 kIPS (Instructions Per Second) machine [2]. In comparison the Digital Signal Processor in an early model Ericsson cell phone is rated at about 40 MIPS [3].

This trend of performance increase was captured by Moore, when he observed that the number of transistors on a chip grows exponentially, doubling every two years [4] and predicted that this would continue for the near-future. This prediction is refered to as "Moore's law" and has become a self-fulfilling prophecy [5]. Figure 1.0.1 shows the validity of "Moore's law" for *Intel* microprocessors in the seventies, eighties and nineties of last century. This trend can not continue indefinitely as physical limitations on the size of transistors will be reached, but Moore's law is expected to remain valid for the next decade or two [6].

1.1 A brief historical overview of computing

Georges Ifrah provides an exhaustive compendium of the history of computing [1], parts of which are summarised here. The abacus mentioned above aids mathematical computation by representing (intermediate) results, an extension of a persons fingers used to count. Napier's bones, invented in 1617, sped up multiplication and made it more reliable by creating a look-up table using a square rod for each digit of a number. The same inventor, John Napier, devised the

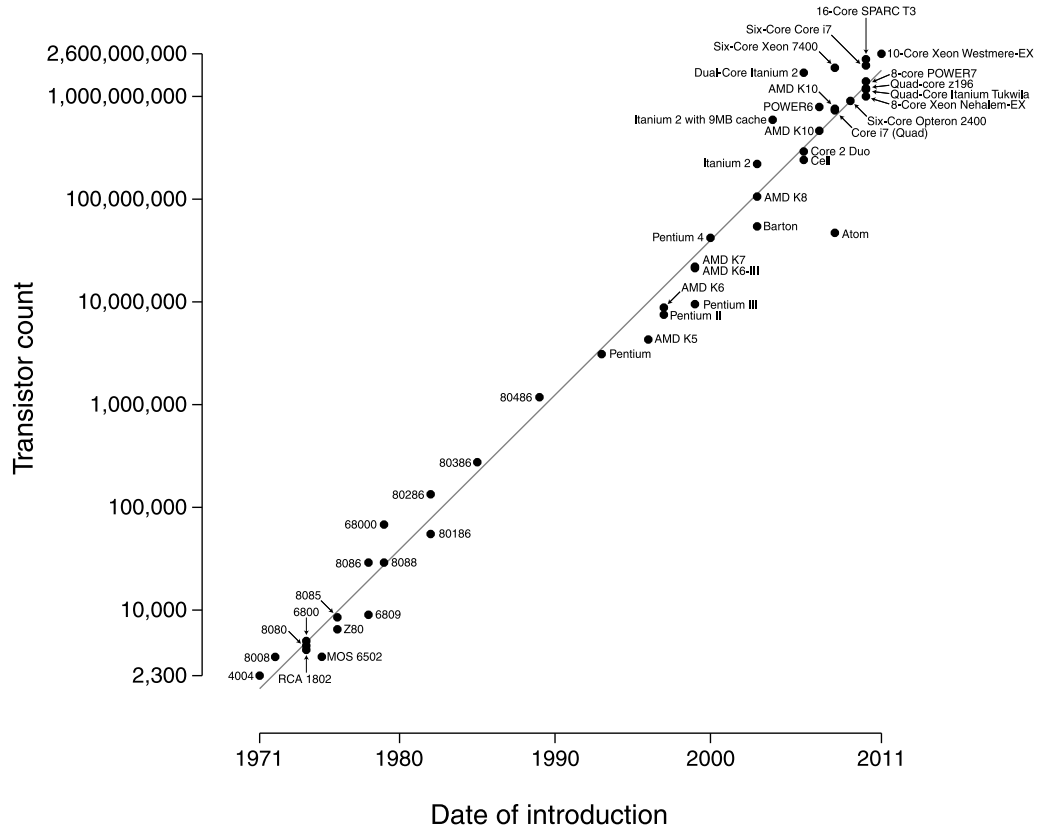

Figure 1.0.1: Evolution of the transistor count of different generations of microprocessors demonstrating "Moore's" law. © Wgsimon / http://commons.wikimedia.org/wiki/file:moore.svg / CC-BY-SA-3.0.

logarithm in 1614 which led Edmund Gunter in 1620 to create the slide rule, an analogue calculation device (where a physical surrogate of the mathematical problem - the analogue - is measured to obtain the desired result).

Although the aforementioned devices help perform computations they can not be considered machines as the operator has to plan and perform the actual action. This changed when Wilhelm Schickard and Blaise Pascal independently developed machines capable of performing addition without intervention of the operator (the former was also capable of subtraction). The first machine to be able to perform the four basic arithmetic operations (addition, subtraction, multiplication and division) mechanically was the Stepped Reckoner conceptualised by Gottfried Leibniz (who also was one of the first to thoroughly study the binary numbering system) in 1673. Charles-Xavier Thomas de Colmar invented a machine in 1820 called "the Arithmometer" that made the calculations more accurate and reliable and was the first to commercialise a calculating machine.

The first to conceptualise a machine that could be (re)programmed to perform any sequence of algebraic operations was Charles Babbage between 1834 to 1836. His Analytical Engine would have read instructions from punched cards, which were invented by Basile Bouchon and successfully applied in the mechanical "Jacquard looms" to define what pattern of threads was woven. Lady Ada Lovelace (née Ada Augusta Byron), the first to code instructions on punched cards, wrote "We can say that the Analytical Engine will weave algebraic patterns, just as

Jacquard looms weave flowers and leaves". The Analytical Engine would also have featured an input/output unit, an arithmetic unit, a control unit (conditional branching and loops) and a memory to store (intermediate) results, but only parts of it were ever built. In 1914 Leonardo Torres y Quevedo showed that it was possible to built an Analytical Engine by using electromechanical components.

From the end of the 19th century the demand for computation increased beyond the capacity of the human "computers". Specific mechanical, electromechanical and electronic machines were built to aid the American census, financial accounting, inventory accounting and code breaking. An example of the last was the entirely electronic "Colossus" calculator design by the British to break Germany ciphers, such as those produced by the Enigma machine, during the second world war.

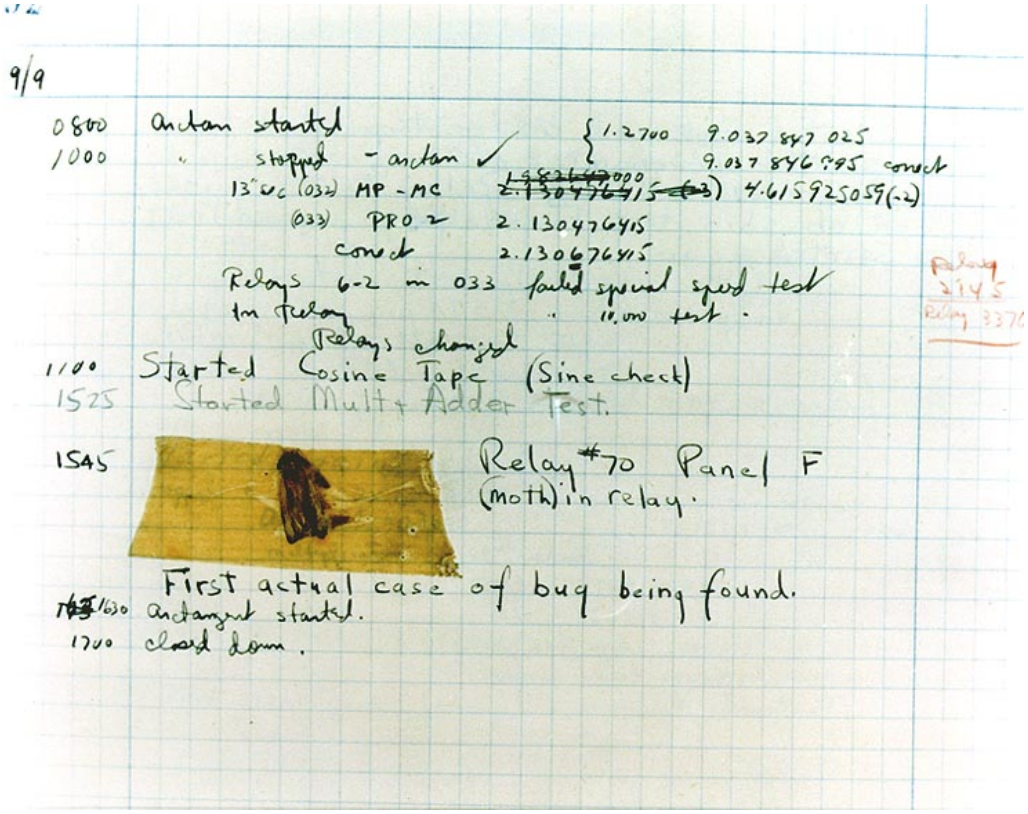

Figure 1.1.1: The First "Computer Bug". Courtesy of the Naval Surface Warfare Center, Dahlgren, Virginia, USA, 1988. U.S. Naval History and Heritage Command Photograph.

Around the same time the first general-purpose reprogrammable calculator, the Harvard Mark I, was designed by Howard Aiken and built by *IBM* and became fully operational in 1944. The Mark I was a mostly mechanical machine as was the Mark II, whose first computer "bug" to be caused by an actual bug (a moth) lead to the introduction of the verb "to debug" [7], a log of which is shown in Figure 1.1.1.

This machine was closely followed by the first completely-electronic, general-purpose reprogrammable calculator, the ENIAC, designed in 1943 by Presper Eckert, John Mauchly and Hermann Goldstine and completed in 1945. It used 18 000 valves and worked 1000 times faster than the Mark I albeit with a reduced reliability.

Although both were reprogrammable and stored (intermediate) results in memory they did not store the instructions in internal memory. Several people independently proposed to do so (e.g. Konrad Zuse in 1936 and Presper Eckert and John Mauchly in 1943) but the theoretical foundation of such machines, was written up by John von Neumann [8] and Alan Turing [9, 10]. Two of the most notable earliest stored-program, completely-electronic, general-purpose reprogrammable calculators (or computers) were the Manchester Mark I and the EDVAC, which both became operational in 1949. The conceptual advantage of storing the instructions in memory is that they can be treated in the same way as data, which means they can be changed by the program itself allowing such concepts as conditional branching and subroutines. Georges Ifrah [1] defines such a machine, a computer, as:

> *"A computer is an artificial automaton comprising a facility for input and output, a memory, a processor capable of effecting all sorts of transformations on data expressed in the form of character-chains (material representations of encoded data) and which, within the limits of its physical capacities, permits the execution of all types of symbolic calculations (and thus the solving of all problems where the solution may be expressed in the form of an algorithm), governed by a control unit instructed by programmes input into the memory (and thus handling the commands to be enacted in the same way as the data to process)."*

The computers that came after followed the same architecture but several major technological improvements have been developed so that they can be grouped in generations. The first generation made us of the valve, which were much faster than their electromechanical equivalents but also expensive (to purchase as well as in use), prone to malfunction and generated substantial amounts of heat.

The second generation computers was introduced in the second half of the nineteen fifties and replaced the valve with the newly developed transistor and combined electrical components on printed circuits. This reduced the size and cost and made them faster and more reliable.

The next decade saw the development of the integrated circuit, which allowed the thousands of transistors and capacitors to be incorporated in a single semiconductor device, or "chip". The third generation of computers applied this technology which resulted in a much lower cost and size.

In 1971 the microprocessor was invented, an integrated circuit which combined memory, input and output devices, a control unit and a processing unit using technology called Very Large-Scale Integration. The fourth generation resulted in essence in a computer on a chip, which saw the development of the "personal computer" for the individual user.

The evolution of technology has brought the cost of computers down orders of magnitude enabling their application in a wide range of fields including science, engineering, finance and entertainment, as long as an algorithm can be devised to produce the desired outcome. In principle any algorithm might be performed by a person (or collection of persons) but in practice the performance will be too slow and too prone to errors to produce results in a

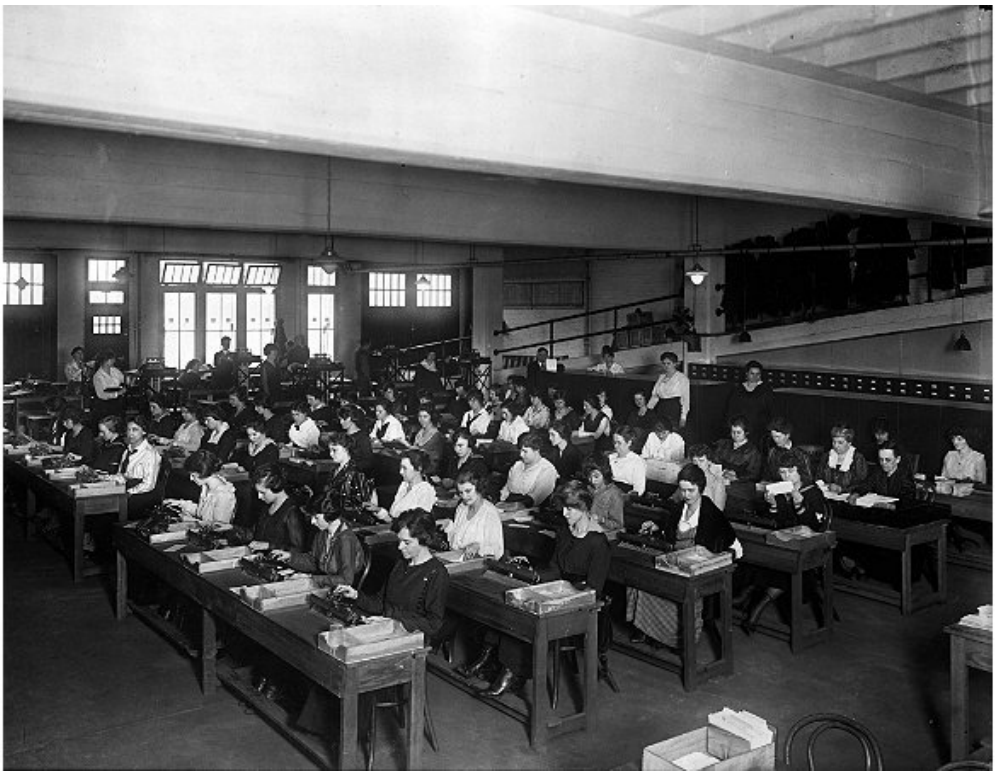

Figure 1.1.2: Picture of "human computers" in Washington, D.C., circa 1920. Courtesy of the Library of Congress, Washington, D.C., USA.

reasonable time frame for many. The advent of the computer therefore unlocked the application of previously infeasible algorithms spawning the science of studying algorithms, "Computer Science". The application of computers therefore is limited by our ability to devise algorithms to perform the desired task.

1.2 Numerical methods in manufacturing

One such application of computers is in manufacturing. Automation in the production process is used for a variety of reasons (e.g. worker safety, cost reduction, increased output and reduction of errors). An early example of the automation in manufacturing has been mentioned previously describing the "Jacquard loom". Early automation mechanically reproduced motion from templates until in the early nineteen-fifties machines were built that used computer numerical control (CNC) [11, 12]. The desired movement steps are input through some information carrier and the machine itself controls the motors based on feedback.

Computers also had an impact on the design of products. Previously technical drawings were produced by hand, a labour intensive process. In computer-aided design (CAD) the drawing is prepared on a computer which results in a numerical representation which can be easily saved and re-used later. It can also easily be shared in numerical format for use in other processes. For example in the engineering analysis of the design using computer-aided engineering (CAE) software or in preparation of manufacturing using computer-aided manufacturing (CAM) software.

As can be seen from the previous sections, the computer has found a place in every step of the

manufacturing process, from the initial product design to the final fabrication. It has made these steps easier to perform, allowed the introduction of new techniques and made easier to share information between these steps.

The above justifies the question whether numerical methods can be used to aid the manufacture of optics. To answer that question one first has to analyse how optics are manufactured and how numerical methods are currently used to produce optics to identify areas where they could be introduced or improved.

1.3 Optical fabrication

Ever since the manufacture of glass optics for non-ophthalmic applications started early in the 17th century it has been primarily a subtractive process[1]. Starting from an oversized block of raw material chunks of smaller and smaller dimensions are removed until the desired lens remains, similar to the approach taken by an artist to create a sculpture. Likewise the manufacturing of optics was more of an art form than science where the quality of the optic depended on the skills and experience of the craftsman, who learned the trade from a master optician as an apprentice. To a certain extend this is still true in the current day and age. But the manufacture of optics was not only the domain of craftspeople, some notable scientists occupied themselves with the production of optics: Descartes, Fermat, Galileo, Hooke, Huygens, Kepler, Newton, Spinoza, Torricelli [14]. For instance Huygens improved the geometry of the machinery to produce optical surfaces with less deviations from the desired form [14] and Newton was the first to documented the use of a pitch lap [15, 16].

Williamson [17] identifies four tasks that need to be accomplished to produce a glass optic subtractively:

- Shaping - creation of the shape of the optic by cutting away parts
- Grinding - forming of surfaces close to specification by wearing away material
- Polishing - creation of a specular surface free of (subsurface) damage
- Figuring - correcting the specular surface form to meet specification

These tasks may be accomplished sequentially in the order as shown above but variations are also possible. For instance Polishing and Figuring may be accomplished in parallel using the same process or part of the Shaping of the external geometry may be done after the optical surfaces have been finished.

Traditionally the processes applied to accomplish the last three of the mentioned tasks involve rubbing abrasive particles on the surface. Preston [18] empirically arrived at Equation (3.1) that states that more material is removed if the abrasives are rubbed on the surface harder, faster or longer.

[1] An alternative to this subtractive approach was developed at the end of the last century in the form of the precision moulding of glass [13], a replicative process.

To accomplish the task of grinding in the least amount of time the abrasives are pushed onto the surface (traditionally by a metal plate called the "lap") with enough force to cause cracks formation and material is removed in flakes. This leaves a rough (non-specular) surface with subsurface damage (cracks) up to a certain depth. This depth is approximately 1.4 times the size of the abrasive particles used [17].

A subsequent process is needed that is capable of removing material without introducing additional cracks in the surface and leaves a smooth, specular surface and enough material has to be taken away so that all the subsurface damage left by the previous step is removed. Traditional polishing techniques rub a polishing abrasive more softly onto the surface by applying a lap with a compliant layer (typically cloth, polyurethane or pitch). Although researched by many [19–29] the removal mechanism during the polishing of glass is not well understood [17]. Evans [30] identifies four main hypotheses:

- Abrasion - material removal by mechanical fracturing similar to grinding
- Flow Hypothesis - plastic flow of locally softened glass by frictional heating
- Chemical Hypothesis - formation and removal of a hydrated, gel-like surface layer
- Friction Wear Hypothesis - glass surface atoms form a bond with polishing grains which is stronger than that with the bulk material

These hypothesis can be grouped in two categories: the first two are purely mechanical removal mechanisms while the latter pair are chemical-mechanical. None of the mentioned hypotheses describe completely all aspects of glass polishing and the development of hybrid hypotheses is still ongoing [30].

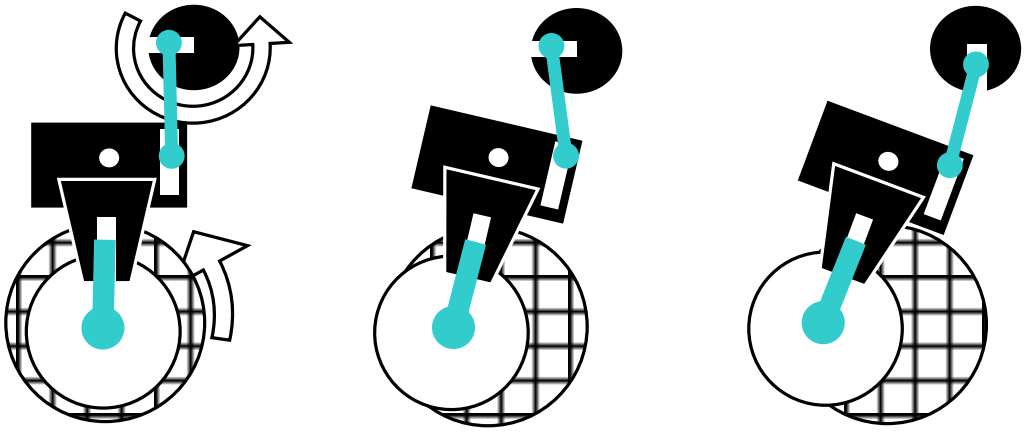

Figure 1.3.1: Diagram showing a traditional overarm spindle polishing machine. © R. Williamson [17]. Reprinted with permission.

In traditional, craft manufacture of optics the figure of the polished surface is controlled by adjusting the parameters (e.g. how fast the optic is rotated, the sweep of the lap and/or the weight pressing both together) of the polishing machine, see Figure 1.3.1. Every now and then the optician measures the optic (e.g. by comparing to a reference test piece or by measurement

with an interferometer) and adjusts these settings to correct the observed surface errors[2]. The convergence of this process depends on the skill and experience of the optician and also how practised he or she is. For instance if an experienced optician doesn't routinely polish high quality optics it will take several months to regain his proficiency as the skill needs to be maintained as well as honed [31]. In this day and age the craft manufacture of optics is still relevant because of the capability to produce spherical surfaces and shallow aspheres with a high form accuracy ($\frac{\lambda}{20}$) at low cost. For the manufacture of steep aspheres and free-form surfaces an alternative fabrication method has been developed.

1.4 Deterministic corrections

The seventies of last century saw the introduction of Computer Controlled Optical Surfacing (CCOS) also know in literature as Computer Controlled Polishing (CCP) and Computer Assisted Optical Surfacing (CAOS) [32–35]. Instead of relying on the expertise of an craftsman (optician) to correct the surface of an optic the process is automated by applying computational power. The misfigure of the surface and the removal characteristics of the process are measured and quantified after which a computer algorithm calculates the process parameters to be used.

The removal of the process is characterised by what is alternatively known in literature as the "influence function", "removal profile" or "footprint". This function reflects the removal per unit of time as a function of the position within the working area of the process. The process is assumed to be linear in time and therefore the removal at a point on the surface, $R(\vec{x})$, depends on where the process is held on the surface, $\vec{x}_p$, how long it is held there, the dwell time $d(\vec{x}_p)$, and the influence function of the process, $f(\vec{u})$,

$$R(\vec{x}) = d(\vec{x}_p) \cdot f\left(\vec{x} - \vec{x}_p\right) \tag{1.1}$$

If the process is moved over the surface of the workpiece along a path $P : \vec{x}_p(t)$, which is a smooth curve, then the velocity along the path at any time t equals

$$\vec{v}(t) = \left.\frac{\mathrm{d}\vec{x}_p(t)}{\mathrm{d}t}\right|_t \tag{1.2}$$

and thus the dwell time over an infinitesimal part of the curve, ds, equals $\frac{\mathrm{d}s}{\|\vec{v}(t)\|}$. Therefore the combined removal when the process is moved along the complete path becomes

$$R(\vec{x}) = \int_P \tfrac{1}{\|\vec{v}(t)\|} \cdot f\left(\vec{x} - \vec{x}_p(t)\right)\ \mathrm{d}s \tag{1.3}$$

$$= d \otimes f \tag{1.4}$$

the convolution of the dwell times with the influence function of the process along the path.

[2] The words "surface error", "surface misfigure", "form error" and "form misfigure" are used interchangeably in this thesis and are understood to have the same meaning.

The desired removal is equal to the misfigure (also known as surface error) present on the surface beforehand, $e(\vec{x})$, however not always does a (practical) dwell time function exist to achieve this removal. For instance limitations exist on the maximum acceleration and maximum velocity that a machine can achieve and therefore there exists a minimal dwell time. Long dwell times do not impose a hard limit as such but in practice the method loses its usefulness if the total process time takes too long. To find the dwell time function that results in a minimal misfigure of the surface a computer algorithm minimizes the predicted residual errors, $r(\vec{x})$,

$$r = e - d \otimes f \tag{1.5}$$

The minimal residual errors reachable do not only depend on machine limitations but also on the influence function of the applied process and measurement errors. For instance if the misfigure consisted of a narrow bell curve then a process with an influence function shaped as a broad bell curve will be able to lower the peak of the misfigure but at the same time create a trench around the original misfigure. Therefore processes used in CCOS generally have a working area that is significantly smaller than the aperture of the surface that is to be corrected, so-called sub-aperture processes.

The actual residual errors after processing the surface also depend on how well the influence function describes the actual removal during processing. Many factors may cause variation of the removal, depending on the specific process used, for instance the temperature, pH value or concentration of abrasive particles. If the variation of the removal can be parametrised the influence function can be modified to take this into account. For instance if the influence function varies (slowly) over time in a known manner it may be modified to become $f(\vec{u}, t)$. However, uncompensated variation in removal causes residual errors and therefore the relevant factors must be controlled for a specific process to be sufficiently predictable for use in a deterministic procedure such as CCOS.

In the following several sub-aperture optical fabrication technologies are described and compared.

1.5 Application of abrasives

Optical fabrication technologies can be divided into two main categories: fixed abrasives (in literature also referred to as bound abrasives) and loose abrasives (in literature also referred to as free abrasives). The latter includes a sub-category where the abrasive particles are not pushed onto the surface by a (solid) tool but through other means (e.g. the hydrostatic pressure in a fluid jet). The name "toolless abrasives" is used here to describe this sub-category.

1.5.1 Fixed abrasives

Since the 1980s techniques have been developed to bind abrasives, generally diamonds, in a solid tool made from a softer material (e.g. cast iron) [36]. A diagram showing these fixed abrasives is shown in Figure 1.5.1. Even though the abrasives wear during the process they will

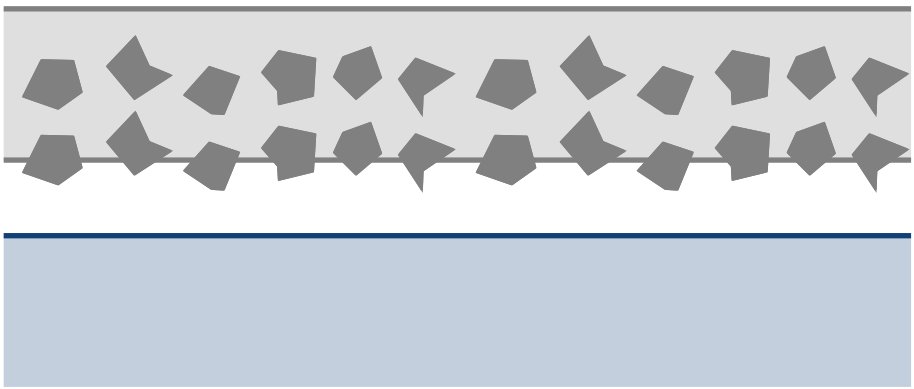

Figure 1.5.1: Diagram showing fixed abrasives embeded in the tool (top) before being pressed onto the workpiece (bottom).

always be exposed as the matrix material wears faster. When enough of the abrasive and matrix is worn down the matrix can no longer keep hold of what is left of the particle and it comes lose, exposing new abrasives underneath. To prevent form errors due to tool wear the tool-path must compensate for the expected wear of the tool.

The abrasive action of the fixed particles has a higher removal rate than if the particles were allowed to roll, however the increased stress introduced on the workpiece may lead to increased subsurface damage in the workpiece [17]. To remove heat (which can cause fracture of the workpiece) generated by the process a coolant, generally water-based, has to be continuously fed into the interface between tool and workpiece. This coolant also removes workpiece debris and rouge abrasive particles (that have been released from the matrix).

The advantages of fixed abrasives are:

- Abrasive removal process provides a high removal rate
- Clean process as only the addition of coolant is required
- Continuous re-dressing of the tool by the workpiece ensures sharp abrasive particles are always exposed on the surface of the tool

Drawbacks of using fixed abrasives are:

- Loosened abrasive particles caught between tool and workpiece may cause a scratch on the surface
- Tool wear leads to form errors if not compensated
- Possibly increased subsurface damage due to higher stress introduced on the workpiece
- Positional errors of the tool are directly replicated into the surface

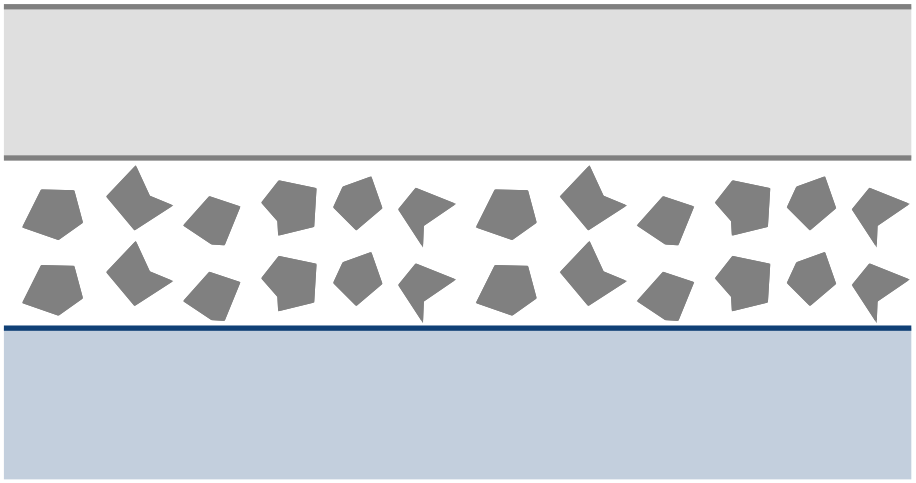

Figure 1.5.2: Diagram showing loose abrasives between the tool (top) and workpiece (bottom).

1.5.2 Loose abrasives

Loose abrasives are mixed with a carrier fluid, generally water based, to form a slurry and are introduced in the interface between tool and workpiece, see Figure 1.5.2. This method has been used since the 1600s when people started to manufacture glass lenses for telescopes and microscopes. According to Preston [18] the amount of material that is removed from the workpiece per unit of time is proportional to the pressure with which the particles are pressed onto the surface and the relative speed between tool and workpiece. The particle size also influences the removal rate as well as the surface quality (e.g. roughness or subsurface damage) therefore a narrow distribution of particle size is preferred to promote uniformity of the surface. The particles wear of fracture over time and have to be replaced by new or fresh ones. This replenishment can either be a total loss system or a continuous recycling system. As the removal rate is also dependant on the concentration of particles in the carrier fluid it has to be controlled to ensure surface uniformity. Other parameters that may influence removal rate or surface quality and therefore may need to be controlled are slurry temperature and pH value.

The advantages of loose abrasives are:

- Low cost tooling compared to fixed abrasives
- In situ cooling and debris removal by the slurry
- Flexibility as the same tool can be used with different abrasives
- Tolerant to positional inaccuracies of the machine

Drawbacks of using loose abrasives are:

- Dirty process, workpiece and machine must be cleaned after processing
- Slurry maintenance is important to guarantee a consistent process
- Tool wear leads to form errors if not compensated

1.5.3 Toolless abrasives

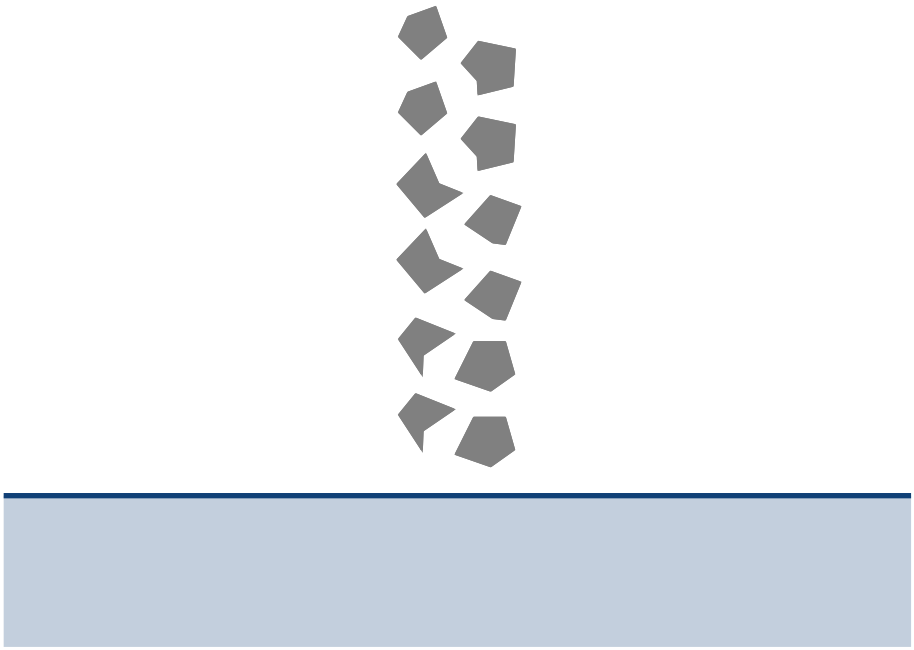

Figure 1.5.3: Diagram showing toolless abrasives pressed onto the workpiece (bottom) by inertia.

As mentioned toolless abrasives are a sub-category of loose abrasives and as such inherent some of the (dis)advantages. The difference however is that the abrasive particles are not pressed onto the surface of the workpiece by a physical object but through some other means. These other means vary greatly between processes, which have started to be developed since the 1980s, and one example is Fluid Jet Polishing were pre-mixed slurry is forced through an orifice forming a jet that impinges the surface of the workpiece, shown in Figure 1.5.3. The means of providing the contact force of the abrasive particles generally require high tech machinery, the complexity of which varies depending on the chosen process.

There are several advantages due the absence of a tool. Rigid tools need to match the local form of the workpiece or uneven removal results, Chapter 2 describes this in more detail. Therefore toolless abrasives are specifically suited for the processing of aspheres and free-form surfaces as their local form varies. Furthermore, there is no tool to wear and thus a highly stable process can be achieved if the process parameters are sufficiently controlled. Also, in the absence of mechanical contact, no stressing of the workpiece takes place and the processes

doesn't suffer from an edge effect due to the change in pressure between tool and workpiece when it is (partly) hanging over the edge. Chapter 3 investigates this last effect in more detail.

The advantages of toolless abrasives are:

- In situ cooling and debris removal by the slurry
- Stable process as there is neither mismatch nor tool wear
- No stressing of the workpiece
- Stable removal profile when the process moves out over the edge

Drawbacks of using toolless abrasives are:

- Potentially high cost of machinery
- Depending on the process, workpiece and machine may need to be cleaned after processing
- Slurry maintenance is important to guarantee a consistent process
- Low removal rate

1.6 Sub-aperture optical fabrication technologies

There exist many sub-aperture optical fabrication technologies many of which have multiple variants. Some of them are well established (as for instance Ion Beam Figuring) while others have been applied only in university laboratories and still have to find their way into industry (e.g. Rigid Conformal tools). Below a selection of sub-aperture optical fabrication technologies is discussed which is by no means exhaustive but should give an overview of the wide range of processes that exist.

1.6.1 Fixed abrasive grinding

The removal mechanism of fixed abrasive grinding of glass is brittle, shear stresses cause cracks to form and material is removed in flakes. Generally the tool is cupwheel shaped and can be made with different hardness and abrasive size as required. The process has a relatively large removal rate and leaves a non-specular surface.

The purely mechanical process produces significant heat and requires in-situ cooling. Machining inaccuracies due to flexing and vibration of the machine and wear of the tool cause surface form errors but as a subsequent process is required to produce a specular surface and to take out the subsurface damage these can potentially taken out at a later stage. The cost of machinery covers a wide range depending on the required accuracies.

1.6.2 Single Point Diamond Turning

Single Point Diamond Turning is a well established process for the manufacture of optical surfaces [37, 38]. The tool is made up of a single, relatively large crystal (which can be considered a fixed abrasive) with a sharp edge that scoops out material from the surface, generally along a spiralling path hence the name.

To produce a surface free of fractures the removal mode has to be ductile. This makes the process specifically suitable to process soft ductile materials such as metals and plastics. If the indentation depth of the tool is controlled carefully then brittle crystals can be processed in the ductile regime as well [39]. Research into the diamond turning of glasses is on-going [40–43].

As only a small part of the tool is in contact with the workpiece during the purely mechanical process it wears relatively quickly degrading performance and requiring tool replacement. The precise control of the indentation depth of the tool requires stiff, low vibration and accurate machinery resulting in a considerable cost of hardware.

1.6.3 Ion Beam Figuring

Ion Beam Figuring [44, 45] is a toolless abrasive process where the workpiece is placed in a vacuum chamber and bombarded by a focused ion beam which removes surface atoms from the workpiece in a sputtering process. The removal profile is very stable allowing very accurate form corrections however the removal rate is very low and the process is not capable of smoothing a surface. This makes the process most suitable as a final finishing step. It is capable to correct surfaces up to the physical edge as the removal profile does not change when the beam leaves the surface. The necessity of a vacuum chamber makes the process cumbersome (especially if the workpiece needs to be removed for measurements) and less suitable for mass production.

1.6.4 Elastic Emission Machining

Elastic Emissions Machining [46] is a purely chemical removal process as the abrasive particles are not pressed into the surface by force. When an abrasive particles comes into close proximity of the surface of the workpiece there is a chance that atoms in the surface of the workpiece bond to the abrasive particle instead. The probability increases if the atom is protruding from the surface. Elastic Emissions Machining increases the number of interactions between abrasive particles and workpiece atoms by creating a localised, high speed, laminar flow of slurry over the surface of the workpiece. This is achieved by submerging the workpiece in a bath of slurry and bringing a spindle mounted polyurethane sphere in close proximity with the surface. As the sphere spins it accelerates the slurry through the gap between sphere and workpiece. The gap is larger than the particle size to prevent mechanical contact.

Initially the process has been applied to create very smooth plano surfaces, but more recently the polishing of steeply curved surfaces has been reported [47]. The toolless abrasives have to be carefully chosen for their chemical reactivity with the material of the surface which limits the flexibility of the process somewhat. The process results in surfaces with low roughness but suffers from a low removal rate.

1.6.5 Plasma Assisted Chemical Etching

Another toolless abrasive process is Plasma Assisted Chemical Etching [48, 49] where in a chamber a capacitively coupled plasma (CCP) is generated by a RF electric field. One side of the chamber is open and brought in proximity of the surface of the workpiece. The energy of the plasma generated ions is not enough to cause sputtering of the surface but sufficient to cause a chemical reaction of which the gaseous product are transported away to the sides. Due to the low energy the temperature of the surface of the workpiece is not raised significantly. The process smooths the surface and leaves little or no subsurface damage and has a constant removal profile when it is moved out over the edge of the workpiece. A suitable gas has to be chosen that reacts with the chemical composition of the workpiece.

Reactive Atom Plasma Technology

Reactive Atom Plasma Technology (RAPT) is a very similar process where the inductively coupled plasma (ICP) is generated by time-varying magnetic field generated by a coiled electrode [50].

Plasma Chemical Vaporization Machining

A related process called Plasma Chemical Vaporization Machining (Plasma CVM) [51] creates the plasma at a higher pressure and has a higher removal rate.

1.6.6 Ductile grinding

The removal mechanism in normal grinding is brittle: shear stresses cause cracks to form and material is removed in flakes. However if the indentation depth is kept low enough then the energy required for fracture is higher than the energy required to plastically deform and thus the removal mechanism becomes ductile [52].

The precise control of the indentation depth of the tool requires stiff, low vibration and accurate machinery and cooling of the tool to prevent thermal growth resulting in a considerable cost of hardware.

1.6.7 Magnetorheological Finishing

Magnetic iron particles and water form a magnetorheological fluid that stiffens when an magnetic field is applied. If abrasive particles are added then they are pushed to the surface of the fluid in the magnetic field. These properties have been exploited in a polishing machine where a ribbon of magnetorheological fluid is delivered onto the rim of a wheel and rotates into a magnetic field and stiffens. After the fluid leaves the magnetic field it separates from the wheel due to inertia and is collected and recycled. The workpiece is held so that its surface contacts the stiffened part of the fluid ribbon which pushes the abrasive particles on its surface against the workpiece [53]. The process has a very stable removal profile which allows very accurate form correction.

The process uses toolless abrasives as they are pressed onto the surface by the stiffened slurry itself. Achieving the very stable removal profile requires complex slurry management controlling slurry viscosity and pH value to prevent oxidation of the iron particles. Due to the complexity of the process the machinery is relatively costly and the size of the spinning wheel limits what radius of curvatures of concave surfaces that can be processed. The process also doesn't allow the pH value of the slurry to be adapted.

1.6.8 Fluid Jet Polishing and variants

In Fluid Jet Polishing (FJP) pre-mixed slurry is forced through an orifice forming a jet that impinges the surface of the workpiece [54] at speeds much lower than Abrasive WaterJet (AWJ) machining to prevent cracks from forming. A diagram was shown previously in Figure 1.5.3. FJP uses toolless abrasives and the complexity of the machinery required is relatively minor. It is a flexible process as the slurry can be adapted to the requirements by changing e.g. the abrasive compound, the particle size, the pH value, the angle of the jet with respect to the surface normal, the nozzle diameter and/or shape [55] or by injecting or extracting gas from the slurry prior to the nozzle [56–58]. The presence of gas in the slurry facilitates the occurrence of cavitation which leads to an increased removal rate and surface roughness. Although FJP is a relatively novel process many variants have been adopted:

Jules Verne

The smoothing effect on the surface is greatest when the fluid flows parallel to the surface. Instead of a nozzle Jules Verne (JV) uses a pressure chamber brought in close proximity to the surface of the workpiece (similar to PACE) to guide the fluid flow along the surface to improve surface roughness [59]. Several pressure chamber shapes have been investigated [60]. Steep aspheric and free-form surfaces are less suitable to be processed by JV as the change in local radius of curvature causes an uneven gap between pressure chamber and workpiece. Similarly the process breaks down when the pressure chamber (partly) hangs over the edge of the workpiece.

MRF-Jet

Certain nozzle shapes can cause jet breakup to occur before it reaches the workpiece causing irregular removal. If a magneto rheological fluid is used as the basis for the slurry the jet can be stabilised by applying a magnetic field around it [61]. The drawback is the same as with regular MRF, limited options available to adapt the slurry to the material that needs to be processed.

HyDra

HyDra is a tool that accelerates a slurry by creating a vortex in a pressure chamber which floats on top of the expelled fluid film [62].

Plasma Jet Machining

Plasma Jet Machining (PJM) is a combination of FJP and PACE where plasma generated reactive particles chemically react with the workpiece surface without causing subsurface damage. However a different polishing process may be required afterwards as it increases the surface roughness [63].

1.6.9 Precessed Bonnet Polishing

To circumvent the problem of mismatch between tool and workpiece, that rigid tools exhibit for steep aspheric and freeform workpieces, the Precessions™ applies an inflatable (rubber) membrane that is pressed onto the workpiece and the surface of the tool in the contact area conforms to the local form of the workpiece [64, 65]. The membrane is covered with an industry standard polishing pad and loose abrasives are supplied in the interface between tool and workpiece.

The membrane is mounted on the end of a spindle to provide relative motion between tool and workpiece and the axis of rotation is angled with regards to the surface normal to improve the removal profile (the point of zero relative velocity no longer lies within the contact area). This also reduces the relative wear of the tool (specifically the wear of the polishing pad). Precessing the spindle axis around the surface normal achieves a rotationally symmetric removal profile if such is desired.

The process has a very stable removal profile which allows very accurate form corrections and it is flexible as any combination of polishing pad and abrasive compound and size, known to be effective from classical polishing, can be readily applied in the process. As such a large range of removal rates and surface roughness can be achieved. The removal rate can also be controlled somewhat by applying a different "tool offset", a process parameter which defines how far the bonnet is compressed into the surface after initial contact[3]. A larger tool offset causes a larger contact area and higher removal.

1.6.10 UltraForm Finishing

UltraForm Finishing [66] also uses a compliant tool in combination with industry standard polishing pads to prevent mismatch between tool and workpiece. But in contrast with Precessed Bonnet Polishing the polishing pad material is not bonded to the tool but is instead belt-shaped and fed over a spherical compliant wheel which pushes the belt and the supplied loose abrasives onto the surface of the workpiece. The process exhibits the same flexibility and complexity of the machinery as Precessed Bonnet Polishing.

1.6.11 Grolishing

To remove mid-spatial frequency errors left in the surface by grinding an intermediate process called "Grolishing" [67] has been proposed before polishing the surface. Several variants of

[3] "Tool offset" is also known in literature as "bonnet offset", "z-offset" and "plunge depth" and are understood to have the same meaning.

tools and abrasives have been investigated [68] but recent results reported [69] removed grinding marks by applying a compliantly mounted rigid (brass) tool using 9 µm aluminium oxide loose abrasive. One could see this as CNC controlled lapping using a sub-aperture tool. As such, mismatch between tool and workpieces is a potential problem and as such the process is not suitable for steep aspheres or free-form surfaces. The process is very flexible and does not require complex hardware. The process does require a subsequent finishing process step.

1.6.12 Rigid Conformal (non-Newtonian) tool

Compliant tools exhibit a very stable removal profile even on steep aspheres and freeform surfaces because they adapt to the local surface form. This makes these processes well suited for deterministic corrective polishing. However, due to the conformal nature of the tool it has no significant effect on surface errors with similar or smaller dimensions than the contact area: the peaks and valleys of the error will be polished equally, which is explained in more detail in Chapter 2. To remove these small scale surface errors a sufficiently rigid tool of sufficient size so that it preferentially removes material from the peaks and not from the valleys has to be applied. These tools however can not conform to the changes in local form of steep aspheres and freeform surfaces.

A rigid conformal (RC) tool made from a non-Newtonian fluid covered by a membrane will adapt to the local surface form if the change is gradual, which is generally the case for the path a tool takes over the surface. However, it behaves as a rigid tool if the time period it is under stress is short and is capable of almost completely removing spatial frequency errors [70]. The loose abrasive process is flexible as different types of polishing pads and abrasive types and sizes and pH values of the slurry can be applied as required. The complexity of the required machinery is relatively low.

1.6.13 Summary

There are many different sub-aperture optical fabrication technologies each with different properties, which are summarised in Table 1.6.1 for the processes discussed previously. Two figures copied from [71] are presented here as well that plot a graph comparing the roughness of the resulting surface with the surface misfigure or the removal rate of the process, Figures 1.6.1 and 1.6.2 respectively. As follows from the previous discussion there doesn't exist a process that combines the best performance in all categories. Therefore a combination of processes is usually applied (either sequentially or alternately) to achieve optimal results (with respect to total process time, surface misfigure, roughness etcetera).

1.7 Tool-path

In classical polishing the tool travels many times over the surface along different paths with many crossings. This in contrast to CCOS where a sub-aperture processes traverses under

Table 1.6.1: Overview of different sub-aperture manufacturing technologies

	Form accuracy	Edge performance	Machine complexity	Flexibility	Removal rate	Mid-spatials
Fixed abrasive grinding	Poor	Good	Medium	Medium	High	Poor
Single Point Diamond Turning	Good	Good	High	Low	High	Poor
Ion Beam Figuring	Good	Good	High	High	Medium	Poor
Elastic Emission Machining	Fair	N/A	High	Medium	Low	Good
Plasma Assisted Chemical Etching	Good	Good	High	Medium	Medium	Poor
Ductile grinding	Fair	Good	High	Medium	Medium	Poor
Magneto-Rheological Fluid	Good	Fair	High	Low	Medium	Poor
Fluid Jet Polishing	Good	Good	Medium	High	Medium-High	Poor
Precessed Bonnet Polishing	Good	Fair	Medium	High	Medium-High	Poor
UltraForm Finishing	Good	Fair	Medium	High	Medium-High	Poor
Grolishing	Poor	Poor	Low	Low	High	Good
Rigid Conformal	Good	N/A	Low	High	Medium-High	Good

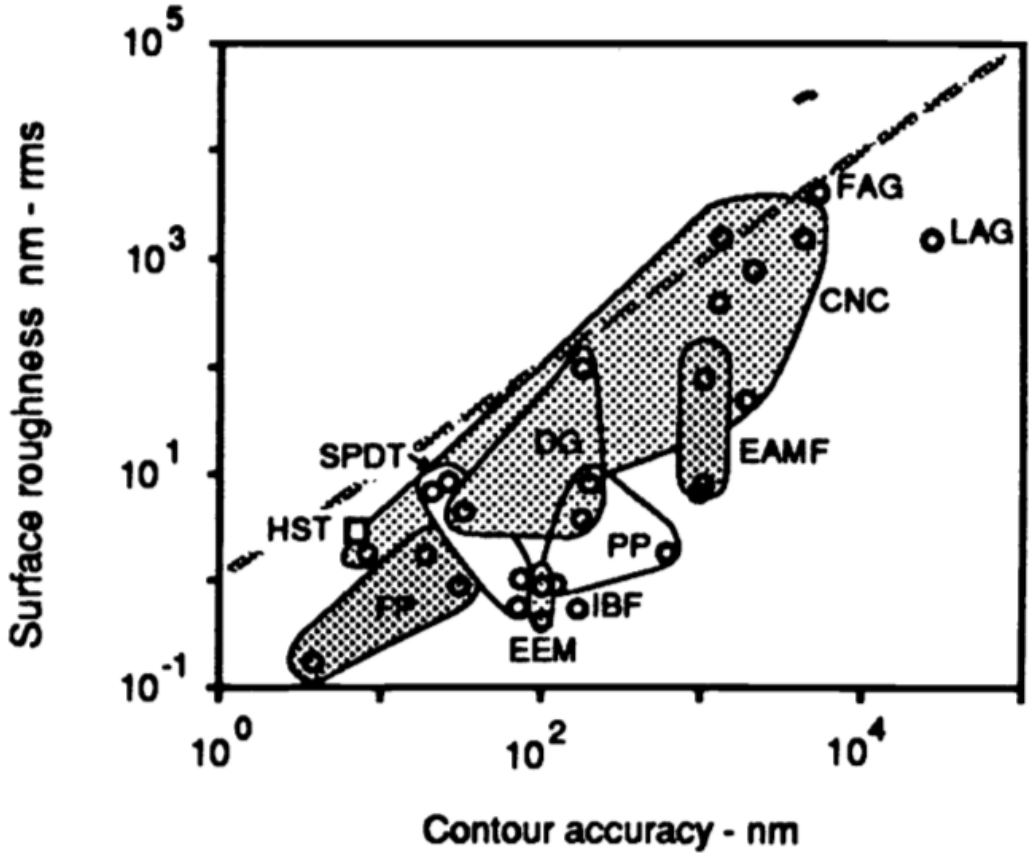

Figure 1.6.1: Comparisson of surface roughness and contour accuracy (misfigure) of several processes. © I. F. Stowers, R. Komanduri and E. D. Baird [71]. Reprinted under the principle of "fair use".

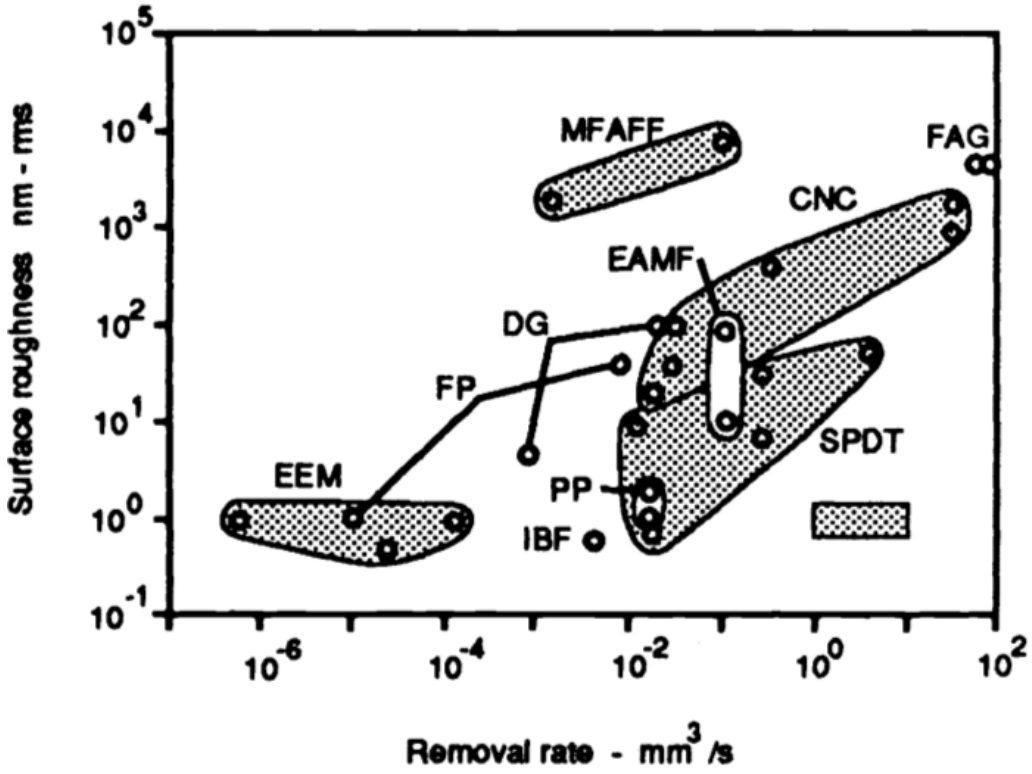

Figure 1.6.2: Comparisson of surface roughness and removal rate of several processes. © I. F. Stowers, R. Komanduri and E. D. Baird [71]. Reprinted under the principle of "fair use".

computer control over the surface of the workpiece along a previously specified, non-crossing tool-path. The dwell time of the process is optimised for each position on the surface of the workpiece to minimize the resulting form misfigure. In general, the misfigure is continuous and therefore the dwell times are continuous as well. If the tool-path features crossings, the machine has to rapidly accelerate and decelerate to make the combined dwell time of all passes over the crossing point equal to the dwell time optimised by the CCOS algorithm. This would lead to surface artefacts due to limitations on the acceleration and deceleration of the machine.

To treat the complete surface of the workpiece, the process has to be traversed along a path that covers it completely. The influence function of most processes extends over a significantly sized area and is non-uniform within that area. To create a uniform removal over the complete surface of the workpiece each point of the working area of the process has to traverse each point of the surface. In praxis this is impractical but can be approximated by applying a tool-path that has the working area overlap multiple past and future tracks of the path. The distance between the current position of the process and the closest of all past and future positions is generally referred to as the "track spacing".

If the track spacing is too large a bump in the surface is left between these two points if the removal of a process goes to zero at the edge of the working area, which is generally the case. This effect is referred to in literature as "cusping". The track spacing where this bump starts to have a significant detrimental effect on the surface figure depends on the specific influence function of the process and total removal but as a rule-of-thumb the misfigure is dominated by other sources if a track spacing is chosen between $\frac{1}{10}$ and $\frac{1}{20}$ of the size of the working area.

Different types of tool-path are possible but the two most common ones by far are raster and spiral tool-paths.

1.7.1 Raster

In a raster tool-path the process sweeps back and forth in one direction while moving in a second, perpendicular direction between sweeps in small increments the size of the track spacing. If only these two dimensions are considered the tool-path has a constant track spacing. However one has to consider the tool-path projected onto the surface of the workpiece and if this surface is curved then the track spacing is no longer uniform. For steeply curved surfaces this causes non-uniform removal and significant surface misfigure unless corrective measures are taken.

As the sweeps are approximately parallel and equidistant so is any signature put into the surface due to the spacing between tracks (the bump referred to in the previous section). Even though the total misfigure of this signature may be within the required tolerances their total diffraction effect may become problematic.

1.7.2 Spiral

A spiral tool-path is generally used for rotationally symmetric surfaces with circular shaped apertures and can have one end-point on the edge of the aperture and one in the centre or both

end-points on the edge. If both end-points lie on the edge of the aperture then the tool-path goes through the centre and spirals outwards again between the tracks of the inward spiral.

The signature due to the spacing between tracks is similar in shape as concentric, equidistant circles which again may present a problem due to diffraction.

1.7.3 Pseudo-random

To prevent the diffraction problem Dunn et. al [72] propose the pseudo-random tool-path, which is non-crossing just as the raster and spiral tool-paths. As such the dwell times calculated by the CCOS algorithm for either of the other paths can be applied to the pseudo-random tool-path without modification. The tool-path is created by connecting points on the surface randomly using corners of 60° and multiples thereof. As such each generated path on the same surface will be different in practice. The density of the points can be specified in analogous of the track spacing of the other two tool-paths.

As the tool-path does not have a periodic structure it is shown [72] to produce a surface that does not exhibit a peak in the PSD graph associated with raster polishing. However the influence of the numerous and sharp corners on the surface figure has not been reported. This may be problematic as the acceleration and deceleration capacity of machine axis is limited potentially causing inaccurate dwell times.

1.8 Tool control

In general CNC axes move the process tangentially to the surface along the tool-path. If the process makes use of a physical tool to push the abrasives onto the surface the position of the tool perpendicular to the surface can be controlled by two different methods, feed control and load control.

1.8.1 Feed control

If feed control is applied the position of the tool perpendicular to the surface is also controlled by CNC axis and stiff mounting of the tool following the pre-defined tool-path. The pressure between tool and surface increases rapidly with increasing tool offset and subsequently decreases rapidly when material is removed, as the tool is not fed after the receding surface. Therefore the resulting surface will be an almost exact copy of the path of the tool, including any position inaccuracies of the machine and wear of the tool. This method does not lend itself for use in dwell time based corrective polishing as the removal is not linear in time. A large range of pressures may be encountered between tool and workpiece.

1.8.2 Load control

The opposite is true for load control of the position of the tool perpendicular to the surface where the pressure between tool and workpiece is held more or less constant. This can be accomplished through different means, for example by weight, pneumatic force or a preloaded spring, and the tool is fed after the receding surface. As such the removal is approximately linear

in time and dwell time based corrective polishing is possible using this method. Therefore a-priori knowledge of the surface misfigure is required.

1.9 Outline of the thesis

The aim of the work described in this thesis was to develop and investigate numerical methods to aid in the manufacture of challenging optics for future astronomical instruments, especially segmented mirrors. Either by applying numerical methods directly in the manufacturing process or indirectly by applying them in the development and optimisation of polishing processes. Two specific case-studies of segmented mirrors have been considered. Foremost is the primary mirror of the European Extremely Large Telescope (E-ELT) that is being developed by the *European Southern Observatory* (*ESO*). Its size will allow, among others, the detection and study of exo-planets, specifically in the habitable zone. The challenges in manufacturing the segmented primary mirror of the E-ELT are the number of segments that will need to be produced and the challenging tolerances imposed on the optical surfaces, specifically in the edge-zones of the segments. Another case-study of a segmented mirror, albeit for a different wavelength application, was the International X-ray Observatory (IXO) mission, specifically the investigation of an alternative manufacturing method of grazing incidence mirror shell segments.

Mid-spatial frequency grinding marks can be removed from an optical surface by applying a recently developed process called "Grolishing". As this process uses a rigid tool to smooth the surface, it can not conform to the changes in local form of steep aspheres and freeform surfaces, which leaves a mismatch between the tool and surface of the workpiece. In Chapter 2, a novel method is introduced to qualitatively and quantitatively analyse the mismatch numerically, which has the advantage that it can readily be applied to aspheric or free-form surfaces for which an analytical approach is difficult or impossible.

Furthermore rigid tools exhibit an edge effect due to the change in pressure between tool and workpiece when they are (partly) hanging over the edge of the workpiece. Chapter 3 investigates this effect, and its relevance to the production of segmented telescope mirrors. A numerical model is introduced that simulates the tool and workpiece as separate entities and models the contact between them, as opposed to the non-contact, single entity model reported in literature. This model is compared to experimental results obtained using a "Grolishing" tool mounted on an industry robot.

Tool-paths are used to traverse sub-aperture polishing processes across the surface of a workpiece. Chapter 4 evaluates a novel tool-path that covers only part of the surface to locally correct edges of mirror segments using a small compliant tool, while leaving the bulk of the surface untreated. The same chapter describes experiments performed to investigate whether it is possible to prevent the creation of a discontinuity in the optical surface at the boundary between the processed and the untreated area.

The advantages of toolless abrasives are: in situ cooling and debris removal, no mismatch nor tool wear resulting in a stable process and no stressing of the workpiece. One such process, Fluid

Jet Polishing, is investigated in Chapter 5 in collaboration with *Chubu University*.

To create the tool-path a numerical description of the desired surface must be produced including the surface edge with reference to the axes of the polishing machine. Any inaccuracies lead to positioning errors of the process which may lead to figuring errors and non-convergence of the corrective polishing process. The numerical design of surfaces is looked at in more detail in Chapter 6 along with validation techniques for two test cases, the E-ELT primary mirror segments and IXO mirror segment slumping moulds.

Compliant tools provide a stable removal profile which is specifically suitable for deterministic corrective polishing. However, due to the conformal nature of the tool it is ill-suited to correct surface errors with similar or smaller dimensions than the contact area, as the peaks and valleys of the error will be polished equally. Chapter 7 introduces a novel method of analysing the surface misfigure with the objective of selecting the optimal size of the contact area along the tool-path: small enough to be able to correct the errors present but as large as possible to increase removal rate and therefore decrease total process time.

Maverick is a word which appeals to me more than misfit. Maverick is active, misfit is passive.

Alan Rickman

2 Aspheric mismatch of rigid tools

2.1 Introduction

2.1.1 Extremely Large Telescopes

In the last decade several projects were started to develop and build a ground-based, filled-aperture, optical telescopes with diameters between 20 m and 100 m. Notable examples of these include

- The Thirty Meter Telescope (TMT) being developed by the TMT Observatory Corporation (a partnership consisting of the Association of Canadian Universities for Research in Astronomy, California Institute of Technology, University of California, Department of Science and Technology of India, National Astronomical Observatories of the Chinese Academy of Sciences, National Astronomical Observatory of Japan).

- The European Extremely Large Telescope (E-ELT), with a 39.3 m diameter primary mirror, by the *European Southern Observatory* (*ESO*), an intergovernmental research organisation for astronomy consisting of Austria, Belgium, Czech Republic, Denmark, Finland, France, Germany, Italy, the Netherlands, Poland, Portugal, Spain, Sweden, Switzerland, United Kingdom and Brazil, whose membership is pending ratification by its parliament.

The aim of these projects is to make new science programs possible that are not available on current, state-of-the-art 8 m class telescopes. Hook et al. [73, 74] provides a list of known science cases enabled by an extremely large telescope (while stressing that scientific progress

based on the use of such telescopes will most likely lead to completely new and unforeseen scientific research areas):

- Detect and study of exo-planets, specifically in the habitable zone
- Observe the formation of planets in proto-planetary disks
- Resolve stellar populations
- Measure the masses of (massive) black holes
- Investigate first galaxies and the physics of galaxy assembly
- Detect low-density inter galactic medium
- Directly observe the expansion of the universe and fundamental parameters

To achieve these goals telescopes with a higher contrast and angular resolution than currently available are needed. As the quantum efficiency of modern CCDs is nearing unity [75] the main way to improve contrast is to increase the light collecting area, which scales with D^2 with D the diameter or the telescope. The performance of current, 8 m class telescopes is close to the diffraction limit [76] due to advances in technology (e.g. the usage of adaptive optics). In that case the signal-to-noise ratio while observing a point source in a large background scales with D^4 [77] furthering the argument for building large telescopes.

Building an extremely large telescope using a monolithic mirror is impractical, the key reasons listed by Nelson [77] are:

- Unavailability of mirror blank material in the required size
- Very expensive mirror results in a high risk of breakage from mishandling
- Vacuum chamber for mirror coatings becomes very large and expensive
- Tool costs for all steps (fabrication and handling) are large
- Shipping is difficult, can't use standard infrastructure (roads, tunnels, containers)

Taking for example the risk of breakage, in Walker et al. [78] a statistical investigation [79] is mentioned that found that the probability of breakage was approximately 6 % for large optics produced between 1960 and 1995.

Unsurprisingly many current and future telescopes are designed utilising segmented mirrors, see Figure 2.1.1, however their use is not without drawbacks [77]: more parts means the telescope is more complex, active position control is needed of the segments, their edges have diffraction and thermal background effects and off-axis surfaces (no local axis symmetry) are more difficult to polish and measure. Due to the effects of segment edges, which are discussed in more detail in Chapter 3, the optical surfaces of the E-ELT primary mirror segments are

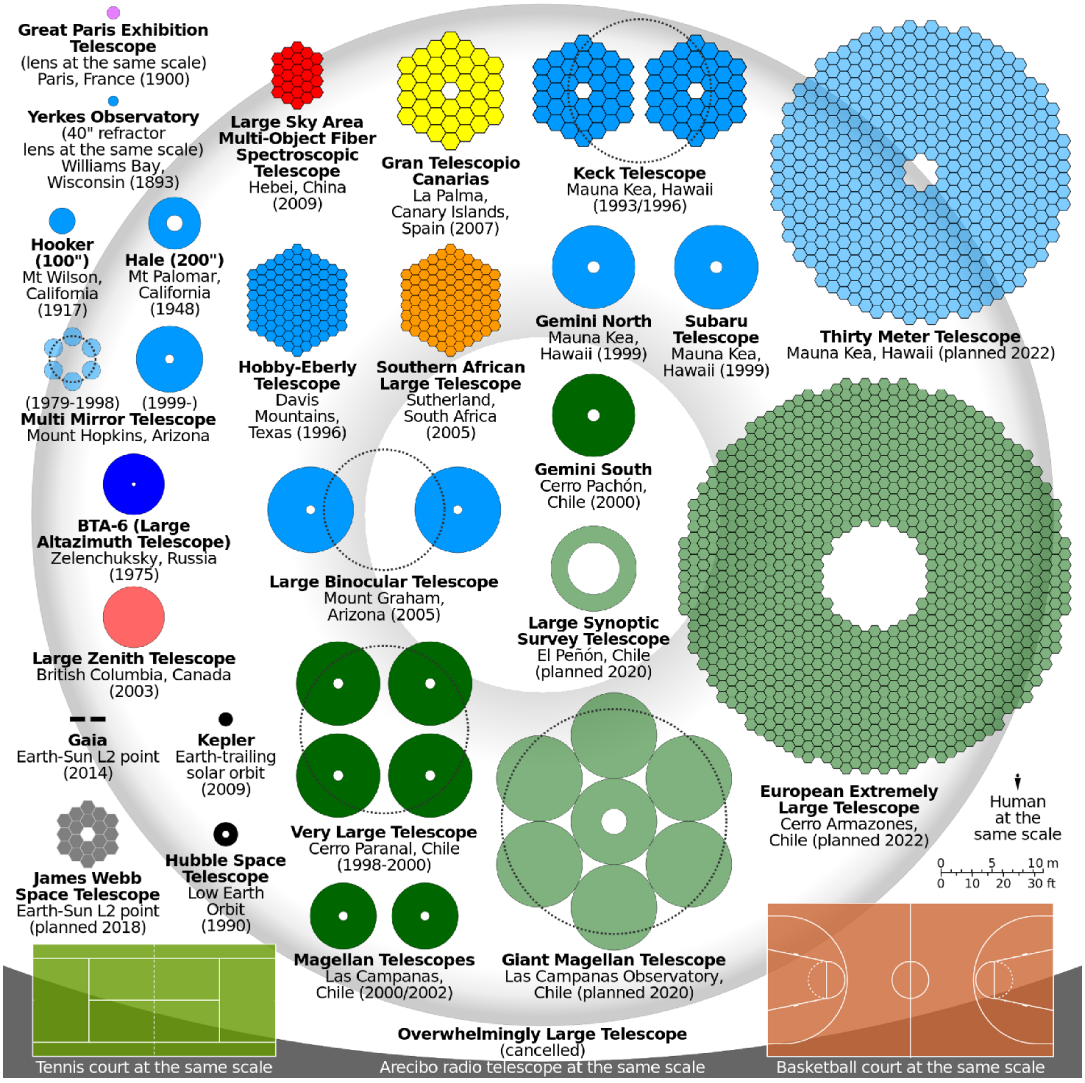

Figure 2.1.1: Comparison of different telescopes that are installed or being developed. © C. M. G. Lee / `http://commons.wikimedia.org/wiki/file:comparison_optical_telescope_primary_mirrors.svg` / CC-BY-SA-3.0. The telescopes are colour-coded by country in which they are located and whether they currently exist (darker shade). Dotted circles show mirrors with equivalent light-gathering ability.

specified up to the physical edge of each segments (apart from a 1 mm bevel at 45°). The total aperture of the E-ELT primary mirror will be 39.3 m and it will consist of 798 segments. A further 133 segments will be produced each of which will serve as a spare for each set of 6 segments in the primary mirror (due to 6-way symmetry). The spares allow the primary mirror segments to be progressively re-coated without any significant telescope downtime. Each segment will have an irregular hexagonal shape around 1.4 m across corners and will be 50 mm thick. The total worth of the segments will be over 100 Me.

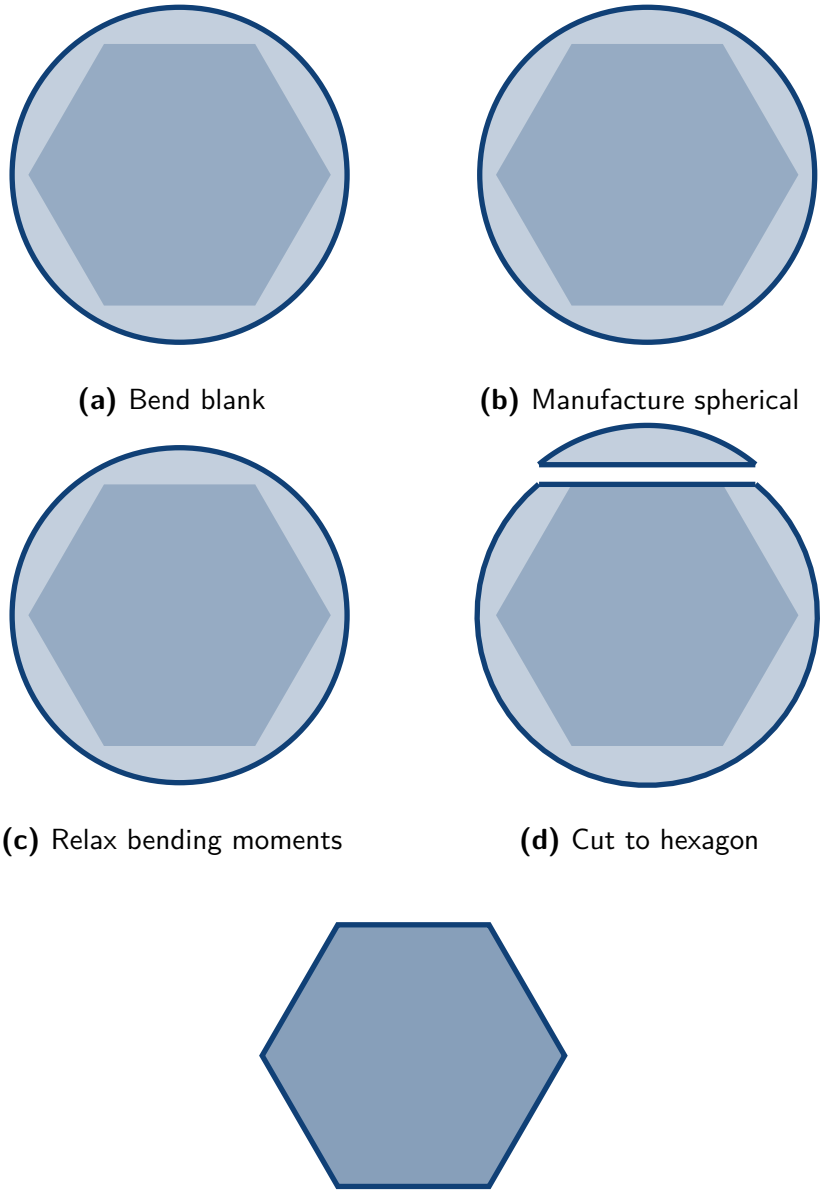

(a) Bend blank

(b) Manufacture spherical

(c) Relax bending moments

(d) Cut to hexagon

(e) Ion Beam Figuring

Figure 2.1.2: Procedure of stressed mirror polishing: first the blank is bent to take out non-spherical components of the surface (a), then it is manufactured spherically (b) and afterwards the bending moments are relaxed (c) and the part is cut to the final hexagonal shape (d), finally the resulting surface form errors are corrected using Ion Beam Figuring (e).

In the past segments for segmented telescopes (e.g. the Keck telescope) have been manufactured using the Stressed Mirror Polishing (SMP) approach [80, 81]: an oversized, round blank is actively deformed forcing upon it the inverse of the non-spherical components of the desired form. This enables the part to be polished using large, spherical tools. Afterwards the bending moments are relaxed and the part is cut to the desired hexagonal shape. This procedure redistributes the internal stresses in the material and causes the surface to deform. Therefore as a final polishing step Ion Beam Figuring (IBF) in vacuum is used which can deal with the aspheric shape of the surface and leaves the edges intact. See Figure 2.1.2 for a diagram of the approach.

Drawbacks of this approach are:

- The danger of damage due to repeated handling between processes and metrology
- Cutting of the final hexagonal shape takes place after significant value has been added by the previous processes
- No process readily available to re-polish after shipping (e.g. to correct segments damaged during transport or at the telescope).

Both SMP and IBF require extensive preparation, mounting and bending the blank and placing the segment in vacuum respectively. This makes the total process chain cumbersome to apply to a total of 931 segments that have to be produced for the E-ELT.

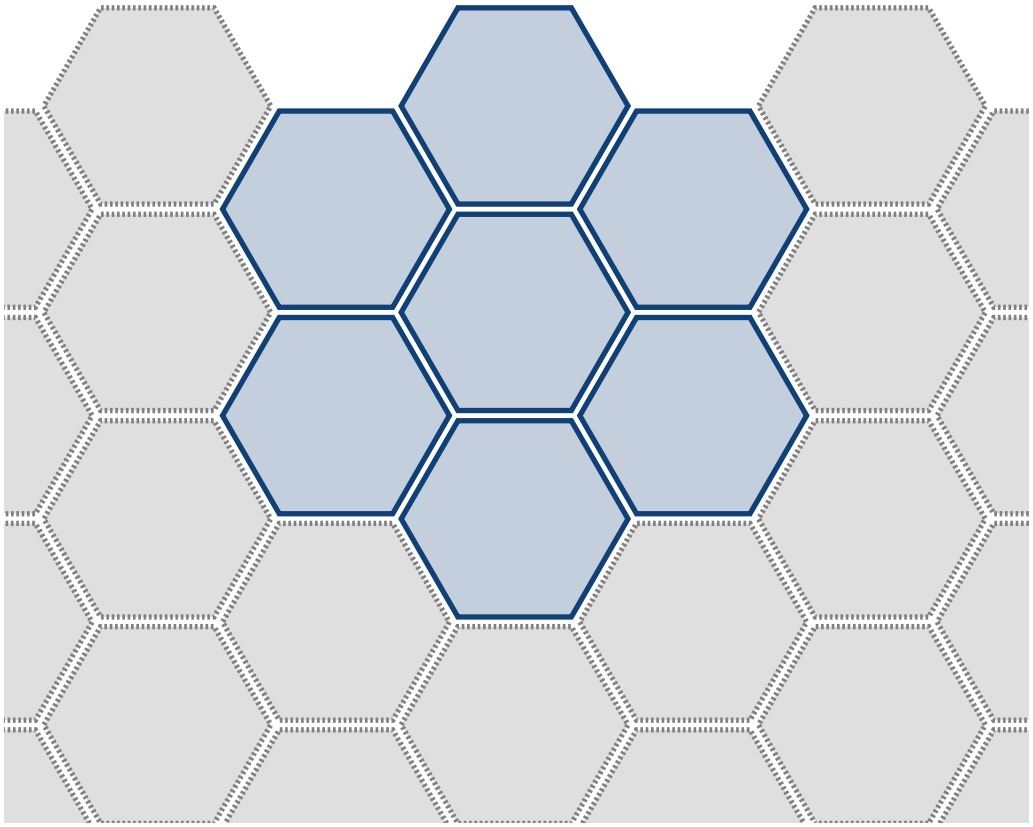

Figure 2.1.3: Diagram showing the position of the selected prototype segments grouped at the edge of the primary mirror, shown at the top of the diagram.

In 2005 *ESO* awarded two contracts to produce prototype segments of the primary mirror of the E-ELT to two different consortia. The selected 7 prototype segments form a group at the edge of the then current design of the primary mirror, which had a base radius of curvature of 84 m and an outer diameter of 42 m. Their full specifications are outlined in the tender document [82]. When the telescope is in operation the segments will deform under their own weight. This deformation changes for different angles of elevation. Therefore, the segments will be mounted in the telescope using warping harnesses, which will actively deform the segments to compensate the low-order terms of this deflection. In the same way the warping harness is able to take out around 90 % of the lower order residual form errors after polishing with the exact percentage depending on the order. All the segments have to be closely matched with regards to their base radius of curvature and conic constant. These are therefore not toleranced separately but included in the overall tolerance on form error.

Table 2.1.1: Summary of the surface error tolerances for the protoype segments of E-ELT's primary mirror specified for the bulk and edge regions. The bulk area has a second specification where set percentages of certain lower order error terms are allowed to be subtracted form the error.

Region	Low-order terms	Measurement	Average	Maximum
Bulk	Included	rms	25 nm	50 nm
	Excluded	rms	7.5 nm	15 nm
Edge	-	PVq (95%)	100 nm	200 nm

The tolerance on form error is specified in two separate regions: the bulk area of the mirror and the edge zone, specified as a 10 mm wide band from the physical edge of the segment. The reasons for this discerner are discussed in more detail in chapter 3. The form error tolerances are summarised in 2.1.1, where one column shows the maximum error for one segment and another the maximally allowed average of all 7 prototype segments.

The consortium led by *Sagem Défense Sécurité* used a variation of the approach outlined previously: instead of Stressed Mirror Polishing an oversized round blank was ground and polished using CNC machines after which the hexagonal shape was cut and the final surface figure achieved with Ion Beam Figuring. Both approaches are driven by the difficulty of polishing cut to final size segments without introducing edge artefacts (e.g. edge roll), which will be discussed in more detail in Chapter 3. The second consortium, led by *Optic Glyndŵr Ltd.* (previously known as *OpTIC Technium* and refered to as *OpTIC* in the rest of this thesis), pursues a different approach: segment blanks are delivered already cut to the final hexagonal shape and are ground and polished using CNC machines while minimising handing and transportation by applying on-machine metrology.

The off-axis aspherical surfaces of the first segments were generated by the *Cranfield University* BoX™ ultra-precision grinding machine [83–85] using a spiral tool-path. Afterwards the *Zeeko Ltd.* Precessions™ bonnet polishing process [64, 86–88] is used to pre-polish and

correct the surface form of the irregular hexagons. The results of processing the first two prototype segments was published by Gray et al. [89].

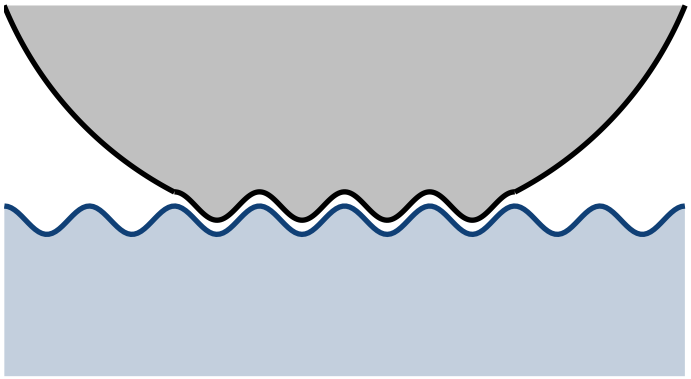

Figure 2.1.4: Diagram showing a conformal tool's inability to correct mid-spatial frequency errors with dimensions smaller than the contact area.

To generate the aspherical surface the grinder uses a cup wheel in point contact mode [90], which achieves low overall surface form errors but introduces mid-spatial frequency marks [69]. A CCOS process applying a conformal polishing tool (e.g. the Precessions™ process) is well suited to correct surface errors that are larger in size than the contact area between tool and surface by applying a different dwell time as needed. However, due to the conformal nature of the tool it has no significant effect on surface errors with similar or smaller dimensions: the peaks and valleys of the error will be polished equally, see Figure 2.1.4.

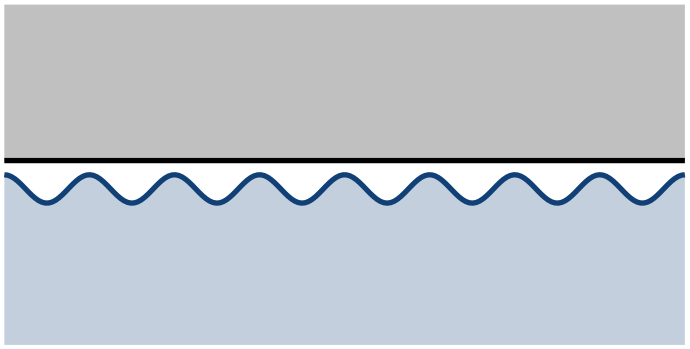

Figure 2.1.5: Diagram showing a rigid tool's ability to correct mid-spatial frequency errors with dimensions smaller than the contact area.

To remove these smaller dimension errors with a bonnet tool the process parameters have to be set so the contact area is sufficiently small (e.g. by using a smaller bonnet or by pressing it into the surface less). However this is impractical for polishing large optics for the following two reasons. Firstly a smaller contact area results in a lower removal rate as it scales roughly with the square of the diameter of the contact area and therefore increases the process time by the same factor. Secondly the removal is effectuated by a smaller area on the tool which leads to more localised wear resulting in deformation of the tool causing an non-uniform removal process over different parts of the processed area leading to surface errors.

The preferred approach therefore is to apply a sufficiently rigid tool of sufficient size so that it preferentially removes material from the peaks and not from the valleys, see Figure 2.1.5. To smooth the ripples the tool has to cover at least two peaks. Therefore a larger tool is capable of smoothing surfaces where the peaks are further apart. A larger tool also benefits from a larger removal rate, reducing the total process time.

Yu et al. [69] were able to remove the mid-spatial grinding marks from a BoX™ ground 1 m spherical hexagon using a brass button tool mounted on a spinning inflatable bonnet using 9 µm aluminium oxide (a process called "grolishing"). Two variants of this tool have been developed at *OpTIC* which are mounted using a ball bearing instead of a bonnet.

The advantage of a ball bearing mounted tool is that it passively adjusts tip and tilt of the tool to compensate for alignment errors of the machine. If a bonnet mounted rigid tool is misaligned with the processed surface it causes a non-uniform pressure distribution between the tool and the surface which leads to uneven removal. This typically manifests itself as a sawtooth profile perpendicular to the raster sweeps.

There are two advantages of a bonnet mounted tool, both related to workpiece edges (which will be discussed in more detail in Chapter 3). Firstly, if a bearing mounted tool overhangs the edge of a workpiece too much it becomes unstable and flips. Rigid body mechanics suggest the limit occurs when half the tool overhangs the edge but in practice the limit is lower as the spinning tool becomes unstable at lower overhangs, because it is not perfectly balanced. For this reason the tool-path has to be selected so that the maximum overhang is well below this limit. This means that a point at the edge of the surface has not been passed by the complete tool (in the way that a point in the centre of the surface has been) because the tool turns around to commence the next sweep before the trailing edge of the tool reaches the edge, see Figure 3.1.3 for a diagram. If all process parameters are kept constant this results in a reduction of the removal by at least half at the edge of the workpiece. A bonnet provides a restoring force preventing a bonnet mounted tool from becoming unstable and it can be moved completely off the edge of a workpiece.

Secondly a bonnet mounted tool provides the option to intentionally introduce a misalignment. For example when non-uniform removal is desired to create a certain surface form (e.g. a sawtooth profile) or to compensate a non-uniform pressure distribution caused by e.g. the tool overhanging the edge.

In the rest of this thesis only ball bearing mounted variants are considered as they are more convenient in use due to their passive alignment, as outlined above.

The first variant enables the grolishing process to be applied by a standard industrial robot by mounting it on a spindle connected to the end of the arm, see Figure 2.1.6. The robot drags the tool over the surface by a ball joint that is free to move up and down inside a cylinder attached to the tool. This allows the tool to compensate for any inaccuracies in alignment and in position (perpendicular to the surface). The spindle rotates the tool around its axis by two driving pins that fit into two slots in the cylinder. While in contact with the surface the tool exerts a force on

(a) Bonnet mounted

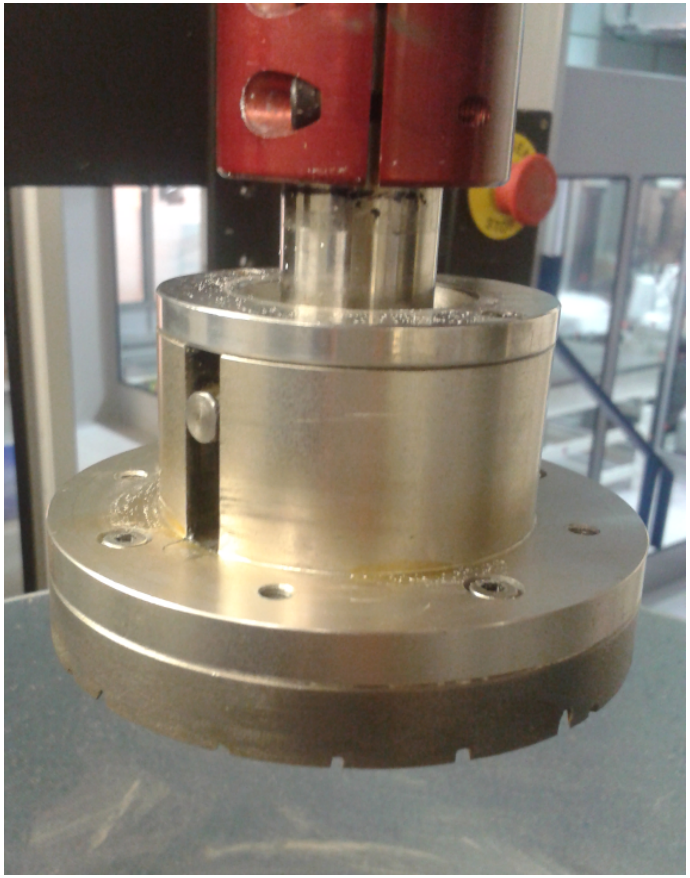

(b) Ball bearing mounted

Figure 2.1.6: Photos of rigid tools intended for removal of mid-spatial frequency errors from BoX™ ground surfaces.

Figure 2.1.7: A photo of an Articulated Rigid Tool used for polishing E-ELT primary mirror prototype segments.

the surface proportional to its weight and the local inclination of the surface. If this inclination changes over the whole surface (as it does for non-flat surfaces) it leads to different removal rates for different positions of the tool on the surface [18], which can be compensated for by varying other process parameters (e.g. surface feed). However during development it has been more practical to use the tool on near-flat surfaces, in which case this effect is minimal. This weight of the tool can be increased by the addition of one or more rings on top of the cylinder.

The second variant, which is essentially polishing, is mounted on a standard *Zeeko* tool spindle, in place of a bonnet tool, and is used with polishing slurry (e.g. cerium oxide) instead of aluminium oxide. To this end a carrier medium (e.g. pitch or polyurethane) is fixed to the surface of the tool, as can be seen in Figure 2.1.7. The tool is connected to a spring loaded piston by a ball bearing, which allows the tool to adapt to any misalignments. When the tool is in contact with the surface and the spring is compressed the tool exerts a force onto the surface proportional to the compression of the spring. The rotation of the tool spindle is transferred to the tool by a single driving pin. This tool is intended for use between corrective bonnet polishing runs to remove mid-spatial frequency surface errors left by the previous process.

All variants of the rigid tool are rotated around their centre to achieve relative motion between the tool and the processed surface, which is necessary for material removal [18]. If the tool has a non-rotationally symmetric form, wear of the tool will make it more rotationally

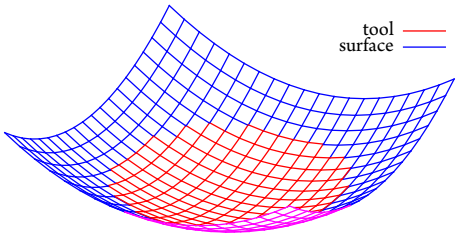

(a) without "mismatch-per-rev"

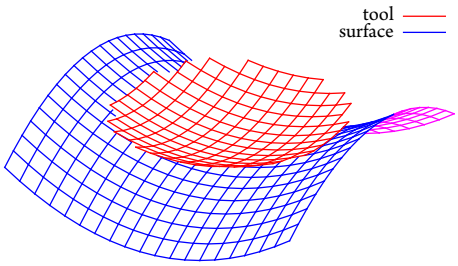

(b) with "mismatch-per-rev"

Figure 2.1.8: Diagram showing a tool on a surface without "mismatch-per-rev" (a) and with "mismatch-per-rev" (b).

symmetric over time. Deformation of the tool over time leads to a change in the removal of material from the workpiece over time, which would lead to uneven removal on the surface. Therefore, a rotationally symmetric form should be selected for the surface of the tool. Furthermore, to achieve a uniform contact the form of the tool's surface should be the inverse of the local form of the surface. With "local" the area of the surface is meant that is covered by the tool. This is trivial for spherical or flat surfaces, as shown in Figure 2.1.8a, but present problems when the surface is aspherical and has a different form in different directions, see Figure 2.1.8b, where only certain parts of the tool will contact the surface. This type of mismatch between tool and surface, subsequently referred to as "mismatch-per-rev", is due to the local surface not being rotationally symmetric around the centre of the tool. Incidentally, in literature mismatch is also know as "misfit" and both terms are understood to be identical: the error in matching the surface of the tool to the surface of the workpiece.

While processing an E-ELT prototype segment with a rigid tool there is another type of mismatch between the tool and the surface of a segment due to the fact that the segment is an off-axis asphere. While the "mismatch-per-rev" refers to the mismatch between the two surfaces when the tool is held in one position on the segment the "scanning-mismatch" indicates the change in the rotationally symmetric parts of the local surface form when the tool is scanned over the complete surface. As the segments constitute part of the rotationally symmetric primary mirror of the E-ELT the local curvature depends only on the distance to the optical axis

of the primary mirror. Therefore the "scanning-mismatch" can be calculated by comparing the local curvature of the surface for two extreme positions of the tool on the surface: when it is positioned closest to the optical axis of the primary mirror and when it is furthest away from it.

Mismatch between tool and surface causes non-uniform removal [18], but it is assumed that for the grolishing process this non-uniformity is not significant if the abrasive particle size is significantly larger than the mismatch [91]. It is postulated here that this rule-of-thumb holds for the polishing process with a sub-aperture, rigid tool. As the mismatch between a sub-aperture tool and surface increases with the size of the tool for a given asphere, this rule-of-thumb provides an upper limit of the tool size that can be used.

The work reported in this chapter presents a numerical analysis of the mismatch of rigid sub-aperture tools, which is validated by comparing it to the results of the analytical approach used by Song et al. [91] to calculate the mismatch of grolishing tools with E-ELT prototype segment surfaces. The numerical approach has the advantage that it can readily be applied to aspheric or free-form surfaces for which an analytical approach is difficult or impossible and furthermore it provides a more detailed analysis of the form of this mismatch, including spatial frequency content. Additionally, an analysis and experimental work is presented to determine the applicability of sub-aperture rigid tools for polishing E-ELT segments.

2.2 Numerical analysis of the mismatch

2.2.1 Procedure

Computer programs have been written in *MATLAB* that generate the complete E-ELT primary mirror's surface for discrete points, see Appendix A. It then moves and rotates the surface so that the centre of a desired sub-aperture is at the origin and the normal at the centre of this sub-aperture is pointing straight up. The surface outside of this sub-aperture is discarded and over the sub-aperture the Zernike's coefficients are calculated. Zernike polynomials [92] are used extensively to describe wavefront aberrations in optical systems [93, 94] by the coefficients a_{nm} of the polynomials $Z_n^m(\rho, \vartheta)$:

$$W(\rho, \vartheta) = \sum_{n=0}^{\infty} \sum_{m=-n}^{n} a_{nm} Z_n^m(\rho, \vartheta) \tag{2.1}$$

The non-normalised Zernike polynomials given by

$$Z_n^m(\rho, \vartheta) = \begin{cases} R_n^m(\rho)\ \cos(m\,\vartheta) & \text{if } m \geq 0 \\ R_n^{-m}(\rho)\ \sin(-m\,\vartheta) & \text{if } m < 0 \end{cases} \tag{2.2}$$

form a orthogonal base on the unit circle with

$$R_n^m(\rho) = \begin{cases} \sum_{s=0}^{\frac{n-m}{2}} \frac{(-1)^s\,(n-s)!}{s!\,(\frac{n+m}{2}-s)!\,(\frac{n-m}{2}-s)!}\ \rho^{n-2s} & \text{if } (n-m) \text{ even} \\ 0 & \text{if } (n-m) \text{ odd} \end{cases} \tag{2.3}$$

the radial part of the polynomial, see Appendix B for more detail.

In the same way the Zernike coefficients can be used to describe the shape of a sub-aperture of the E-ELT primary mirror. The procedure of fitting Zernike polynomials to discrete data is well known [95]. Because the tool can be positioned and orientated with respect to the surface using a CNC machine we can disregard the piston (Z_0°) and tip and tilt ($Z_1^{\pm 1}$) terms of the sub-aperture.

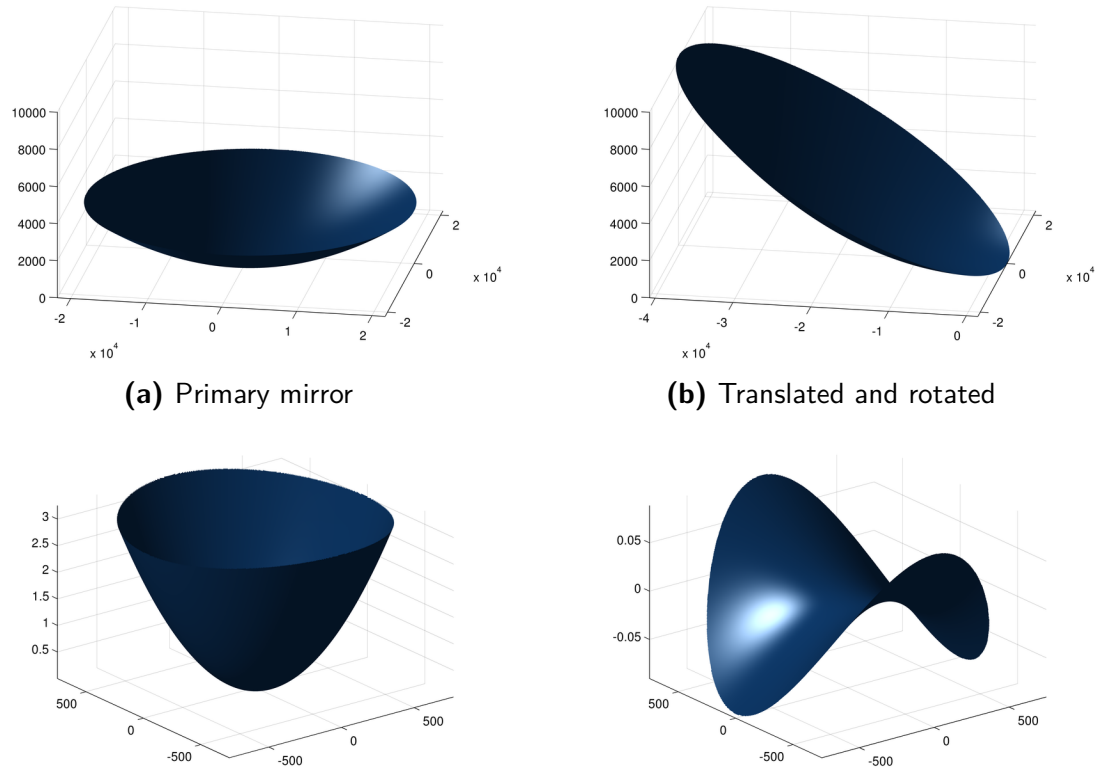

(a) Primary mirror **(b)** Translated and rotated

(c) Sub-aperture **(d)** Aspheric departure

Figure 2.2.1: Graphs demonstrating the numerical procedure by estimating the aspherical departure of a 1.5 m diameter sub-aperture located at 20.25 m from the axis of the primary mirror of the E-ELT. All units in mm.

As previously discussed the form of the tool has to be rotationally symmetric. For the "mismatch-per-rev" we assume that this shape is well adapted to the rotationally symmetric Zernike terms (Z_n°) of the local surface. The remaining terms can be put back together using Equation 2.1 to generate a heightmap of the "mismatch-per-rev" over the chosen sub-aperture of which the peak-to-valley (PV) value is calculated.

The "scanning-mismatch" is the difference taken between two heightmaps created from the rotationally symmetric Zernike terms at two extreme positions of the sub-aperture on the segment of which again the PV is computed.

The procedure is demonstrated in Figure 2.2.1 using a 1.5 m sub-aperture located at 20.25 m from the axis of the primary mirror. This is comparable with a complete segment at the edge of the primary mirror. Discounting piston, tip and tilt and power (Z_2°), the PV value of the

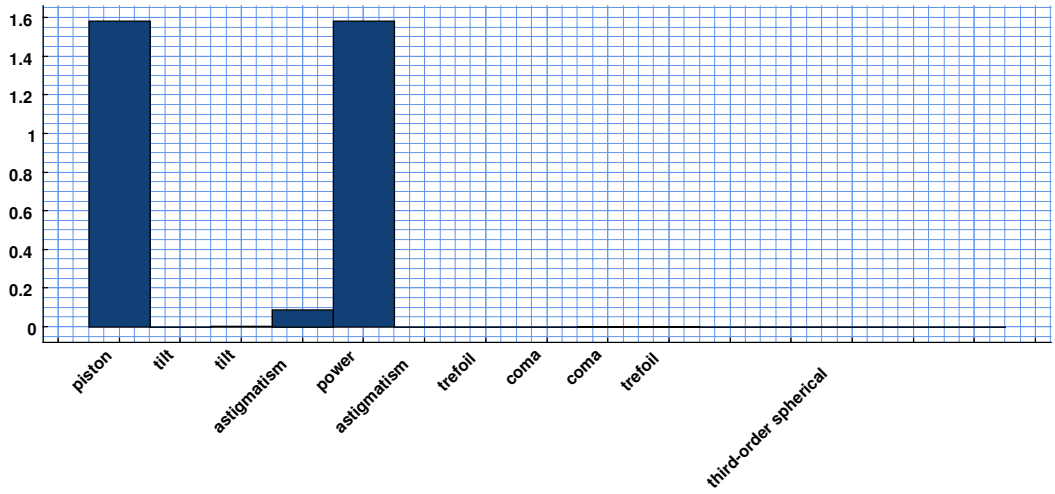

(a) Including piston, tilt and power terms

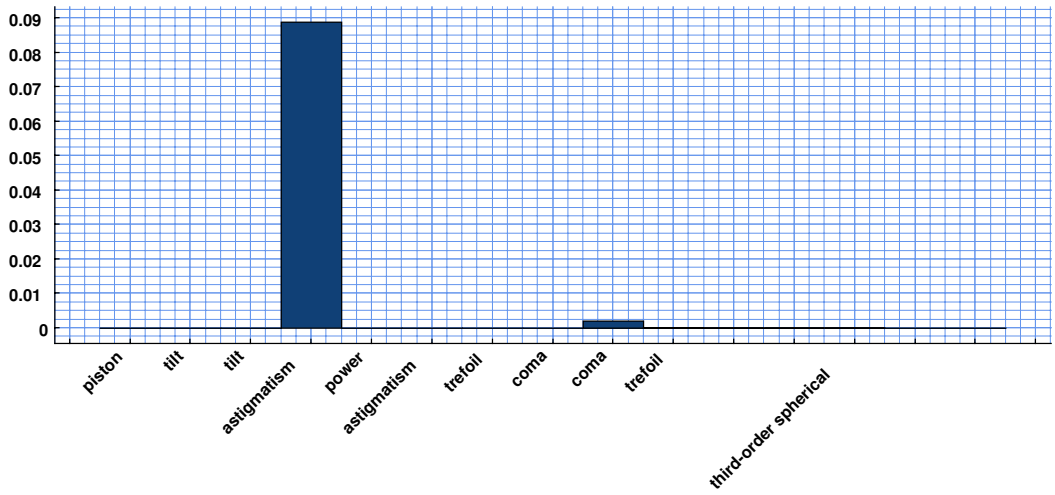

(b) Without piston, tilt and power terms

Figure 2.2.2: Absolute values (in mm) of the first 15 Zernike coefficients for the example of Figure 2.2.1.

resulting aspheric departure is 177.87 µm which is in agreement with the analysis by *OpTIC* of the E-ELT prototype segment bid.

In Figure 2.2.2 the first 15 Zernike coefficients are shown of this sub-aperture with (a) and without (b) piston, tilt and power terms. As can be seen from Figure 2.2.2a the aspheric departure is clearly dominated by the astigmatic term.

2.2.2 Accuracy

Because of the numerical approach taken there are discretisation errors. These errors become smaller with increasing resolution of the analysis, see Figure 2.2.3. In Figure 2.2.4 a plot is shown of the mismatch versus the resolution. Due to constrained computational power a resolution has to be selected that is practical (providing a solution in a reasonable time) but sufficiently accurate (for the desired application) at the same time. For each of the tool sizes evaluated below an analysis of the accuracy has been performed, the results of which are shown in C.1. Based on the outcome of that analysis a resolution of 10 000 pixels for the diameter of the primary mirror was chosen for all the subsequent analyses.

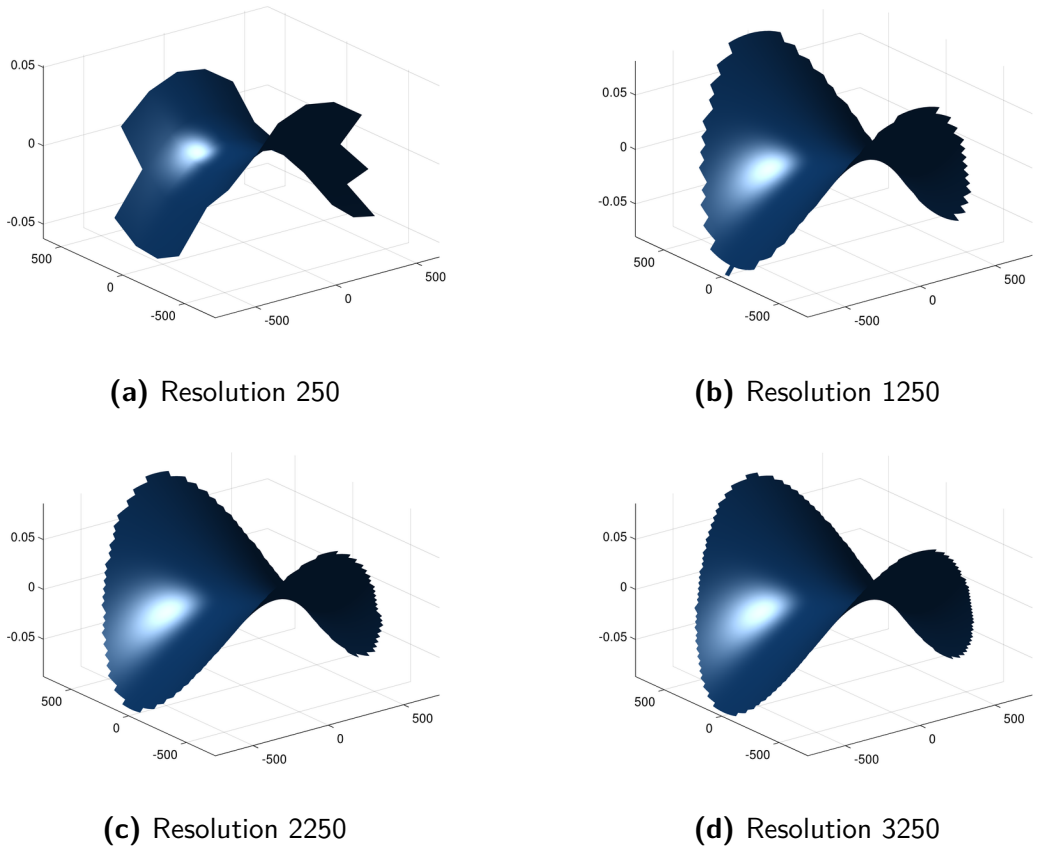

(a) Resolution 250

(b) Resolution 1250

(c) Resolution 2250

(d) Resolution 3250

Figure 2.2.3: Aspheric departure of the sub-aperture from the example of Figure 2.2.1 for different resolutions (number of pixels used for the diameter of the primary mirror). All units in mm.

Furthermore, the expressions of certain higher order Zernike polynomials on a discrete surface are no longer orthogonal to that of the lower order ones, depending on the resolution

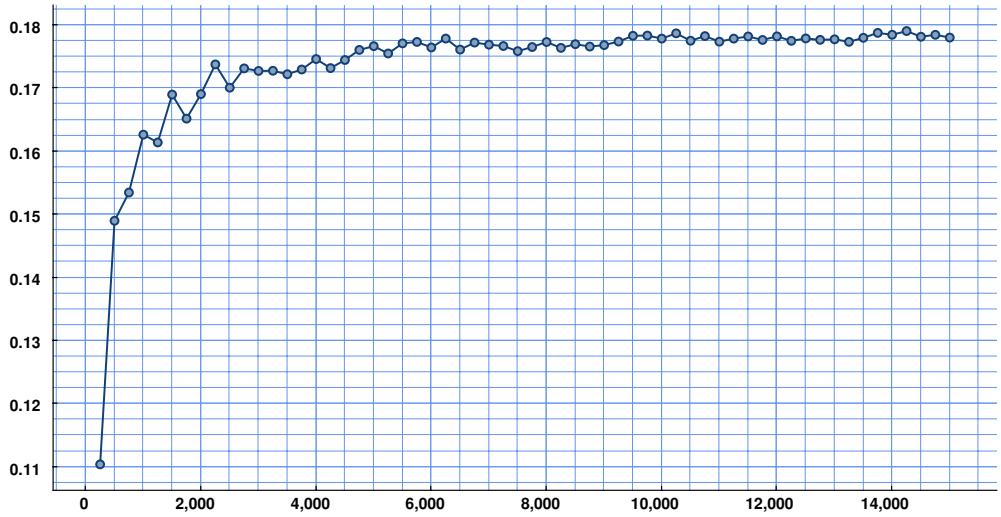

Figure 2.2.4: Aspheric departure (in mm) versus resolution (number of pixels used for the diameter of the primary mirror) for the sub-aperture from Figure 2.2.1

chosen. This is analogous to the Nyquist sampling theory for discrete signals [96]. Because of this and computational constraints only the 15 lowest order Zernike terms were considered. This is possible because the surface is sufficiently smooth, the residuals are in the order of 0.1 %.

2.2.3 Results

100 mm diameter tool

For a 100 mm diameter tool located at 19.5 m, 20.25 m and 21.0 m from the axis of the primary mirror the PVs of the "mismatch-per-rev" are 636.14 nm, 671.74 nm and 738.57 nm respectively, if the tool's shape is the best fit sphere of the primary mirror at that position. The difference in sag over the diameter of the tool of these best fit spheres between the two extreme positions, the "scanning-mismatch", is 118.92 nm.

50 mm diameter tool

For a 50 mm tool located at 19.5 , 20.25 and 21.0 m from the axis of the primary mirror the PVs of the "mismatch-per-rev" are 134.87 , 144.72 and 149.04 nm respectively, if the tool's shape is the best fit sphere of the primary mirror at that position. The difference in sag over the diameter of the tool of these best fit spheres between the two extreme positions, the "scanning-mismatch", is 21.36 nm.

Discussion

The results are summerised in Table 2.2.1 and are in agreement with analytical work done by Song [91]. The advantage of the numerical method presented in this chapter that it can be readily applied to aspheric and free-form surfaces that are difficult or impossible to analyse analytically.

Table 2.2.1: Results of the mismatch analysis of a rigid tool on an E-ELT primary mirror segment at the edge of the parent mirror.

		Tool diameter	
Mismatch type	Radial position	100 mm	50 mm
"mismatch-per-rev"	19.50 m	636.14 nm	134.87 nm
	20.25 m	671.74 nm	144.72 nm
	21.00 m	738.57 nm	149.04 nm
"scanning-mismatch"	-	118.92 nm	21.36 nm

The total mismatch is dominated by the "mismatch-per-rev", which is predominately astigmatic in shape. It is largest when the tool is positioned furthest from the optical axis of the parent mirror. This is to be expected as it's shape is close to being parabolic (with a conic constant of $-0.993\,295$). Both tool sizes have a maximum mismatch smaller than the particle size of the cerium oxide intended for use during polishing (1 µm), although the mismatch of the 100 mm diameter tool is of the same order of magnitude. If the rule-of-thumb regarding mismatch and abrasive particle size holds for polishing with rigid tools then both diameter tools can be used for polishing a E-ELT prototype segment, where the larger tool is preferred because of it's larger volumetric removal and capacity to remove errors with lower spatial frequency (as it is capable to bridge larger "gaps"). The fact that the spatial frequency of the mismatch is in the order of one per tool diameter further reduces the risk of the smoothing effect of the tool changing the form of the surface.

A further argument for the importance of the "mismatch-per-rev" over the "scanning-mismatch" is that the latter can be compensated for in practice by tool wear if the tool-path is chosen such that the "scanning-mismatch" varies only slowly. This can be achieved with raster sweeps close the tangential of the parent E-ELT primary mirror.

2.3 Practical verification

2.3.1 Design of experiment

The objective of the experiment was to quantify the effects on the surface of using a rigid tool on an aspheric surface due to "mismatch-per-rev". Because it is not feasible to do this test on a full sized segment it was performed on a smaller test workpiece. Processing this smaller test workpiece mimics processing of part of the bulk area of a segment. The aspheric form of the test workpiece was generated by corrective polishing of an available test workpiece with the standard *Zeeko* bonnet process.

Test workpiece size

It is desired to process an as large as possible surface area to properly quantify the effects. Unfortunately practical constrains such as metrology and available test workpieces limit the size.

A sensible analysis area over which the effect is quantified seems to be the size of the tool. Since this analysis area should be processed by the complete tool this means that the test workpiece size should be three times as large: if part of the tool overhangs the edge of the test workpiece the removal process changes [18] and is no longer representative.

Available test workpieces are 200, 300 and 400 mm across corners hexagons (Zerodur and Borosilicate). Since the 200 mm across corner hexagons are even smaller (in places) than two 100 mm tools side by side, the larger test workpieces are preferred. *Qioptiq Ltd.*, a project partner in the early stages of the consortium, generated a spherical surface into four Borosilicate 300 mm test workpieces into which an aspheric departure was polished at *OpTIC*.

Form definition

The form of the test workpiece should mimic the aspheric departure of a sphere in the bulk area of a segment. The same numerical analysis was performed as described previously in this chapter for a 300 and 400 mm diameter circular sub-aperture and the resulting PVs of the mismatch were 6.95 and 12.49 µm respectively. The form of the test workpieces was defined as pure astigmatism scaled to have a PV corresponding to the numerical analysis.

Metrology

Polishing the aspheric departure into workpieces requires measurement of the surface, typically by interferometer using a spherical wavefront. Because the aspheric departure is almost completely astigmatic the highest slopes of the departure occur at the edge of the test workpiece. For a 300 mm test workpiece the maximum slope would be 100.19 nm mm^{-1}, for a 400 mm test workpiece 135.63 nm mm^{-1}, based on numerical simulation. Imaging this with a standard interferometer (where optical path difference is twice the surface error) results in a minimal width of one set of fringes of 3.16 and 2.33 mm respectively.

At *OpTIC*'s laboratory several interferometers made by *4D Technologies* are available. They stand apart in that they do not capture individual phase maps sequentially. Instead a pixel mask in front of the CCD camera allows them to be acquired simultaneously [97–99]. These interferometers are especially suited for environments where vibration is present. The $f/6$ objective images a diameter of 500 mm a 3 m RoC part, the $f/8$ objective images 375 mm. With a non-standard 9 mm wide laser beam instead of a 7 mm one both the 300 and the 400 mm test workpieces should be measurable with either objective.

The lowest resolution interferometer (the *4D* PhaseCam 4000) has a resolution of 512×512 $pixel^2$ and a standard width laser(7 mm) so that imaging a 3000 mm RoC part with the $f/6$ gives us 0.98 mm $pixel^{-1}$. The number of millimetre per pixel of the other objective can be found in Table 2.3.1 as well as the data for the higher resolution (1024×1024 $pixel^2$) interferometer (the *4D* PhaseCam 6000) that has a wider beam width (9 mm). From these it is possible to calculate the worst-case number of pixels per fringe on the test workpieces.

If we consider the rule-of-thumb that more than 4 pixel per set of fringes are needed we can see that the only feasible combination of the *4D* PhaseCam 4000 interferometer is to use a

Table 2.3.1: Metrology analysis

			Objective	
			$f/6$	$f/8$
PhaseCam 4000 512×512 pixel^2 7 mm beam width	Measurable diameter		500 mm	375 mm
	Inv. pixel density		0.98 mm pixel^{-1}	0.73 mm pixel^{-1}
	Min. fringe width	ø 300 mm	3.22 pixel	4.33 pixel
		ø 400 mm	2.38 pixel	3.19 pixel
PhaseCam 6000 1024×1024 pixel^2 9 mm beam width	Measurable diameter		643 mm	482 mm
	Inv. pixel density		0.63 mm pixel^{-1}	0.47 mm pixel^{-1}
	Min. fringe width	ø 300 mm	5.02 pixel	6.72 pixel
		ø 400 mm	3.70 pixel	4.96 pixel

300 mm part with the $f/8$ objective. The margin is rather low (0.33 pixel fringe^{-1}), especially if we consider that the surface will have additionally errors and artefacts that need to be imaged.

On the other hand, the higher resolution interferometer with the $f/8$ objective gives a decent margin for both the 300 mm and 400 mm test workpieces. Because this interferometer uses a larger beam width the aberrations of the objective need to be quantified and subtracted from subsequent measurements. This can be done by using the classically pre-polished spherical surface before polishing the aspheric departure into it.

Unfortunately at the time of the experiments only the *4D* PhaseCam 4000 interferometer was available for use and therefore the 300 mm test workpieces were selected for the experiments.

Form accuracy of test workpieces

To mimic the aspheric mismatch properly the form error after generating the aspheric departure into the surface has to be well below the expected mismatch of the rigid tool at any position of the tool on the test workpiece (and thus effectively the complete surface). If we choose 10 % of the mismatch as the PV form error limit, this leads to a maximum form error of 81 nm (or $\lambda/8$) and 18 nm (or $\lambda/35$) for the 100 mm and 50 mm tool under test respectively. This last one is impractical so the 100 mm tool has been selected for verification.

Experiments

The aspheric departures were generated by the standard *Zeeko* bonnet corrective polishing process using the parameters listed in the first data column of Table 2.3.2 and an inverse of the required departure as an error map and the bonnet was clothed with "LP66", a polyurethane polishing pad, pre-shaped to fit the bonnet. A 100 mm diameter rigid tool was then used to polish the resulting surface at *OpTIC* by Colin Williams of *Qioptiq*. Because the experiment is to mimic the exact processing of the bulk area of the aspheric segments, the exact same parameters were used, shown in the second data column of Table 2.3.2. The tool was faced with pitch and

Table 2.3.2: Process parameters used during the experiments.

Parameters		Tool	
		Bonnet	ART
General	Precess Angle	13°	2.25°
	Head Speed	1000 min^{-1}	10 min^{-1}
	Tool Offset	0.8 mm	0.55 mm
	Overhang	6.0 mm	−34.5 mm
	Tool Pressure	1 bar	-
	Point Spacing	1 mm	1 mm
	Track Spacing	1 mm	1 mm
	Surface Feed	-	2750 mm min^{-1}
Edge	Accel/Decel Zone	6 mm	-
	Feed	100 %	-
	Lift Off	1.6 mm	-
	Precess Angle	20°	-

grooved with a square pattern to allow the polishing slurry to be evenly distributed between the tool and workpiece. Both the generation of the aspherical shape and the testing of the rigid tool were performed on *Zeeko*'s IRP 1200 polishing machine using 1 µm cerium oxide polishing slurry with a specific gravity of 1.03.

An error was made during the set up of the software for the generation of the aspheric departure during the first experiment which resulted in unnecessary "head speed moderation". Normally the different removal for different parts of the workpiece is achieved by having the tool linger more or less in an area as required. However if the desired removal is smaller than what is possible to achieve by going across the region at maximum machine speed then the software applies what is called "head speed moderation", lowering the speed of the tool spindle to reduce removal. In this case, due to a software bug which has since been fixed, this resulted in the final form to be globally correct but non-smooth. The surface consisted of discrete steps, as shown in Figure 2.3.1a. The rigid tool was applied on this surface anyway and the result is shown in Figure 2.3.1b.

For the second experiment the removal was increased for the bonnet process to prevent "head speed moderation" and the result was a smooth astigmatic surface onto which the rigid tool was applied again.

2.3.2 Results and discussions

For both experiments the difference between heightmaps before and after applying the rigid tool have been taken, see Figure 2.3.2. The PV of the difference of the first experiment,

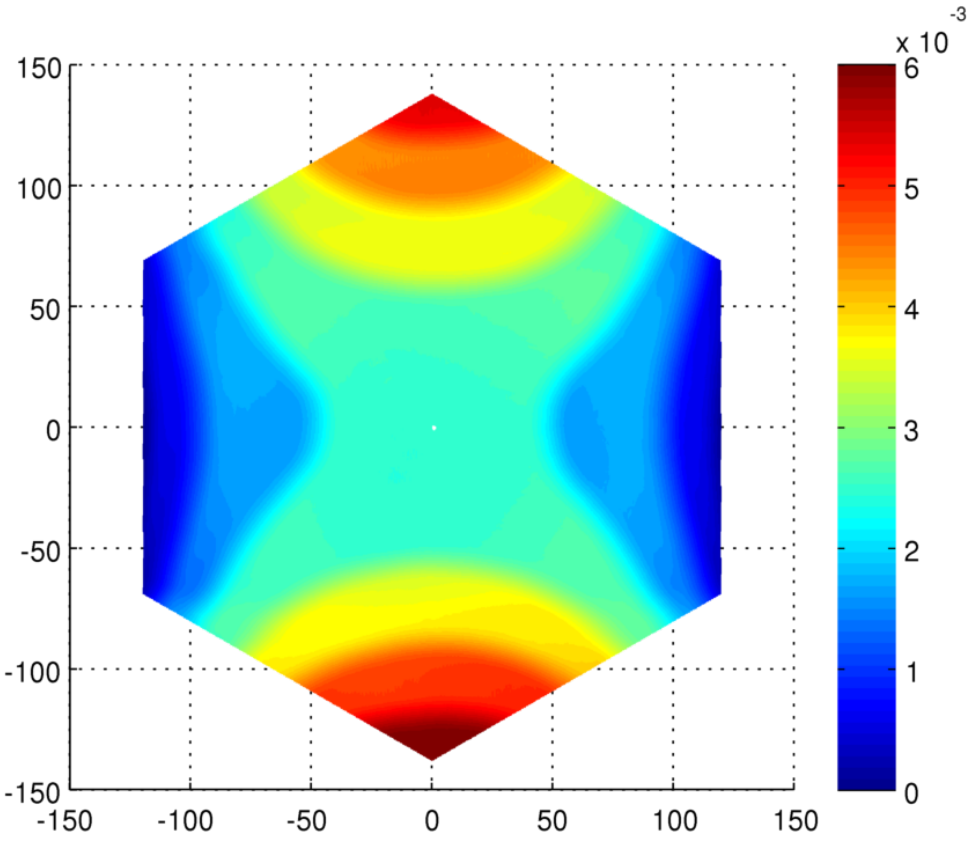

(a) After aspherisation.

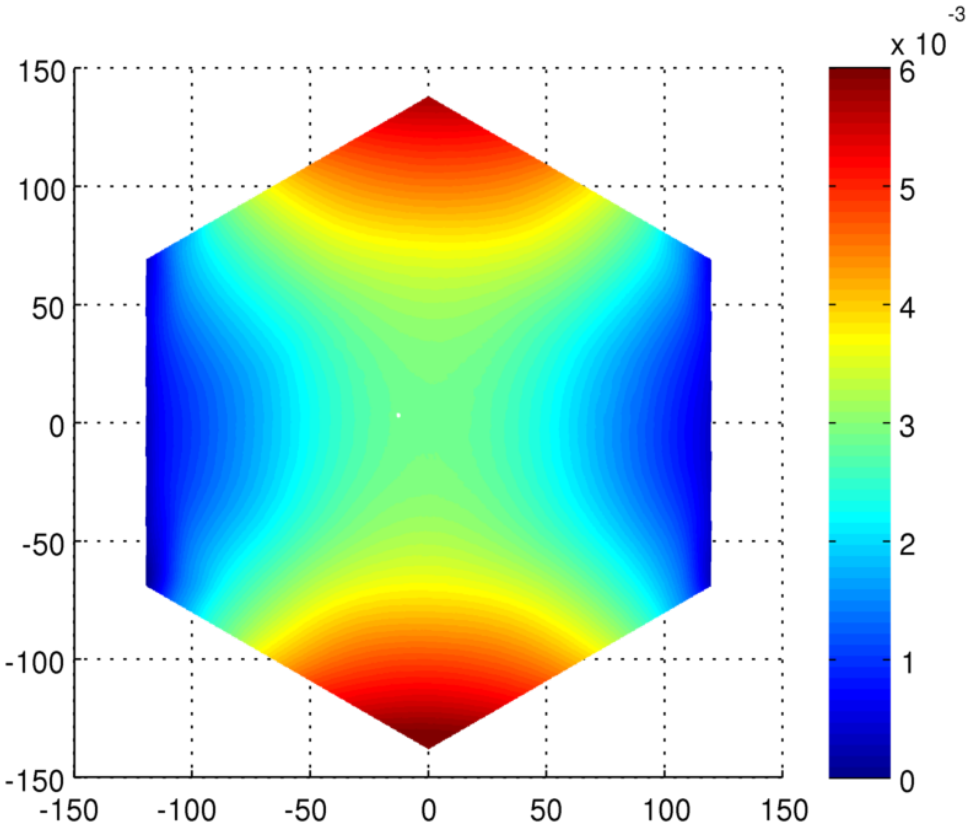

(b) After smoothing.

Figure 2.3.1: Heightmap of the surface after using bonnet (a) and rigid (b) tools during experiment №1 with 10 mm of the edges cropped to remove noise and edge artifacts. All units in mm.

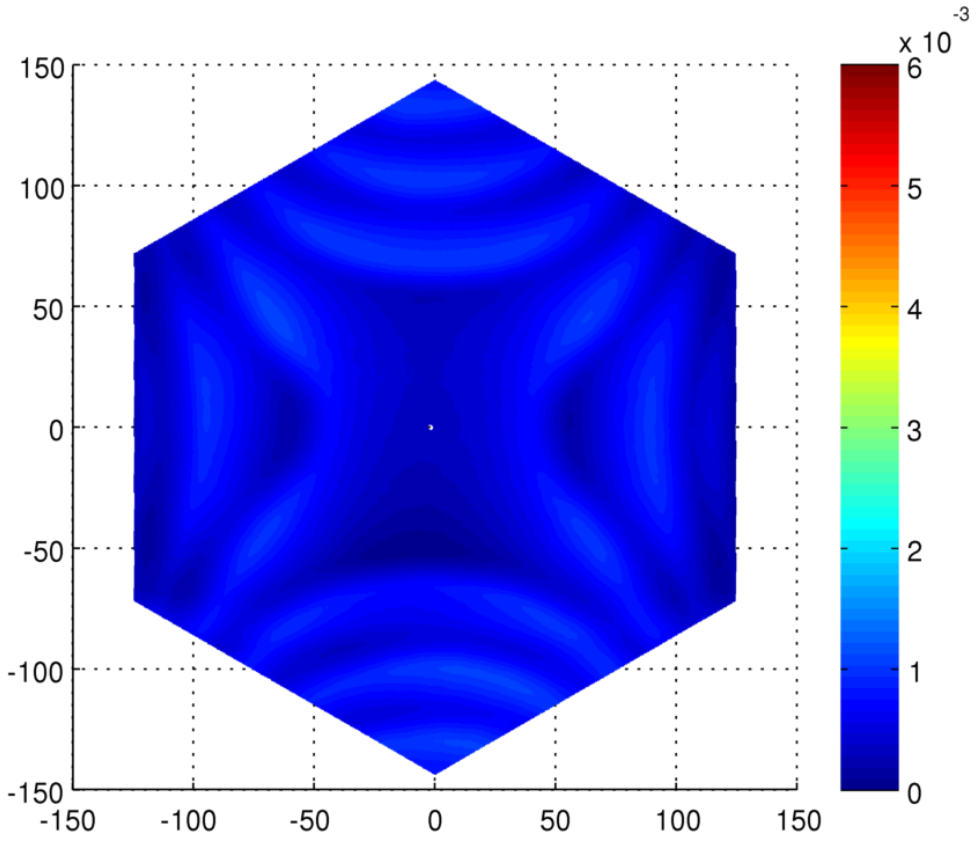

(a) Experiment №1.

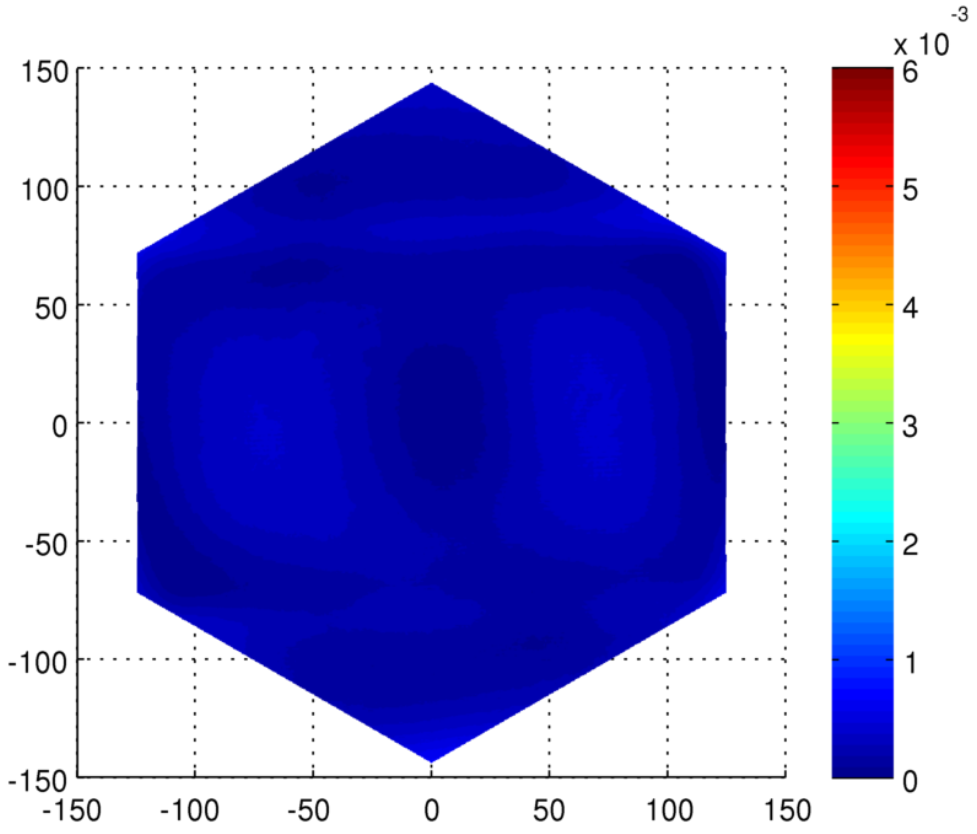

(b) Experiment №2.

Figure 2.3.2: Difference between heightmaps before and after applying the rigid tool for both experiments with 5 mm of the edges cropped to remove noise and edge artifacts. All units in mm. The same color scale was used as in Figure 2.3.1.

Figure 2.3.2a, is 1.10 μm, however this is largely due to the tool actually *improving* the surface form by smoothing out the discrete steps in the input surface, as indicated by the shape. The PV of the input surface with tip, tilt and astigmatism removed is 1.15 μm, slightly larger than the removal by the rigid tool.

The total PV of the surface before and after applying the rigid tool are very similar, 6.15 μm and 6.16 μm respectively. When taking out the astigmatic term from the heightmap after using the rigid tool and cropping the result to the central 200 mm diameter circular region to remove any edge effects the PV equals 0.33 μm. Together this indicates that the tool is capable of smoothing out local defects but leaves the global form intact.

For the second experiment the difference between the before and after heightmap of the surface, Figure 2.3.2b, cropped again to the central 200 mm diameter circular region to remove any edge effects shows a PV of 0.41 μm. It is therefore concluded that the rigid tool is capable of removing local defects with minimal detrimental effect on the global form.

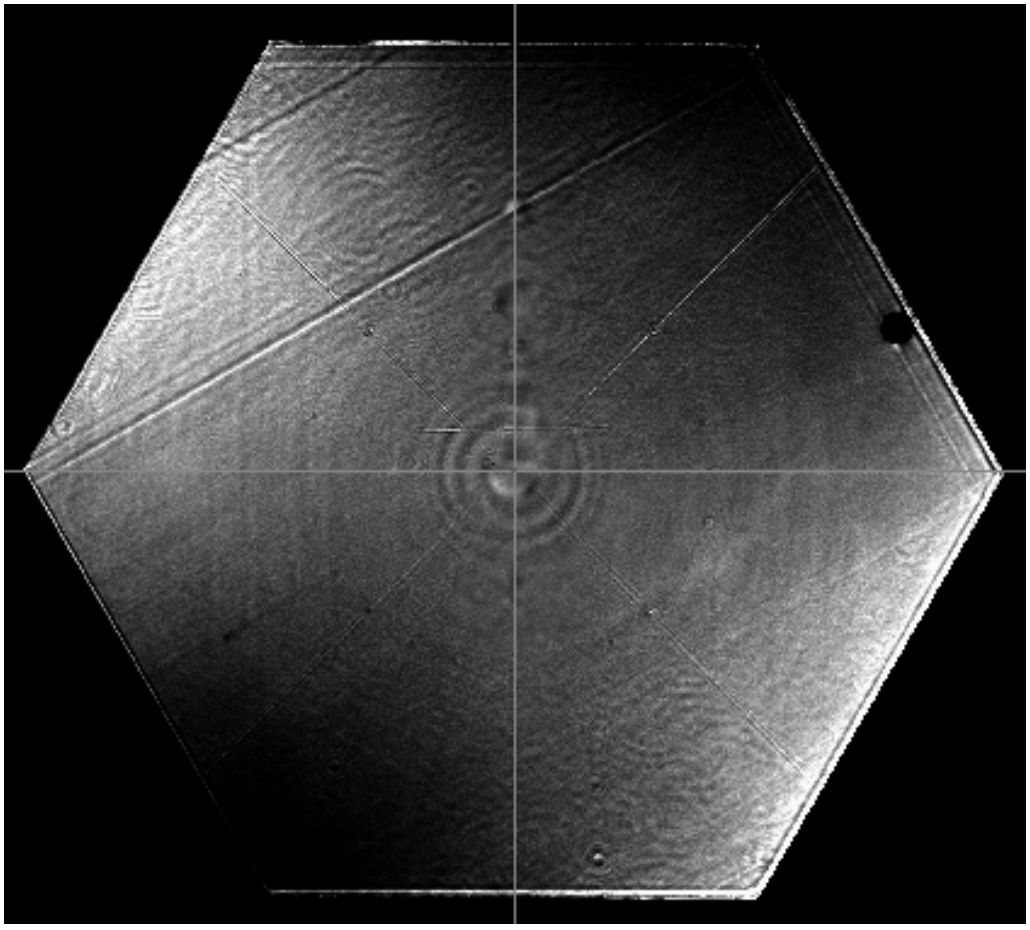

Figure 2.3.3: Artificial interferogram of prototype segment "SPN01" after polishing. The ring shapes and diagonal lines through the centre are artefacts from the measurement setup.

The tool has subsequently been used successfully by *OpTIC* during the polishing of 1.5 m scale E-ELT prototype segments, where it has been used in between bonnet based corrective polishing runs. As an example an interferogram is shown in Figure 2.3.3 of prototype segment "SPN01" after polishing was finished (ending with a rigid tool polishing run). The rms form

error of the surface excluding a 10 mm wide edge-zone is 25.4 ± 4.8 nm, with only tip and tilt removed. When further, low-order terms are removed (as per the E-ELT primary mirror prototype segments specifications) the resulting rms form errors is reduced to 7.5 ± 2.0 nm. This segment has been accepted by *ESO* to meet the specification.

2.4 Conclusion

To achieve their science goals the next generation ground-based telescopes will use very large mirrors. As it is impractical to use monolithic mirrors a large number of mirror segments will need to be produced. A consortium led by *OpTIC* was tasked by *ESO* to produce prototype mirror segments. Rigid grolishing and polishing tools are used to remove mid-spatial frequency surface errors that are difficult to remove by bonnet based processes used for corrective polishing. When these tools are applied on surfaces other than flats or spheres there is the risk of non-uniform removal due to a mismatch between the surface of the tool and the surface of the workpiece, which leads to surface errors.

The procedure outlined in this chapter applies computational power to perform a numerical analysis of the mismatch of rigid tools on aspherical surfaces. For the E-ELT prototype segment test-case a modern laptop was sufficient to provide the required computational power and the results confirmed the analytical results of Song [91], which had not been validated nor published at the time the work described in this chapter was performed.

There are two benefits of this numerical analysis of the mismatch. Firstly, it can also be applied to aspherical or free-form surfaces that are difficult or impossible to analyse analytically. Secondly, it readily provides the means for a qualitative analysis of the mismatch on top of quantitative data. The mismatch is easily divided into different groups (e.g. rotationally symmetric versus non-rotationally symmetric term or low-order versus high order terms). This is relevant when estimating the effects of the rigid tools on the polishing process and the potential combination with other polishing processes.

Previously a rule-of-thumb has been documented [91] that indicates that for the grolishing process the errors produced on a surface due to the mismatch of a rigid tool are insignificant if the mismatch is smaller than size of the abrasive particle used in the process. A rigid polishing tool with a size selected to adhere to this rule-of-thumb was tested and it is shown that this rule-of-thumb holds for polishing processes. This rule-of-thumb together with the mismatch analysis presented in this chapter allow the selection of the optimal tool size to be used: as large as possible to maximise smoothing proficiency without introducing errors on the surface due to mismatch. Where this chapter looked into the effect that rigid tools have on the bulk area of a workpiece the next chapter investigates the effect of rigid tools on edges.

I want to stand as close to the edge as I can without going over. Out on the edge you see all the kinds of things you can't see from the center.

Kurt Vonnegut

3

Edge effect of sub-aperture rigid tools

3.1 Introduction

Many manufacturing processes treat the area near the edge of an optical surface differently than the bulk of the surface. In certain cases this effect is a benefit that can be used to control the overall profile of the removal to achieve the desired surface form. For instance in classical optical polishing the stroke of the polishing machine can be altered so that more material is removed from the centre of the surface than from the area near the edge. In CCOS however, the effect is undesired as, in general, the influence function of the tool is assumed constant and not dependant on the position of the tool. Thus any edge effect leads to surface misfigure [100]. A well known problem for instance is the so-called "edge-roll" which is a major reason why, in general, optical surfaces are manufactured on a part that is larger than the desired clear aperture.

Edge roll-off is caused by a sudden steep increase in removal rate closer to the physical edge of the part, see Figure 3.1.1. Returning to the example of classical optical polishing it is a well known fact that different materials used as a carrier of the polishing compound cause different widths of the edge roll-off [17]. For example cloths (e.g. felt) produce a larger edge roll-off, polyurethanes an in-between and pitches the smallest. Not always is it possible to use an oversized part to circumvent this issue, for instance in the case of segmented mirrors for extremely large telescopes.

As with monolithic mirror telescopes, the aperture and support structure (e.g. of the secondary mirror) cause diffraction of the incoming light limiting the angular resolution of the telescope. As an example, the influence of the aperture diameter on the diffraction limited

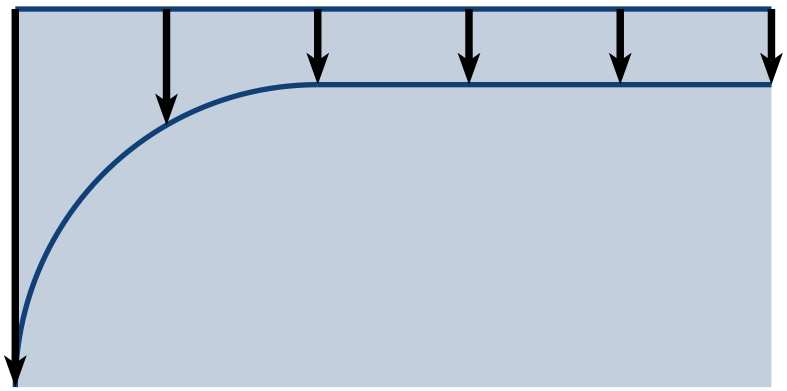

Figure 3.1.1: Diagram showing "edge-off" due to a higher removal rate closer to the edge of the part (on the left hand side of the diagram).

angular resolution is shown in Figure 3.1.2 for several astronomical instruments. The edges of hexagonal segments introduce additional diffraction of the incoming light in a pattern perpendicular to the edges [101–103]. In the ideal case, where individual segments are well aligned (no piston or tip and tilt errors) and where there is no gap (including bevels) between segments nor any surface misfigure, the far-field diffraction pattern due to the segmentation of the mirror has just a single peak. However, gaps and surface misfigure cause energy to be spread from there into the wings and higher order peaks appear in the point spread function.

In addition to the effect the gaps have on the diffraction pattern they also cause thermal radiation, either directly in the case of the segment bevels or in-directly by allowing radiation originated behind it to pass in the case of the physical gaps between segments. This radiation contributes to the background in the thermal infrared (wavelengths greater than 2.5 μm) if the telescope is at ambient temperature. Furthermore, edge misfigure potentially reflects thermal emissions from the environment (including the telescope itself) into optical path of the telescope. Masking the misfigure area by painting or roughening it up to prevent specular reflection does not provide a solution as it causes direct thermal emissions instead.

As previously mentioned, edges of the segments are not the only origin of background noise and if the gaps and edge misfigures are sufficiently small, other sources will dominate. This is why the E-ELT primary mirror segments have a specific tolerance for the edge region, defined as a 10 mm wide band from the physical edge of the segment. As shown in Table 2.1.1 the maximum allowed misfigure for one edge of a segment is 200 nm PVq (95%). The average misfigure for all six edges is limited to 100 nm PVq (95%).

This chapters investigates the causes of these edge artefacts and possible remedies for sub-aperture rigid tools. This type of tools is typically employed to take out the mid-spatial frequency artefacts left in the surface by a previous processing step, as discussed previously in Chapter 2.

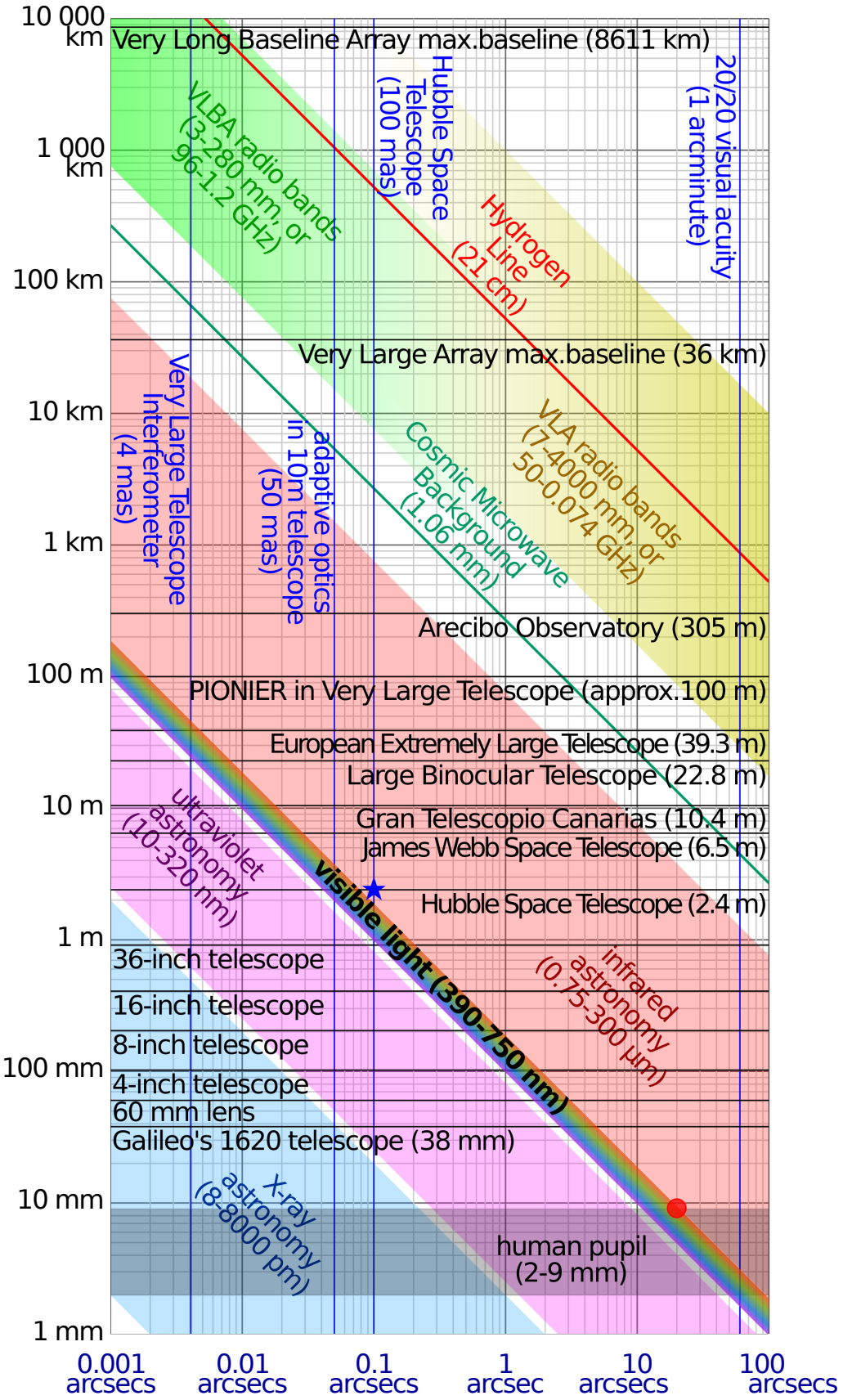

Figure 3.1.2: Log-log plot of aperture diameter versus angular resolution at the diffraction limit for various light wavelengths comparing several astronomical instruments. © C. M. G. Lee / http://commons.wikimedia.org/wiki/file:diffraction_limit_diameter_vs_angular_resolution.svg / CC-BY-SA-3.0.

3.1.1 Edge artefacts

There are different mechanisms that cause edges to be treated differently by sub-aperture rigid tools than the bulk area of the surface. Those that contribute most significantly to non-uniform removal are discussed in the next paragraphs.

Incomplete raster

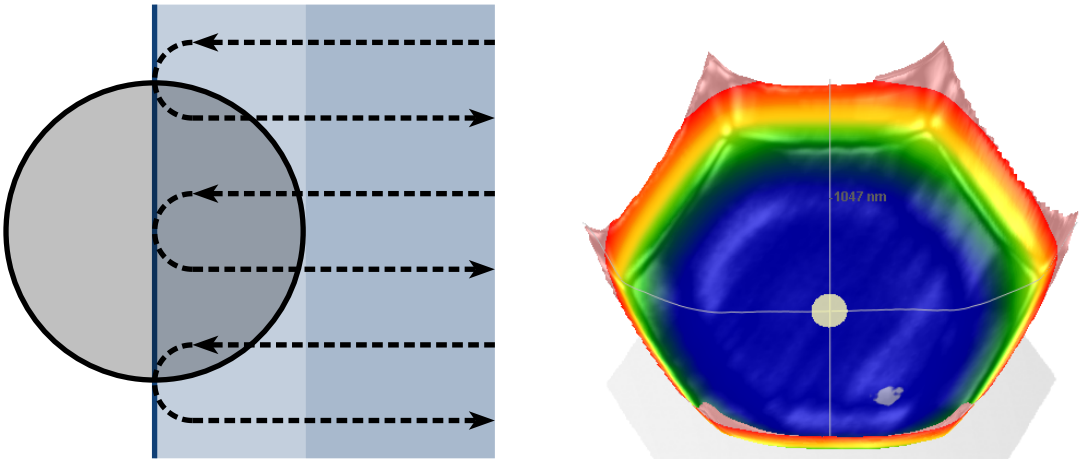

(a) Diagram of an incomplete raster

(b) Example of upturned edges of a hexagonal workpiece

Figure 3.1.3: Diagram and example showing an upturned edge due to an incomplete raster near the edge of a part. The dashed line shows the path of the centre of the circular tool and it is positioned at the end of its stroke, which in this case means that half the tool is hanging over the edge of the part for this particular raster. The lighter colour shows the area of the part that is not completely processed by the whole tool when the raster is completed.

As discussed in Chapter 2, the advantage of a ball bearing mounted tool is that it passively adjusts tip and tilt of the tool to compensate for alignment errors of the machine. However, if a bearing mounted tool hangs over the edge of a workpiece too much, it becomes unstable and flips. Rigid body mechanics suggest the limit occurs when half the tool hangs over the edge but in practice the limit is lower as the spinning tool becomes unstable when a smaller area hangs over the edge, because it is not perfectly balanced. For this reason the tool-path has to be selected so that the maximum extension over the edge is well below this limit. This means that a point at the edge of the surface has not been passed by the complete tool (in the way that a point in the centre of the surface has been) because the tool turns around to commence the next sweep before the trailing edge of the tool reaches the edge, see Figure 3.1.3 for a diagram. If all process parameters are kept constant this results in a reduction of the removal by at least half at the edge of the workpiece and thus an "edge-upstand" of typically several µm. The width of the artefact is approximately equal to the diameter of the tool minus the amount the tool hangs over the edge at the end of it's sweep.

Change of pressure

In general during lapping and polishing a tool is rubbed onto the surface being processed with abrasives carried by a fluid in the interface between the tool and surface. The Preston equation [18] relates material removal rate, $\frac{\partial h}{\partial t}$, to operating parameters:

$$\frac{\partial h}{\partial t} = cPv \tag{3.1}$$

where c is the Preston coefficient, P the pressure between tool and workpiece and v the relative speed between tool and workpiece. All variants of the rigid tool introduced in Chapter 2 are circular shaped and rotated around their centre by a spindle to achieve relative motion between the tool and the processed surface and therefore the relative speed between the tool and the workpiece increase linearly with the radial position within the contact area between tool and workpiece. The tools are pressed onto the surface by their own weight in case of the grolishing tool and by a pre-loaded spring in case of the polishing tool. Thus, using rigid body mechanics, we can model the influence function of a circular rigid tool as a cone within the contact area between tool and workpiece and zero outside.

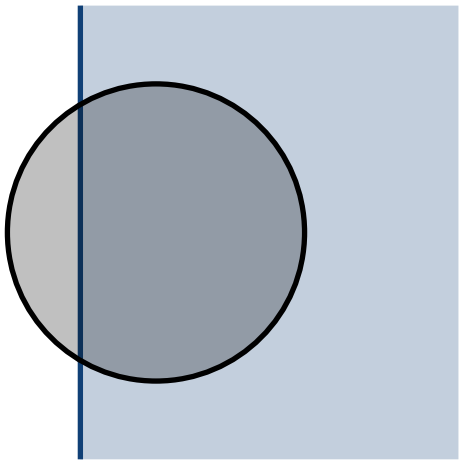

Figure 3.1.4: Diagram showing pressure change near the edge of a part. The dark grey colour shows the area of the part that is still supported by the part.

If the tool is pressed onto the workpiece with equal force then the average pressure between tool and workpiece increases if part of the tool hangs over the edge due to the reduced contact area between tool and workpiece. From Equation (3.1) it follows that this causes increased removal at the edge resulting in "edge-roll" as shown in Figure 3.1.1. By calculating the contact area for all different positions of the tool overhanging the edge the average pressure, and therefore the removal rate (relative to the removal rate when the tool is completely supported by the workpiece) can be estimated.

Apart from the effect that the tool hanging over the edge has on the average pressure it also causes a non-uniform pressure distribution between the tool and workpiece. If the ball-bearing mounted tool does not tip over then the moments must be equal to zero. Due to the lost contact area on one side of the tool the contact force between tool and workpiece can not be uniformly

distributed in the contact area whilst keeping the moments equal to zero. If the tool does not flip then there must be a pressure distribution that is increasing towards the edge of the workpiece to compensate for the lost moment contribution of the part hanging over the edge. This effect is more pronounced the more the tool overhangs the edge and the removal is distributed more towards the edge of the workpiece resulting in an "edge-roll" artefact that is narrower and steeper than if only a uniform pressure distribution is considered.

Process instabilities

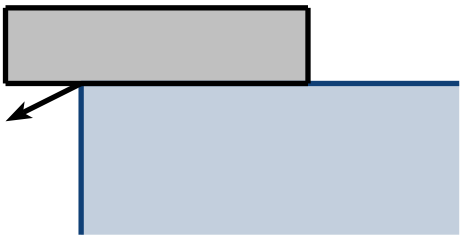

Figure 3.1.5: Diagram showing loss of slurry near the edge of a part indicated by the arrow.

Although the pressure and relative velocity are the most significant factors that govern the removal rate there are others, for instance chemical processes [29]. Different manufacturing processes are influenced differently, for example the removal rate in beam or jet based processes is directly depend on the number of particles in the stream [104]. Similarly different processes are affected in different ways by the discontinuity of the edge. For instance in Fluid Jet Polishing the hydrodynamics change when the jet extends beyond the edge of the workpiece, however the effect has negligible effect on the removal in the edge zone [105, 106]. The same is true for analogous reasons for the Ion Beam Figuring process [107]. If a rigid tool extends over the edge of a workpiece slurry flow dynamics change causing loss of slurry, as shown in Figure 3.1.5, and changes in the slurry film thickness, which leads to variations in the removal rate [108–111]. However these effects on the removal rate are deemed to be of secondary order when compared to the previously outlined mechanisms and are therefore not further investigated here.

3.2 Remedial strategies

From the previous it is clear that if the changes in removal when the tool is near the edge of the workpiece is not taken into account then the resulting surface will exhibit edge misfigure. Different remedial strategies to improve the edge figure can be applied individually or in combination.

Changing the local influence function

One mitigation strategy is to take measures that bring the removal rate and/or profile at the edge more in line with that on the bulk area of the workpiece. Some examples are outlined below.

An obvious method would be to use so-called "wasters": pieces of a material that exhibits the same removal rate are attached to the sides of the workpiece. The process does no longer

encounter the edge singularity and the removal is consistent when the tool moves beyond the edge. However the use of "wasters" is not very practical for the following reasons:

- The segments are not regular hexagons and therefore the angles between and the lengths of individual edges differ. Each symmetry family of six segments would required a custom made set of six "wasters" and thus an equal number of wasters would need to be produced as there are segments in the primary mirror.
- attaching and especially releasing these "wasters" carries the inherent risk of damaging the segment at a stage where considerable value has been added previously

Li [112] mentions a further four reasons:

- Bonding the "wasters" to the segments by adhesive introduces stress which leads to deformation of the surface. When the "wasters" are removed the stress is released and the surface springs back, analogous to Stressed Mirror Polishing. If this spring causes the surface form to exceed acceptable tolerances a rectification process would be necessary.
- The polishing force might cause accidental detachment of a "waster" risking damage to the segment or in the best case an edge artefact that the "waster" was supposed to prevent.
- During the cleaning of the segment edges to remove adhesive residue after releasing the "wasters" the segment is at risk of damage
- To complete the raster the contact area has to leave the segment surface completely. Thus, in the case of the E-ELT primary mirror segments with a largest projected spot size of 60 mm (using a 160 mm radius bonnet), the "wasters" will weight approximately 5 kg, requiring machine-driven positioning.

For the reasons outlined above the development of a process to polish E-ELT (prototype) primary mirror segments without the application of "wasters" was preferred by the *OpTIC* led consortium, while retaining the option as a backup.

In case of conformal tools (e.g. bonnet or MRF) it is possible to locally change how far the tool is compressed into the surface, thus the size of the contact area can be controlled [87, 100]. Additionally the precession angle of bonnet tools can be increased or decreased to change the removal near the edge [112].

If a rigid tool is mounted on a bonnet tool it's restoring force could be used to keep the removal uniform when part of the tool hangs over the edge, as outlined in Chapter 2.

Optimising process parameters

In CCOS a surface is improved iteratively by applying dwell times that are calculated by an algorithm that takes the current surface errors as an input. The errors introduced by non-uniformity of the removal process near the edge can be taken into account a-priori by the algorithm to minimize surface misfigure [100].

Or the input surface errors could be decoupled from the errors introduced near the edge due to the non-uniform removal. The input surface errors would be corrected by applying optimised dwell times, as with standard CCOS, and the edge misfigure would be minimised by another optimised process parameter. Likely candidates for this second parameter are the tool rotational speed and in case of a rigid sub-aperture tool the force with which it is pressed on the surface. This last can be achieved by varying the tool offset in case the tool is using a pre-loaded spring or by varying the air pressure if the tool is pressed on the surface using a piston.

As the effects of the in-complete raster and the change of pressure are opposite (but not inverse) it is possible to optimise the maximum tool position at the end of a sweep of the tool-path such that the combined edge artefact is minimized.

Another potential option is to permanently change the removal profile (e.g. changing the fill factor of the tool will change where the tool contacts the surface and thus the removal profile [113]) in a way that minimizes the edge artefact after the complete tool-path is executed.

TRIAL AND ERROR VERSUS DETERMINISTIC

Apart from the passive remedy of applying "wasters" all methods require some kind of optimisation to find the parameter set that results in the least amount of edge misfigure. There are two routes to achieve this optimisation, the first is by trial-and-error. An initial parameter set is selected and applied during manufacture. Afterwards the result is analysed by the operator and based on this evaluation the parameter set is modified and tested again. This loop continues until the edge misfit is within the required tolerance. The drawback of this method is that the convergence rate and even whether it converges at all highly depends on the skills of the operator. Furthermore it is possible that this method converges on a local minimum of the edge misfigure and the global minimum is not found and thus not taking full advantage of the capabilities of the remedial strategy.

Another approach would be to create a model of the removal process, including the influence of the edge discontinuity and the mitigation techniques, and optimise the parameter set computationally. The advantage is that this method doesn't require repeated, time consuming experiments and, depending on the optimisation strategy used, can identify the global optimal parameter setting. The drawback is that the accuracy of the approach is limited by the accuracy of the developed model of the removal process.

The work reported in this chapter presents a numerical model of the removal of rigid sub-aperture tools, which is evaluated using experiments performed with the ball bearing mounted rigid grolishing tool introduced in Chapter 2 and mitigation strategies are evaluated.

3.3 Uniform pressure distribution

The most basic model investigated here of the pressure between a rigid tool and a workpiece near to the edge assumes a uniform pressure distribution. If the load on the tool is kept constant the pressure between the tool and the workpiece increases the more the tool hangs over the edge of the tool as it is supported by a smaller contact area [114].

3.3.1 Model

This effect has been simulated using MATLAB for a circular 50 mm diameter rigid tool on a square workpiece for different values of "tool overhang", which is a machining parameter that governs the maximum the tool is allowed to hang over the edge. The same definition of "tool overhang" is used as by *Zeeko* in their Tool Path Generator software: if the "tool overhang" is zero then the maximum position of the tool is where the center of the tool coincides with the edge of the part. If the outer most position of the tool along the tool-path is inward of the edge then the "tool overhang" value is negative and vice versa.

The relative pressure and velocity have been estimated using a discrete method and from that the removal is calculated. The results of the simulations are shown in the figures 3.3.1a and 3.3.1b. The first shows a simulated surface height profile measured from one face of the square workpiece to the opposite face. The second shows a similar profile, but from one corner to the opposite.

3.3.2 Remedial strategies

Two types of remedial strategies are investigated to minimise the edge effect, one that changes the overall form of the influence function of the tool and another that changes the process parameters locally.

Circular rigid tool with central exclusion

The same simulations as before have been performed using a 50 mm diameter rigid tool with a central exclusion zone (e.g. by cutting a circular hole in the polishing cloth at the center of the tool).

The simulations have been repeated using a tool with a central exclusion zone of 30 mm. The results of which are shown in figures 3.3.2a and 3.3.2b.

Comparison with the results from section 3.3.1 shows that the shape of the edge artefacts changes when using a rigid tool with a central exclusion but the P-V of the error does not change significantly. Furthermore, the removal in the bulk area of the tool with central exclusion is lower, as is to be expected. So unless it is followed by a polishing process that benefits from this specific shape of the edge artefact, it is preferred to use a rigid tool without a central exclusion.

Dynamic polishing force

Another way to control edge effects (i.e. edge roll and upturn) is by actively controlling the force applied to the workpiece depending on the overhang of the tool. This can be achieved by actively raising and lowering a spring loaded tool where required during polishing, using Hooke's law [115, 116] to control the force and thereby the pressure of the tool applied on the workpiece. To this end three sets of measurement data, provided by Colin Williams of *Qioptiq Ltd*, of the force applied by the spring for different compression distances of the tool have been

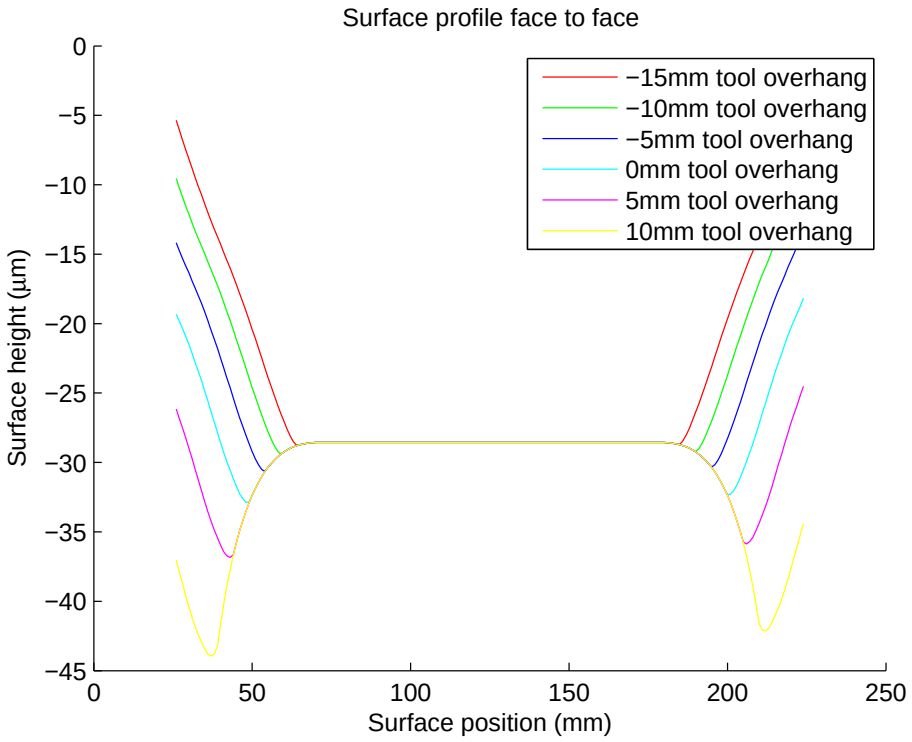

(a) Measured from one face of the square workpiece to the opposite face.

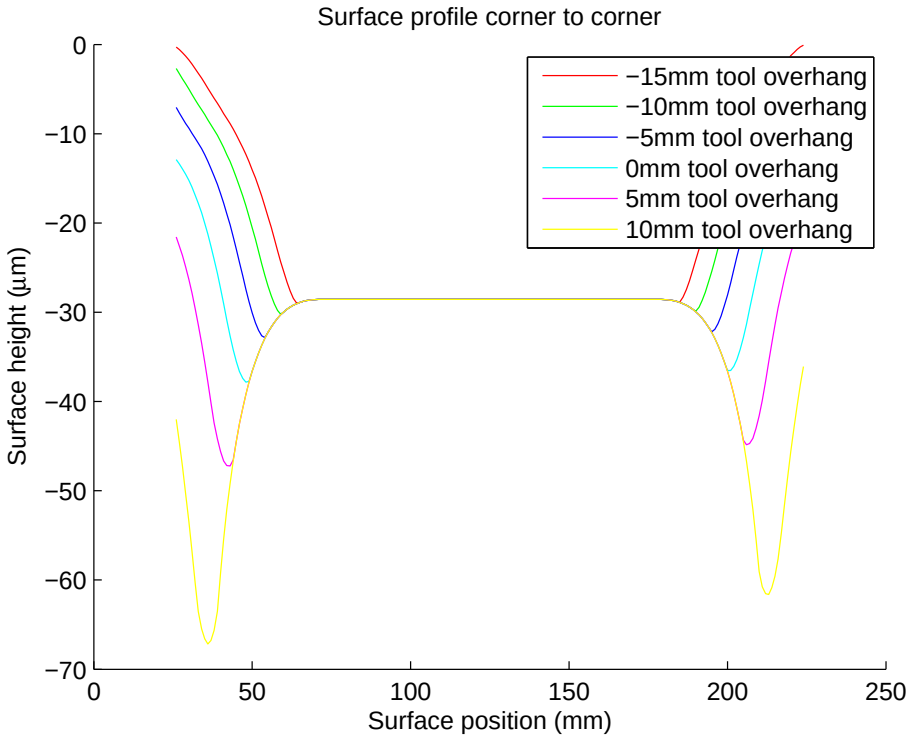

(b) Measured from one corner of the square workpiece to the opposite corner.

Figure 3.3.1: Simulated surface height profiles after applying a rigid tool with different values of tool overhang.

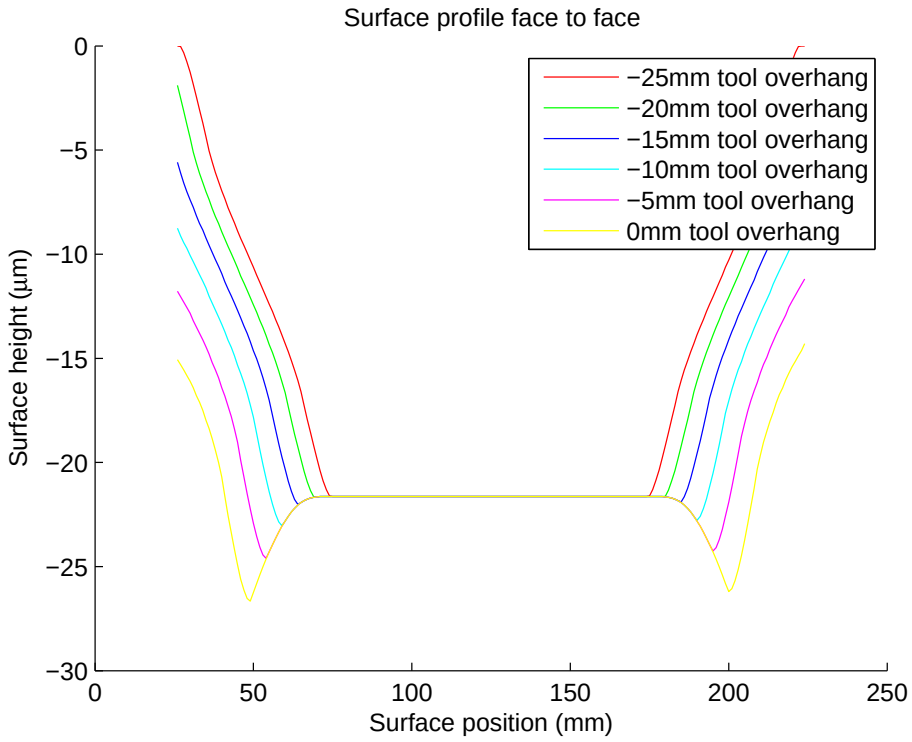

(a) Measured from one face of the square workpiece to the opposite face.

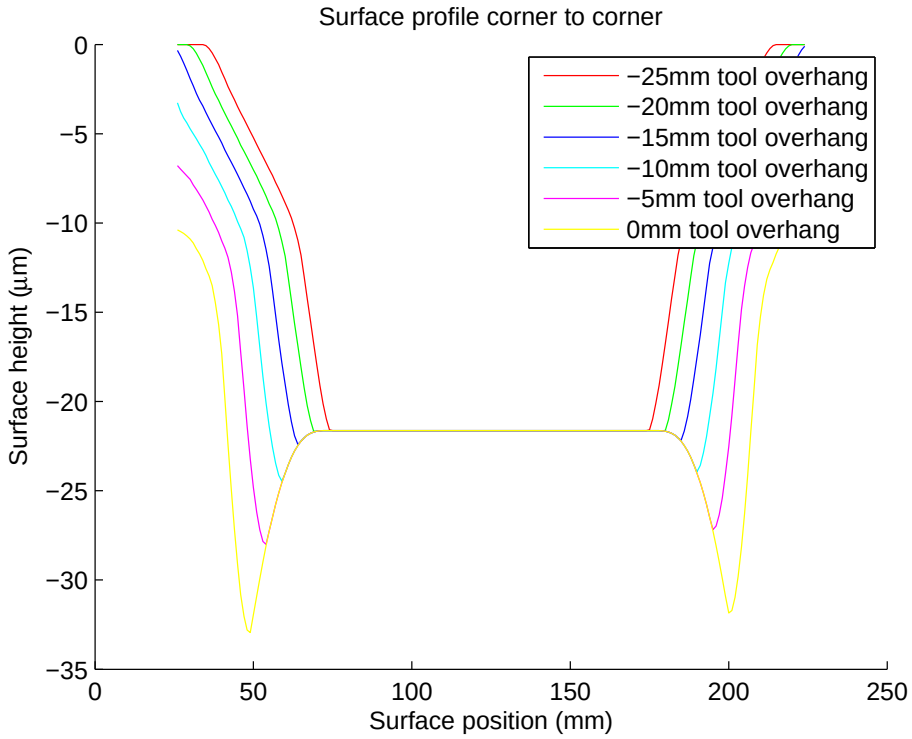

(b) Measured from one corner of the square workpiece to the opposite corner.

Figure 3.3.2: Simulated surface height profile for different values of tool overhang using a tool with a central exclusion zone.

analysed. Afterwards the effects of dynamically changing the pressure on the surface height profile have been simulated using the approach outlined above.

As outlined before, the possibility to control the pressure using different compression distances of a spring loaded tool have been investigated. To this end, three sets of measurement data have been taken of the force applied by a spring loaded tool for different compression distances. The sets differ because so-called "nulling" of the compression distance has been redone before each set. To each set of data a linear fit has been applied, which are shown together with the measurement data in Figure 3.3.3.

The three linear fitted curves can be averaged to obtain the following equation that relates the force the tool applies on the workpiece to the compression distance of the tool:

$$F = (4.9917 \pm 0.2929) \cdot \delta + (25.4693 \pm 1.0388) \tag{3.2}$$

where F denotes the force and δ the compression distance of the tool. The coefficient of determinations, R^2, equals 0.91. Therefore the fit represents the measured data quite well. The fact that the fitted lines do not cross the y-axis at the origin can be explained by the fact that to "null" the compression distance it has to be in contact with the workpiece and therefore will exert a (relatively small) force on the surface for zero compression distance.

The range of the force is sufficient to compensate for the largest range in pressure due to changes in the contact area caused by the tool hanging over the edge. This largest pressure range occurs for the tool-path that moves the tool out over the edge the most without risking the tool tipping (i.e. a tool overhang setting of zero). The resulting profiles of the compression distance are shown in figure 3.3.4.

The effect of this pressure compensation on the edge has been simulated for different values of the tool overhang and the results are shown in figures 3.3.5a and 3.3.5b.

3.3.3 Conclusion

Apart from the force exerted onto the tool, other parameters can be varied, for instance the dwell time (or feed rate) and the rotational velocity of the tool. A change in one of these parameters multiplies the polishing influence function by a factor, but doesn't change the shape of the influence function (within certain limits, e.g. aqua planing at high rotational velocities). Therefore the results are analogous for all those parameters. Looking at a combination of parameters might be worthwhile if parameters reach their (practical) limit or if one is used to compensate the edge effect of the tool and another to correct the surface misfigure.

As can be seen from the results, the edge roll can be prevented but only at the cost of leaving the edge upturned. Furthermore, if the tool is held at the center by a pivot the highest value of tool overhang is less than zero to prevent the tool from tipping over. The results show that for this tool overhang the upturn is already roughly twice as high as the dip, for both the regular tool

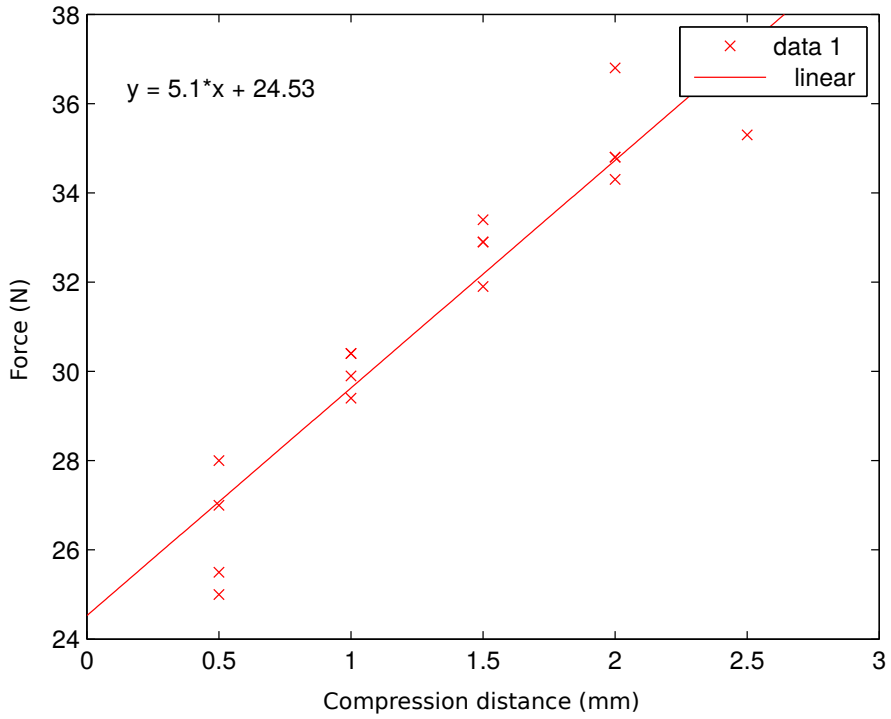

(a) First dataset

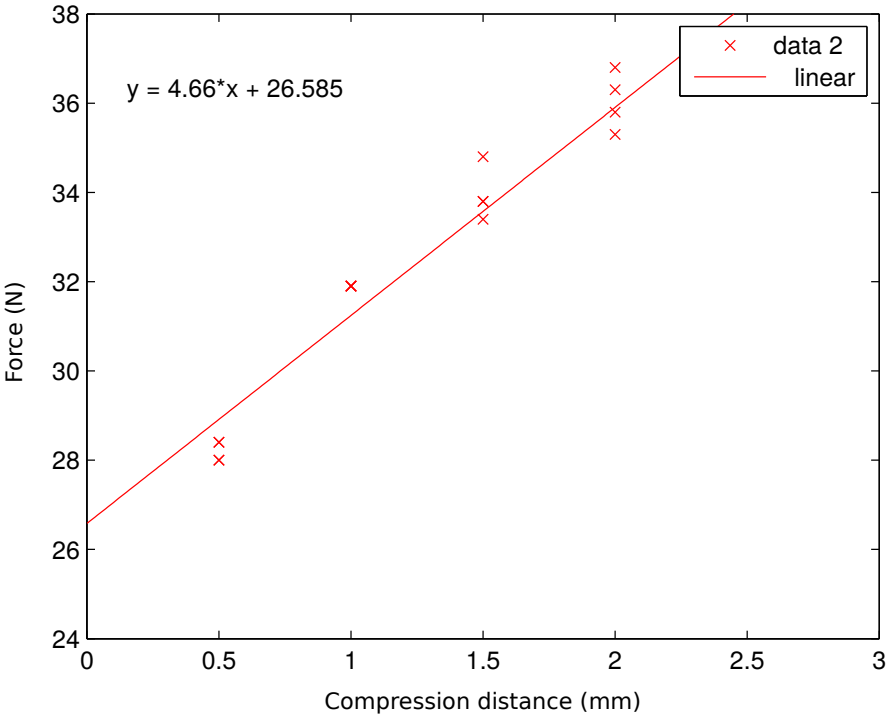

(b) Second dataset

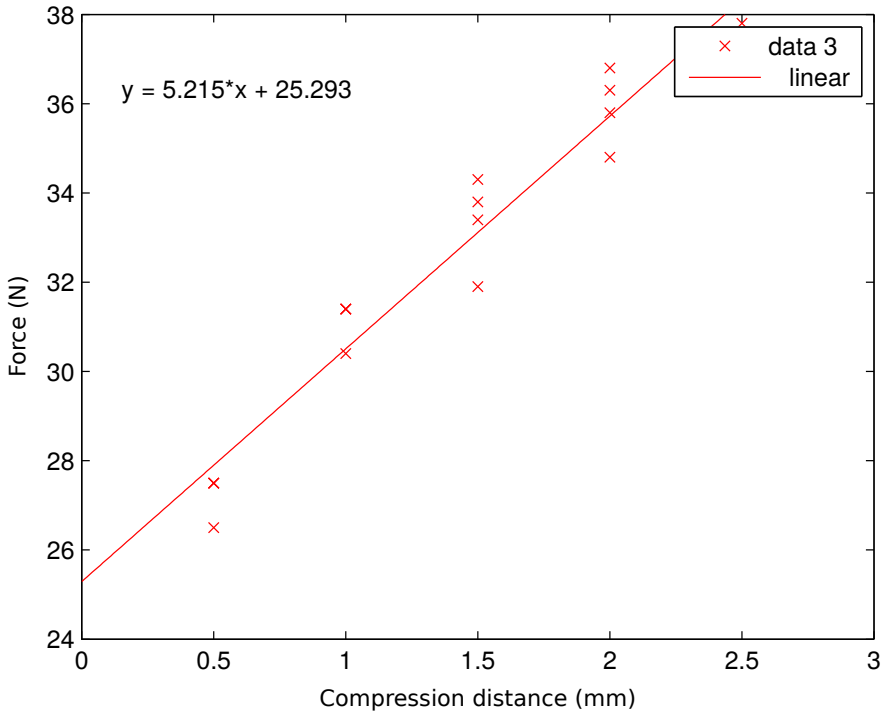

(c) Third dataset

Figure 3.3.3: Force measurement data for different compression distances of a spring loaded sub-aperture rigid tool. The same tool has been measured three times to create three datasets.

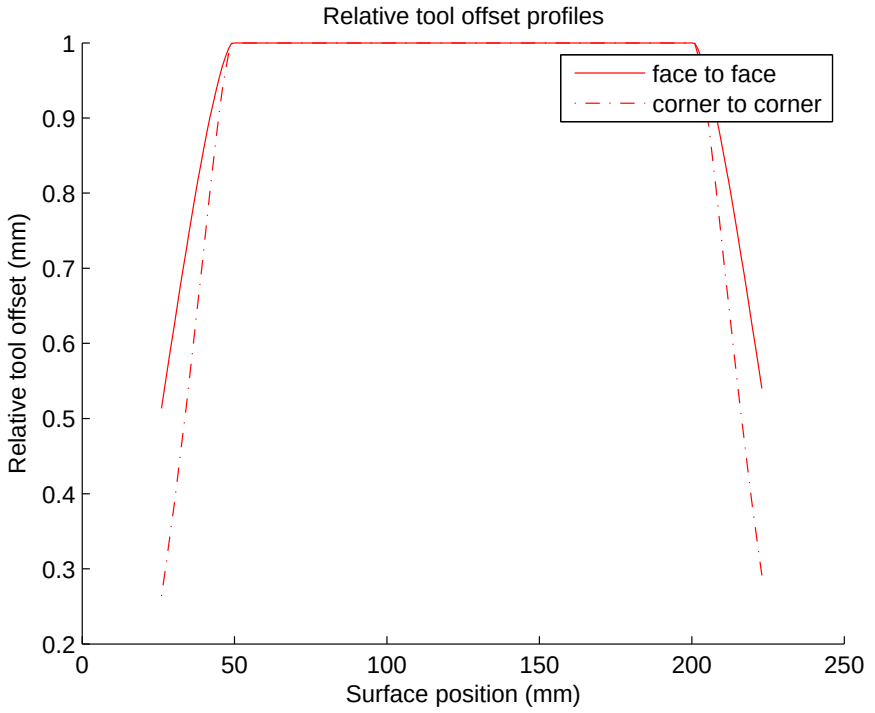

Figure 3.3.4: Profiles of the relative compression distance needed to compensate for the change in pressure due to changes in contact area caused by the tool overhanging the edge of the workpiece.

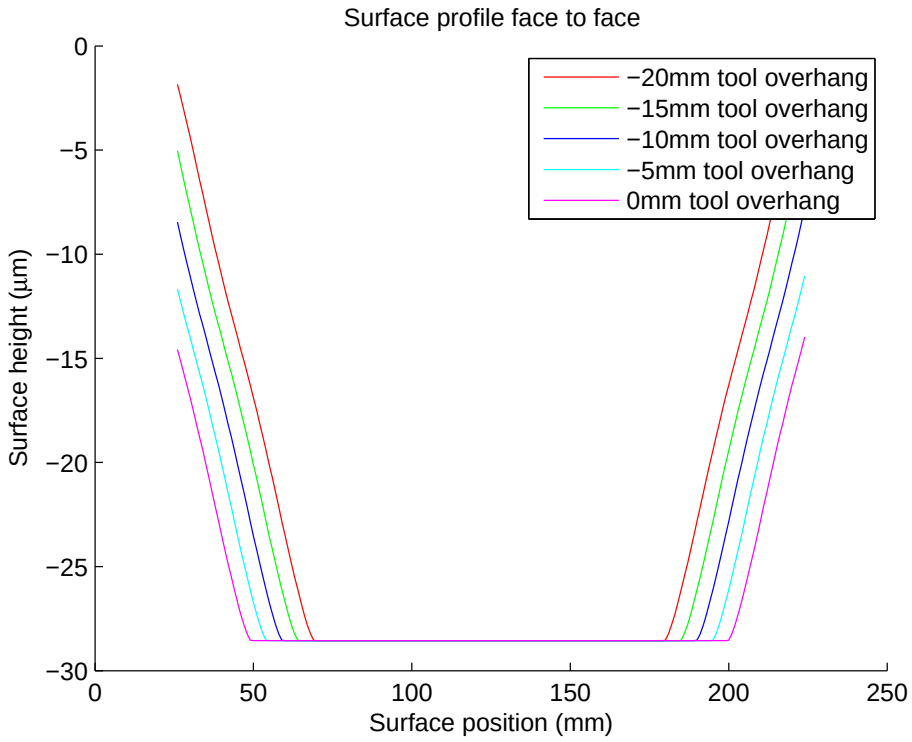

(a) Measured from one face of the square workpiece to the opposite face.

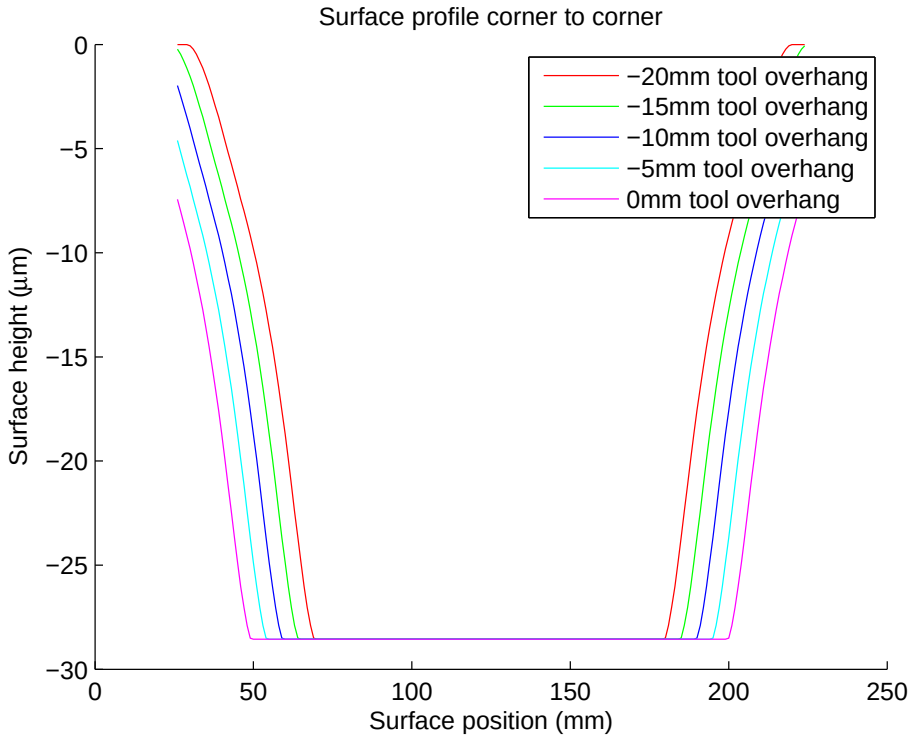

(b) Measured from one corner of the square workpiece to the opposite corner.

Figure 3.3.5: Simulated surface height profiles for different values of tool overhang using compensated tool pressure by varying the compression distance of the tool.

as well as the tool with the central exclusion zone.

According to this model, polishing with a rigid tool leaves edge roll, edge upturn or a combination of the two. It would need to be followed by a different polishing process to remove the edge artefacts. As such, an upturned edge is preferred, as the total volume of material that has to be removed to correct the artefact is much lower. This is more relevant the larger the optics, because the ratio between surface-area and edge-contour is higher.

3.4 Non-uniform pressure distribution

As previously outlined in the introduction of this chapter, when a rigid tool is positioned so that part of it hangs over the edge of the workpiece and it is observed that it does not flip over then the pressure must be redistributed non-uniformly so that mechanical equilibrium is maintained [33]. This section investigates different models of this pressure distribution within the contact area between tool and workpiece for rigid tools that hang over the edge of a workpiece.

3.4.1 Rigid body mechanics

If the pressure distribution is modelled using rigid body mechanics and the tool is in mechanical equilibrium partly hanging over the edge of a workpiece, then

$$\iint_A p(x,y)\,\mathrm{d}x\,\mathrm{d}y - F_0 = 0 \tag{3.3a}$$

$$\iint_A x \cdot p(x,y)\,\mathrm{d}x\,\mathrm{d}y = 0 \tag{3.3b}$$

$$\iint_A y \cdot p(x,y)\,\mathrm{d}x\,\mathrm{d}y = 0 \tag{3.3c}$$

where A denotes the contact area between tool and workpiece, $p(x,y)$ the pressure distribution, x and y the Cartesian coordinates with respect to the centre of the tool and F_0 the force pressing the tool onto the workpiece (e.g. gravity or a pre-loaded spring). As the tool is in mechanical equilibrium the total force exerted by the workpiece on the tool must be equal to the force pressing the tool onto the workpiece, as reflected in Equation 3.3a, and the x- and y-moments must be equal to zero, as reflected in Equations 3.3b and 3.3c.

Wagner et al. [33], Jones [117], Luna-Aquilar et al. [118] and Cordero-Dávila et al. [119] assume that the pressure distribution can be described by some proposed mathematical function (e.g. a linear function) and solve its parameters analytically using Equations 3.3. Here a different approach is adopted: instead of imposing any assumptions on the form of the pressure distribution it has been simulated discretely in MATLAB for a circular rigid tool near the corner of a hexagonal workpiece for different amounts of the tool hanging over the edge. Starting with

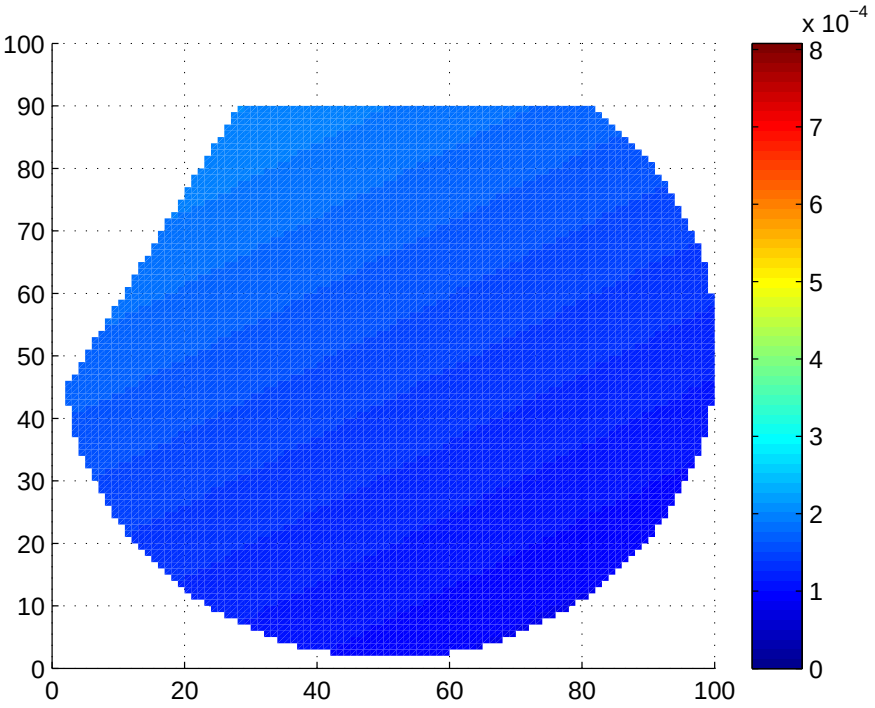
x 10^-4
100
90
80
70
60
50
40
30
20
10
0
0
20
40
60
80
100
8
7
6
5
4
3
2
1
0

(a) 40 mm

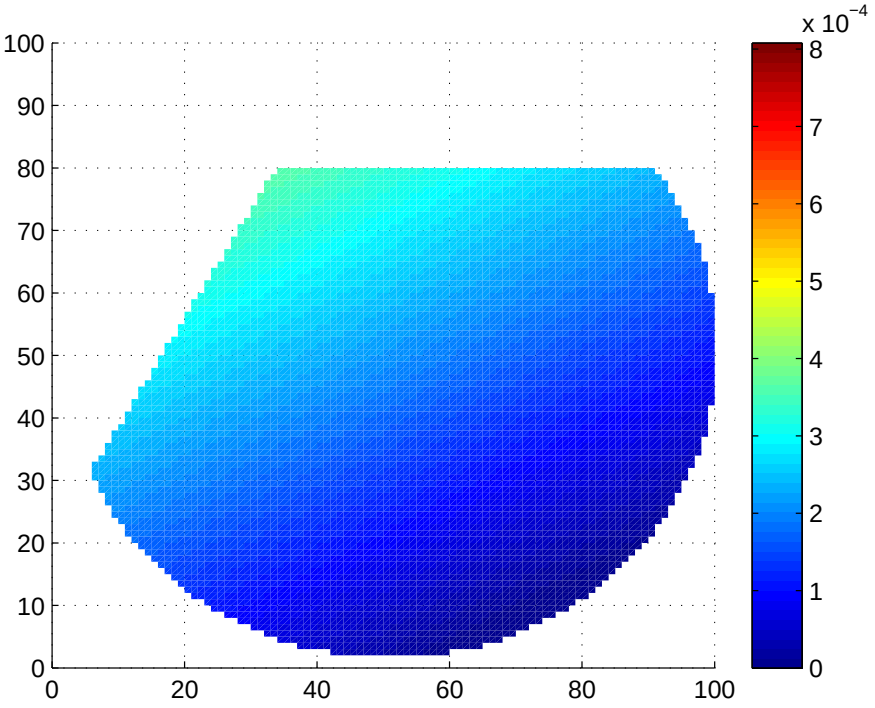
x 10^-4
100
90
80
70
60
50
40
30
20
10
0
0
20
40
60
80
100
8
7
6
5
4
3
2
1
0

(b) 30 mm

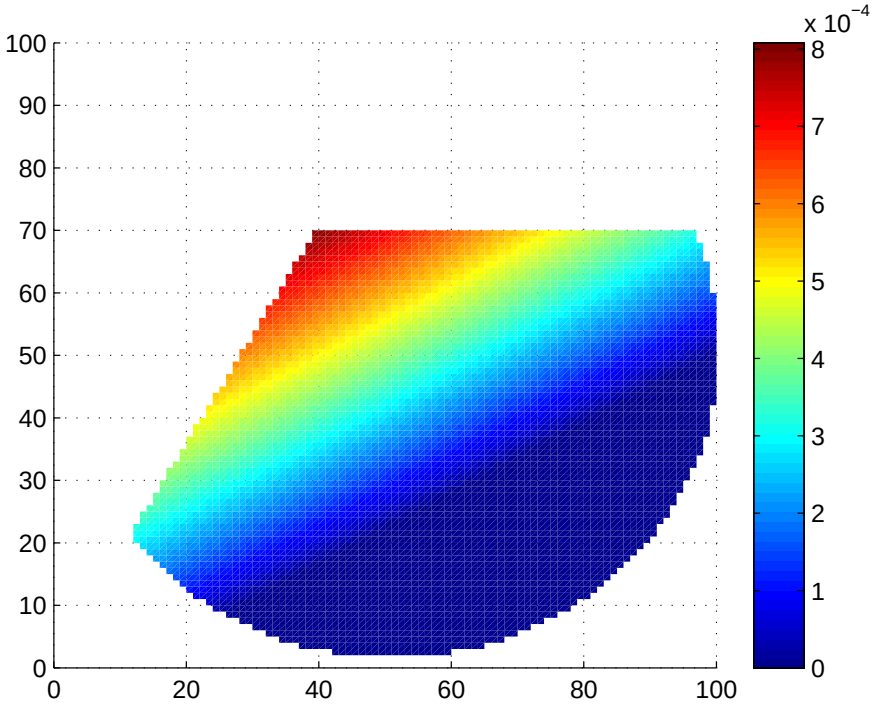

(c) 20 mm

Figure 3.4.1: Pressure distributions for different distances of the tool's centre to the workpiece edges with pressure in arbitrary units. Both spatial units in mm.

a uniform pressure distribution over the contact area an iterative optimisation has been performed finding the least squares solution of Equations 3.3.

The resulting pressure distributions for different distances of the tool's centre to the edges of the workpiece are shown in Figure 3.4.1. It is noted that these results are a local minimum and not necessary the global minimum of the set of equations given before because the problem is under-defined: in practice the number of discrete points for which the local pressure must be found is much larger than the number of equations. The results show a linear distribution of the pressure in the contact area between tool and workpiece that is truncated at the zero pressure level so no negative values of the pressure are present.

In Figure 3.4.2 the removal distributions are shown when the pressure and velocity distributions are combined using the Preston equation for different distances of the tool's centre to the workpiece edges. The results are in agreement with the linear pressure distribution model used by Kim et al. [120, 121] but as mentioned by the same authors the linear distribution does not explain the "edge-roll" that is observed when polishing with a rigid tool that is (at times) hanging over the edge of the workpiece.

Part of the work in this section is included in [122] of which the author is a co-author.

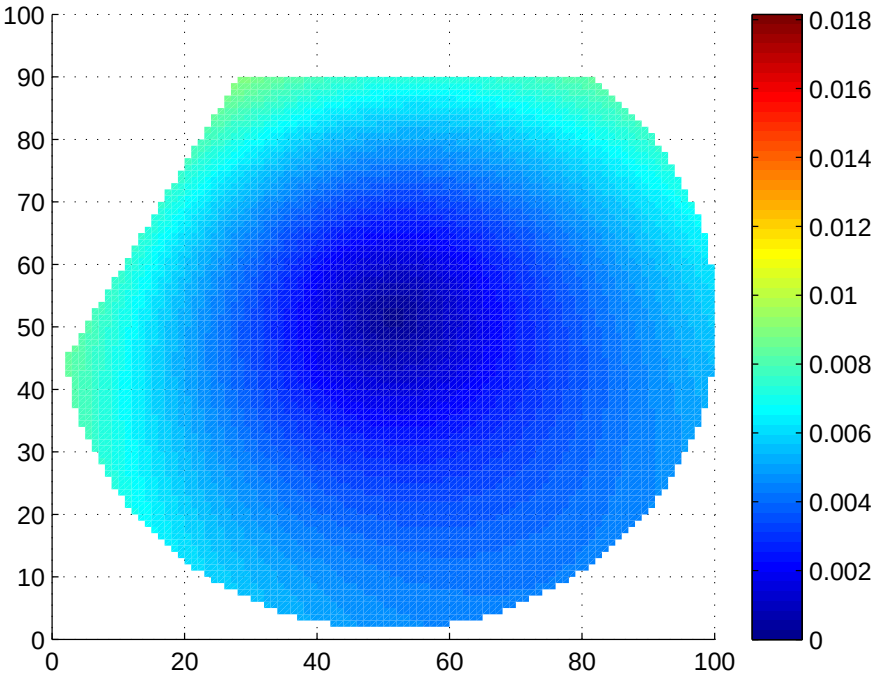
100
90
80
70
60
50
40
30
20
10
0
0
20
40
60
80
100
0.018
0.016
0.014
0.012
0.01
0.008
0.006
0.004
0.002
0

(a) 40 mm

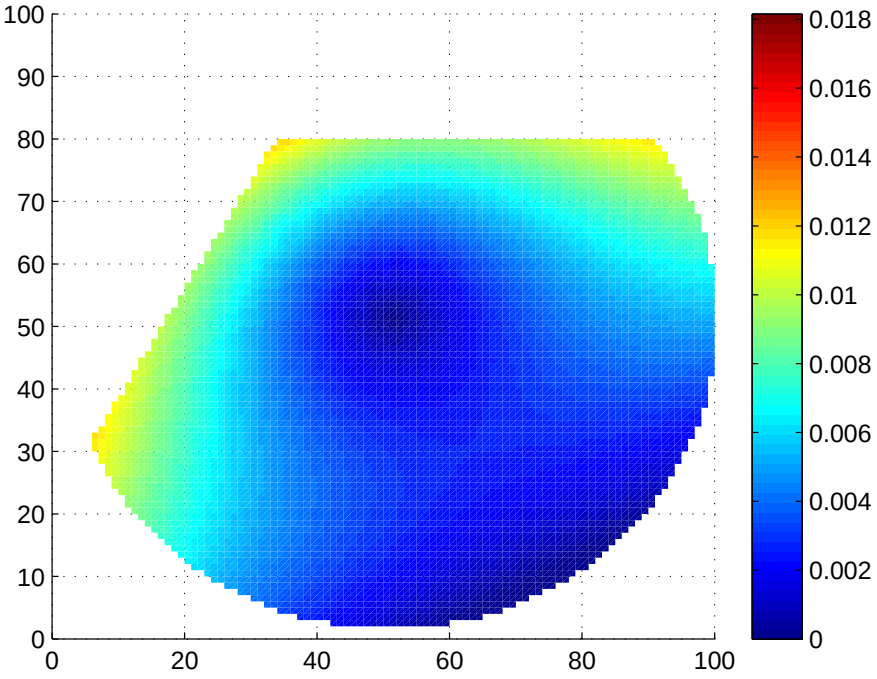
100
90
80
70
60
50
40
30
20
10
0
0
20
40
60
80
100
0.018
0.016
0.014
0.012
0.01
0.008
0.006
0.004
0.002
0

(b) 30 mm

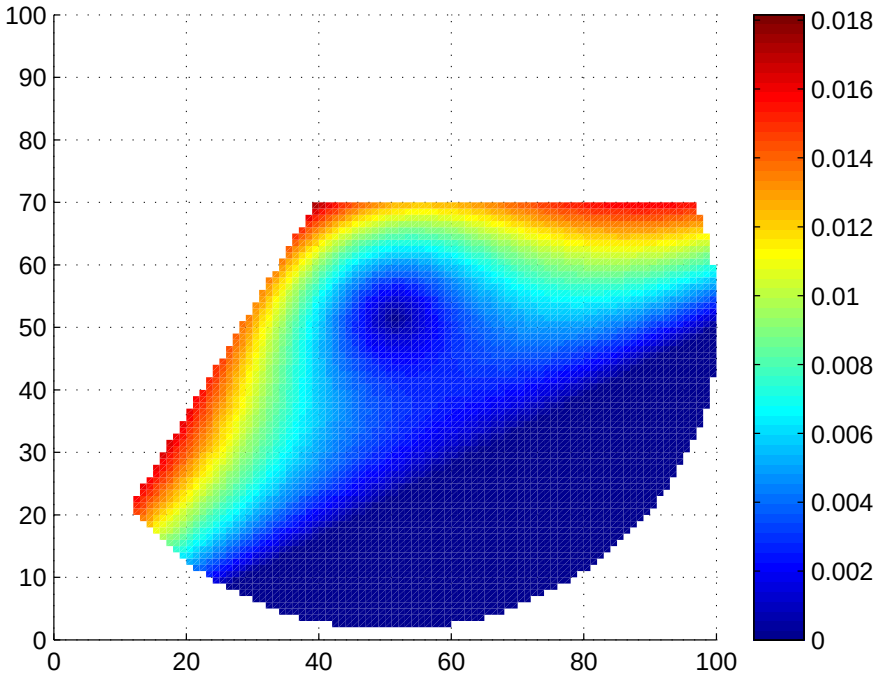

(c) 20 mm

Figure 3.4.2: Removal distributions for different distances of the tool's centre to the workpiece edges with removal in arbitrary units. Both spatial units in mm.

3.4.2 Continuum mechanics

As can be gathered from the previous, a more complex model is needed to derive the pressure pressure distribution, starting by incorporating the elasticity of the materials. In a Finite Element Analysis (FEA) software package (namely *Code_Aster*) the tool and workpiece have been modelled and their material properties (Young's modulus, Poisson's ratio) have been assigned.

As explained by Cook et al. [123], in a Finite Element Analysis the problem is divided into a finite number of elements inside of which physical properties are assumed to be constant and the equations of the selected physical model are established for each element, including the interactions with its neighbouring elements. Afterwards the properties (e.g. displacements, strains and stresses) of each individual element are numerically optimised to solve the previously established equations. The physical model is not limited to static mechanics but may include dynamics (e.g. varying load or vibration) or a different branch of physics (e.g. thermodynamics, electromagnetism and fluid dynamics). As the number of elements increase the (average) size the elements becomes smaller until at the limit they become infinitesimally small representing a continuum. However computational constraints limit the total number of elements that can be used. The properties of the elements have to be kept in memory as well as a number of previous estimates, depending on the solver, thus the amount of memory available limits the number of elements that can be used. At the same time, additional elements means more equations have to be solved which takes longer. This does not impose a hard limit on the number of elements used but in practice the method loses its usefulness if it takes too long to arrive at a solution.

Kim et al. [120, 121] have used FEA to model the pressure distribution between a rigid tool and the workpiece while partly hanging over the edge. The tool and workpiece were not modelled as separate entities but as one solid with different physical properties in the regions representing the tool and workpiece. In effect the two are bonded together at the interface between the two. As such the model only needs to be fixed once (generally the bottom surface of the workpiece) to limit the degrees of freedom. A similar model has been implemented in *Code_Aster* in 2D and the results are shown in Figure 3.4.3.

(a) Tool completely supported by the workpiece

(b) Tool overhanging the workpiece

Figure 3.4.3: Simulated stress distribution for two different values of tool overhang for a 2D "bonded" FEA model.

The degrees of freedom of the model were constraint by fixing the lower edge of the workpiece and a uniform pressure was applied to the top edge of the tool. Using a static non-linear model the displacement of and stress at predefined points in both geometries was calculated. As can be seen from the results the stresses increase exponentially towards the edge of the workpiece.

Kim at al [120, 121] found that the model did not completely predict experimental data: their model predicted less removal than measured after experiments in the region furthest away from the edge within the contact area. Furthermore the model allows more than 50 % of the

(a) Before pressing the tool onto the surface

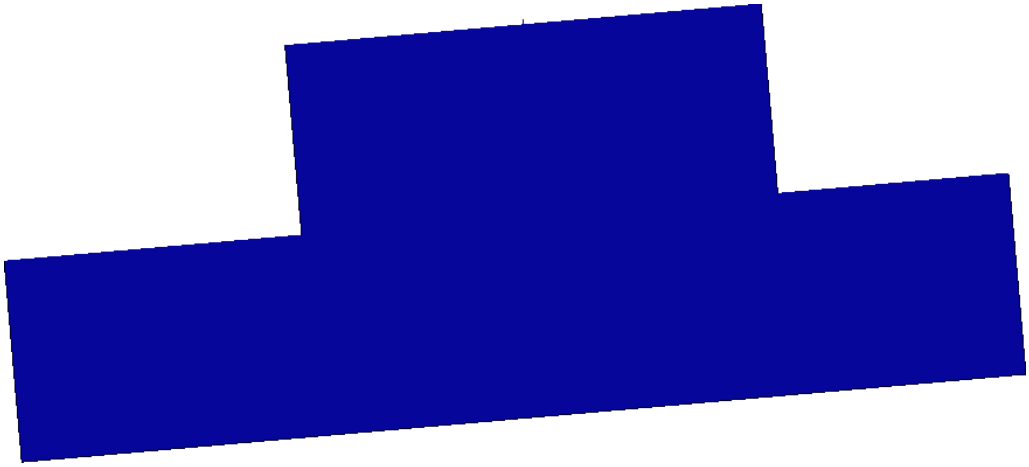

(b) Pressing tool onto the surface

Figure 3.4.4: FEA simulation of the functionality of a ball bearing to passively align tool and workpiece.

tool to protrude over the edge, which in practice results in mechanical instability of the tool.

Here a different model is implemented where tool and workpiece are considered separate entities and their contact is modelled. This allows the tool to slide across the surface and it is possible to model the functionality of a ball bearing (used to passively align tool and workpiece), as shown in Figure 3.4.4. This kind of model also allows other types of investigations, for instance the analysis of the effect of "mismatch" (discussed in Chapter 2) on the pressure distribution. More on this later in this chapter.

In such an FEA contact model both the tool and the workpiece have to be fixed separately to limit the degrees of freedom of the model, for instance by fixing the bottom of the workpiece in all three dimensions and the top of the bearing in both lateral dimensions (as in general the tool is held in position by a machine).

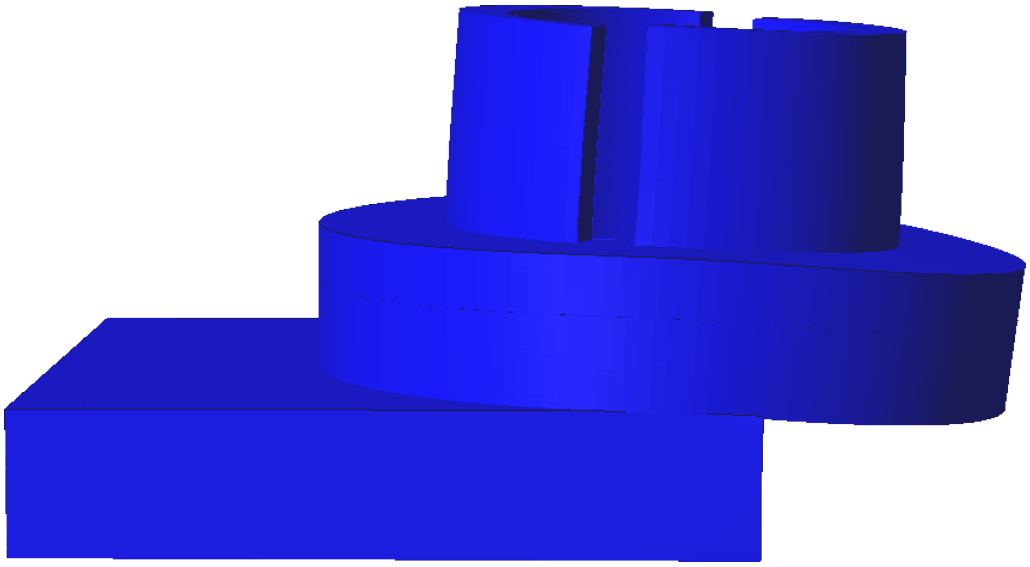

Figure 3.4.5: Results of FEA simulation of the grolishing tool protruding over the edge by 40 % of its diameter, the deformations are magnified by a factor of 5×10^5 for visibility.

The geometry of the ball bearing mounted, 100 mm diameter grolishing tool introduced in Chapter 2 has been recreated in software and subjected to an FEA contact model. The tool is composed of two materials, aluminium and cast iron. Typical values for their physical properties have been taken from literature as the exact materials used were not know. The workpiece was modelled by a rectangular box and the physical properties of Borosilicate were used. *Code_Aster* was set up to apply gravity and the model was solved for different positions of the tool, from no part hanging over the edge to almost 50 % protruding over the edge. The results of the deformation of tool and workpiece for that last position are shown in Figure 3.4.5, albeit exaggerated by a factor of 5×10^5 for visibility. Figure 3.4.6 shows the pressure distribution on the bottom of the tool for that same position.

As in general when using numerical methods the fact that the computation results in a solution is no indication of the accuracy of the result. Several sanity checks of the results were performed. First the mass as calculated by the model for the two materials of the tool were

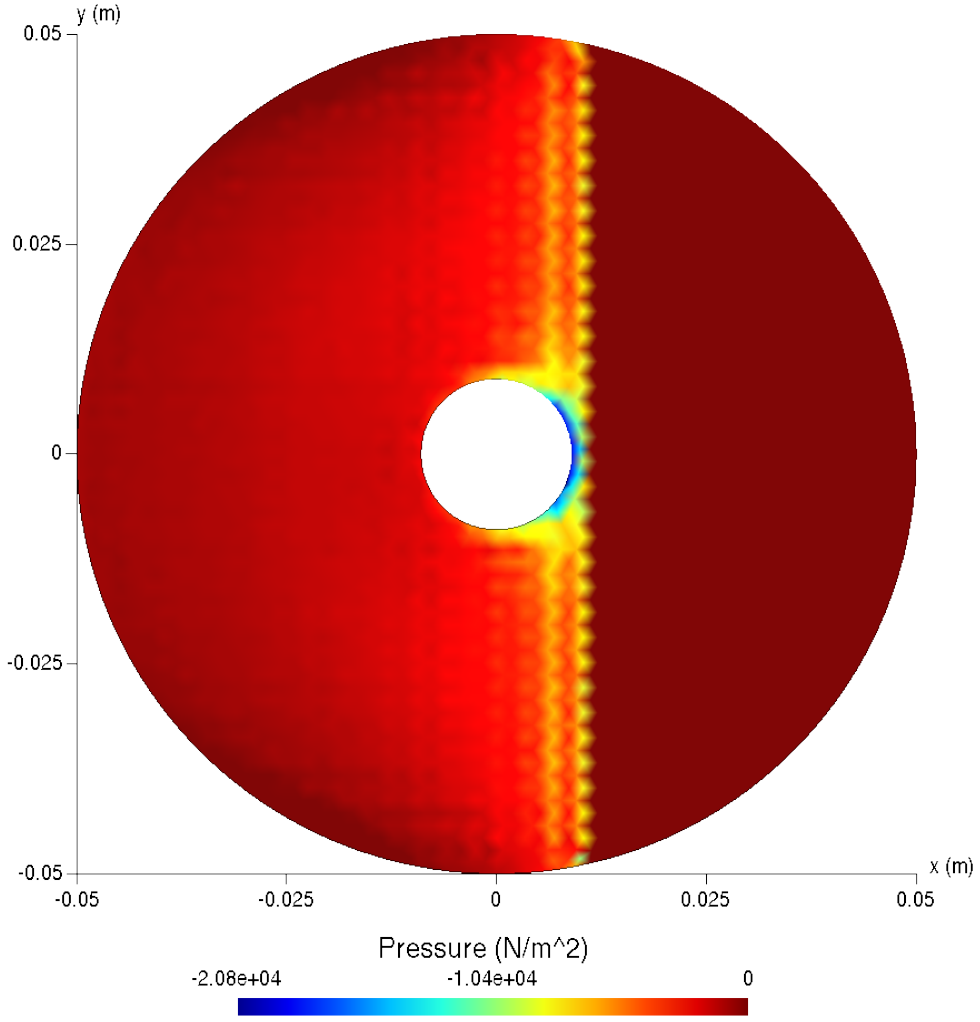

Figure 3.4.6: Pressure distribution resulting from FEA simulation of the grolishing tool while it hangs over the edge by 40 % of its diameter. The negative sign indicates that the normal of the surface of the tool is oriented downwards. The sawtooth shape is a descretisation effect due to the mesh size and orientation.

compared with actual measurements. Secondly the weight of the tool was calculated based on the modelled mass of the two components and compared with an estimate of the total force between tool and workpiece. This total force, F_o, was arrived at by

$$F_o = p_o \times \pi \times (r_1^2 - r_2^2) \tag{3.4}$$

where the average pressure when the tool is fully supported by the workpiece, p_o, is multiplied by the contact area between tool and workpiece (with r_1 and r_2 the diameter of the tool and the diameter of the central cavity respectively). The results of these checks are summarised in Table 3.4.1 and there are no obvious discrepancies.

Table 3.4.1: Sanity check of the results of the Finite Elements Analysis

	Model	Measurement
Cast iron mass	0.698 kg	0.679 kg
Aluminium mass	0.220 kg	0.257 kg
Total mass	0.917 kg	0.936 kg
Weight	9.0 N	-
Average pressure	1200 N m^{-2}	-
Contact area	0.0076 m^2	-
Contact force	9.1 N	-

Next it was confirmed that the maximum resulting deformation was within the limits of the applied contact model. For larger deformations a different contact model would have to be applied.

Additionally the resulting pressure distributions are observed to vary mainly perpendicular to the edge, as expected from symmetry considerations, increase exponentially towards the edge and are more pronounced with increasing protrusion, as expected. Thus the results are deemed sane, however the question remains whether they are accurate.

3.4.3 Validation

To evaluate the accuracy of the model an experiment has been designed to validate the results. To simplify measurement and average out removal variation due to uneven slurry application or other parameters not under control it is preferred to evaluate the removal of the grolishing tool when it is scanned along a track instead of held in one place on the workpiece for a certain amount of time.

For a spinning tool in pole-down configuration the relative speed between tool and workpiece is a function of the distance to the centre, $r(x, y)$:

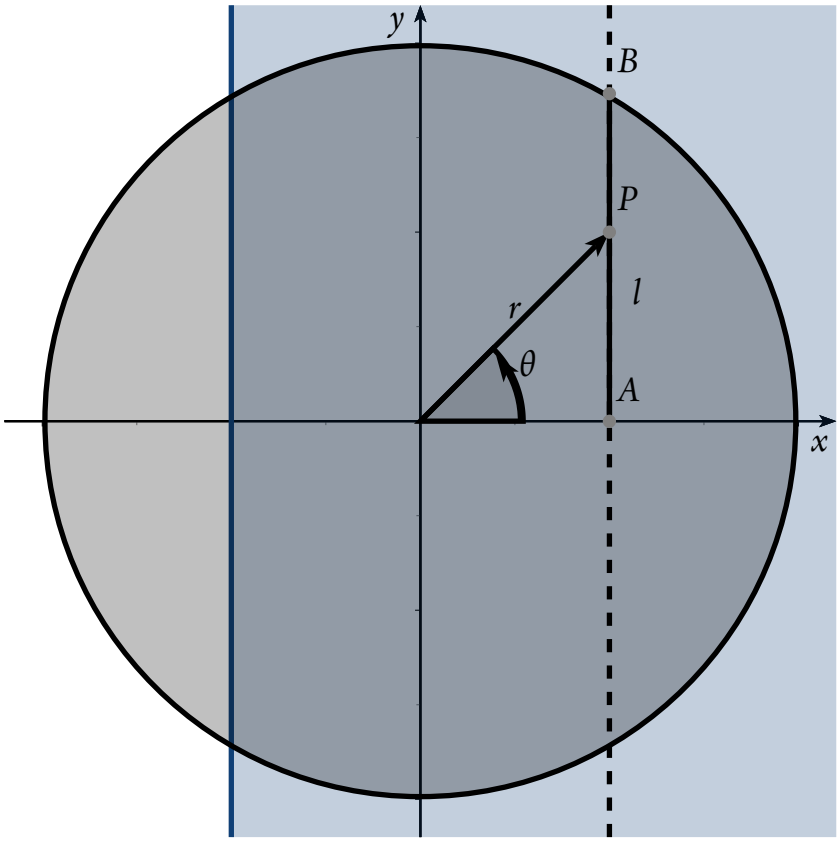

Figure 3.4.7: Diagram showing the calculation of the removal profile, perpendicular to the scanning direction, when the tool is scanned parallel to the edge.

$$|\vec{v}(x,y)| = \begin{cases} v(r) & \text{if } r \leq D/2 \\ 0 & \text{if } r > D/2 \end{cases} \tag{3.5}$$

with r and θ polar coordinates

$$r^2 = x^2 + y^2 \tag{3.6}$$

$$\tan(\theta) = \frac{y}{x} \tag{3.7}$$

If the tool is not overhanging the edge (i.e. the tool is located on the bulk surface) and pressed onto the surface of the workpiece with a constant force through a ball joint or under its own weight we assume the pressure between tool and workpiece to distributed rotationally symmetric due to symmetry

$$P_b(x,y) = \begin{cases} P_b(r) & \text{if } r \leq D/2 \\ 0 & \text{if } r > D/2 \end{cases} \tag{3.8}$$

and with Preston's equation (3.1) the removal rate when processing the bulk surface, $\frac{\partial h_b(x,y)}{\partial t}$ becomes

$$\frac{\partial h_b(x,y)}{\partial t} = \begin{cases} u(r) & \text{if } r \leq D/2 \\ 0 & \text{if } r > D/2 \end{cases} \tag{3.9}$$

with

$$u(r) = cP_b(r)v(r) \tag{3.10}$$

If the tool is moved with constant speed, v_t, along the y-axis the total removal for any point on the surface, R_b, depends only on its x-coordinate and is proportional to the integral over line segment l (see Figure 3.4.7) of the removal rate and inverse proportional to the traversal speed of the tool

$$R_b(x) = \int_{-\infty}^{\infty} \frac{\partial h_b(x,y)}{\partial t} \cdot \frac{\mathrm{d}y}{v_t} = 2 \int_l \frac{u\left(r(x,y)\right)}{v_t}\,\mathrm{d}y \tag{3.11}$$

With

$$r = \frac{x}{cos\left(\theta\right)} \tag{3.12}$$

$$\mathrm{d}y = \frac{x}{cos^2\left(\theta\right)}\mathrm{d}\theta \tag{3.13}$$

$$\cos(\theta_B) = \frac{x}{D/2} \tag{3.14}$$

this becomes

$$R_b(x) = \frac{2x}{v_t} \int_0^{cos^{-1}(2x/D)} u\left(\frac{x}{\cos(\theta)}\right) \frac{\mathrm{d}\theta}{\cos^2(\theta)} \tag{3.15}$$

the removal profile perpendicular to the direction of travel with the tool on the bulk surface.

If the tool is placed so that part of it is hanging over the edge (at $x = h$) then the pressure distribution between tool and workpiece will change. Due to symmetry we assume that the pressure distribution at the edge can be expressed as a function, $f(x)$, times the pressure distribution when the tool is placed on the bulk surface

$$P_e(x,y) = \begin{cases} f(x) \cdot P_b(r) & \text{if } r \leq D/2 \\ 0 & \text{if } r > D/2 \end{cases} \tag{3.16}$$

where x is the coordinate axis perpendicular to the edge. The results of the Finite Element Analysis agree with this assumption as the ratio between the pressure when the grolishing tool is hanging 40 mm over the edge and the pressure when the tool is completely supported by the workpiece changes mainly with the x coordinate, as shown in Figure 3.4.8. Thus the removal

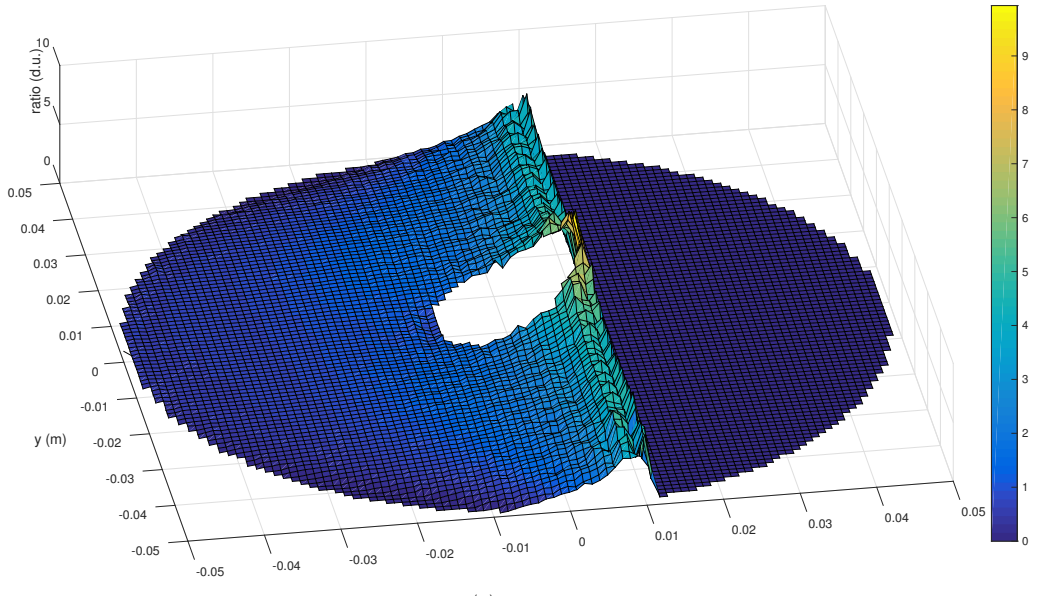

Figure 3.4.8: Ratio between the pressure when the grolishing tool is hanging 40 mm over the edge and the pressure when the tool is completely supported by the workpiece.

profile perpendicular to the direction of travel for a tool hanging over the edge, R_e, equals

$$R_e(x) = \frac{2xf(x)}{v_t} \int_{\circ}^{cos^{-1}(2x/D)} u\left(\frac{x}{\cos(\theta)}\right) \frac{\mathrm{d}\theta}{\cos^2(\theta)} \tag{3.17}$$

$$= f(x)R_b(x) \tag{3.18}$$

with the function $f(x)$ depending on the amount the tool hangs over the edge of the workpiece. Therefore if the removal profile of a track of the tool predicted by the Finite Element Analysis model matches the removal profile obtained after an experiment then the predicted pressure distribution must be correct.

To evaluate the performance of the Finite Element Analysis model its results have been compared to the experimental results of the ball bearing mounted, 100 mm diameter grolishing tool. This tool has been mounted by *OpTIC* on a on a spindle attached to a *FANUC* industrial robot. It was set up to process tracks parallel to the edge with different amounts of protrusion over the edge by Zheng Xiao of *Glyndŵr University*, who also prepared the Borosilicate, 400 mm across corners, regular hexagon sample, executed the experiments and performed the measurements using *Taylor Hobson*'s Extended Range Form Talysurf, a picture of which is shown in [124]. The parameters used during the experiments are shown in Table 3.4.2.

The pressure distributions in the contact area for different amounts of the tool hanging over the edge as predicted by the FEA model have been imported into MATLAB and multiplied with the velocity profile of the spinning tool to create predicted 3D tool influence functions. These influence functions were then summed in the direction parallel to the edge resulting in the predicted removal profile perpendicular to the track when the tool is moved with constant speed

Table 3.4.2: Parameters used during validation experiments using a ball bearing mounted, 100 mm diameter grolishing tool.

Parameter	Value
Head speed	500 rpm
Feed rate	3 mm s^{-1}
Abrasive component	Al_2O_3
Particle size	9 µm

along the edge. These influence functions and profiles are not calibrated, however, as the Preston coefficient, c in Equation 3.1, is not known for this process. For each experiment the constant has been estimated by performing a least squares fit of the model to the experimental data.

Results and discussion

The resulting removal profiles of the model and experiments are plotted in Figure 3.4.9. The coefficient of variation of the estimated c constants is 0.10 which indicates that the Preston coefficient of the model is reasonably constant between experiments. However the model matches poorly the shape of the removal profile, particularly close to the edge for the larger protrusions. The root-mean-squared-difference are 0.30 µm, 0.49 µm, 0.28 µm, 0.67 µm and 0.89 µm for increasing protrusions. The obvious explanation would be that the used model does not correctly describe the removal process. However the model does show the exponentially increased removal close to the edge that causes "edge-roll", which is known to occur during polishing with rigid tools.

The experimental data does not show this exponentially increased removal close to the edge. Potentially this is due to the fact that when material is removed non-uniformly a mismatch is created between tool and workpiece that leads to a different pressure distribution. Put differently, that the smoothing effect of the tool undoes any uneven removal. As the maximum removal, 3 µm, is much smaller than the abrasive particle size, 9 µm, this would violate the rule-of-thumb discussed in Chapter 2 that the mismatch between tool and workpiece does not change the removal if it is smaller than the abrasive particle size [91]. It must be noted that the experiments with 0 mm, 20 mm and 40 mm protrusion have been performed on one single edge without reconditioning in between as well as the experiments with 10 mm and 30 mm protrusion. Even so, the total maximum removal for all experiments for a single edge is still smaller than the abrasive particle size.

The same parameter settings have also been used to process a track in the middle of the workpiece and the profile through this track has been measured twice several millimetre apart. The results are plotted in Figure 3.4.10 as well as the profiles of the model and experiment for 0 mm protrusion for comparison. The root-mean-squared-difference of the two profiles of the repeat experiment compared to the experiment near the edge of the part are 0.29 µm and

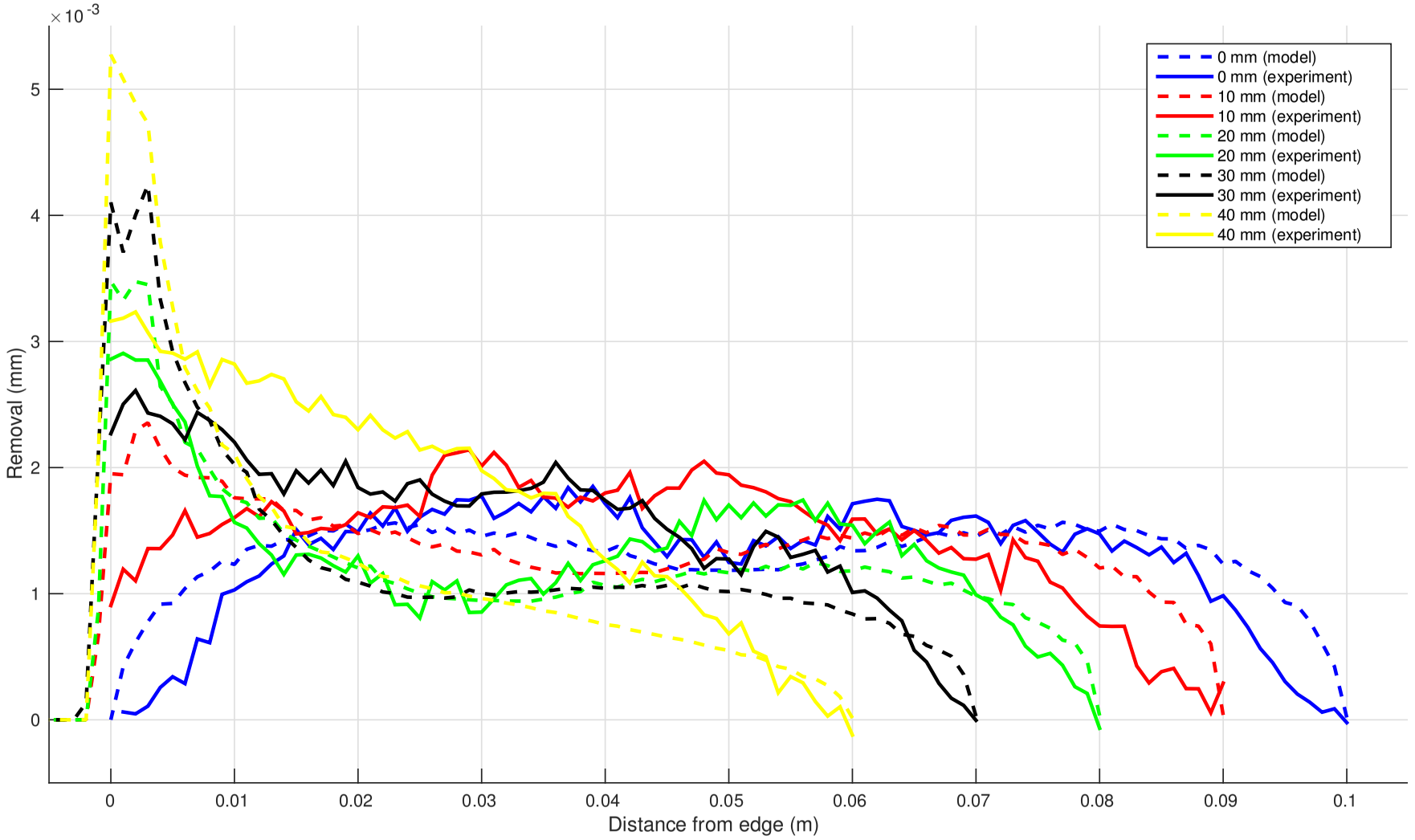

Figure 3.4.9: Comparisson of the predicted removal profiles by the FEA model with the removal profiles obtained by experiments.

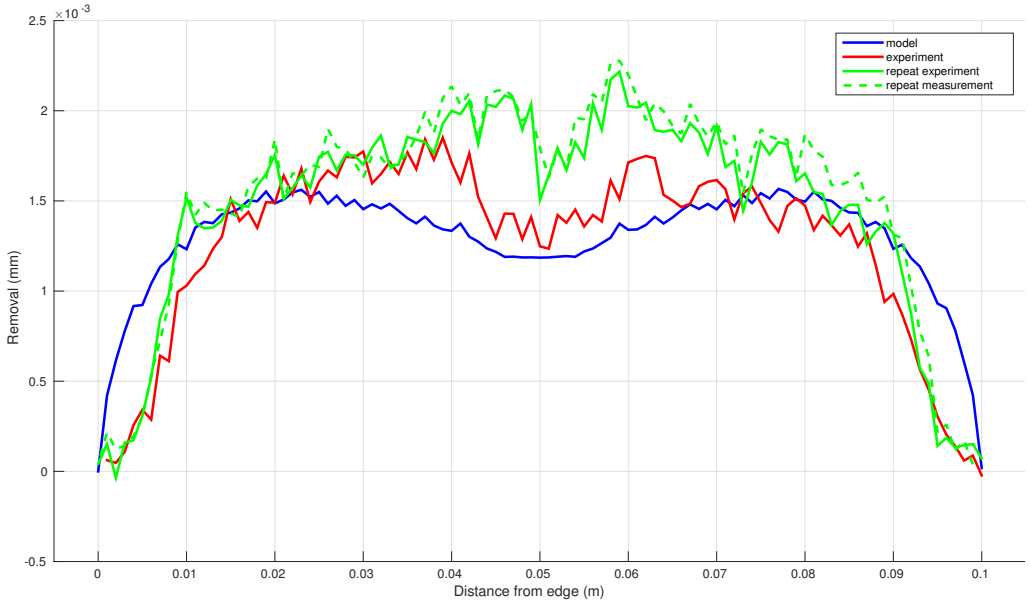

Figure 3.4.10: Analysis of the repeatability by comparing the predicted removal profile to the removal profiles obtained by repeat experiment and measurement when the tool is completely supported by the workpiece.

0.36 µm, the root-mean-squared-difference of the two measurements of the profile in the middle of the workpiece equals 0.11 µm. Thus it is concluded that removal process is stable within one track and the measurements are repeatable.

Taking another look at the experiments near the edge shows that the FEA model predictions for the 0 mm and 20 mm protrusions are as accurate as the repeatability of the process, although it must be noted that two experiments is a low statistical basis for the establishment of the repeatability. For the lower amounts of protrusion the model seems to fit better to the experimental data but results of the 10 mm protrusion are significantly worse than those of 0 mm and 20 mm. A contributing factor may be that the 10 mm experiment was performed on a different edge than the other two.

3.4.4 Applying the model to selected cases

Corners

The FEA model has also been applied to the special case when the tool is overhanging a corner. The results of the simulations are shown in Figures 3.4.11 and 3.4.12. As the tool is supported by a much smaller area than as shown in Figure 3.4.6 the pressure in the interface between tool and workpiece is much higher. For a tool that is hanging over the edge of a workpiece and not a corner the contours of constant pressure are close to parallel to the edge of the workpiece. When the tool, hanging over a corner, protrudes the two edges equally the orientation of the contours of constant pressure is the average of the orientation of the two edges of the corner. When the tool protrudes both edges of a corner unevenly, as in the case of Figure 3.4.13, the contours of constant pressure are skewed towards the edge that is protruded most.

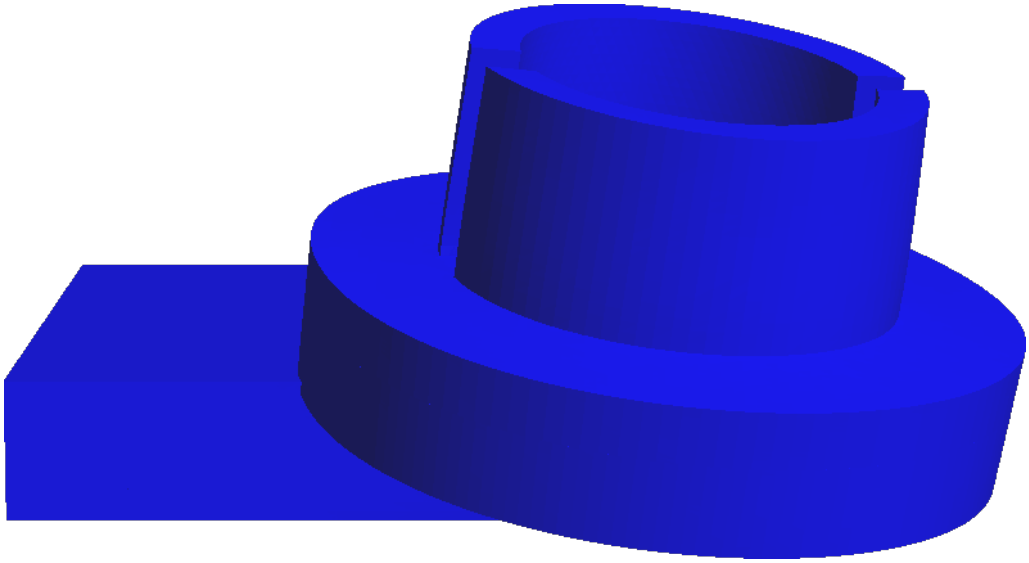

Figure 3.4.11: Results of FEA simulation of the grolishing tool protruding over a corner, the deformations are magnified by a factor of 5×10^5 for visibility.

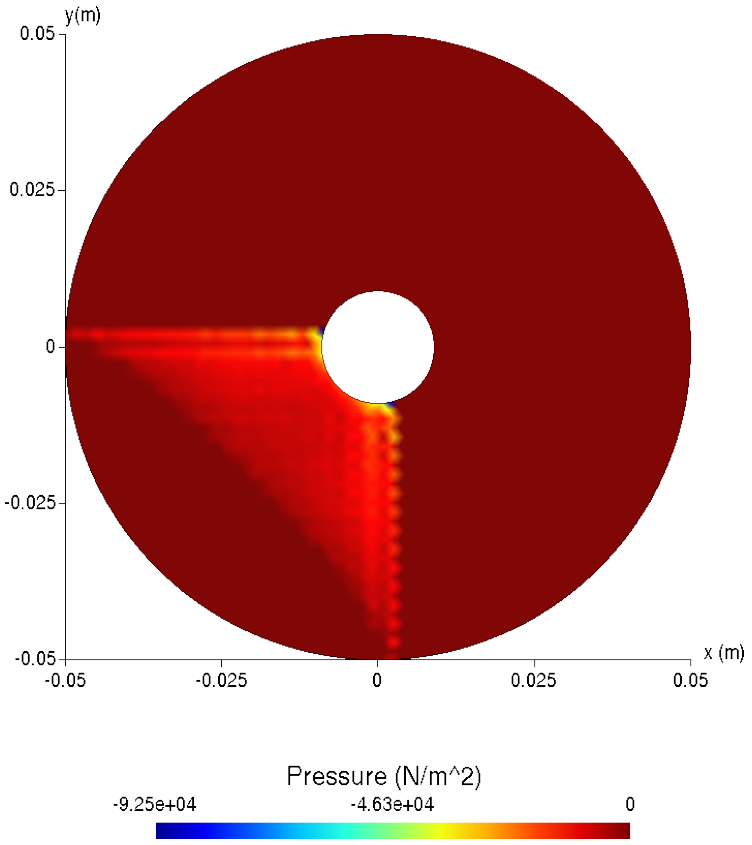

Figure 3.4.12: Pressure distribution resulting from FEA simulation of the grolishing tool while it protrudes equally the two edges of a corner. The negative sign indicates that the normal of the surface of the tool is oriented downwards. The sawtooth shape is a descretisation effect due to the mesh size and orientation.

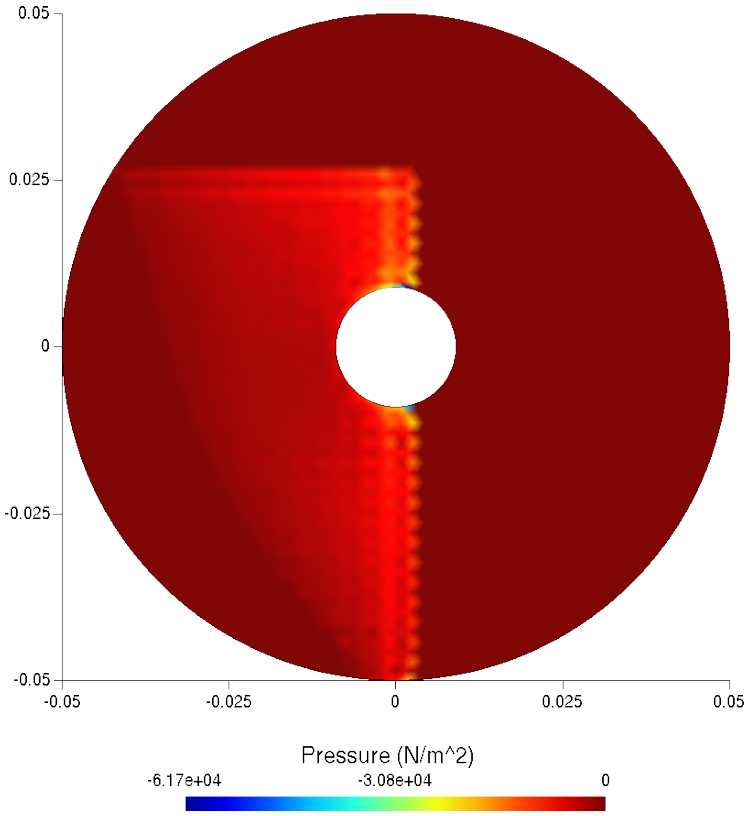

Figure 3.4.13: Pressure distribution resulting from FEA simulation of the grolishing tool while it hangs over a corner unevenly. The negative sign indicates that the normal of the surface of the tool is oriented downwards. The sawtooth shape is a descretisation effect due to the mesh size and orientation.

Mismatch

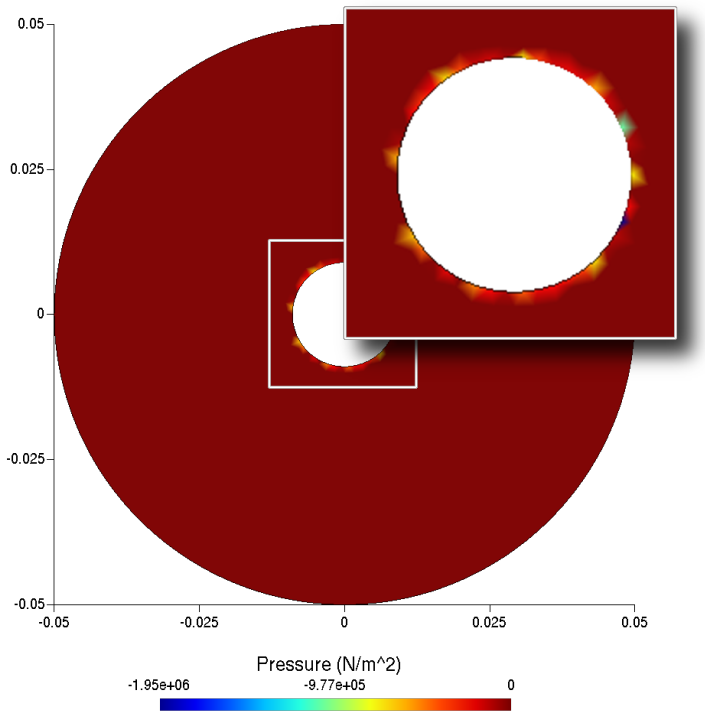

Figure 3.4.14: Pressure distribution resulting from FEA simulation of a mismatch between the grolishing tool and the workpiece. The negative sign indicates that the normal of the surface of the tool is oriented downwards.

A two entity FEA model can also be applied to the special case when there is a mismatch between tool and workpiece, as discussed in Chapter 2. However as the deformations in that case become larger the FEA model introduced in this chapter is no longer valid. A suitable FEA model has been chosen and applied to the mismatch between a plano tool surface and a convex workpiece surface. The maximum mismatch between the two surfaces was set as 10 µm along the outer edge of the tool and the results of the FEA simulation are shown in Figure 3.4.14. The results predict that the tool is supported exclusively by the inner edge around the cavity in the tool. Future research could focus on the pressure distribution between tool and workpiece in the case of mismatch, particularly in the context of the "rule-of-thumb" regarding mismatch mentioned in Chapter 2.

Remedial strategy

If the influence function is known for different protrusions of the tool over the edge of the workpiece the combined removal can be calculated when the tool traverses along the tool-path (e.g. a raster) to cover the complete surface of the workpiece. It is then possible to numerically optimise the feed of the tool along the tool-path to minimise the edge artefact. This is demonstrated here for a raster with sweeps parallel to the edge of a workpiece and a spacing of 5 mm between tracks. The results of the FEA simulations are used to calculate the influence

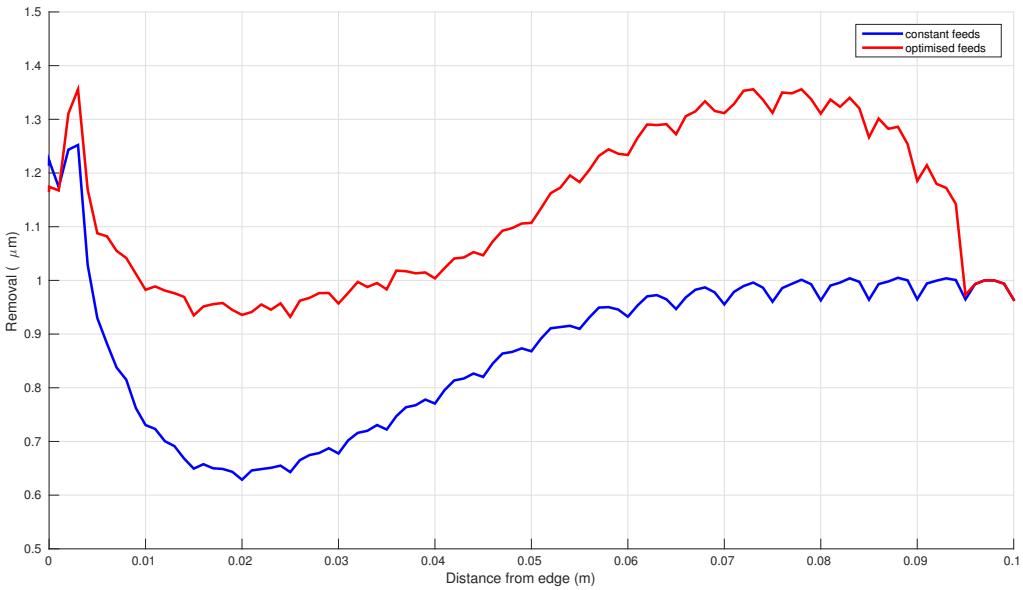

Figure 3.4.15: Removal profiles near the edge for simulated rasters with tracks spaced 5 mm apart for the 100 mm diameter grolishing tool with constant feeds for all tracks in blue and with optimised feed per track to minimise peak-to-value in red.

functions for 5 mm increments of the protrusion of the 100 mm diameter grolishing tool.

Shown in blue in Figure 3.4.15 is the removal profile near the edge of the workpiece if the tool moves with constant feed calibrated to produce a removal of 1 µm in the bulk area of the part. In this case the peak-to-valley of the edge artefact is 0.62 µm. The red profile of Figure 3.4.15 shows the removal near the edge when the feed of the tool is optimised for each track to produce the smallest edge artefact in terms of peak-to-valley. The resulting peak-to-valley is 0.42 µm, a modest reduction of a third of the original error. It is clear that reducing the peak removal near the edge, associated with the application of this particular tool, introduces form error further inwards due to the extent of the tool.

If no accurate model of the influence function of the tool hanging over the edge is available experimental data can be used to numerically optimise the edge profile. The drawback is that for each increment of the protrusion of the tool over the edge experimental data must be acquired. This becomes even more cumbersome if the edge of the workpiece has corners as each unique combination of protrusions over each of the two edges requires experimental data.

3.5 Conclusion

The specifications of the E-ELT primary mirror segments limit the allowable misfigure all the way up to the physical edge of segments to reduce background noise due to reflections of thermal radiation from the environment (including the structure of the telescope itself). The removal of rigid sub-aperture tools that are typically used to smooth mid-spatial frequency errors introduced by previous processing steps (e.g. grinding) changes when they hang over the edge of the workpiece. Bearing mounted tools have a maximal allowed protrusion above which they are no longer mechanically stable. As the tool can not completely leave the workpiece, the surface near the edge is not completely processed by the tool. The reduced contact area between

tool and surface also leads to changes in pressure in the interface between the two. This chapter has looked at different numerical models to simulate the pressure between tool and workpiece.

An FEA model is introduced here that simulates the tool and workpiece as separate entities and models the contact between them, as opposed to the non-contact, single entity model reported on by Kim et al. [120, 121]. This allows the modelling of a ball bearing mounted tool as well as the modelling of mismatch between tool and workpiece. The results of the simulations have been compared to results obtained from experiments with a robot mounted grolishing tool. The results only partly match the simulations, specifically they do not exhibit the predicted sharp peak in removal close to the edge of the workpiece. Potentially this is due to a mismatch between the tool and workpiece, during the experiments. It is noted that peak removal close to the edge for rigid sub-aperture tools is known from literature and has also been reported for the grolishing process [69] mounted on a bonnet. The reason why the ball bearing mounted grolishing process does not exhibit this peak removal is an interesting subject for future research. For comparison, it is suggested to conduct similar simulations and experiments for a polishing tool. This tool features a thin, compliant layer (e.g. polyurethane) on top of the rigid body of the tool. This layer serves as a carrier of the polishing abrasives and its compliance makes the tool less susceptible to mismatch between tool and workpiece.

It is possible to reduce the edge artefact by optimising process parameters (e.g. feed) along the tool-path. This does not allow the complete prevention of an edge artefact however, as reductions of the error on one end of the tool leads to increased misfigure on the other side due to the size of the tool. To be able to smooth mid-spatial frequency errors introduced by previous processing steps rigid tools need to have a span wide enough to cover the distance between peaks of the error. Their contact area is therefore significantly larger than that of the process step that introduced the errors. For the polishing of E-ELT prototype segments the consortium lead by *OpTIC* therefore alternates a bonnet based process with one that uses a rigid tool.

From the results presented in this chapter it is concluded that rigid tools on their own are not capable of producing surface edges that conform to the demanding specifications of the E-ELT primary mirror segments. The next chapter looks at the use of a small bonnet tool to correct surface edge misfigure on large, metre-scale optics.

Where force is necessary, there it must be applied boldly, decisively and completely. But one must know the limitations of force; one must know when to blend force with a maneuver, a blow with an agreement.

Leon Trotsky

4

Local edge correction using small conformal tools

4.1 Introduction

As follows from the previous chapter, a polishing process that can correct edge artefacts left by rigid tools is desired. A compliant bonnet tool is an appropriate candidate: the pressure distribution in the contact zone is generated by a combination of the air pressure and geometric and material properties of the membrane. Thus, when the tool hangs partly over the edge the pressure distribution remains mostly constant.

As documented in Chapter 2, the ESO specifications of E-ELT primary mirror segments stipulate a maximum allowable error in the edge zone (from 10 mm inside to the physical edge of the segments) of 200 nm peak-to-valley (PV) surface error per edge and an average error of 100 nm PV surface error over all six edges. In practice smaller surface errors become increasingly more difficult to achieve. In order to achieve the specification for the average a maximum PV surface error of 100 nm is targeted for each individual edge zone.

Any artefacts within the edge zone are by definition narrower than 10 mm; probably significantly smaller. Because a compliant tool, when used in a deterministic corrective process, provides poor capability to correct artefacts with dimensions smaller that its footprint (see Chapter 2) it is beneficial to investigate the feasibility of using a small tool to correct the edge zone. The designed input quality for this process would be an optical surface that meets the ESO specifications over the bulk area and has an upstanding edge up to 1 µm PV of surface error (from experience the expected output of a preceding process)

The 10 mm width edge zone of a 1.5 m across corners, regular hexagon has an area of approximately $6 \times 750 \times 10 = 45 \times 10^3$ mm^2. The total area of the hexagon equals $6 \times \frac{1}{2} \times 750 \times \frac{\sqrt{3}}{2} 750 = 1461 \times 10^3$ mm^2. Therefore, the edge zone consists of only 3 % of the

total surface area of the hexagon. Because of concerns regarding tool wear and overall process times when processing metre scale optics, it is desirable that the edge zone alone is polished using this small tool, and not the bulk area. However, afterwards the edge zone still has to blend in well with the unprocessed bulk area, without leaving a step function or other artefact on the surface.

The work outlined in this chapter consists of steps towards this ultimate goal of locally correcting edges of large optics by applying small, compliant tools without introducing a surface discontinuity between the edge zone and bulk area. Firstly, the effectiveness of a small compliant tool for the deterministic correction of edges was investigated. Subsequently, the blending of the bulk area with the edge zone was studied. Finally, a special type of tool-path that is capable of conforming to non-circular edge geometries is evaluated.

4.2 Corrective polishing of edge zones

4.2.1 Starting condition

Performing experiments on full-scale E-ELT primary mirror segments is impractical for several reasons:

- Risk of damage to a high valued workpiece
- Limited availability of machines capable of processing large parts
- Long process times
- Cost of returning the workpiece to the initial surface condition

Therefore, witness samples of smaller dimensions, but hexagonal in shape and with a shallow concave surface, are used to study potential processes and procedures, during initial process development.

The part selected was a 200 mm across corners, Zerodur (a low thermal expansion coefficient material out of which the prototype E-ELT primary mirror segment that was polished first was made), regular hexagon, with a 3 m radius of curvature concave spherical surface. This part was pre-polished using a 21 mm spot size of an R80 bonnet to provide a specular surface to allow interferometric measurement providing full-aperture surface form data. This part was used to evaluate whether two adjacent edge zones could be corrected individually. To correctively polish a surface a CCOS process is used as outlined in Chapter 1. The current surface misfigure and process parameters (e.g. bonnet size, precess angle, tool offset and track spacing) are input into the machines control software which outputs a command file instructing the machine at which location on the surface to dwell longer (and remove more material) and where to traverse more rapidly (removing less material). A secondary objective was to prevent a surface discontinuity appearing at the boundary between the adjacent edge zones. Whether or not a surface discontinuity was observed between the two zones would give an early indication as to the feasibility of correcting edge zones while keeping them blended to the bulk area.

The initial condition of the part was measured using a *4D* interferometer (see Chapter 2 for more information), averaging 64 measurements. Spatial resolution was calibrated by inserting a flexible strip of a known length in contact with the part and setting a fiducial at both ends in the analysis software. The results of the measurements of the two edges together can be found in Figure 4.2.1a. Each edge had a surface form error of roughly 1 µm PV. The part was placed in the polishing machine and positioned to horizontally align the centre of the part with the centre of *x*- and *y*-axes of the machine to an accuracy of 70 µm. Using a dial gauge contacting the top surface at a radial positional of 85 mm a total run-out of 160 µm was observed while rotating the part 360°.

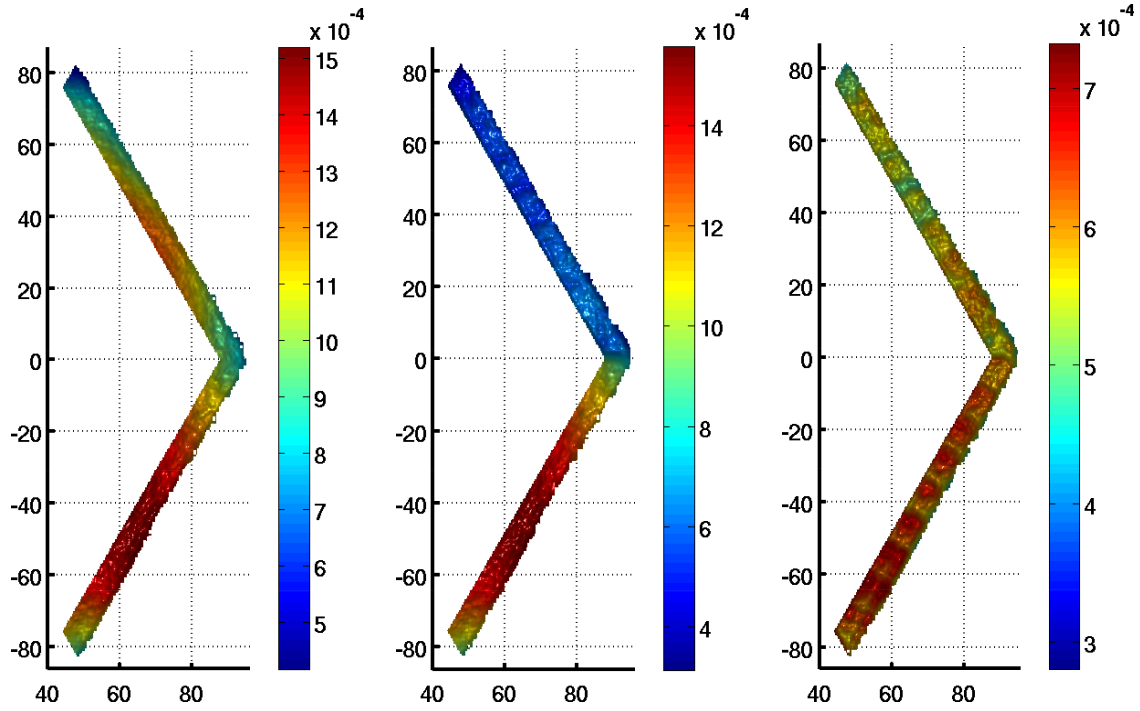

(a) Starting condition of the two edges

(b) After correcting the top most edge

(c) After the second correction

Figure 4.2.1: Interferometer data showing two individually corrected edges using a small tool (all units in mm).

4.2.2 First edge correction

The polishing machine used was an IRP600 (the second CNC polishing machine manufactured by *Zeeko Ltd*), which produces a known ripple effect with a PV of around 90 nm for a typical polishing run and a spacial frequency of roughly 0.1 mm^{-1}. This is not present in any other CNC polishing machine of the same manufacturer, two of which are used daily in *OpTIC*'s laboratory. One of the possible causes of this ripple effect is that this machine is the only one that lacks the facility to follow a splined path between set points, but this has not been confirmed.

The used tool was a standard R20 bonnet, to which the industry standard polishing cloth LP66 was glued. Afterwards the surface of the cloth was "dressed" using a single point tool to create a spherical surface whose centre coincided with the virtual pivot of the machine. The

virtual pivot is the point around which the tool axis is rotated to maintain a constant angle with the local surface normal of the workpiece. Coincidence of the centre of the tool and the virtual pivot ensures a constant removal profile during polishing. This is necessary for most applications of CCOS including the standard Precessions™ bonnet polishing, outlined in Chapter 1, applied here.

Because of the small dimensions of the errors that are to be corrected, the referencing of the metrology data, the machine coordinate frame and the workpiece is crucial. The part was rotated to align the orientation to the machines axis, achieving less than 10 µm run-out along one side of the hexagon as measured using a dial gauge.

The control software of the polishing machine was set-up to correct the surface of the top most edge zone in Figure 4.2.1a using a standard raster. *Zeeko*'s polishing machines offer the possibility to probe the surface at a number of pre-selected points, the results of which are used to compensate errors in the z-position of the machine. This procedure is referred to as "performing a non-linear correction" and two were performed in these experiments. The first correction was to estimate the tilt in the part and the second (applying compensation of the estimated tilt) to perform a normal non-linear correction.

The interferometer data was imported into the machine's control software and was used to generate a corrective polishing tool-path. The parameters used during all the experiments described in this chapter are shown in Table 4.2.1.

Table 4.2.1: Parameters used during local edge corrections using a small, compliant tool.

Parameter	Value
Bonnet	R20
Polishing cloth	LP66
Precess angle	10°
Head speed	800 rpm
Tool offset	0.15 mm
Tool overhang	0 mm
Bonnet pressure	1 bar
Point spacing	0.2 mm
Track spacing	0.2 mm
Abrasive component	CeO_2
Nominal particle size	1 µm

These settings were based on experience gained during initial experiments not reported here and resulted in an estimated spot size of 5 mm. The measurement data was offset in the z-direction such that the desired removal at the lowest point was close to zero. The total process time of the tool-path was roughly 40 min.

After polishing, the specific density of the slurry (which is know to affects the removal rate)

was found to be 1.028 kg m^{-3}. At the start the slurry was conditioned, replacing evaporated water which brought the specific density to 1.030 kg m^{-3}. From experience this variation has no significant influence on the removal rate and thus does not affect the residual surface error. Using the same interferometer the workpiece was measured after polishing and the results are shown in Figure 4.2.1b.

4.2.3 Second edge correction

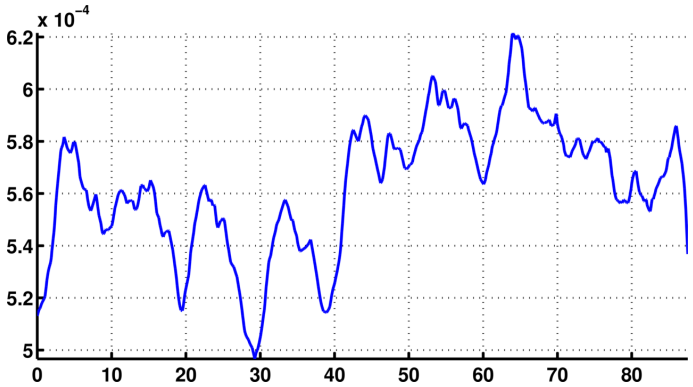

(a) The top edge

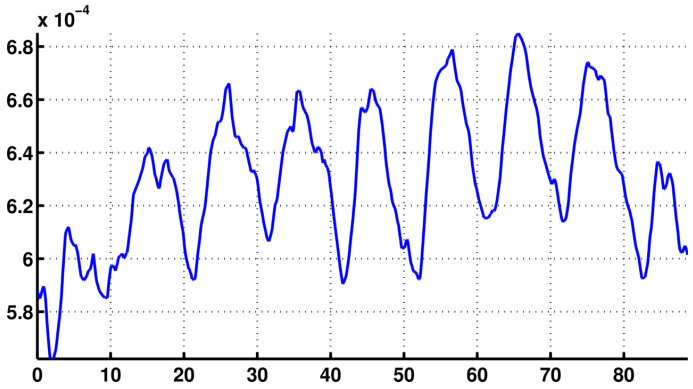

(b) The bottom edge

Figure 4.2.2: Profiles parallel to the edge extracted from the interferometer data shown in Figures 4.2.1b and 4.2.1c (all units in mm).

The correction of the second edge zone was prepared in the same way as the first, applying the same parameters. Again the measurement data was offset in the z-direction. This time in such a way that the targeted removal would blend both edges zones well together without causing a discontinuity at the boundary between them. The total process time of the tool-path was also roughly 40 min. After polishing, the specific density of the slurry was measured again and was found to be 1.028 kg m^{-3}. Using the same interferometer the workpiece was measured after polishing the second edge zone and the results are shown in Figure 4.2.1c. Two profiles have been extracted from this interferometric data, for the sake of clarity, one for each edge zone. They are presented in Figures 4.2.2a and 4.2.2b and the rightmost part of the former and the leftmost part of the latter represent the corner shared by both edges zones.

4.2.4 Discussion of results

For each of the corrected edges zones the residual form error was dominated by the known ripple effect produced by the IRP600 machine, which was discussed previously. The total residual form error is 125 nm and 123 nm PV surface error for the first and second edge zones respectively. Without the mentioned ripple effect the form error is estimated to be half of that. No noticeable trough, ridge or step function is present at the boundary between the two zones.

The next step towards the ultimate goal of locally correcting the edge zone of large optics, consisted of correcting a single edge exhibiting an edge artefact likely to be encountered on E-ELT prototype segments, without introducing a surface discontinuity between the edge zone and bulk area.

4.3 Continuity with the bulk area

4.3.1 Initial condition

Again a 200 mm diameter across corners, 3000 mm radius of curvature, concave hexagon made from Zerodur was used. It had previously been lapped, pre-polished (using a bonnet with a 35 mm spot size), grolished and pre-polished again using a 35 mm spot size by a team from *OpTIC* and *UCL*. The procedure it had undergone was the procedure under development for the polishing of E-ELT segments. The process parameters had been chosen to produce an increasing edge misfigure towards the edge ("upstanding edge") rather then a decreasing one ("turned down edge"), as the former is easier to correct in general. The initial condition of the part prior to local edge correction was measured using a *4D* interferometer, averaging 64 measurements.

To be able to resolve the fringes in the edge zone of the part, power was introduced in the measurement set-up, after nulling the fringes in the bulk area of the workpiece. Spatial resolution was calibrated by inserting a flexible strip of a known length in contact with the part and fiducialising both ends.

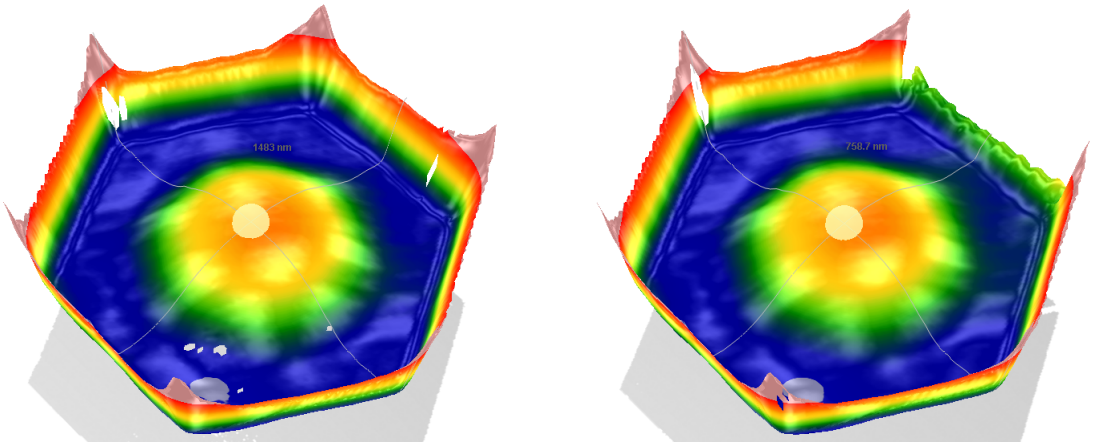

(a) Initial condition **(b)** After correction of a single edge

Figure 4.3.1: Interferometer data of the whole workpiece before and after correcting a single edge demonstrating the power introduced in the bulk area to resolve the fringes of the edge upstand.

The result of the measurements can be found in Figure 4.3.1a and a profile extracted from this measurement, perpendicular to the edge is shown in Figure 4.3.2a. The edge up-stand has a PV of roughly 1.5 µm. The measurement software was set up to remove tip, tilt and power of the measurement data estimated over the whole surface area. As can be seen from the figures, there is still power left in the bulk area of the measurement because the edge zone skews the estimation of the power. This was not realised until after the experiment and subsequent measurements have estimated the power and tilt on the bulk area only (excluding the edges).

After placing the part in the polishing machine the centre was aligned horizontally to centre of the axes of the machine. The accuracy of the alignment was 60 µm, measured by applying a dial gauge to opposing edges. Using a dial gauge contacting the top surface at a radial positional of 85 mm a total run-out of 190 µm was observed while rotating the part 360°.

4.3.2 Correction process

The slurry was conditioned (adding water abrasive compound lost due to evaporation sedimentation respectively), while it was flowing through the machine, until the specific density stabilised at 1.030 kg m^{-3}. Generally when a machine is not in operation the slurry is by-passing the machine and fed directly back into the tank. This may cause a change in specific density of the slurry after switching the slurry from the by-pass to the machine, because of the different specific density of the slurry left in the machine or loosened sedimentation. Therefore the slurry was kept flowing through the machine to make sure conditions were as stable as possible during polishing.

The part was placed in the polishing machine and the position adjusted, with less than 10 µm run-out along one side of the hexagon, measured using a dial gauge. The same R20 bonnet and LP66 polishing cloth was used as in the previous experiments. As before, two non-linear corrections were performed. The first to estimate the tilt in the part and the second (using the estimated tilt) to perform a normal non-linear correction. Estimated tilt values were 0.096°

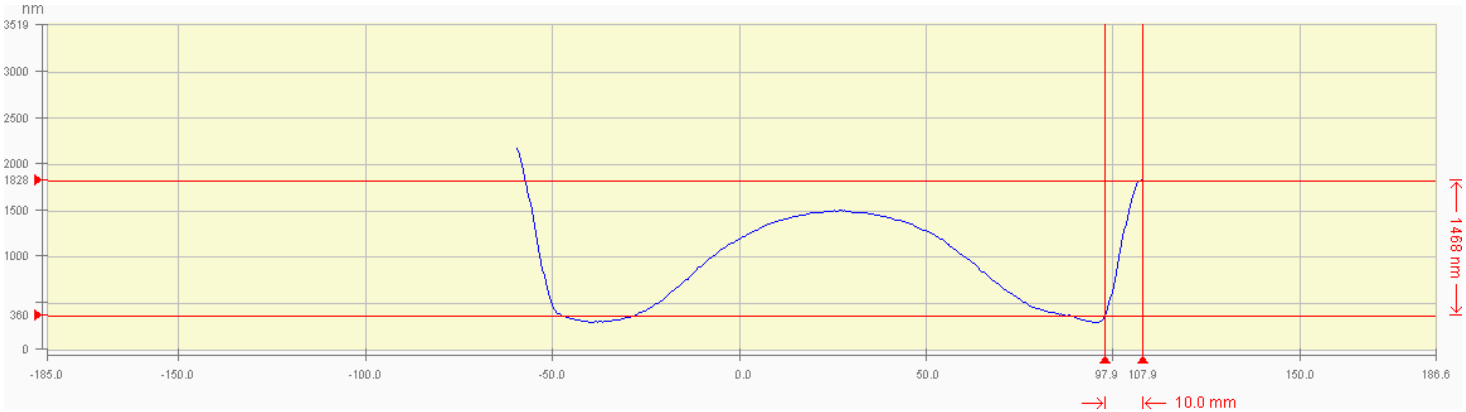

(a) Initial condition

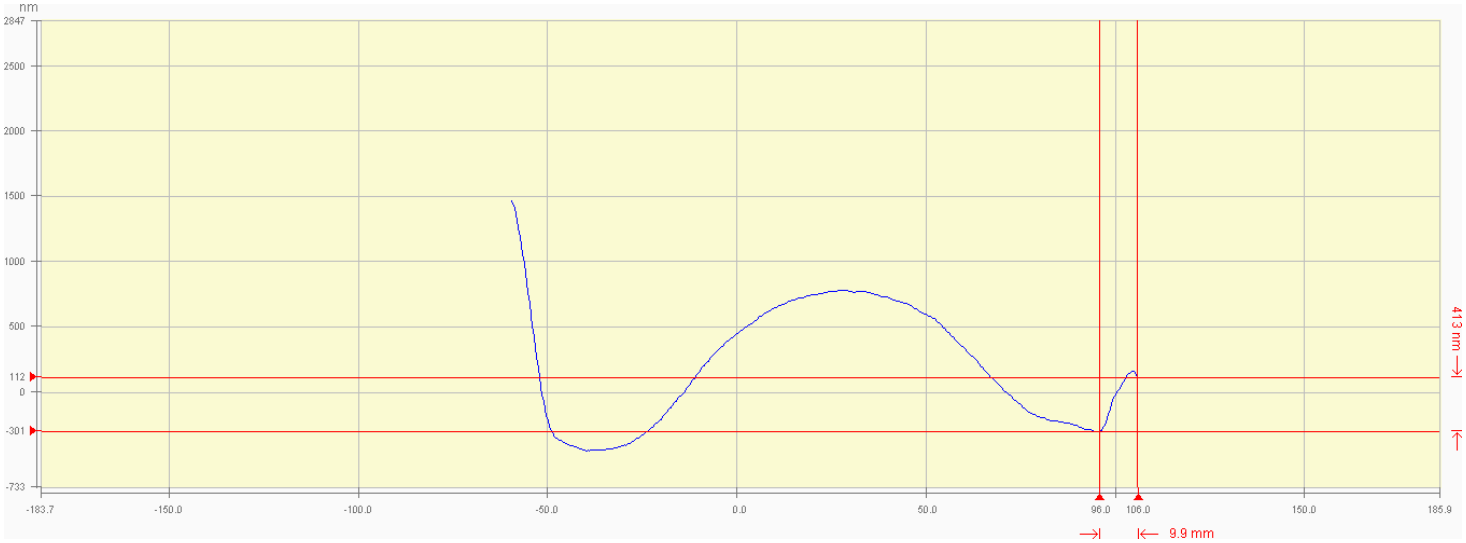

(b) After correction of a single edge

Figure 4.3.2: Profiles perpendicular to the corrected edge extracted from the interferometer data from Figures 4.3.1a and 4.3.1b. The cursors mark the dimensions of the edge zone before and after correction.

around the x-axis and 0.0099° around the y-axis.

The interferometer data was imported into the control software of the machine and used to generate a corrective polishing tool-path over a single edge zone using the same settings as previously, see Table 4.2.1. The measurement data was offset in the z-direction in such a way that the desired removal along the boundary between the polished zone and the bulk area was close to zero. The total process time of the tool-path was roughly 60 min.

After polishing the specific density of the slurry was measured again and was found to be 1.024 kg m^{-3}. This drop was most likely caused by slurry settlement inside the polishing machine, due to insufficient containment of the polishing area.

4.3.3 Result

The part was measured after polishing using the same method as before the experiment. The results of the measurements can be found in Figures 4.3.1b and 4.3.2b. The same remarks regarding the estimation of power and tilt over the whole surface area apply here as well. The polishing has left an edge up-stand with a PV of roughly 450 nm.

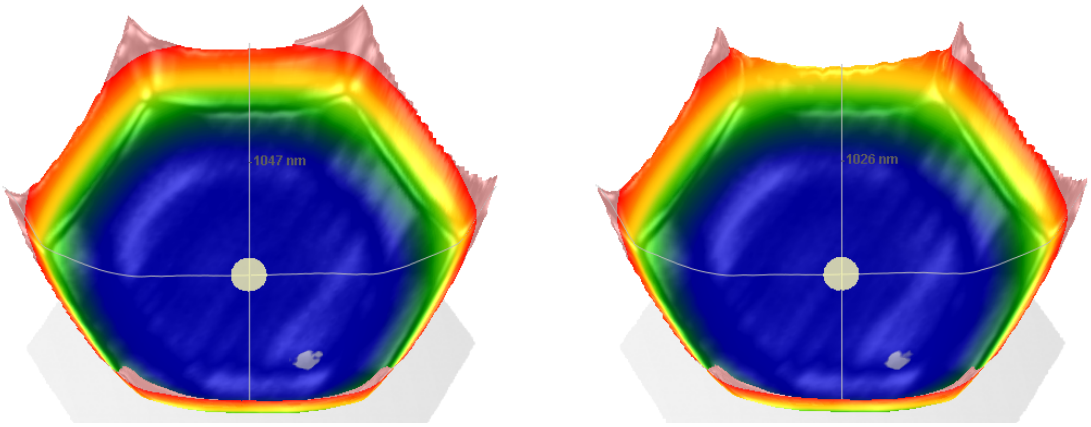

(a) Initial condition **(b)** After correction

Figure 4.3.3: Interferometer data of the whole workpiece before and after correcting a single edge with power, estimated in the bulk area only, removed.

Afterwards the measurements were corrected by estimating the power only in the bulk area. A hexagonal, 100 mm across corners, central area mask was used. Removing the power estimated in this way, the corrected before and after measurements are shown in Figures 4.3.3 and 4.3.4. Based on these measurements the corrected edge zone initially had an up-stand of 2.2 µm PV, not 1.5 µm as previously estimated. After correction the up-stand in the edge zone measured 1.1 µm PV, not 450 nm. The actual reduction in PV was therefore 1.1 µm. The targeted reduction in PV was 1.5 µm, i.e. the original measured error.

Whether the original or the corrected measurements are used it is clear that the process did not fully remove the up-stand. The convergence rate, defined as the ratio between achieved error PV and targeted error PV, were calculated from the corrected measurements and found to be 73 %.

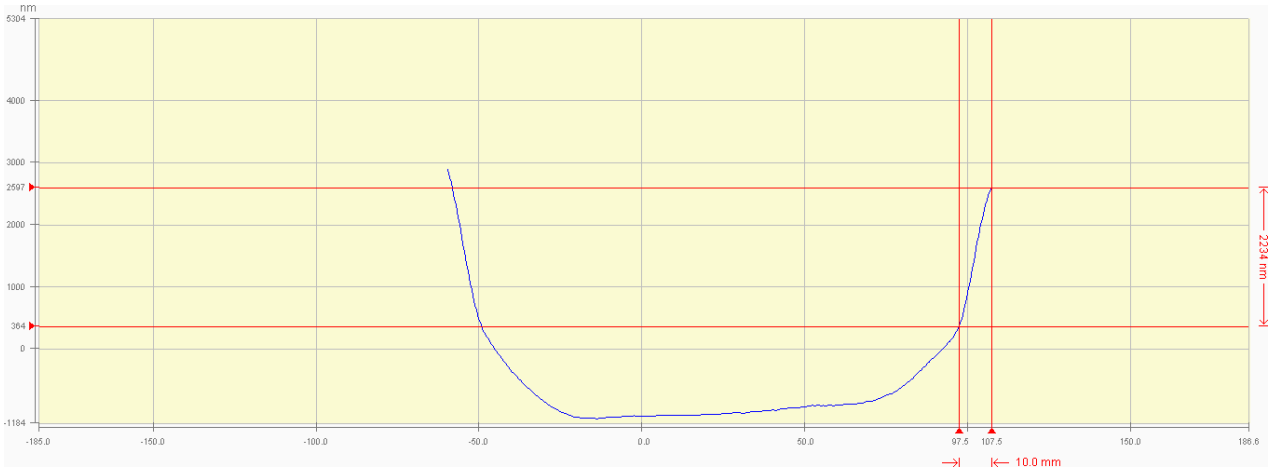

(a) Initial condition

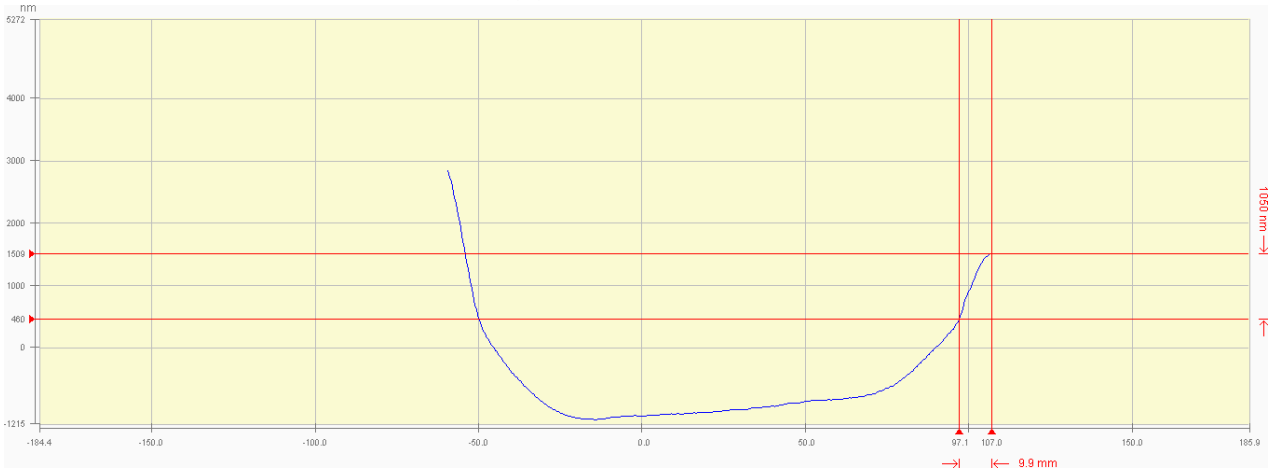

(b) After correction of a single edge

Figure 4.3.4: Profiles perpendicular to the corrected edge extracted from the interferometer data from Figures 4.3.3a and 4.3.3b. The cursors mark the dimensions of the edge zone before and after correction.

4.3.4 Discussion

The corrective polishing was only moderately effective in correcting the edge up-stand, as it did not remove the error completely. The convergence rate of 73 % was significantly lower than that of the previous edge zone corrections, which was estimated to be 95 %. Two reasons are hypothesised for this difference. Firstly, because of the drop in specific gravity of the slurry. However, from past experience this drop in specific gravity can not fully explain the change in convergence rate. Secondly, because of the difference in magnitude and shape of the error. The earlier experiments corrected a surface error with a magnitude of 1.0 µm, the input error of these experiments was 2.2 µm. More importantly, the error of the earlier experiments did not show an up-stand and was only slowly varying in the spatial domain, as can be seen in Figure 4.2.1a. The input error in this experiment, an edge up-stand, varied maximally over the narrow width of the polished zone. As discussed in Chapter 3 compliant tools are ill-suited for the correction of errors with dimensions of the same comparable to the spot size. This is even more so if the total removal is constrained, as is the case here.

The corrected edge area blends in well with the bulk area: no discontinuity was introduced between the bulk and corrected edge. Although this serves as a proof-of-concept for the feasibility of local correction of surface defects without disturbing continuity, repeatability needs to be demonstrated before it can be applied at an industrial scale.

A further challenge is to control six edges, either in one polishing run or by blending six separate corrections of each edge individually. The following section investigates the possibility of corrective polishing all six edges in a single polishing run.

4.4 Hexagonal to hexagonal tool-path

4.4.1 Tool-path design

To perform corrective polishing a process has to traverses the surface along a previously specified, non-crossing tool-path, as outlined in Chapter 1, with two standard types: raster and spiral. The surface consisting of all six edge zones of a hexagonal workpiece can not be traversed by a standard raster tool-path without taking the tool off the surface. This is due to the exclusion of the central area. A spiral tool-path does not need to take the tool off the surface to deal with a central exclusion but the path does not follow the hexagonal edges. Dr. Anthony Beaucamp of *Zeeko* has developed a tool-path that spirals "hexagonally" and thus follows the hexagonal edges. This type of tool-path is called "hexagonal to hexagonal tool-path" ("hex-hex" for short) because it starts at the hexagonal physical edge of the workpiece and stops at the hexagonal boundary between the edge zone and bulk area of the workpiece.

If each spiral of the tool-path consisted of hexagons with sharp corners, then the practical limits on the deceleration and acceleration associated with the sudden change in direction would create polishing artefacts on the surface. Together, they would create a radial structure in the surface misfigure towards each corner of the workpiece. To minimise the deceleration and acceleration between changes in direction direction, the corners of the tool-path are rounded.

An "adaptive spiral" which morphs the spirals to the shape of the edges without creating sharp edges in the tool-path has been reported in the literature for cutting processes such as high speed routing [125] and 5-axis milling [126]. To create a tool-path consisting of adaptive spirals one possibility is to calculate the solution of Poisson's equation:

$$-\nabla \cdot (\nabla u(x,y)) = 1 \tag{4.1}$$

with the Dirichlet boundary conditions

$$u(x,y) = \begin{cases} 0 & \text{if } (x,y) \in \text{outer boundary} \\ 1 & \text{if } (x,y) \in \text{inner boundary} \end{cases} \tag{4.2}$$

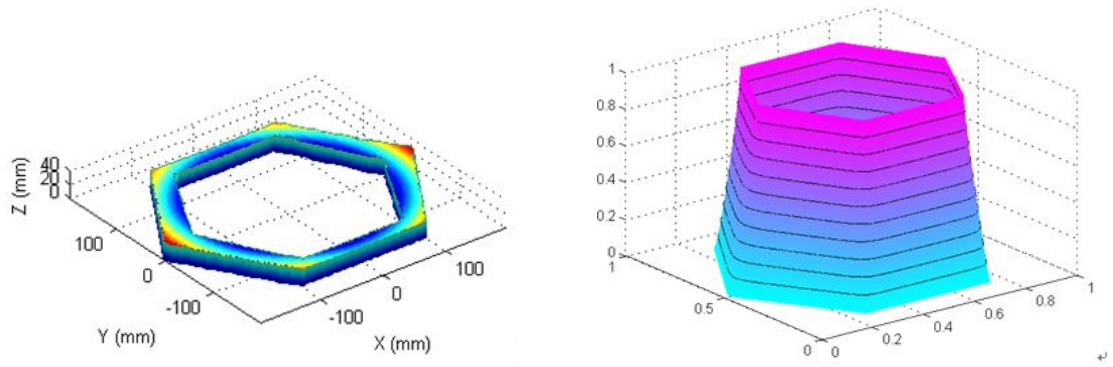

(a) Surface consisting of a combination of six edge zones

(b) Solution of Poisson's equation with contour lines

Figure 4.4.1: Surface formed by the combination of six edge zones of a concave hexagonal workpiece and the solution of Poisson's equation for that surface. Courtesy of A. Beaucamp, *Zeeko*.

Figure 4.4.1a depicts a surface formed by combining the six edge zones of a concave hexagonal workpiece while Figure 4.4.1b shows the solution of Poisson's equation for that surface. Hexagonal tracks with smooth corners can be created by following contour lines of the solution. However the spacing between tracks is not uniform over the surface, which results in local variations of the removal rate. To compensate this effect, the feed rate of the process along the path can be moderated by calculating the relative track density of the tool-path across the surface. The track density is found by convolving the points in the tool-path with a Gaussian filter

$$g(x,y) = \frac{1}{2\pi\sigma^2} \cdot e^{-\frac{x^2+y^2}{2\sigma^2}} \tag{4.3}$$

where σ is proportional to the diameter of the contact area between bonnet and workpiece.

A hexagonal to hexagonal spiral tool-path with rounded corners, for the edge zone of a hexagonal workpiece is shown in Figure 4.4.2a. The track density of this tool-path is depicted in

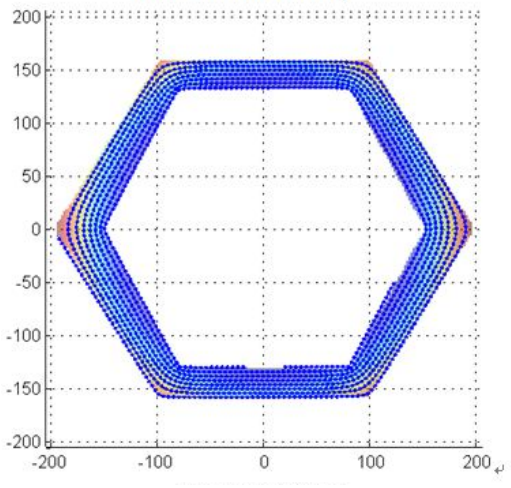

(a) Hexagonal to hexagonal spiral tool-path for the edge zone of a hexagonal workpiece

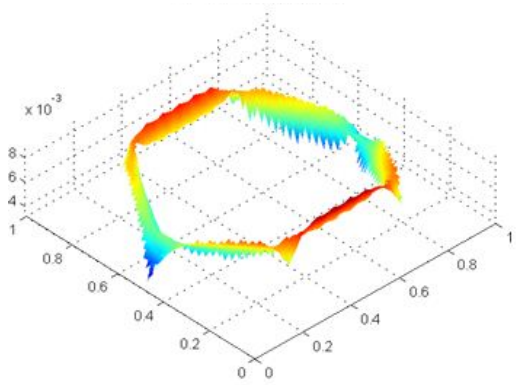

(b) Relative track density of the hexagonal to hexagonal spiral tool-path

Figure 4.4.2: Relative track density of the hexagonal to hexagonal spiral tool-path for the edge zone of a hexagonal workpiece. Courtesy of A. Beaucamp, *Zeeko*.

Figure 4.4.2.

The path generation implemented by Dr. Anthony Beaucamp of *Zeeko* introduces extra parameters in Poisson's equation which allows the user to balance the track density on the one hand and the smoothness of the corners on the other:

$$-\nabla \cdot (c_1 \nabla u(x,y)) + c_2 u(x,y) = c_3 \tag{4.4}$$

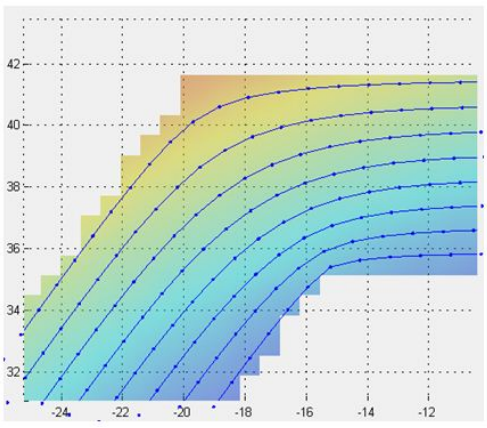

(a)

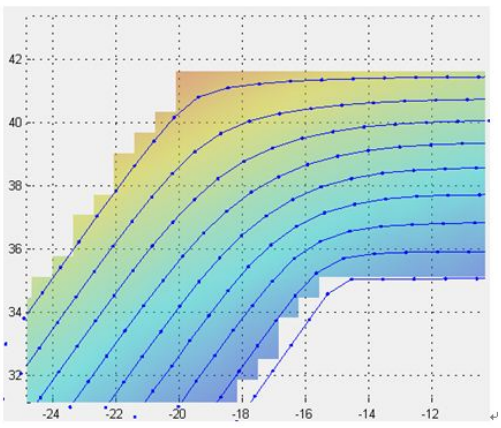

(b)

Figure 4.4.3: Graphs showing the same corner area of two hexagonal to hexagonal tool-paths calculated using different coefficients of the partial differential equation (4.4). Courtesy of A. Beaucamp, *Zeeko*.

Figure 4.4.3 shows the same corner area of two hexagonal to hexagonal tool-paths that were created by applying different coefficients of Equation (4.4).

4.4.2 Uniform removal test

A uniform removal test was performed to evaluate the performance of the hexagonal to hexagonal tool-path as well as the moderation of the feed rate along the path to compensate removal rate variation due to track density variation. A 200 mm diameter across corners, 3000 mm radius of curvature, concave hexagon made from Zerodur was used for this experiment. It was previously lapped and then pre-polished using a 21 mm spot size to be able to measure it interferometically.

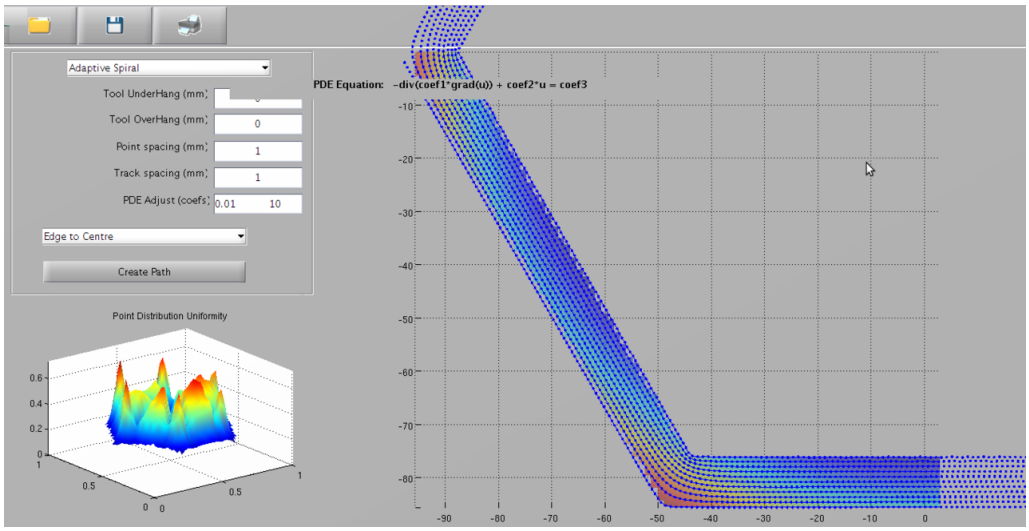

Figure 4.4.4: Screenshot of the control software of the polishing machine which shows a zoomed-in view of the designed hexagonal to hexagonal tool-path as well as a graph of the track density.

In the control software of the polishing machine a design was made of only the edge zone and a hexagonal to hexagonal tool-path was created, see Figure 4.4.4.

A command file for the polishing machine was generated to polishing the edge zone uniformly using the following parameters in Table 4.2.1 and a constant surface feed of 1000 mm min^{-1}. The tool-path, information of which is shown in Figure 4.4.5, was executed twice, without taking the part off the machine.

After the experiment the part was measured again interferometically and the result is shown in Figure 4.4.6, generated by subtracting the before and after measurements. As can be seen from the results, the functionality of the hexagonal to hexagonal tool-path including feed rate compensation was verified to work as designed, for the first time.

4.5 Conclusions

The capacity to locally correct edge misfigure of large optics, such as E-ELT primary mirror segments, using a small conformal tool is advantageous due to the reduced total process time and tool wear. The work presented in this chapter is a feasibility study of such a process. A risk

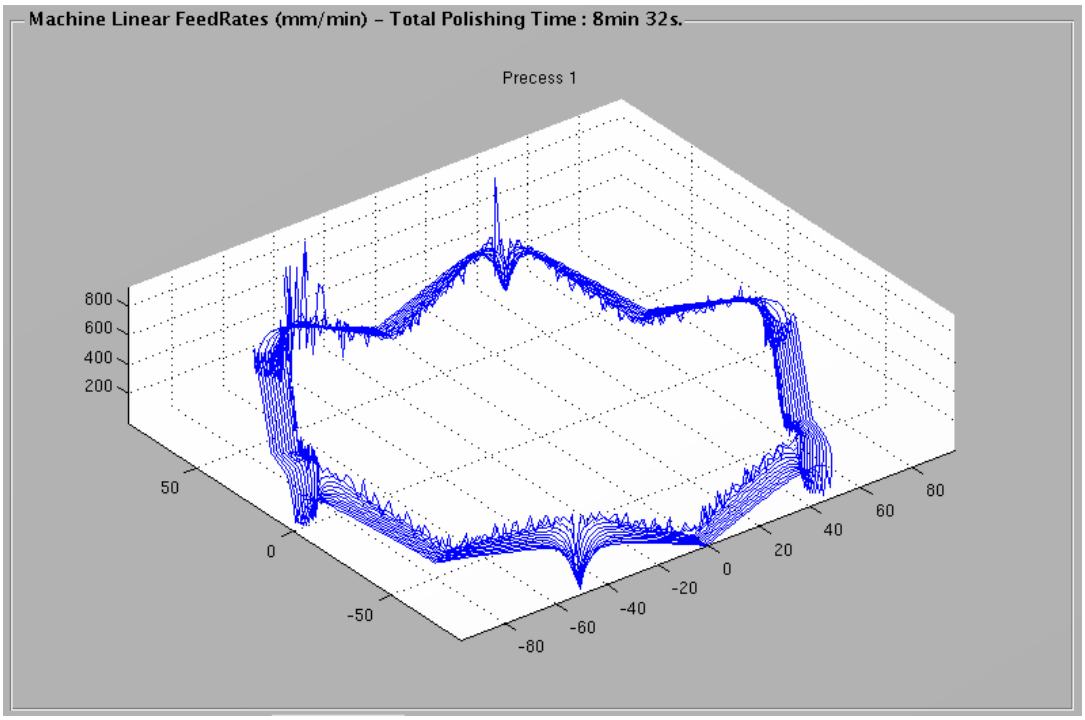

Figure 4.4.5: Screenshot of the control software showing a graph of the variable feed rate, compensating track density variations, along a hexagonal to hexagonal tool-path targeting uniform removal (horizonal units in mm and vertical unit $\mathrm{mm\,min^{-1}}$).

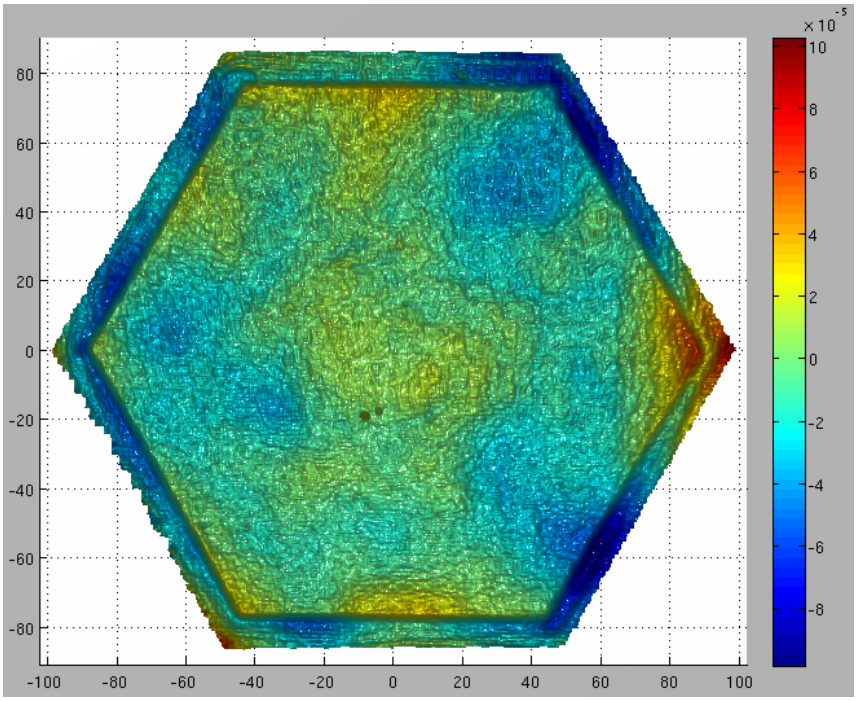

Figure 4.4.6: Result of polishing using a hexagonal to hexagonal tool-path targeting uniform removal of the edge zone. Shown is the substraction of before and after interferometric measurements of the complete surface (all units in mm).

assessment of the applicability of a small bonnet tool for the correction of the edge zone of a full sized E-ELT segment was done and is documented in Appendix E.

One possible route to locally correct the edge zone of a hexagonal workpiece is by correcting each of the six edge zones individually. Yu et al. [127] have taken this approach and documented an average surface misfigure PV per edge of 90.5 nm on a 200 mm across corners regular hexagonal witness sample. This misfigure complies with the specification of E-ELT segments.

Another route is to correct all six edges zones in one polishing run by applying a new type of tool-path, created by solving a partial differential equation numerically. The tool-path consists of hexagonal tracks, whose corners are rounded to prevent polishing artefacts on the surface due to deceleration and acceleration of the machine. The rounded corners however cause track density variations along the path which, if not compensated, lead to removal rate variation and therefore uneven polishing. Coefficients of the partial differential equation allow the balancing of the rounding of the corners with the track density variation. By further applying feed rate compensation along the path, calculated from the remaining track-density variation, uniform removal can be achieved, which is demonstrated for the first time by the experiment presented in this chapter. Future work should focus on understanding the effects of the new parameters of the partial differential equation that govern the numerical creation of the hexagonal to hexagonal tool-path.

The results presented in this chapter also showed that a small bonnet was only moderately successful in correcting an edge up-stand. This edge up-stand was the result of the procedure under development for the polishing of E-ELT segments. It is hypothesised that this is because the spatial dimensions of the error artefacts is comparable with that of the contact area of the tool. This problem is compounded by the restriction on the total removal to prevent a discontinuity at the boundary between the polish area and the bulk of the surface.

The algorithm used to calculate the dwell times only used the surface misfigure data at the centre of the contact area, for all the experiments presented in this chapter. Another algorithm is available from *Zeeko* that calculates the dwell times by de-convolution of the influence function of the tool and the error height map over the whole surface. This results in a better corrective performance of bonnet based tools, specifically for error features with comparable dimensions as the contact area. Future work should therefore focus on using this method to calculate the dwell times.

During the work outlined in this chapter it was also discovered that the standard method of measuring workpieces with large edge up-stands led to miss-characterisation of the up-stand. To resolve the fringes in the edge zone of the part, power has to be introduced in the measurement set-up, after nulling the fringes in the bulk area. The standard method subtracted power from the measurement data by estimating it over the whole surface. However, the presence of edge up-stand skews the estimated power, reducing the magnitude and lateral dimension of the up-stand (and leaving residual power in the bulk area of the measurement). A new measurement method was introduced that estimated the power solely in the bulk area. This new method was used to analyse the results of the proposed procedure for the polishing of E-ELT segments. The

standard method of measuring showed an up-stand of 1.5 μm and a width of 10 mm. The new method measured an up-stand of 3.5 μm and a width of 30 mm. To produce an optic free of edge up-stand there are three options: 1. correct a wider edge zone with a small tool 2. change the procedure for the polishing of E-ELT segments to leave a narrower up-stand 3. combination of both.

Local edge correction by small conformal tools reduces, but does not completely remove, the edge up-stand left by the preceding process of the E-ELT primary mirror prototype segment polishing procedure. An alternative process is required to achieve the challenging edge specification of the E-ELT primary mirror prototype segments. In the next chapter a different, sub-aperture polishing process is evaluated that is documented to exhibit a very small spot size and a relatively constant removal when the process traverses over the edge of a workpiece.

From the heart of the fountain of delight rises a jet of bitterness that tortures us among the very flowers.

Lucretius

5 Fluid Jet Polishing

5.1 Introduction

As an industrially sponsored PhD student the author undertook a concurrent program of commercial research to investigate an alternative, highly localised polishing process, namely Fluid Jet Polishing (FJP), with Professor Namba's group at *Chubu University* in Nagoya, Japan. *Zeeko*, the industrial sponsor, had two polishing machines permanently present at *Chubu University* at the time, as well as a full-time researcher. From the previous chapters it follows that the manufacture of segmented mirrors would benefit from the availability of a highly localised polishing process that is stable, even when it traverses over the edge of the workpiece. The work done in cooperation with Professor Namba's group allowed the author to evaluate the applicability of FJP as part of the process chain for the polishing of segmented mirrors. This evaluation is presented in the conclusion of this chapter.

FJP is a polishing process which has been developed over the last decade and a half [55, 128]. It is a sub-aperture fabrication technique that applies an abrasive slurry jet for the polishing of optical surfaces in brittle materials, e.g. glass, as well as ductile materials. Slurry is guided through a nozzle onto the surface of a workpiece at pressures ranging from 2 to 20 bar. Because there is no tool wear, the abrasive process is determined by geometric parameters, such as the shape of the nozzle and the orientation of the slurry beam with respect to the local surface normal, as well as slurry parameters (e.g. particle size, mass and jet velocity). The process has been applied to a variety of substrates: from the polishing of glass [129] to the removal of diamond turning marks on electroless-nickel plated moulds [130].

Because there is no physical tool in contact, the forces exerted on the workpiece are much lower than for processes which apply such a tool. This makes it a suitable process for the

polishing of thin optics. Furthermore the author has shown previously while working at *Fisba Optik* in Switzerland that the influence function of the FJP process remains constant even if the jet is traversed off the edge of the workpiece [105]. Both these properties together make it a potential alternative to the small conformal tool based process introduced in the previous chapter for the polishing of edges of thin segmented optics. For these optics the surface form specification may extend to the physical edge of the workpiece as documented in Chapter 3. The two larger of the three polishing machines installed in *OpTIC*'s laboratory have Fluid Jet Polishing capability.

In general mirrors of optical, astronomical telescopes are manufactured from low thermal expansion materials such as ULE®, Zerodur®, Astrositall®, CLEARCERAM®-Z or Cer-Vit®. Recently, lightweight mirrors made from Silicon Carbide (SiC) are considered because of its high stiffness [77], mainly for space-faring optics but for earth-based mirrors as well (e.g. for the tertiary mirror for Thirty-Meter Telescope [131]). Mirrors have also been manufactured from Tungsten Carbide (WC) [132]. The more general application of carbides is as a material for tooling and moulds. Traditionally carbide grains are embedded in a metallic binder by hot press sintering [133]. More recently technologies have been developed to produce cement-less carbides (e.g. spark plasma sintering [134] and microwave radiation sintering [135]). Binderless carbides are more resistant to corrosion and have similar or higher hardness than their cemented counterparts, but exhibit a lower fracture toughness.

The laboratory at *Chubu University* was tasked to apply FJP to Tungsten Carbide samples made from 0.6 µm grains of WC-TiC-TaC [136, 137]. The author designed, built and programmed an experimental FJP set-up and performed initial polishing trials using a variety of polishing slurries of different compounds and sizes. Subsequent experiments and simulations using Finite Element Analysis were performed by Dr. Phillip Charlton of *Zeeko* and Dr. Anthony Beaucamp of *Chubu University*, all of which are discussed and reported on in a joint paper [138], as well as in this chapter with this author's further interpretation.

5.2 Experimental set-up

To test different polishing slurries (e.g. varying abrasives, particle size and pH value) and parameter settings (e.g. pressure and nozzle size) an experimental set-up was built instead of using the IRP200 polishing machines available at *Chubu University*. The reason to do so was two-fold: because of machine availability and the risk of (practically) irreversible contamination. The design requirements were: an easy to clean or replaceable slurry loop, well contained processing area, low operating volume of slurry needed and the ability to traverse the fluid jet along a raster. The built set-up consisted of two linear stages, a containment area, a slurry tank and pump (see Figure 5.2.1). Inside the containment area a workpiece holder and a nozzle holder were mounted. The linear stages were controlled by a programmable controller. Four programs were created for the controller to provide loading, alignment, jet initialising and raster polishing.

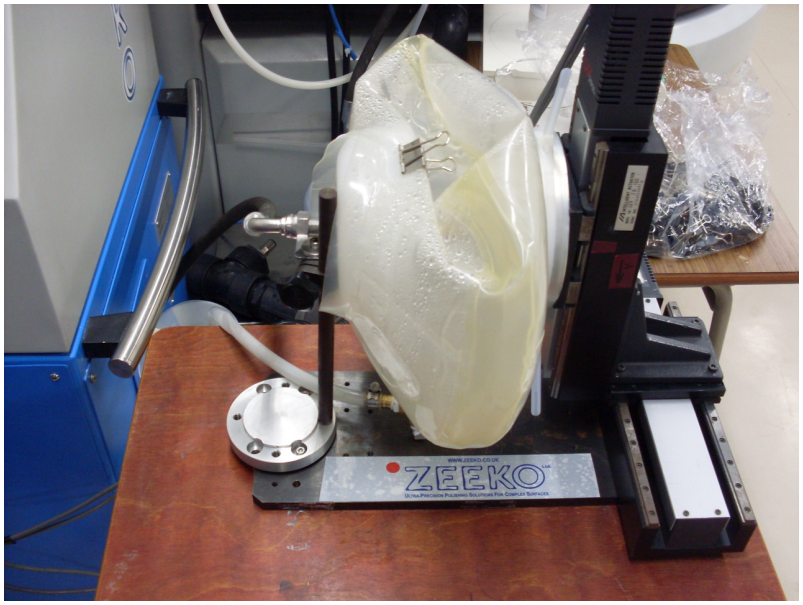

(a) Front view

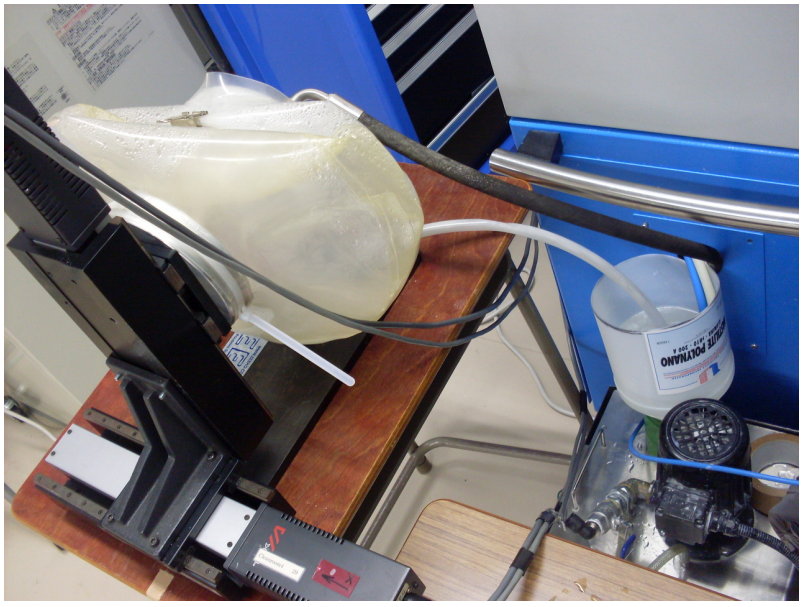

(b) Back view

Figure 5.2.1: Pictures of the experimental Fluid Jet Polishing set-up. The plastic baloon constituted the containment area, the linear stages are shown on the right in (a) and the slurry tank is shown on the right in (b).

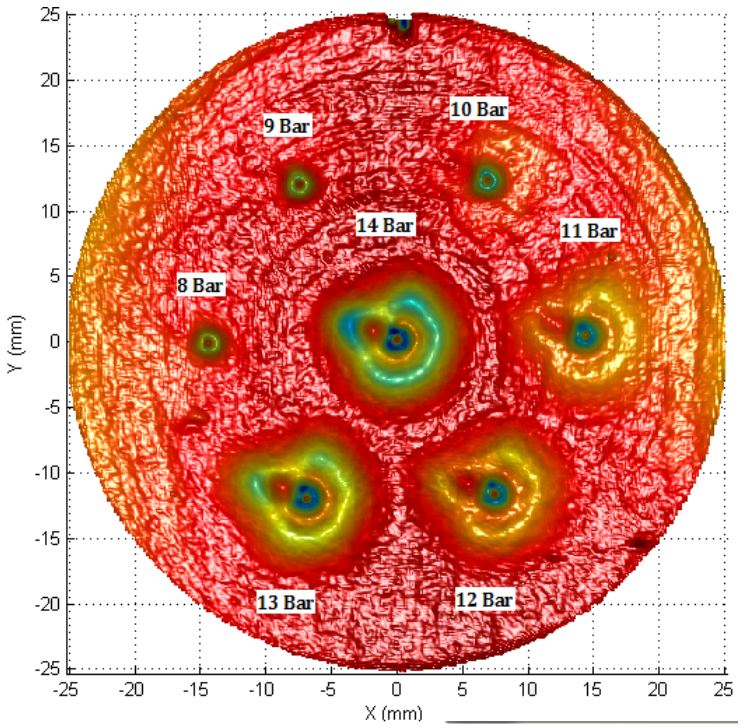

Figure 5.2.2: Influence functions of a 0.51 mm diameter nozzle at various pressure settings. Courtesy of A. Beaucamp, *Zeeko Ltd./Chubu University*, Japan.

Previous results at *Chubu University* had shown that the nozzles used there provided poor jet and footprint stability as shown in Figure 5.2.2. Using experience gained previously by the author while working at *Fisba Optik*, different nozzles were procured that make use of a hydrodynamic phenomenon called "hydraulic flip" to improve fluid jet regularity.

Normally cavitation is an undesired effect, as it may cause damage to structural materials [140] or degrade the performance of pumps [141]. Cavitation occurs if the fluid pressure locally drops below the saturation pressure and fluid transforms to its gaseous state. This causes bubbles of gasified fluid to appear in an otherwise liquid stream. Usually, sharp bends or obstacles in the fluid stream are the cause of local pressure drop and thus cavitation.

Cavitation can be beneficial, however, for the creation of stable water jets. If a fluid is pressurised to flow through an orifice with sharp edges, cavitation will occur along the sharp edges of the orifice and the cavitation bubbles will be transported along the orifice wall downstream [142].

If the operating pressure is high enough, the cavitation void reaches the other end of the orifice and the jet no longer contacts its walls (apart from the sharp, upstream edge). This condition is known as "hydraulic flip" and is shown in detail in Figure 5.2.3. Because the water jet separates from the wall of the orifice, it is free from friction-induced instabilities and therefore is stable over a longer distance after leaving the nozzle. To prevent wear of the sharp edge, the orifice is made in highly durable sapphire.

As can be seen from Figures 5.2.4 and 5.2.5 the nozzle using hydraulic flip produces a stable

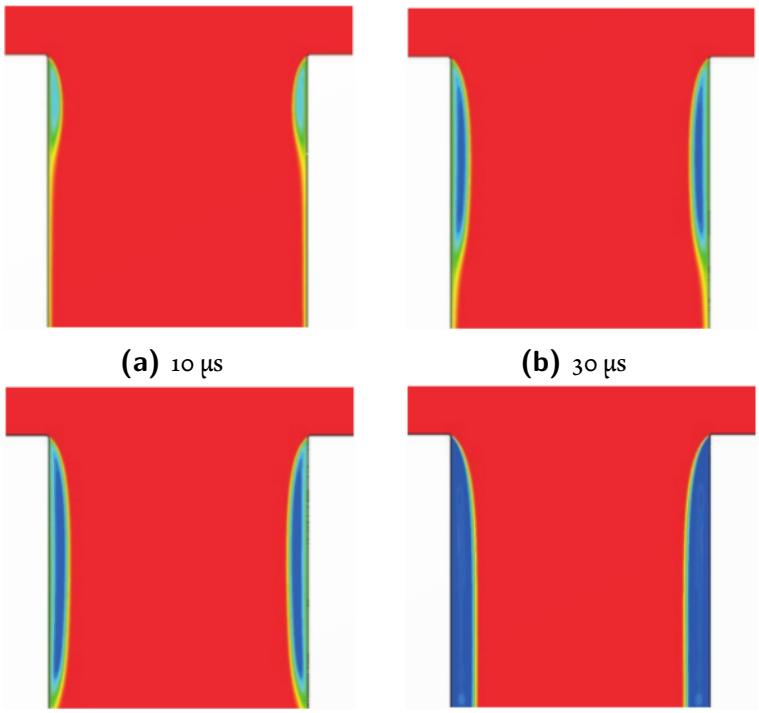

(a) 10 µs **(b)** 30 µs

(c) 50 µs **(d)** 60 µs

Figure 5.2.3: Graph showing contours of mixture density for a radial section of a nozzle after 10, 30, 50, and 60 µs of operation demonstrating hydraulic flip. The nozzle is pressured from the top and sharp corners of the nozzle causing cavitation are visible near the top.
© H. Vahedi Tafreshi and B. Pourdeyhimi [139]. Reprinted under the principle of "fair use"

Figure 5.2.4: Picture showing a stable fluid jet of a nozzle applying hydraulic flip.

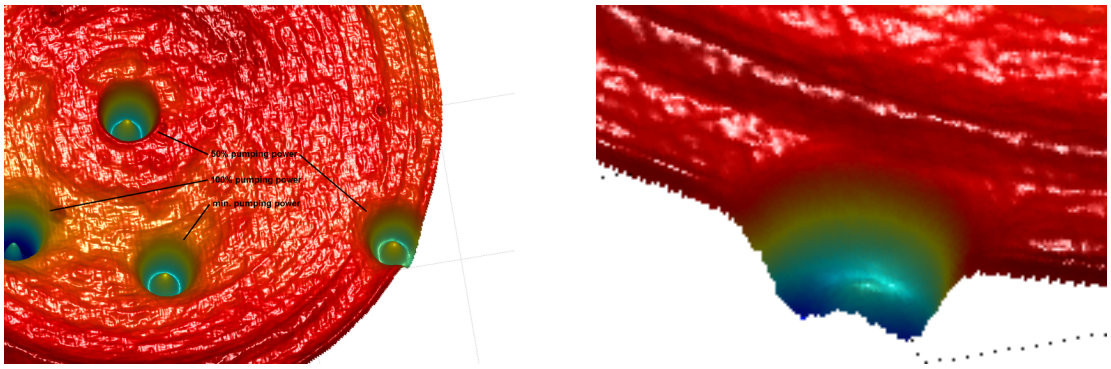

(a) Influence functions at various pressures and locations

(b) When 50 % hangs over the edge

Figure 5.2.5: Graph showing stable, interferometrically measured influence functions created by FJP from a nozzle applying hydraulic flip.

jet and regular footprints. When the fluid jet is traversed out over the physical edge of the workpiece the removal rate and profile remain constant, as can be seen from Figure 5.2.5b.

5.3 Initial experiments

Different polishing slurries (e.g. varying abrasives, particle size and pH value) were tested by this author, applying FJP to plano WC-TiC-TaC made from 0.6 µm grains. All experiments were performed using a square raster covering 6.34×6.3 mm² with a track spacing of 0.1 mm. A nozzle with an orifice diameter of 0.8 mm was used and the results are summarised in Table 5.3.1.

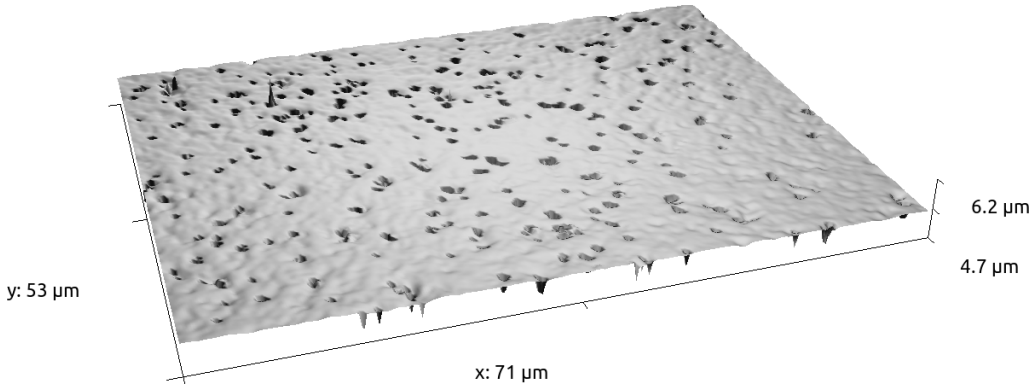

Figure 5.3.1: Typical roughness measurement (experiment number 5) by confocal laser scanning microscope.

No degradation in the jet formation was observed over the course of the experiments. These types of nozzles are used in the water cutting industry and operated at pressures up to 4000 bar. Therefore, wear of the nozzle, specifically the sharp edge of the upstream opening of the nozzle, is not expected to be a concern over the duration of a polishing run (typically from a few minutes up to a few hours).

Table 5.3.1: Results of the initial FJP experiments evaluating the removal rate and surface texture of different abrasive compounds.

Exp.	Compound	Particle Size µm	Density g cm^{-3}	Spec. Grav.	pH	Raster count	Removal nm	rms nm
1	Hastilite Polytron 3.0	3	3.52	1.079	7	2	0	0
2	Green Silicon Carbide	5.6	3.21	1.083	7	2	30	15
3	Green Silicon Carbide	17.9	3.21	1.084	7	2	80	128
4	Green Silicon Carbide	17.9	3.21	1.084	7	2	25	16
5	Green Silicon Carbide	17.9	3.21	1.08	5	2	40	35
6	Diamond	3	3.52	1	7	20	2	8
7	Diamond	3	3.52	1	7	3	0	0
8	Cerium Oxide Trent #95	5	7.65	1.085	4.76	3	8	5
9	Cerium Oxide Trent #95	5	7.65	1.085	9.17	3	2	4

The experiments show material removal using FJP is possible on binderless tungsten carbide. However, in the experience of the author, the removal rate is much lower than the removal rate for optical glasses when the same slurries are applied in FJP. This was expected as the Knoop hardness of tungsten carbide (1000 g mm^{-2} to 2500 g mm^{-2} [143]) is much higher than that of typical optical glasses (550 g mm^{-2} for SF6 and 610 g mm^{-2} for BK7 [144]).

The increase in roughness that accompanies the removal on WC in these experiments is due to large pits created in the surface, as shown in Figure 5.3.1. A likely cause of these pits is removal of entire grains from the surface, similar to the observations of Gant and Gee [145]. Further investigation was needed to minimise the stress between individual grains of tungsten carbide.

During some experiments embedding of the abrasive particle was observed on the surface. These particles proved difficult to remove from the surface, even though a wide range of solvents and an ultrasonic bath was applied. The prevention of particle embedding is therefore preferred.

Another conclusion can be drawn by comparing the data of slurries made from different particle sizes of the same compound. Since the specific gravity of the two mixtures was kept the same, it is to be expected that the concentration of the slurry (number of particles per unit of volume) decreases with the same factor as the mass per particle increases (due to the larger volume of the particles). If the removal in FJP were solely governed by the number of particles multiplied by the kinetic energy ($\frac{1}{2}mv^2$), as is sometimes assumed [55], it would remain the same for both experiments (because the velocity profile of the jet remains the same). Since the removal clearly is not constant for different particle sizes of the same compound, the removal process must be more complex, meriting further research.

As mentioned previously, the experiments and simulations described in the next two sections were performed by Dr. Phillip Charlton of *Zeeko* and Dr. Anthony Beaucamp of *Chubu University*. These experiments and simulations investigated in more detail the grain dislocation and particle embedding and are summarised here in this author's own words. The collaboration resulted in a jointly published paper [138]. Upon further reflection it is the opinion of this author that an alternative hypothesis explaining the grain dislocation is more likely. A critical assessment of both hypotheses is presented in section 5.6.

5.4 Pure water experiments

To effectuate removal, abrasive particles are added to water to create an abrasive slurry. It is generally assumed that any removal is caused by the abrasive particles and that the water only serves as a medium to transport the particles. To test this hypothesis, that water does not cause removal, pure water FJP experiments were performed, instead of applying a premixed slurry. Furthermore, the pure water jet was tested under two conditions. The experimental set-up was modified to allow the FJP process to be operated in two different modes:

- Submerged - the fluid level in the containment area was raised to cover nozzle, jet and workpiece.
- Non-submerged - as in previous experiments the jet travelled through air.

The jet, produced by a 0.8 mm nozzle, was not traversed along a raster over the surface. It was held at 2.0 mm distance from the surface for 15 minutes at a single location for each setting of nozzle input pressure, between 2 to 18 bar.

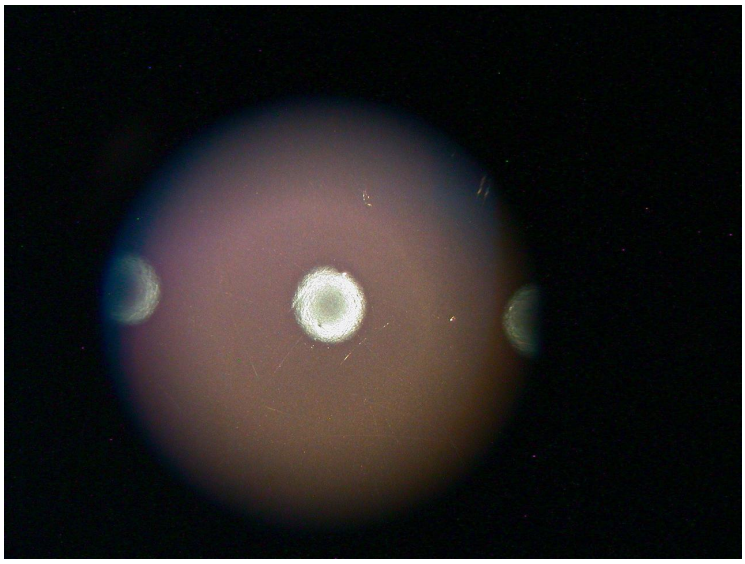

(a) Non-submerged jet

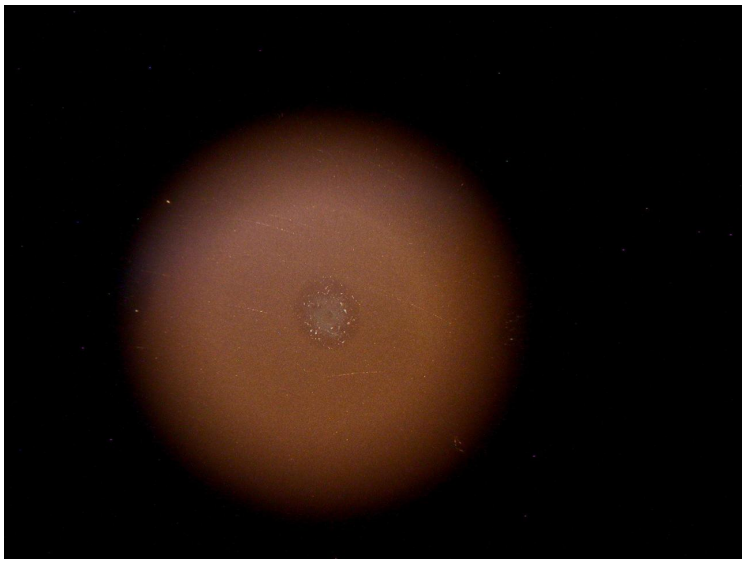

(b) Submerged jet

Figure 5.4.1: Pictures of optical microscope observations of pure water experiments for a standard, non-submerged jet and a submerged jet. Courtesy of A. Beaucamp, *Chubu University*.

After the experiments the processed locations were observed by optical microscope, two examples of which are shown in Figure 5.4.1. At pressures above 4 bar light scattering was observed due to degradation in the surface texture for the standard modus of FJP (non-submerged), see Figure 5.4.1a. None of the submerged jet experiments exhibited the same degradation. As can be seen in Figure 5.4.1b the only change observed was a darkening of the surface, assumed to be the result of the removal of a thin oxide layer from the surface [146]. Therefore, contamination or residual abrasive particles in the fluid can be disregarded as a cause of the surface texture degradation of the non-submerged jet.

The lateral scale of the defects in the surfaces, treated with the non-submerged jet, was compared to the WC grain size, by applying a confocal laser scanning microscope. This confirmed the dislocation of WC grains from the surfaces that were treated by the non-submerged jet above 4 bar nozzle inlet pressure.

The difference between the two operating modes, with regards to the resulting surface texture, occurred for a wide range of nozzle inlet pressures. The actual impact velocity of the jet on the surface was calculated by Computational Fluid Dynamics, a numerical method related to Finite Element Analysis (FEA) discussed in Chapter 3, using the software package COMSOL.

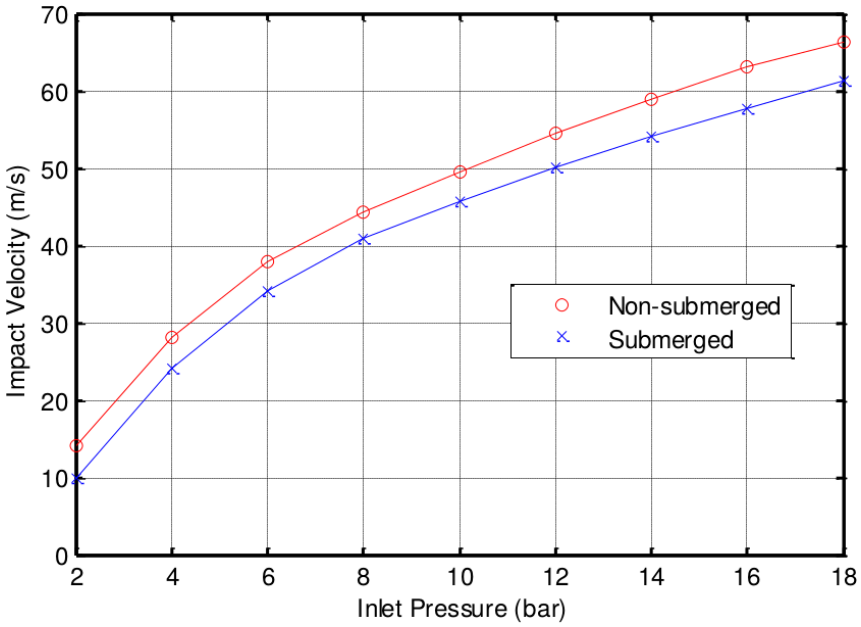

Figure 5.4.2: Graph showing the impact velocity magnitude as function of inlet pressure for submerged and non-submerged conditions of the nozzle resulting from CFD simulations. Courtesy of A. Beaucamp, *Chubu University*.

As can be seen from Figure 5.4.2 the magnitude of the impact velocity of the submerged jet is slightly lower than that of the standard, non-submerged jet for the same nozzle inlet pressure. However both ranges of impact velocity magnitudes show a large degree of overlap. The magnitude of the impact velocity can therefore be discarded as a cause of the difference in resulting surface texture. Further research is necessary to understand the different results of the non-submerged and submerged jet when applied to binderless tungsten carbide.

5.5 Particle embedding

Subsequent experiments applied slurries with abrasive particles of different sizes on WC samples in the submerged modus of FJP. For certain combinations of abrasive particle size and nozzle inlet pressure, abrasive particles embedding in the WC surface occurred. This is similar to the observations of Tsai et al. [147] for the abrasive jet processing of steel moulds.

Figure 5.5.1 depicts for which combinations of abrasive particle size and nozzle inlet pressure particle embedding on the surface was observed. Alumina abrasive particles were used with

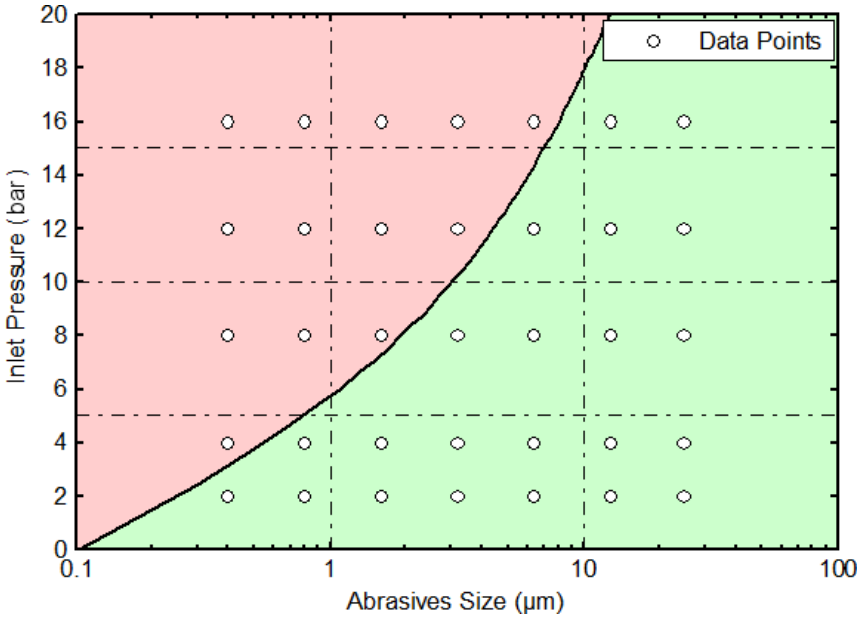

Figure 5.5.1: Graph showing for which process parameters particle embedding on the surface was observed. Courtesy of A. Beaucamp, *Chubu University*.

nominal size from 0.4 µm to 24 µm. From these results it follows that to reduce the risk of particle embedding on the surface either a low nozzle inlet pressure or large abrasive particles should be used. The multi-physics FEA software package COMSOL was used to simulate impacts of spherical particles on the WC surface.

From the simulations it followed that the peak contact pressure during impact increases with increasing nozzle inlet pressure, as is to be expected. However the simulations indicate that the peak contact pressure is hardly dependent on the size of the abrasive particle, as is shown in Figure 5.5.2.

At the same time the area of contact between the particle and surface varies with both the nozzle inlet pressure and the abrasive particle size. This can be seen in Figure 5.5.3 which shows the deformations resulting from the simulations.

Figure 5.5.4 shows the ratio of the peak contact area to the particle weight for different abrasive particle sizes. These were calculated from the results of the FEA simulations using a constant nozzle inlet pressure of 8 bar. Between abrasive particle sizes of 0.5 to 8.0 µm the peak contact area to particle weight ratio decreases by two orders of magnitude. Therefore during the impact of smaller abrasive particles a higher ratio of surface energy is lost to stored elastic energy for a given nozzle inlet pressure and a larger force is needed to achieve separation according to the Johnson-Kendall-Roberts (JKR) model of elastic contact [148].

5.6 Assessment and alternative hypothesis

In this section the hypothesis, introduced in the joint paper [138] to explain the difference in grain dislocation for submerged and non-submerged water jets, is assessed and an alternative

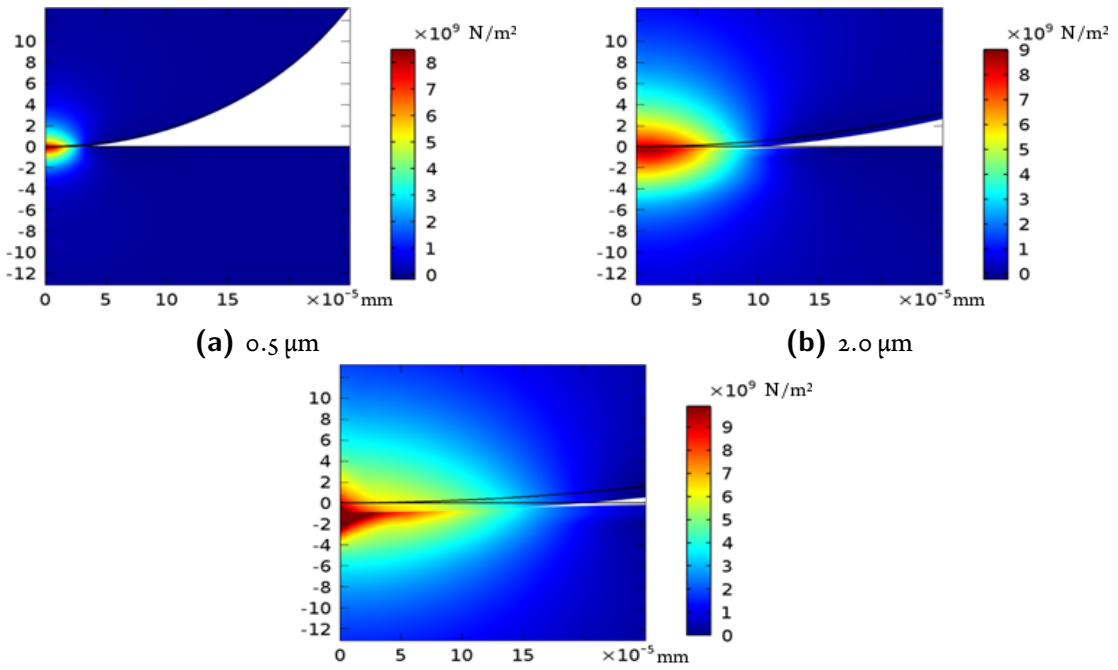

(a) 0.5 µm **(b)** 2.0 µm

(c) 8.0 µm

Figure 5.5.2: Graph showing peak pressure during alumina abrasive particle impacts of different sizes on tungsten carbide based on FEA simulation with a nozzle inlet pressure of 8 bar. Courtesy of A. Beaucamp, *Chubu University*.

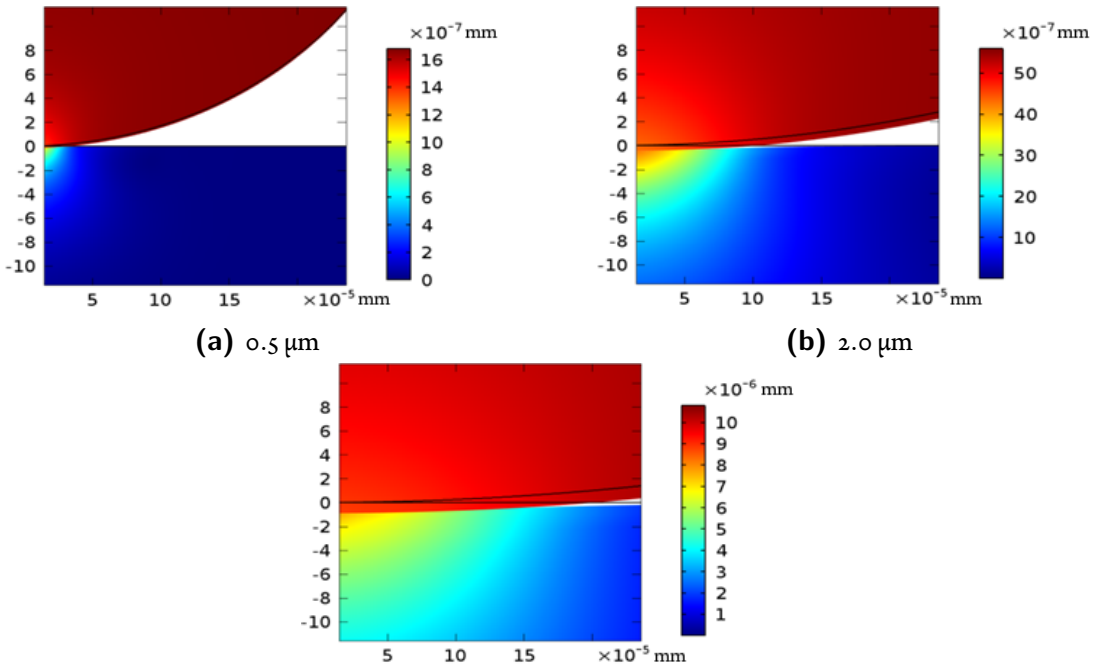

(a) 0.5 µm **(b)** 2.0 µm

(c) 8.0 µm

Figure 5.5.3: Graph showing peak displacement during alumina abrasive particle impacts of different sizes on tungsten carbide based on FEA simulation with a nozzle inlet pressure of 8 bar. Courtesy of A. Beaucamp, *Chubu University*.

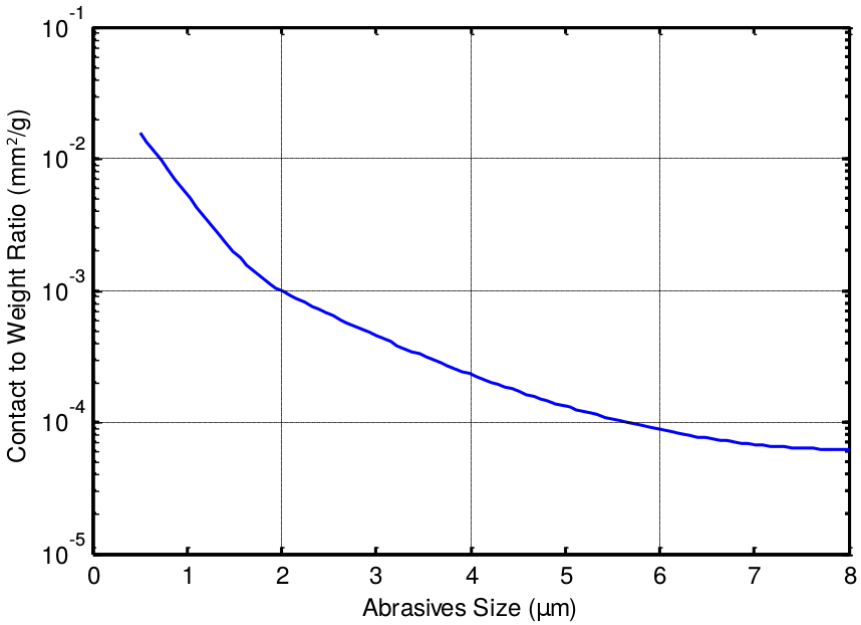

Figure 5.5.4: Graph showing the peak contact area to particle weight ratio versus abrasive particle size for a constant nozzle inlet pressure of 8 bar. Courtesy of A. Beaucamp, *Chubu University*.

hypothesis is introduced by the present author.

5.6.1 Wind-induced breakup

As previously mentioned, water jets created by hydraulic flip feature a longer intact length than jets created by a regular nozzle. Before the jet disintegrates however, the diameter of the jet oscillates in a breakup mode referred to as the "first wind-induced breakup mode"[149]. Instead of having the appearance of a column of water, the jet in this mode resembles a pearl necklace of equally sized, connected water droplets.

In [138] it is hypothesised that the wind-induced breakup of the non-submerged jet causes violent oscillations of the impact force. It is postulated that the vibrational energy transferred to the surface dislocates WC grains.

However, examination of the optical microscope images of the surface damage (Figure 5.4.1) seems to indicate that the most of the dislocation occurs in a ring shaped zone around the centre of the impact. Further more this ring shaped area is estimated to have an outer diameter of 1.3 mm. Water jets created by hydraulic flip have jet diameter which is smaller than the diameter of the nozzle, which in this case was 0.8 mm. The higher surface damage outside of the jet cross-section can not be explained by the wind-induced breakup hypothesis.

5.6.2 Micro bubble implosion

It is known from literature that cavitation may cause extensive damage to structural materials [140]. This is caused by the collapse of micro bubbles which produces an acoustic shock-wave and a micro-jet if it occurs close to a hard surface [150]. The impact pressures of both of these phenomenon is 1000 bar or more [150]. These micro bubbles are formed when

the main cavity disintegrates downstream of the cause of the cavitation.

It is postulated here that the impact of the laminar jet on the surface causes cavitation. Micro bubbles are formed and transported outward by flow of the water. When they implode the resulting acoustic shock-waves and micro-jets cause dislocation of WC grains from the surface. This explains the ring-shaped removal observed on the surface and the removal outside of the cross-section of the jet.

Figure 5.4.2 shows that a submerged jet exhibits a lower impact velocity on the surface than a non-submerged jet for the same nozzle inlet pressure. The loss of energy of the submerged jet is caused by friction with the surrounding water. It is hypothesized here that this causes a different jet profile, for instance a reduction of fluid velocity towards the exterior of the jet or the introduction of turbulence, that prevents the occurrence of cavitation due to the impact on the surface.

The author has previously reported on the increased removal of FJP on glass when air bubbles are introduced in the slurry stream [56, 57] and on the more homogeneous texture of the resulting surface if air is extracted from the slurry [58]. And it is known from literature that the presence of gas in water facilitates the occurrence of cavitation [151].

Although the validation of this theory is outside of the scope of this thesis, some experiments are suggested here to do so. Firstly, CFD analysis of the jet impact area to establish under which conditions cavitation occurs. Secondly, repeating the pure water experiments, but adding small gas bubbles to the stream before the nozzle. Thirdly, repeating the experiments but adding a surfactant to the water to reduce surface tension (which promotes bubble formation).

5.7 Conclusion

Fluid Jet Polishing is a sub-aperture polishing process without physical contact between a tool and workpiece. This results in lower exerted forces on the workpiece and a constant removal even when the jet is traversed off the edge of the workpiece. These properties are desirable if the surface form is specified up to the physical edge of thin optics, such as segmented mirrors and lithography photomasks used in semiconductor microfabrication.

In collaboration with *Chubu University* experiments were conducted applying FJP to binderless tungsten carbide surfaces. Carbides provide high stiffness allowing lightweight construction of mirrors. They are considered mainly for space-faring optics but also for earth-based mirrors.

An experimental FJP set-up was constructed and a variety of slurries were tested. Although removal was achieved the resulting surfaces suffered from two issues: the removal of entire grains from the surface and embedding of abrasive particles on the surface. Further experiments and simulations were performed by Dr. Phillip Charlton of *Zeeko* and Dr. Anthony Beaucamp of *Chubu University* and the collaboration resulted in a jointly published paper [138]. The paper hypothesises that the WC grain removal from the surface is caused by vibration energy of the jet in wind-induced breakup mode. This hypothesis is critically assessed in this chapter and an alternative hypothesis is presented. Several experiments are suggested for the validation of the

introduced hypothesis, which lies outside the scope of this thesis.

The Finite Element Analysis of fluid dynamics and abrasive particle impact provided useful insight into both the grain dislocation and particle embedding phenomenon and under which process conditions they occur. This work has demonstrated the power of numerical analysis and models to optimise fluid transport phenomena to deliver physically useful results. It would be extremely difficult to design and optimise FJP systems by purely experimental means and numerous sources report on the application of FEA during the development of FJP and related processes (e.g. [60, 152, 153]). FEA has proved to be an indispensable tool, without which the development of FJP as a industry grade polishing process would have been unthinkable.

As previously mentioned, the manufacture of E-ELT primary mirror segments would benefit from the availability of a highly localised polishing process that is stable, even when it traverses over the edge of the workpiece, such as FJP. However, several practical difficulties are identified that prevent the process from readily being applied to the polishing of E-ELT primary mirror segments.

This first is containing the processing area to ensure full recycling of the polishing slurry. This is important as the process is more sensitive to variations in slurry conditions than polishing with a tool rubbing on the surface. Ensuring containment and slurry stability while polishing a metre scale optic is a considerable challenge. The next difficulty is related to the containment issue: this chapter shows that, to prevent surface degradation of a WC sample, the FJP has to be applied submerged. Previous work has shown that FJP can be applied to optical glasses through the air without causing this surface degradation, however this needs to be confimed for the substrates that are considered for the E-ELT primary mirror segments, as submerging an optic of this scale and its support structure is practically impossible.

Furthermore, a small jet (used for the correction of small error dimensions) requires a high track density to prevent cusping and has a low removal rate (e.g. $<0.01\,\mathrm{mm^3\,min^{-1}}$ for a 1.2 mm diameter nozzle [154]). The required track spacing and removal rate are unacceptable for polishing the full surface of an optic of the scale of an E-ELT primary mirror segment. The track spacing due to computational constraints during tool-path generation and the process time is unacceptably long due to the low removal rate. The only viable application of FJP in the E-ELT primary mirror segment polishing process chain would therefore be the local correction of subsections of the surface, such as the edges and corners of the segments, where processes with tools in contact with the surface encounter difficulties (as outlined in the previous chapters).

Lastly, the application of a highly localised polishing process for corrective polishing is beneficial only if the available surface error data is of a high enough resolution, typically higher than one pixel per spot size. The test available at *OpTIC* for measuring E-ELT primary mirror prototype segments provides data at a resolution of 5 mm per pixel. A sub-aperture, on-machine, stitching interferometer would need to be commissioned to take advantage of the highly localised polishing area of FJP.

From the previous it is clear that FJP has much potential for polishing segmented mirrors as it complements the strengths and weaknesses of processes with a physical contact between tool

and workpiece. However, the practical difficulties outlined above require significant further investigation and development before FJP can be applied to E-ELT primary mirror segments. This is why an alternative procedure for the polishing of E-ELT primary mirror prototype segments was prefered, appling bonnet and rigid tools alternating, which proved to be successful (see Chapter 2 for results).

This success is due, in part, to the accurate positioning of the polishing tools with respect to the workpiece surface. The following chapter uses E-ELT primary mirror segments as a case study to investigate the numerical description of surfaces. These numerical designs are necessary to generate tool-paths for the CNC polishing machine. Any inaccuracies lead to positioning errors of the process which may lead to figuring errors and non-convergence of the corrective polishing process.

Our inventions mirror our secret wishes.

Lawrence Durrell

6

Surface designs and reference frames

6.1 Introduction

In Computer Controlled Optical Surfacing (CCOS) the dwell time of a sub-aperture polishing process is varied locally to provide differential removal of material, and so improve the surface figure of an optic, as discussed in more detail in Chapter 1. The dwell times are optimised using measurement data of the surface figure taken beforehand, by minimising the predicted surface error after applying the process. The dwell times are calculated along a tool-path: a sequence of points on the surface along which the process is to be traversed so that it is treated completely. The dwell times and tool-path points together are used to create a set of numerical instructions for a CNC polishing machine to execute. This sequence of measurement, optimisation, instruction generation and polishing is repeated until the misfigure of the surface converges bellow acceptable tolerances, as defined by the optical designer.

There may be many reasons why low convergence or even divergence may be observed, in practice. Some examples are:

- Positional errors tangential to the surface causing the process to be applied on a different position on the surface than intended.
- Positional errors perpendicular to the surface causing the tool to be held at an incorrect distance above the surface. If bonnet type tools are compressed into the surface by varying amounts, the contact area, and subsequently the removal rate, varies.
- Other variations in removal rate, for instance caused by changes in the slurry specific density.

- Use of a surface misfigure error map that uses a different coordinate system than that of the polishing machine, for instance reflection and/or rotation.
- Geometric distortion of the surface misfigure measurement causing sub-optimal dwell time values to be applied.
- The surface misfigure consists of errors with high spatial-frequencies. Compliant tools are ill-suited for the correction of errors with dimensions smaller than the contact area.

Due to machine limitations the process can only traverse the surface at finite speeds. Therefore, material is removed even at the lowest points of the surface error (the valleys). The minimal removal anywhere on the surface is named the "DC" component of the removal. For locations on the surface where the surface error is larger than the minimum the feed rate is proportionally lower. For example, if a surface error has a PV of 1.0 μm and the minimum removal is 0.1 μm due to the maximum speed of the machine, then the feed at the peaks in the error map is equal to $\frac{1.0}{1.0+0.1}$ times the maximum speed. If the removal rate of the process varies by 10 % then the resulting surface has a surface PV error similar to the starting PV. Thus, it can be seen that variation of the removal rate limits the surface misfigure that can be achieved.

By temporally applying fiducials to the optical surface, the geometric distortion of the measurement can be estimated and compensated for. Chapter 7 investigates the spatial frequency content of surface misfigure in more detail and how it can be dealt with in corrective polishing using compliant tools.

The positional errors mentioned above may be caused by machine construction or control system errors. Another possibility is an incorrect surface shape, and position of its edges, in the controlling software of the polishing machine. This results in incorrect coordinates of the points along the tool-path. The numerical representation of the surface in the control software is called a "surface design". For a sphere with a round edge this design is trivial but for off-axis aspheres defined in coordinate frames other than the machining coordinate frame there are several potential sources of error. These are investigated for two test cases, E-ELT primary mirror segments and IXO segment slumping moulds.

6.2 Prototype E-ELT primary mirror segments

The specifications of the seven prototype segments for the primary mirror of the European Extremely Large Telescope (E-ELT) are outlined in the call for tenders [82] and discussed in Chapters 2 and 3. Their location in the primary mirror is depicted in Figure 2.1.3. To minimise the gap between segments they consist of non-regular hexagons. It is impossible to tessellate a curved surface with regular hexagons with uniform gaps between them.

The surface form of the entire primary mirror is defined by *ESO* in the "Primary Mirror coordinate system" using

$$z(r) = \frac{r^2}{R + \sqrt{R^2 - (1+k)r^2}} + A_4 r^4 + A_6 r^6 + \cdots + A_{2N} r^{2N} \qquad (6.1)$$

with r the distance to optical axis of the primary mirror, R the base radius of curvature, k the conic constant and A_i aspheric coefficients. The Primary Mirror coordinate system has its origin at the vertex of the primary mirror, the x- and y-axis perpendicular to the optical axis and the z-axis along the optical axis. For the prototype segments the primary mirror was specified by $R = 84$ m, $k = -0.993\,295$ and all aspheric constant equal to zero. The centre ("C0") and corner coordinates ("C1" through "C6") of each of the seven prototype segments are provided by *ESO* [82] in the Primary Mirror coordinate system.

6.2.1 Prototype Segment coordinate system

The optical surfaces of the prototype segments form parts of the primary mirror. Each prototype segment has an associated "Prototype Segment coordinate system" [82]. The conversion from Primary Mirror coordinates to Prototype Segment coordinates is done in two "steps":

1. The segment is translated in x, y and z so that the centre (C0) is located in the origin of the Primary Mirror coordinates system

2. The segment is rotated first around the x- and then around the y-axis so that the surface normal at the centre (now the translated C0) is facing in the positive z-direction.

In the default position of the segment on the "IRP 1600" polishing machine built by *Zeeko* the Prototype Segment coordinate frame coincides with the machine coordinate frame. The polishing procedure, developed for the E-ELT prototype primary mirror segments, calls for the orientation (rotation around the z-axis) of the segments to be alternated between polishing runs.

6.2.2 Surface design

As mentioned previously, to calculate the coordinates of the tool-path, a numerical representation of the surface has to be created, in the polishing machine's controlling software. *Zeeko*'s software allows surface definitions by specifying Equation 6.1 and providing the values of the coefficients. However, this defines the surface form in Primary Mirror coordinate system. To transform the surface to the Prototype Segment coordinate system, the software allows offsets and rotations to be entered. Furthermore, the software allows the definition of the edge of the surface by supplying the corner coordinates of a polygon.

Zeeko's SegmentAligner.m script

The manufacturer of the polishing machine provided a MATLAB script to calculate all the relevant input values for their software, to create a surface design for the prototype segments. This script, `SegmentAligner.m`, was evaluated by creating the surface designs for each of the seven prototype segments. The results were verified by creating a so-called "sag table" and comparing it to one created independently by *OpTIC* from *ESO*'s specifications. A sag table is an array of surface heights for a select number of points on the surface. Sag tables are commonly used in industry to check whether the correct aspheric surface is implemented. This is because

different organisations, software developers and machine manufacturers use slight variations of Equation 6.1 for the definition of aspheric surfaces.

After creating seven surface designs in the control software of the polishing machine, sag tables were generated on a 50 mm spaced, rectangular, equidistant *XY* grid in Prototype Segment coordinates. After comparing the results with the sag table provided by *OpTIC* two problems were identified. Firstly, the script was designed to perform a different coordinate system transformation (a rotation around the *z*-axis to place the centre in the *YZ* plane, a translation to place the centre at the origin and a rotation around the *x*-axis to bring the normal at centre in line with the positive *z*-direction). As a result only the 3 segments with a centre *x*-coordinate equal to zero (the three stacked vertically in Figure 2.1.3) make use of the *ESO* specified Prototype Segment coordinate system. Secondly, the calculated corner positions, used to create the boundary of the irregular hexagon in the control software, were translated but not rotated. A modified version of the script that addressed the latter problem was provided by *Zeeko* before polishing commenced.

The first prototype segment that was polished, called "SPN01", was one of those three mentioned above. However, when the surface was inspected after the first polishing run (which targeted uniform removal) uneven removal was observed, specifically along four edges. Eventually it would be discovered that this was due to the corner coordinates used still being incorrect, but this was not known at the time. The author addressed both problems, the coordinate transformation and the corner coordinates, and a new MATLAB script was developed by the author and provided to the E-ELT team of *OpTIC*.

6.2.3 Coordinate transformation

Rotations around multiple axes are noncommutative, therefore it was necessary to determine the sequence of the operations in the control software of the polishing machine. *Zeeko* kindly gave the author access to the source code of the software. It was verified that the sequence of the rotations conformed to the one used in the base transformation between Primary Mirror and Prototype Segment coordinate system.

A MATLAB script was subsequently created that takes as an input the ESO specifications and provides the *Zeeko* software with the offsets and rotations needed to perform the base transformation. Again, sag tables were created on a 50 mm spaced, rectangular, equidistant grid, using the parameters provided by the new script and compared to *OpTIC*'s results. The difference between the sag tables was several orders of magnitude smaller than the positional accuracy of the machine.

6.2.4 Corner coordinates

The observed symptom, variations in polishing depths after targeting uniform removal, may be caused different, unrelated error mechanisms. This makes troubleshooting a difficult task, especially when multiple error mechanisms are compounding the problem, as turned out to be the case with the corner coordinate errors of surface designs of the prototype segment. To find

the cause of the observed problem the different error mechanisms have to be explored in as much isolation as possible, by devising practical tests. One such error mechanism relates to the preparation of the tool.

Before use, a bonnet based tool has to be dressed, as described in Chapter 4. An incorrectly dressed tool is one of the causes of variations in polishing depths after using the Precessions™ polishing process (outlined in Chapter 1) when a uniform removal is targeted. The tool axis (centre line of the spindle) is rotated around the virtual pivot to maintain a constant angle with the local surface normal of the workpiece during polishing. If the centre of the tool and the virtual pivot do not coincide, different angles of the tool axis result in different sizes of the contact area between tool and surface, and thus different removal rates.

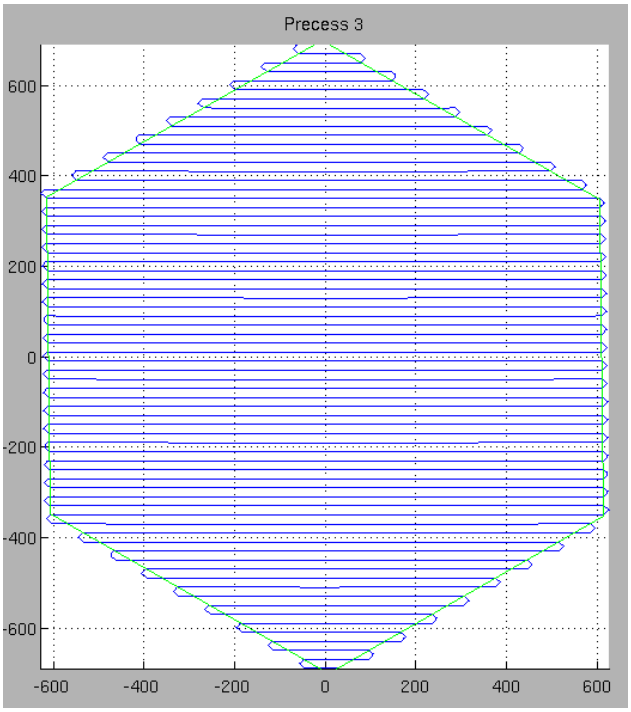

Figure 6.2.1: Screenshot of the control software of the polishing machine, showing the tool-path designed for validation of the corner positions of the irregular hexagonal prototype segments, using a pen tool. The polygon created by the software as a boundary of the surface is shown in green. All units in mm.

To investigate the problem and discount any issues related to the virtual pivot, a felt-tipped marker was mounted on the tool spindle in place of the bonnet tool. The tip of the marker was positioned close to the virtual pivot of the machine, by measuring the distance to a reference surface with a ruler. The control software was used to create instructions for the polishing machine to move the virtual pivot along a "polishing" raster on the surface, using a wide track spacing. Figure 6.2.1 shows the resulting tool-path. Also shown is the boundary of the surface as used by the control software. It can be seen that the machine is instructed to move from one sweep of the raster to the next along two sides of a triangle. One corner of this triangle is located at the boundary of the surface (as calculated by the software), if a certain process parameter, "tool overhang", is set to zero.

This tool-path was executed on the machine with the marker in contact with the surface. The lines left by the marker on the surface were observed, specifically the triangle corners between tracks and their alignment to the physical edge of the prototype segment. This test was performed for different orientations of the prototype segment, using the turntable of the polishing machine. In the default orientation, where the Prototype Segment coordinate axes coincide with the machine axis of the polisher. And in the orientations specified in the polishing procedure developed for the E-ELT prototype segments. These latter orientations differed from the default orientation. These different tests were performed to decouple potential error sources. In the end, two problems were identified: 1. remaining errors in the calculated positions of the corners in Prototype Segment coordinate system, and 2. errors introduced by rotating the prototype segment from its default position.

Second correction of the corner positions

After analysing the `SegmentAligner.m` script, provided by *Zeeko*, an additional error in the calculation of the corner positions of the polygon boundary in machine coordinates was identified. The script assumed that the corner positions were defined in the plane tangential to the surface at the centre of the prototype segment. In reality, the corner positions defined by *ESO* are located on the surface of the primary mirror.

Rotation of a prototype segment

As mentioned previously, the orientation (rotation around the z-axis) of the segments has to be alternated between polishing runs, as per the polishing procedure, developed for the E-ELT prototype primary mirror segments. The control software of the polishing machine requires that the surface misfigure data (used to optimise the dwell times along the tool-path) is imported in the same orientation as the prototype segment during polishing. The control software also has a parameter that defines the rotation of the surface design before the tool-path is created. This rotation is also included in the instructions provided to the polishing machine. It was identified that the control software and the polishing machine were not set up to used the same sign of the rotation, but used opposite sign.

For rotationally symmetric surfaces with symmetric contours this mismatch in sign convention does not lead to a different tool-path, for typical rotations. And because the surface misfigure data is imported in to the control software in the same orientation as that of the workpiece during polishing, which the operator can observe, this problem was not noticed during development work performed on regular, spherical hexagons. These witness samples were used instead of prototype segments for reasons outlined in Chapter 4.

But for the prototype segments, this sign mismatch caused an incorrect tool-path to be created by the control software. An incorrect boundary polygon was used to create the tool-path due to the irregular hexagonal contour of the prototype segments. And because the surface is non-rotationally symmetric, positional errors perpendicular to the surface occur.

6.2.5 Results

A new MATLAB script has been written by the author and provided to the segment polishing team, which resolved all the issues described previously, see Appendix F. This script has been used to create the surface designs for all seven prototype segments. Their sag tables and boundary coordinates were compared to data provided by *OpTIC* and the difference between the two methods was found to be several orders of magnitude smaller than the positional accuracy of the machine.

Using the surface designs, a tool-path has been generated for a "marker-tool" that plots a 50 mm wide raster on the surface of the optic to be polished. Inspection of the raster showed the edges of the surface design and prototype segment were aligned within a mm (corresponding to a rotational error smaller than 0.076°) and no obvious difference (in the mm range) in sag existed (the line-width of the cone tipped marker was uniform).

Subsequently the surface designs have been used, by the consortium led by *OpTIC*, to polish two E-ELT prototype segments with a third about to be completed. Both finished segments have been accepted by *ESO*. And, in contrast to their only competitor, the consortium was able to achieve the demanding specifications of the E-ELT prototype segments. The resulting surface error of the first segment is documented in Chapter 2. The second segment accepted by *ESO*, "SPN04", has a surface error of 23 nm rms, with tip and tilt removed, and 10 nm rms, with further low order terms removed, as per specification. The segment that is about to be certified by *ESO* has surface error rms values of of 24.9 nm, with tip and tilt removed, and 9.8 nm, with further low order terms removed.

6.3 IXO segment slumping moulds

6.3.1 Introduction

For the International X-ray Observatory (IXO) mission, the *Brera Observatory*, Italy, is researching alternative manufacturing methods of grazing incidence mirror shell segments. Specifically, this comprises of the slumping of glass onto a mould (see Figure 6.3.1) to replicate its shape by applying heat and pressure [155]. Together the segments form a set of surfaces of revolution. In the axial direction the shape of the mould is either parabolic or hyperbolic depending on the position of the segment within the complete mirror. The author was asked by *Zeeko* to create and evaluate surfaces designs for one of each type of moulds. These would subsequently be used by *Zeeko* to polish two demonstration parts provided by *Brera Observatory*.

6.3.2 Surface design

With *XZ* a cylindrical coordinate system (with the x-axis as the revolution axis) the parabola and hyperbola are described respectively in the Telescope Coordinate system as

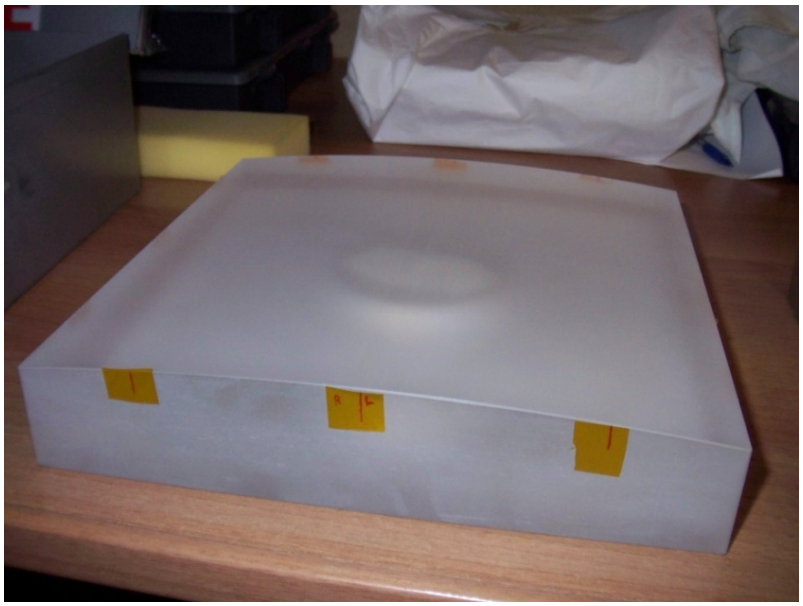

Figure 6.3.1: Picture of an IXO slumping mould blank, provided by *Brera Observatory*, Italy. The finished mould is intended to be used in the production of grazing incidence mirror shell segments.

$$z = \sqrt{24.9804968 \cdot (x + 20031.2295)} \tag{6.2}$$

$$z = \sqrt{1.001249025 \cdot (12.49024839 + x)^2 - x^2} \tag{6.3}$$

To manufacture the slumping moulds, their surfaces have to be defined in the Mould Coordinate system: the coordinate system with its origin in the centre of the clear aperture of the mould with the x- and z-axes rotated over the smallest angle such that the x-axis is perpendicular to the surface normal at the centre of the mould. The y-axis is perpendicular to the x- and z-axes following a right-handed convention.

Two MATLAB scripts have been created (see Appendix F) which generate the surfaces of revolution and do the coordinate system transformation. The output of the scripts is a `.CSV` file of a point cloud of the surface, which can be imported into the polishing machine's control software to create a surface design.

6.3.3 Validation

The surface design has been validated by creating a sag table in the control software of the polishing machine. This sag table was imported into MATLAB and the points were compared to the sag table provided by the optical designer, see Figure 6.3.2. The PV of the difference between the two was 144 nm for the paraboloid and 100 nm for the hyperboloid over the clear aperture. This error is several orders of magnitude smaller than the required positional accuracy of the polishing tool.

The created surface designs were used by *Zeeko* to successfully polish one parabolic and one

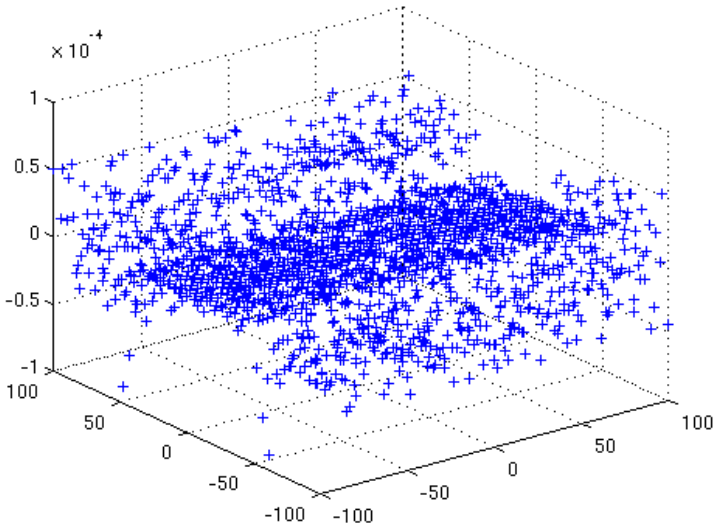

(a) Paraboloid

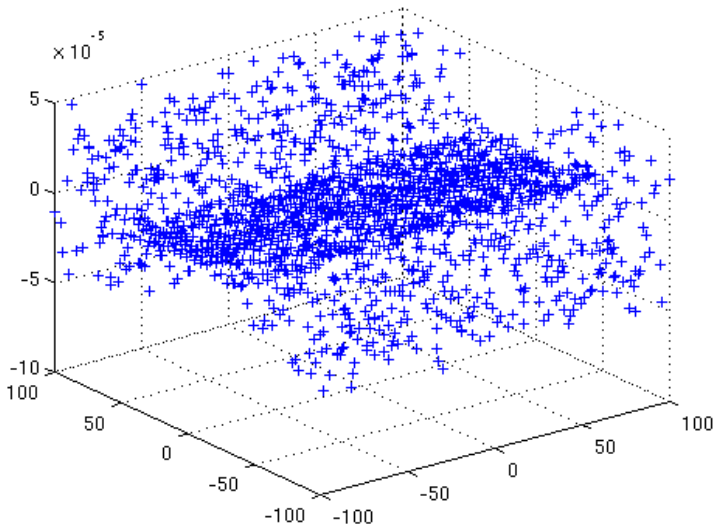

(b) Hyperboloid

Figure 6.3.2: Difference in sag between the IXO mould surface design and the sag table provided by the optical designer. All units in mm.

hyperbolic mould at *Zeeko*'s facility in Coalville and at *OpTIC*'s laboratory in St. Asaph, demonstrating the surface designs to be sufficiently accurate for polishing.

6.4 Conclusions

The creation of numerical surface representations, necessary for the creation of tool-paths, is investigated, for two test cases (E-ELT primary mirror segments and IXO segment slumping moulds). In the case of the E-ELT primary mirror segments several, compounding issues were identified regarding: 1. the coordinate transformation from the parent mirror to the segment coordinate frame and 2. the coordinates of the corners that define the boundary of the surface. These issues were corrected by the author and the consortium led by *OpTIC* was provided with software for the generation of surface designs for the seven E-ELT primary mirror prototype segments. Subsequently these surface designs have been used successfully to polishing prototype segments, certified by *ESO* to comply with the E-ELT primary mirror specifications. This in contrast to their main, and only, competitor. The author's contribution has been instrumental to meeting these demanding requirements.

It should be noted here that the investigation into the causes of the reported issues took significantly longer then resolving them. Especially in the case of compounding errors, it can be difficult to troubleshoot the problem from polishing results alone. Several tests, that have been used to analyse the problems, have been outlined in this chapter.

In the next chapter another potential source of poor convergence of successive, corrective polishing runs is investigated: the contact area of a conformal tool depends on how far is pressed onto the surface and poor convergence occurs, if this area is larger than the dimensions of the error features.

Moreover, photography has made it possible to fix these images and now provides us with a permanent record of each observed spectrum, which can be measured out at any time.

Pieter Zeeman

7

Spatial frequencies and corrective polishing

7.1 Introduction

In classical, craft polishing the tool travels many times over the surface along different paths with many crossings. This is in contrast to Computer Controlled Optical Surfacing (CCOS) introduced in the seventies of the last century where a sub-aperture processes traverses under computer control over the surface of the workpiece along a previously specified, non-crossing tool-path, see Chapter 1. As described in the same chapter, this may cause mid-spatial frequency errors on the surface of the workpiece, depending on the process and track spacing used, due to cusping. A good example of process-introduced, mid-spatial frequency errors is presented by Aikens et al. [156].

In CCOS, numerical surface error data is used to optimise the values of locally varied process parameters to improve surface form. Although in principle it is possible to optimise multiple process parameters, in practice only one parameter (usually the local dwell time of the process) is optimised due to computational constraints.

In recognition of this fact, the author has successfully adapted software of *Zeeko Ltd.* (used to calculate local dwell times and create instructions for polishing machines) to run on *HPC Wales* supercomputing hardware and take advantage of the large number of cores by making part of the code multi-threaded. Although this proved successful, as demonstrated by the fact that the resulting machine instructions were identical to those created by the original software on a standard desktop computer for a test-case, access to supercomputers is limited.

To optimise multiple process parameters on a standard personal computer, an alternative, two-staged approach is taken here. In the final stage, the dwell time of the process is optimised, as customary. But instead of requiring that all other process parameters pre-selected by the

operator, in the first stage another process parameter is optimised computationally. For conformal tools an obvious candidate for optimisation in the first stage is the size of the contact area between tool and surface. Due to the conformal nature of the tool, it is less effective at correcting mid-spatial frequency errors with periods comparable to the size of the contact area, as outlined in Chapter 2. Therefore, if a smaller contact area is used a larger range of mid-spatial frequencies can be corrected effectively. However, using a smaller contact area results in a lower removal rate and thus in a longer process time if the same removal is to be effectuated.

Standards for surface specification and tolerances, such as MIL-PRF-1383 and ISO10110, discuss surface form tolerances but have no provisions for mid-spatial frequency errors despite the fact that they can lower the optical performance of a system [157]. Even if a surface is fabricated within specified tolerances according to one of the mentioned standards, the optical performance may be inadequate for the desired application due to being finished by using a small, sub-aperture tool [158].

The tolerance on surface misfigure is commonly given in peak-to-valley (PV) or root mean square (rms). For the specification of the tolerance on mid-spatial frequency errors several other characteristics have been proposed, e.g. power spectral density (PSD) [158], surface slope error [157] and structure function [159].

7.1.1 Power spectral density

The Fourier transform is a useful tool to analyse the frequency content of a given signal. The power spectral density (PSD), based on the Fourier transform, gives the contribution to the (squared) rms of the surface error per spatial frequency and a bounding function can be used to specify a (peak) tolerance for all spatial frequencies or to specify a limit on the rms found by integrating the PSD curve for different ranges of the spatial frequency [158].

A surface has two principal directions and periodicity is expressed in spatial frequencies in each direction. The PSD bounding function is defined as a 1D function however, as, in general, the orientation of the periodicity is not the limiting factor in the optical performance of the surface. There are several options to evaluate a given surface against a 1D PSD bounding function.

Power spectral density along a profile

One or more 1D profiles can be taken of the surface error (e.g. by using a tactile measurement device or by extracting a profile from a 2D surface error height map) which are each evaluated individually or the PSDs of the profiles are averaged and compared against the bounding function. Special care has to be taken to define the location of the profile(s) to make sure they form a statistically representative subset of the whole surface.

Integration of a two-dimensional power spectral density

The power spectral density (PSD) can be calculated for a 2D surface error map and then integrated either azimuthally [160] or in one spatial direction [161] to obtain a 1D PSD. Again,

special care has to be taken to select the appropriate integration and in case of the latter the appropriate orientation.

Whatever method is used to arrive at the 1D representation, it is impossible to identify where on the surface these periodic signals are present. Furthermore, due to the reduction in dimension, multiple surface error height maps can have the same 1D PSD representation. As such, the PSD data can not be directly linked to the manufacturing process and the operator needs to interpret the data with the objective of improving the manufacturing process.

7.1.2 Surface slope error

According to Kumler et al. [157] the slope error of an optical surface may be specified in different units:

- Waves per centimetre
- Waves per inch
- Radians, milliradians or microradians
- Degrees

and each of these has to be evaluated over the whole clear aperture to obtain a peak or rms value.

The spatial sampling used to measure the surface of the workpiece and any filtering applied, for instance to remove dust or defects from the measurement, have a strong influence on the slope measurement [157].

As the surface slope error characterises the surface in 2D, there is a direct link between the two. Problematic zones that cause the optic to exceed specified tolerance can be identified and localised. However, two different surface errors may result in the same maximum slope error. Take for instance the two periodic errors defined by $a \sin 2ax$ and $2a \sin ax$, both of which have a maximum gradient of $3a$. The value of the surface slope error at a point on the surface is not conclusive to determine the full characteristics of the error. For instance, as discussed above, knowledge of the spatial frequency of the error is highly relevant for selection of the size of the contact area, when a conformal tool is applied in the manufacturing process. Therefore, the operator needs to further analyse and interpret the surface slope error data, and potentially combine it with other information, in order to decide what process to apply next and which parameters to use.

7.1.3 Structure function

The structure function (SF), $S_h(r)$, for surface a height map, h, is the rms height difference for points a distance r apart [159]. Under the assumptions that h has a zero mean (surfaces with the Zernike piston term removed) and the surface irregularities are sufficiently small,

$$S_h^2(r) = 2\left(h_{RMS}^2 - \Re_{hh}(r)\right) \tag{7.1}$$

with h_{RMS} the rms value of the height map [159]. The autocorrelation function, $\Re_{hh}(r)$, determines its limiting behaviours:

$$S_h(0) = 0 \tag{7.2}$$

$$S_h(r \to \infty) = \sqrt{2}\, h_{RMS} \tag{7.3}$$

and the rms gradient of the height map is equal to the slope of the SF at origin

$$S'_h(0) = \frac{(\nabla h)_{RMS}}{\sqrt{2}} \tag{7.4}$$

and because the autocorrelation function oscillates with the same spatial period if the height map contains a periodic signal, so does the SF [159].

The SF represents a surface map in the 1D spatial frequency domain and it can be used to specify a tolerance on a range of spatial scales, Δr, between r_1 and r_2 [159]:

$$h_{RMS}(\Delta r) = \frac{S_h(r_2) - S_h(r_1)}{\sqrt{2}} \tag{7.5}$$

However because of the 1D representation it is impossible to identify where on the surface these periodic signals are present or what orientation they have. For instance Zhelem [159] presents an example of two surface error height maps, one radial periodic and one periodic in one dimension, for which the SF is equal.

7.1.4 Summary

Mid-spatial frequencies can have a detrimental effect on the optical performance of an optical surface even if the surface conforms to the specified tolerances using industry standards. Several surface characteristics have been proposed that analyse the spatial frequency content of the surface misfigure and allow tolerances to be specified. Although these characteristics allow a straightforward evaluation of the compliance of the surface to the specifications they offer the manufacturer limited information on how to remedy any non-compliance and an in-depth analysis is necessary.

7.2 Conformal tools and mid-spatial frequency errors

As discussed in Chapter 2 a CCOS process applying a conformal polishing tool (e.g. the Precessions™ process) is well suited to correct surface errors that are larger in size than the contact area between tool and surface by applying a different dwell time as needed. However, due to the conformal nature of the tool it has no significant effect on surface errors with similar or smaller dimensions: the peaks and valleys of the error will be polished equally, see Figure 2.1.4.

To remove these smaller dimension errors with a bonnet tool the process parameters have to be set such that the contact area is sufficiently small (e.g. by using a smaller bonnet or by

pressing it into the surface less). Fähnle et al. [162] have used the PSD to analyse the spatial frequency content of two influence functions made with differently sized contact areas (using the FJP process with different nozzle diameters, but the procedure can be applied to any conformal polishing process) and found that the smaller influence function indeed has a higher cut-off frequency in the PSD meaning it can be used to deterministically correct surface errors with higher spatial frequency content.

Although this analysis using the PSD allows an informed selection of the size of the contact area for processing the complete surface, a balance has to be found between the expected resulting surface misfigure and total process time as the smaller contact area leads to a smaller removal rate.

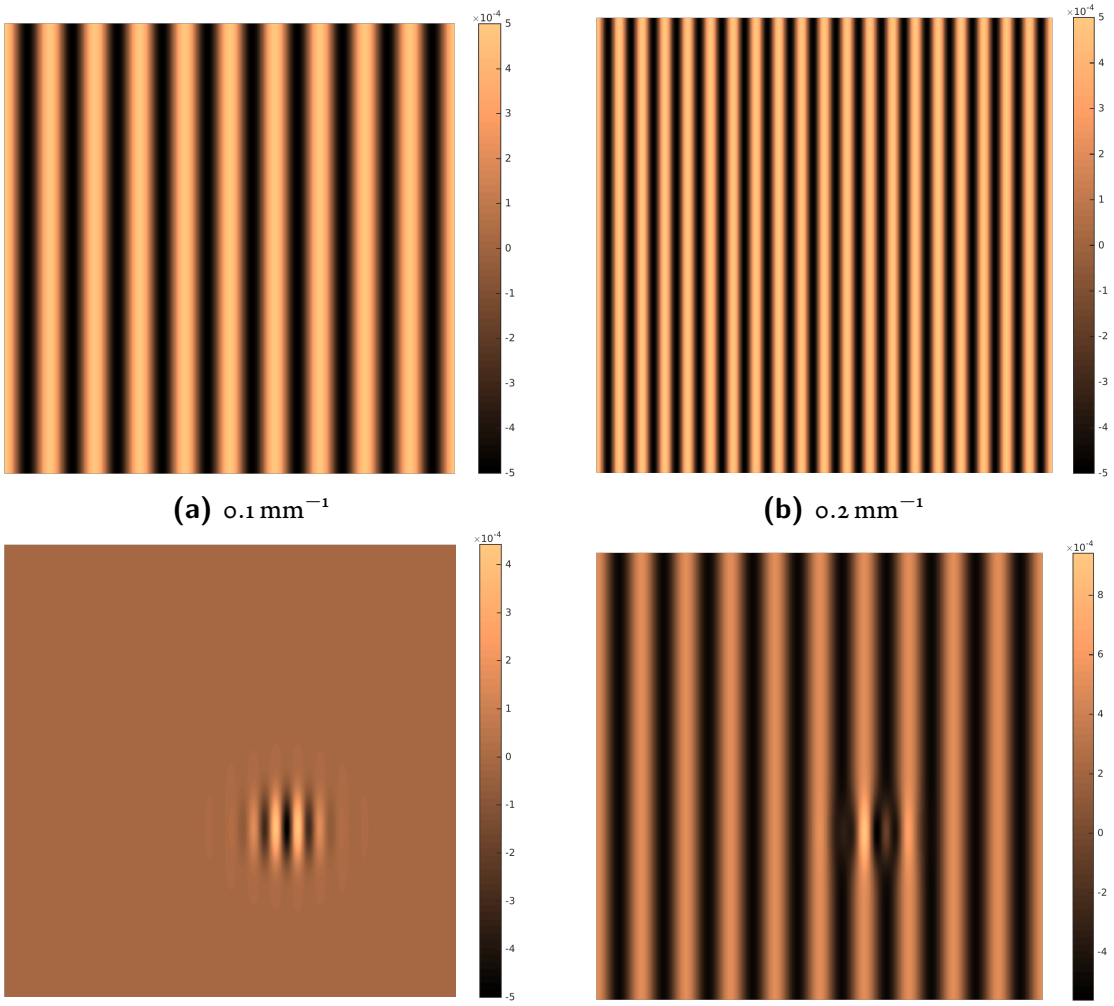

(a) 0.1 mm^{-1} **(b)** 0.2 mm^{-1}

(c) Windowed 0.2 mm^{-1} **(d)** 0.1 min^{-1} and windowed 0.2 mm^{-1}

Figure 7.2.1: Several full-aperture (100 × 100 mm^2) and sub-apeture (Gaussian window with a standard deviation of 5 mm) periodic example inputs to PSD analysis.

As mentioned previously care has to be taken when the 2D surface data is reduced to a 1D PSD as relevant information may be lost. This is exemplified by taking the PSDs of the inputs of Figure 7.2.1 in the x- and y-direction, which are shown in Figures 7.2.2 and 7.2.3 respectively. As

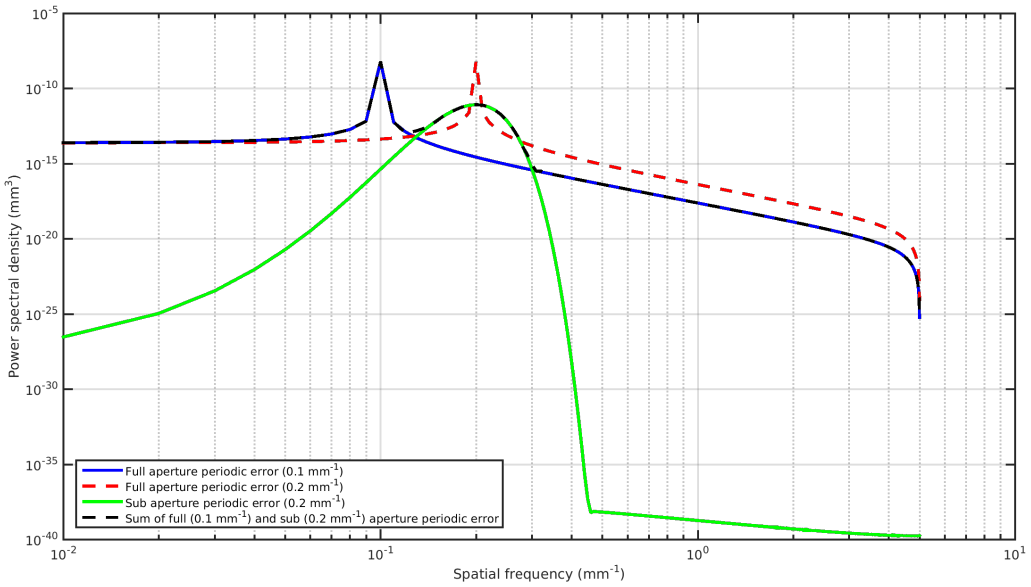

Figure 7.2.2: Graph showing the x-direction averaged PSDs of the inputs of Figure 7.2.1.

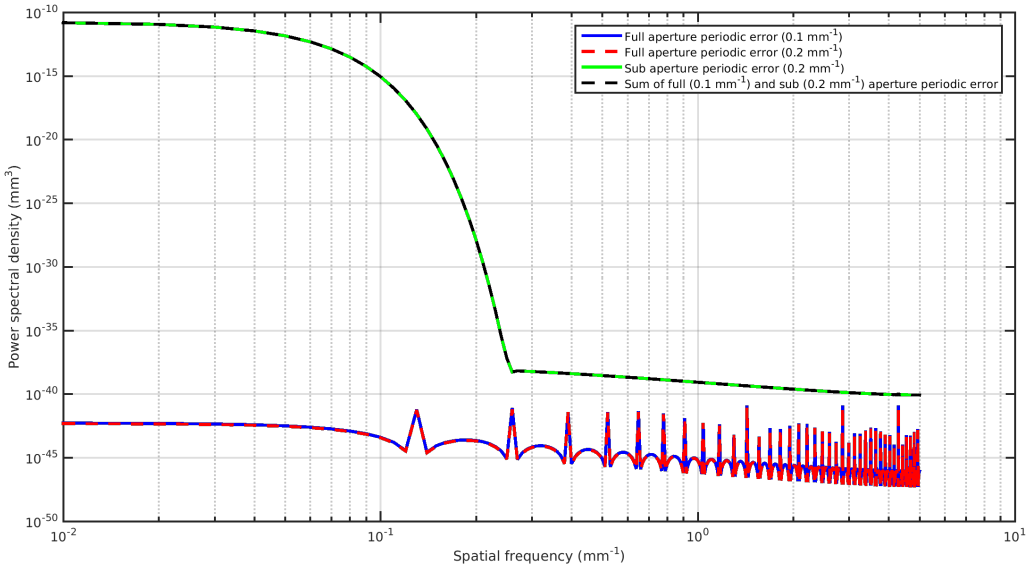

Figure 7.2.3: Graph showing the y-direction averaged PSDs of the inputs of Figure 7.2.1.

the signals are periodic in the x-direction the PSDs in the y-direction do not provide any information of the periodic signals.

Furthermore the PSD is not well suited to identify a periodic sub-aperture signal. The full-aperture periodic inputs each produce a clear peak in the x-direction PSDs but the sub-aperture response is spread out due to the convolution with the response of the window function in the frequency domain. The smaller the sub-aperture the more the response is spread out and it can easily become unidentifiable if other responses are present (e.g. from other sub-aperture periodic signals or noise).

For the reasons outlined above it would be beneficial to analyse the surface error height map in both the spatial and frequency domains simultaneously. Especially in the case of the application of conformal tools where the spot size is controlled by the tool offset, which would allow a dynamic spot size during processing of the surface. This means that a small spot size can be applied there on the surface and only there where high spatial frequencies are present while applying a larger spot size and associated larger removal rate elsewhere to reduce process time.

7.3 Space-frequency analysis

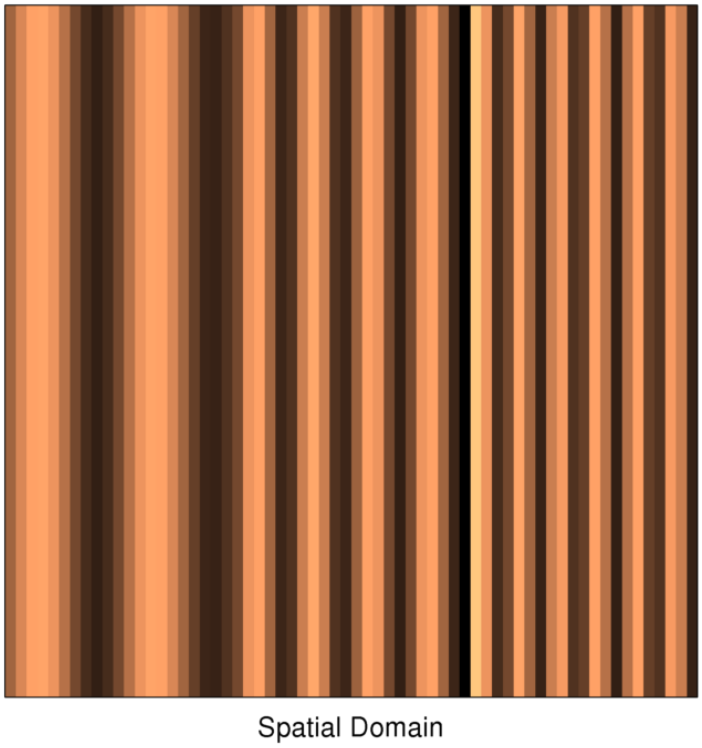

Figure 7.3.1: Graph showing an example of a 1D signal consisting of three roughly equal length sections, each a sine wave of different spatial frequency, and half a period of a sine wave at the Nyquist frequency between the 2nd and 3rd sections with 1.5 times the amplitude of the other signals, whose amplitudes are equal. The signal is represented colour coded: the darker the lower the signal value and visa versa.

To demonstrate the analysis in both the spatial and frequency domains simultaneously a 1D spatial signal is considered. The conclusions are valid for 2D signals as well but difficult to

present in this format. The signal consists of three roughly equal length sections. In each section the signal is a sine wave with a different spatial frequency for each section and in between the 2nd and 3rd sections a short, half period of a sine wave at the Nyquist frequency is inserted of 1.5 times the amplitude of the other signals, whose amplitudes are equal.

In Figure 7.3.1 the signal is represented colour coded: darker colours represent lower values of the signal, and lighter colours represent higher values.

7.3.1 Discrete Fourier Transform

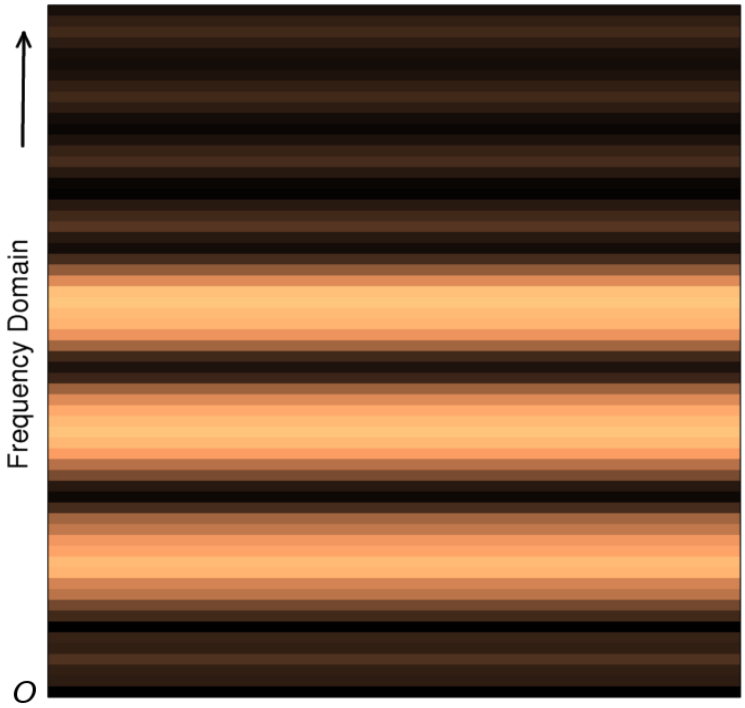

Figure 7.3.2: Graph showing the spectrum of the 1D signal shown in Figure 7.3.1, similarily colour coded as Figure 7.3.1.

The Discrete Fourier Transform (DFT) of the signal is shown in Figure 7.3.2, colour coded in the same way as the signal. The three peaks representing the frequencies of the three sections are clearly shown, but the signal at the Nyquist frequency is too short to be identified in the spectrum of the signal. The spectrum is only defined in the frequency domain and therefore does not provide any spatial information and thus the graph does not vary in the spatial domain.

7.3.2 Discrete Windowed Fourier Transform

The Discrete Windowed Fourier Transform (DWFT) splits the signal in equally sized chunks (by windowing) and applies the DFT to each chunk individually creating a set of successive spectra called a spectrogram. More discrete signal elements in each chunk results in more "bins" in the frequency domain but at the same time number of spectra in the spatial domain is reduced as the signal is split in less chunks due to their increased size. An example spectrogram

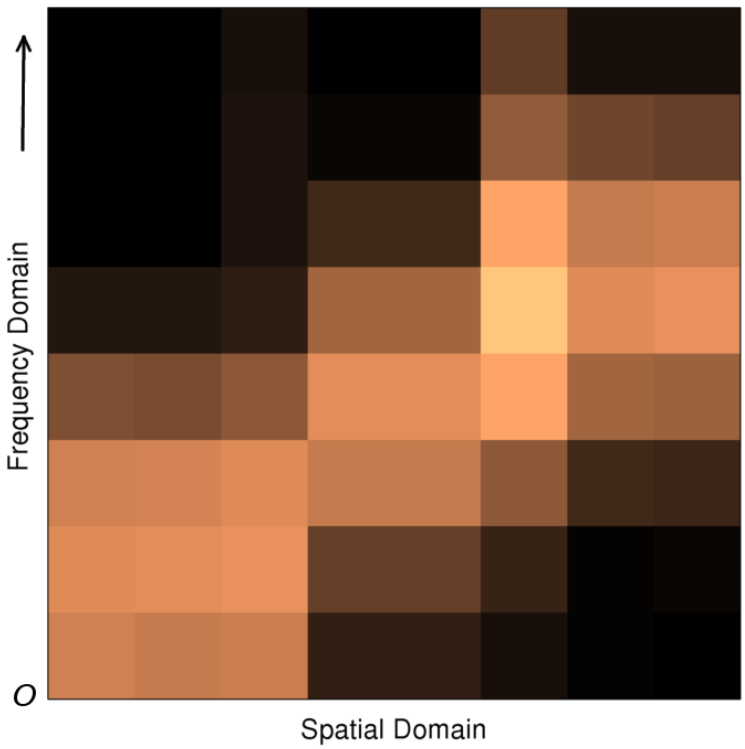

Figure 7.3.3: Graph showing the spectrogram of the signal shown in Figure 7.3.1 and similarily colour coded.

is shown in Figure 7.3.3 with a chunk size chosen to result in the same number of "bins" in the frequency domain as the number of spectra in the spatial domain and thus the graph varies in both the frequency as the spatial domain. The fact that one has to trade-off the resolution in the frequency domain with the resolution in the spatial domain to prevent interference is known as the uncertainty principle of signal processing [163]. From an information theory point of view this can be clarified by considering that the number of independent discrete samples in the whole spectrogram can not exceed the number of discrete samples in the original signal. The analogy from quantum mechanics is that wave packets containing a larger spread of frequencies occupy a smaller area of space which leads to the Heisenberg uncertainty principle.

Figure 7.3.3 clearly shows that the signal has a different frequency in the three different sections and the short signal at the Nyquist frequency has an effect on the spectrogram but can not be clearly identified. A drawback of the Discrete Windowed Fourier Transform is that the window size is fixed for the whole of the spectrogram. To localise the short Nyquist frequency signal in the example one would want to use a short window function but to accurately estimate the frequencies in the three sections one would want to use a much larger chunk size.

7.3.3 Discrete Wavelet Transform

The basis of the Fourier transform is formed by sine functions, which are not localised but extend from minus infinity to plus infinity. Instead, the Discrete Wavelet Transform (DWT) has a basis that consists of scaled and translated versions of an undulating function, called the mother wavelet, that is localised in both the frequency as well as the spatial domain. An example of such an undulating function is the Haar wavelet defined by

$$\psi(x) = \begin{cases} 1 & 0 \leq x < 1/2, \\ -1 & 1/2 \leq x < 1, \\ 0 & \text{otherwise.} \end{cases} \tag{7.6}$$

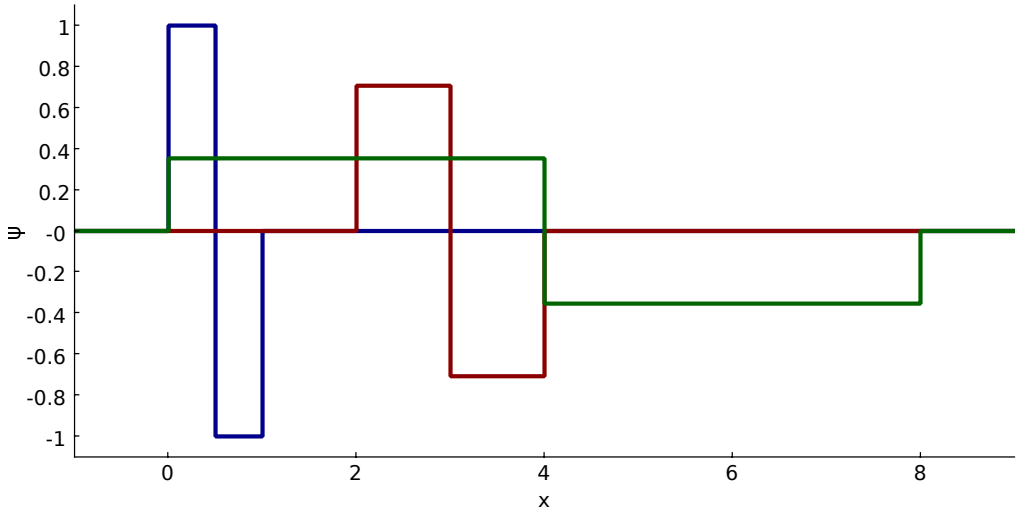

Figure 7.3.4: Graph showing the Haar mother wavelet ($\psi(x)$ in blue) and scaled and translated versions thereof ($\psi_{1,1}(x)$ in red and $\psi_{3,0}(x)$ in green).

and scaled (by parameter m) and translated (by parameter n) versions of it are produced by

$$\psi_{m,n}(x) = 2^{-m/2}\psi(2^{-m}x - n) \tag{7.7}$$

and it can be shown that this family of scaled and translated Haar wavelets are orthonormal [164] and the DWT of a signal, $f(x)$, is obtained by

$$\left[W_\psi f\right](m,n) = 2^{-m/2} \int_{-\infty}^{\infty} f(x)\, \psi(2^{-m}x - n)\, \mathrm{d}x \tag{7.8}$$

As an example the wavelet transform using the Haar wavelet of the signal from Figure 7.3.1 is shown in Figure 7.3.5. The frequency domain is represented by the scale parameter, m, of the wavelet. Each step in scale reduces the "frequency" by a factor 2 and enlarges the width of the wavelet by a factor 2 or visa versa. This leads the high frequencies to be well localised in the spatial domain and good localisation of the low frequencies in the frequency domain, as can be seen from Figure 7.3.5. This property of the discrete wavelet transform is desirable for the analysis of surface error height maps to accurately target the peaks of "fast" changing errors. If the peaks are missed the valleys are deepened, exacerbating the misfigure, and for higher spatial frequency errors the peaks and valleys are closer together. In Figure 7.3.5 the short signal at the Nyquist frequency can be clearly identified and localised. It is possible to identify and localise the three other signals but not as clear in the DWFT spectrogram.

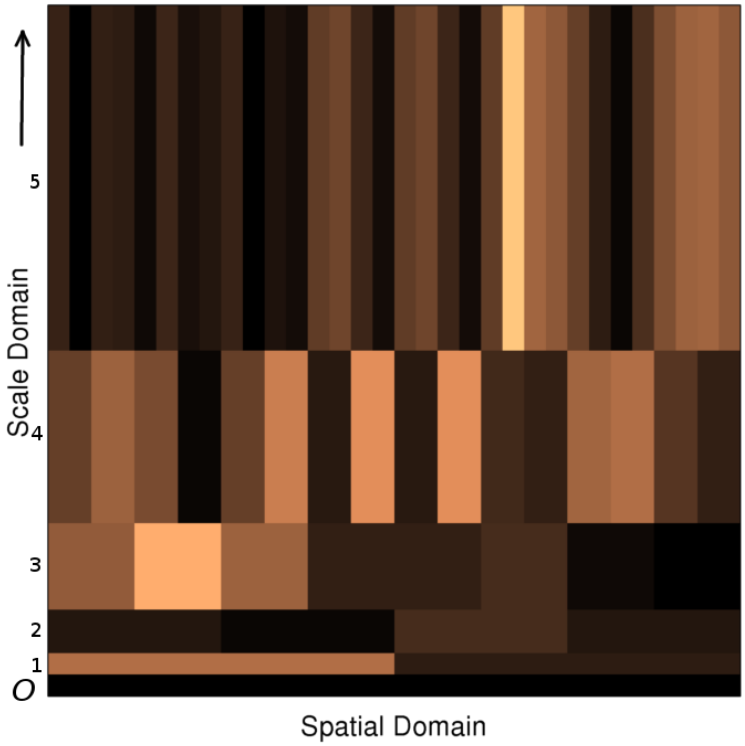

Figure 7.3.5: Graph showing the wavelet transform of the signal shown in Figure 7.3.1 using the Haar wavelet. Similarily colour coded as previous figures.

It needs to be stressed that "frequency" in the context of the wavelet transform is somewhat misleading as the signal is not compared to a sine function of a certain frequency. Instead the wavelet transform shows how well the signal compares to a scaled version of a mother wavelet and a variety of different mother wavelets have been developed with different shapes, properties and applications [164–167]. Furthermore it should be noted that the scale of the highest "frequency" of the wavelet is often referred to in literature as "Level 1" with subsequent scales numbered incrementally due to way the discrete wavelet transform is implemented [168]. In that case higher scale "levels" represent lower frequencies of the signal. In this chapter a different convention has been adopted: the scales used in the decomposition of the signal are numbered incrementally from low to high "frequency" starting from scale "1" with the residual, lower-order components labelled as scale "0".

7.4 Dynamic spot size selection using the DWT

It follows from the previous that the DWT is a good candidate for the analysis of the spatial frequency content of surface error height maps with the objective of automatically selecting which spot size, and therefore what tool offset, to use where on the surface. Before the DWT can be applied a mother wavelet has to be chosen as mentioned in the previous section. Because the objective is to assign dynamic tool offsets a mother wavelet should be chosen whose DWT differentiates maximally between the influence functions generated by these different tool offsets.

7.4.1 Evaluation of mother wavelets

From Walker et. al [64] it is known that the influence functions of *Zeeko*'s Precessions™ bonnet polishing process are near-Gaussian. Gaussian influence functions of different diameters have been generated in MATLAB and analysed using different mother wavelets.

To compare the performance of the different mother wavelets in differentiating between the influence functions a figure of merit is introduced. First, for each influence function the energy distribution over the different wavelet scales is calculated. Next, for each scale the variance of the energy distributions is computed. The figure of merit is then defined as the sum of the variances at the different scales.

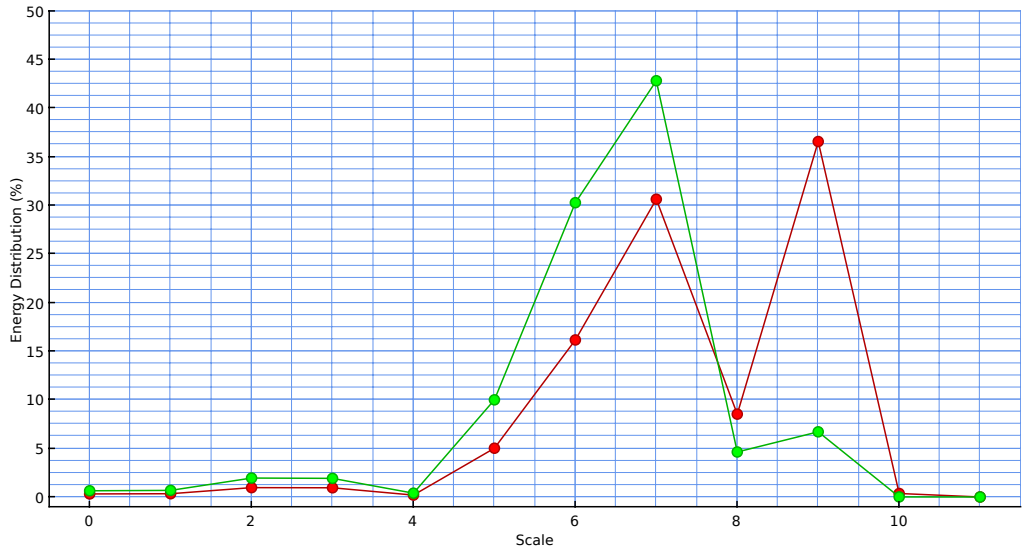

Figure 7.4.1: Graph showing the energy distribution of the DWT based on the reverse biorthogonal [164] 3.9 mother wavelet for two influence functions of spot size 14.95 mm (in red) and 21.12 mm (in green).

This procedure is demonstrated using two simulated influence functions of equal amplitude and different spot sizes (equal to 4 standard deviations of a Gaussian distribution): 14.95 mm and 21.12 mm, which correspond to the spot sizes of an R80 bonnet using a tool offset of 0.35 mm and 0.70 mm respectively.

The figures of merit for different mother wavelets are shown in Figure 7.4.2 for the two simulated influence functions mentioned previously. According to the introduced figure-of-merit the reverse biorthogonal [164] 3.9 mother wavelet is best able to differentiate between the two influence functions. An example of a mother wavelet that has poor capability of differentiating between the two simulated influence functions is the Haar wavelet. Both simulated influence functions have a peak in the energy distribution, shown in Figure 7.4.3, at the same scale level, making them difficult to distinguish.

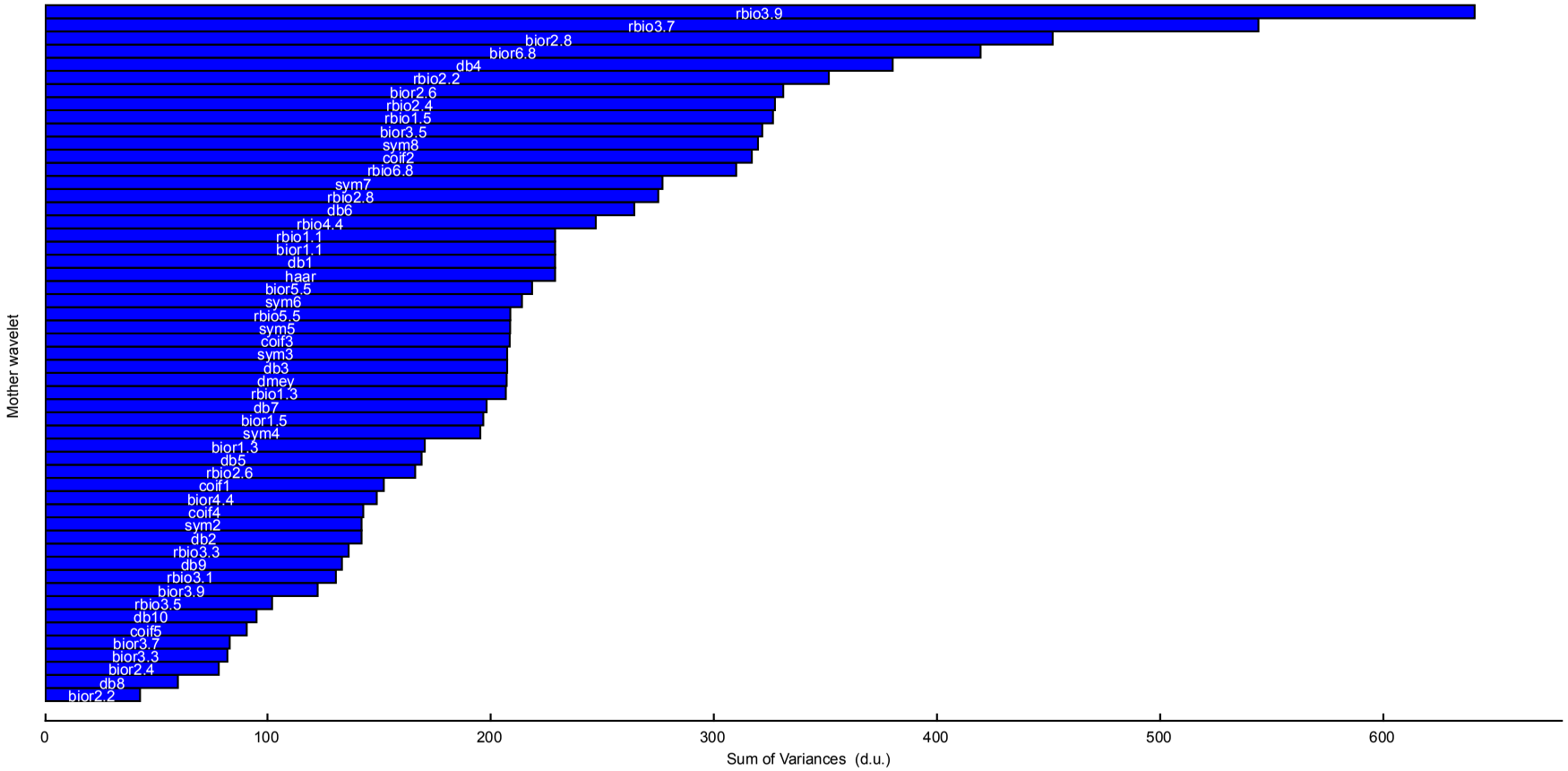

Figure 7.4.2: Graph showing the figures of merit of different mother wavelets for two influence functions of spot size 14.95 mm and 21.12 mm.

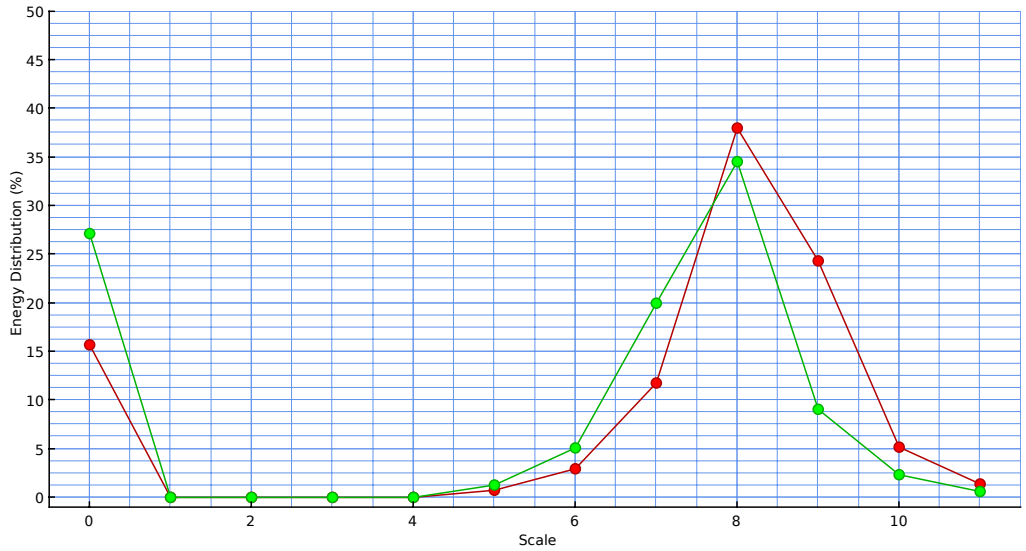

Figure 7.4.3: Graph showing the energy distribution of the DWT based on the Haar mother wavelet for two influence functions of spot size 14.95 mm (in red) and 21.12 mm (in green).

7.4.2 Simulations

To correctively polish an optical surface using CCOS the dwell times of the process have to be calculated, as outlined in Chapter 1. To this end *Zeeko* provides a software packaged called "Precessions". This software takes as an input a design of the surface that is to be corrected, the path of the tool over that surface, the current surface error and the influence function of the tool. The output is a map of the dwell times and the predicted residual errors on the surface after the process is run using the calculated dwell times. The software optimises the dwell times minimising the predicted residual surface error.

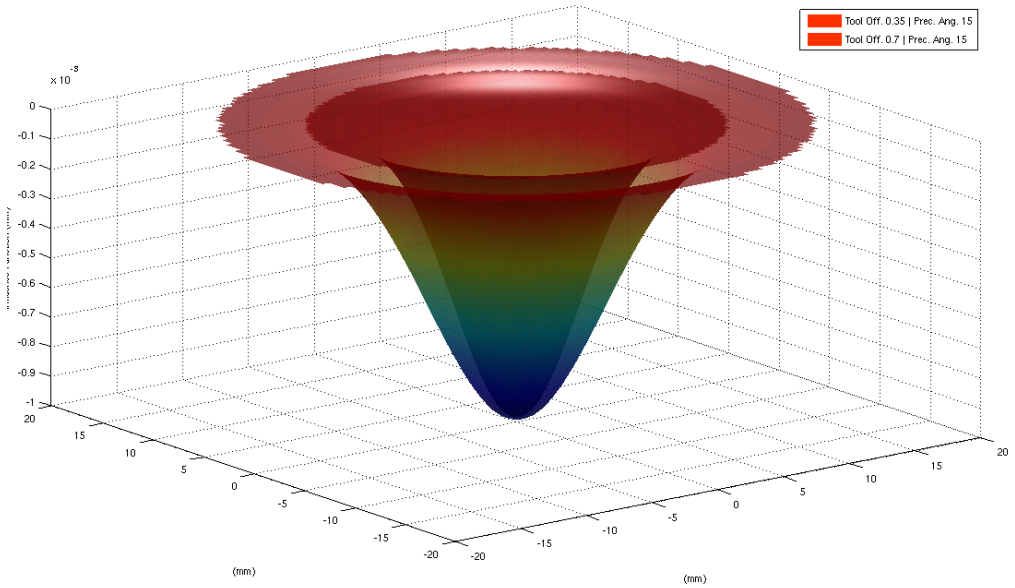

Figure 7.4.4: Screenshot of the Precessions software showing an imported set of influence functions of spot sizes 14.95 mm and 21.12 mm.

If a set of influence functions is imported into the Precessions software, as shown in

Figure 7.4.4, a map has to be provided that specifies which influence function has to be applied where on the surface because the software is not capable of automatically selecting which influence function to use while minimising the predicted residual surface error.

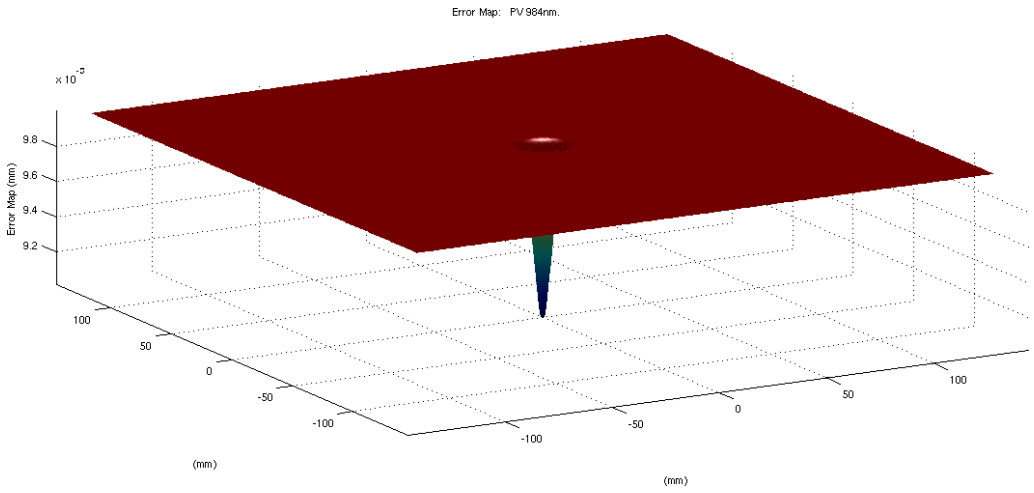

Figure 7.4.5: Screenshot of the Precessions software showing a simulated error map of a simulated influence function of spot size 14.95 mm in an otherwise error free surface.

Software has been written by the author in MATLAB to create a map that optimises the tool offset as a function of the location on the surface based on the DWT analysis of the surface error. This constitutes the first stage of the two stage optimisation approach, as discussed previously. To test this procedure a simulated 250 × 250 mm² surface error height map has been generated consisting of a simulated influence functions of spot size 14.95 mm with a depth of approximately 1 µm in an otherwise uniform error of 10 µm. The simulated surface error height map is shown in Figure 7.4.5. This error map is chosen because it has high spatial frequency components that are difficult to correct with the larger influence function. At the same time low spatial frequency components occupy a large area of the surface which would take longer to correct with the smaller influence function than with the larger influence function.

In Figure 7.4.6 a graph is depicted of this software showing the imported bonnet offset map optimised by DWT analysis of the simulated error map of Figure 7.4.5 using the reverse biorthogonal 3.9 mother wavelet. The calculated tool offset map was subsequently imported into a software package called "Precessions", supplied by *Zeeko* to calculate dwell times from surface error data.

In the second stage of the two stage optimisation, the "Precessions" software was used to calculate the dwell time map and the predicted residual error using the two simulated influence functions and the offset map generated by the DWT analysis of the simulated error map. To provide a baseline the dwell time map and predicted residual error have also been calculated for each of the influence functions individually when they are uniformly applied to the surface, which is the standard method of corrective polishing.

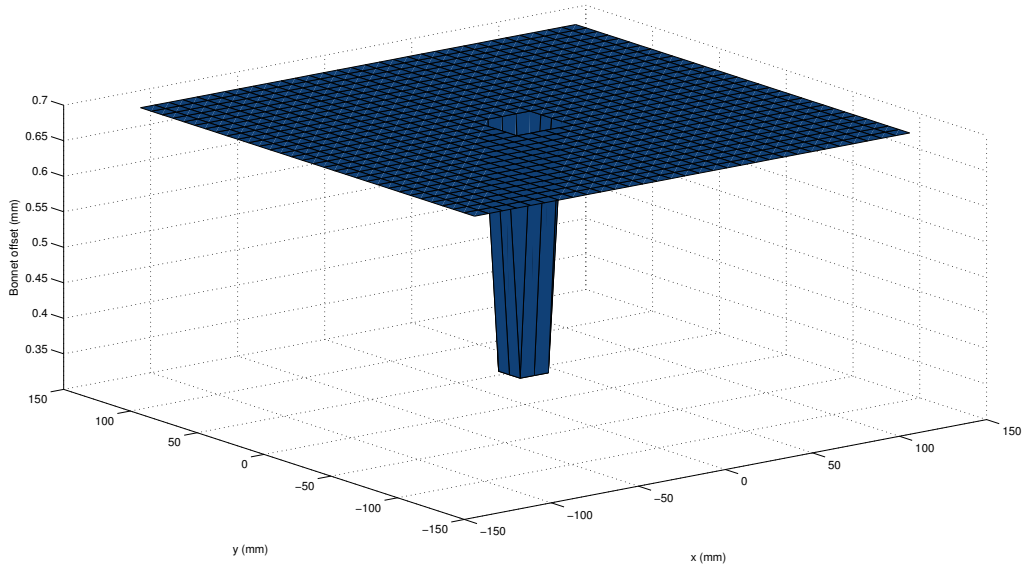

Figure 7.4.6: Graph showing the calculated bonnet offset map by DWT analysis of the simulated error map of Figure 7.4.5 using the reverse biorthogonal 3.9 mother wavelet.

Table 7.4.1: Simulated results of polishing using two tool offsets, either using one of the two offsets over the complete area or dynamic application of either offsets based on analysis of the error map using the reverse biorthogonal wavelet 3.9.

Tool offset	Process time	Residual PV	PV Reduction
before	N/A	984 nm	
0.35 mm	8006 min	122 nm	88 %
0.70 mm	4050 min	344 nm	65 %
dynamic	4071 min	195 nm	80 %

7.4.3 Results and discussion

The results of the simulations using the Precessions software outlined in the previous section are summarised in Table 7.4.1. As expected the fastest correction is achieved by applying the largest spot size uniformly, however the PV of the expected residual surface error is the largest. The smallest PV of the expected residual surface error is achieved by uniformly applying the smallest spot size, but as the removal rate of this smaller influence function is much lower this results in the longest process time. The results of the dynamic application of both spot sizes over the course of the polishing run lie in between those two extremes but close to the best results for both the total process time as well as the predicted residual surface error.

7.5 Conclusion

In general, due to computational constraints, only the values of a single process parameter are automatically optimised to be used in CCOS while the others are kept constant. Usually the dwell times are optimised. Although it would be possible to make use of supercomputers for the multi-dimensional optimisation of process parameters, in this chapter an alternative, two staged approach is taken. First the spot sizes to be used along the tool-path are calculated. Next, the dwell times to be used in combination with the calculated spot sizes are optimised to minimise the expected residual surface errors. This two staged approach can be performed on a standard personal computer in a couple of minutes.

The dynamic application of different spot sizes over the course of a polishing run, based on the automated analysis of spatial frequency content of surface error height maps by applying the discrete wavelet transform, results in near optimal performance with regards to both the total polishing time as well as the residual surface errors, at least for the test-case presented here. The dynamic application of spot sizes potentially allows the best of both worlds: the high removal rate of a large spot size and the capability of correcting high spatial frequency errors of a small spot size. Current state-of-the-art does not allow the automated selection of spot sizes.

The work outlined in this chapter serves as a proof-of-concept of the application of automatically selected, dynamic spot sizes. In the following several ideas for future research are presented.

Two directions of future research are obvious. Firstly, the replication of the results using actual polishing data, generating and measuring influence functions, and applying the resulting polishing run on an actual workpiece and evaluating the result. Although it must be noted that the predictive software applied is regularly used by customers of *Zeeko* to produce high quality optics. This provides confidence in the predictive capability of the software. Secondly, the inclusion of more spot sizes in the procedure to expand the binary choice presented here.

In the discrete wavelet transform the trade-off between localisation in both the frequency and spatial domains is fixed: high frequency signals are well localised in the spatial domain but not in the frequency domain and visa versa. By using the continuous wavelet transform or wavelet packets the trade-off can be selected as desired but care has to be taken that a orthogonal base is

formed.

Several shift-invariant alternatives to the (shift-variant) DWT are available [169], among others the dual tree complex wavelet transform (DTCWT).

In this chapter the tool offsets to be used on the surface are specified on a rectangular, equidistant grid due to the ease of implementation. If they are specified along contour lines of the offset map they provide a better distribution for the same number of points.

As outlined in Chapter 1 it is possible to use a larger track spacing for larger spot sizes before significant cusping occurs than if a smaller spot size is used. For the current industry standard of polishing with a uniform spot size everywhere on the surface the track spacing is also constant over the whole surface. When applying a dynamic spot size a further reduction of the total process time and residual surface misfigure may be achieved by allowing a dynamic track spacing as well, larger where a larger spot size is used and visa versa. The tool-path will then no longer look like a regular raster but more like an interferogram, with high track density in areas with high surface slopes and low track density in areas of low slope.

Further research is required before dynamic spot size calculation through spatial-frequency analysis of surface misfigure is a fully-fledged part of CCOS, but it has the potential of achieving previously unavailable combinations of total process time and residual surface error. Furthermore, it offers a significant step towards further automation of the polishing process.

Доверяй, но проверяй. (Translated from Russian: "Trust, but verify.")

Ronald Reagan

8 Conclusion

Moore's law, predicting a doubling of transistor count per microprocessor every two years, remains valid, demonstrating exponential growth of computing power. This led to the introduction of numerical machine control enabling a completely new discipline of optical fabrication technologies. In Computer Controlled Optical Surfacing (CCOS) a small, sub-aperture process is traversed over the surface of the optic. This thesis has provided a review of several of these sub-aperture processes. In CCOS, numerical surface error data is used to optimise locally varying process parameters to improve surface form. Although in principle it is possible to optimise multiple process parameters along the tool-path, in practice only one (usually the local dwell time of the process) is optimised due to computational constraints. A small inroad into the application of supercomputers to CCOS has been made by successfully adapting software of *Zeeko Ltd.* (used to create instructions for polishing machines) to run multi-threaded on *HPC Wales* hardware.

In the traditional manufacture of optics the resulting surface quality depends on the skills and experience of the craftsman. To a certain but lesser extend this is also true for CCOS. Although the dwell time is optimised to minimise the resulting surface misfigure, the operator has to select many other parameters (e.g. tool size, distance between tool-path tracks, abrasive compound and particle size). These other parameters can also have a direct influence on the resulting surface form accuracy. This thesis has examined the application of numerical methods to understand these sub-aperture processes better and where possible to provide automatic selection of these parameters.

Rigid tools are well suited to smooth mid-spatial frequency errors, introduced by previous processing steps, and larger tools show a better performance in this regard. However their rigidity leads to a mismatch between the surfaces of tool and aspheric or freeform workpieces,

and this mismatch increases with the size of the tool. A novel, numerical method has been introduced to analyse the mismatch qualitatively and quantitatively, with the advantage that it can readily be applied to aspheric or free-form surfaces, for which an analytical approach is difficult or impossible. As a rule-of-thumb, the errors produced on a surface due to the mismatch of a rigid tool are negligible if the mismatch is smaller than size of the abrasive particle used in the process. Therefore, the numerical analysis introduced here provides a maximal allowable tool size.

The removal properties of rigid, sub-aperture tools change when they hang over the edge of a workpiece. A numerical model has been introduced that simulates the tool and workpiece as separate entities and models the contact between them, as opposed to the non-contact, single entity model reported on in the literature. This allows the modelling of a hinged, rigid tool as well as the modelling of mismatch between tool and workpiece. The numerical simulations are partly conformant to the validation experiments that have been performed, with observed discrepancies, potentially due to a mismatch between the tool and workpiece in the experiments.

Segmented optics such as the primary mirror of the European Extremely Large Telescope (E-ELT) have a surface specification up to the physical edge of the segments. Many processes encounter difficulties (e.g. unstable removal properties) when dealing with the edge of an optic, making this a highly challenging task. Two processes are evaluated with regards to their suitability to correct edges of E-ELT segments: the application of small, inflatable bonnet tools and Fluid Jet Polishing (FJP). During the investigation of the former a novel type of tool-path, newly developed by *Zeeko Ltd.*, was tested experimentally for the first time and evaluated by the present author. This tool-path, created by solving a partial differential equation numerically, allows the polishing of the edge zone alone and leaves the bulk area untreated. For an E-ELT primary mirror prototype segment the processed area in that case is approximately 3 % of the total surface area, reducing both the total process time and tool wear. Experiments have been performed to show it is possible to prevent the creation of a discontinuity in the optical surface at the boundary between the processed and the untreated area. An experimental FJP set-up has been built at *Chubu University*, Japan, and a variety of abrasive slurries were tested on binderless tungsten carbide. Continuation of the work by *Chubu University* has been critically assessed and an alternative hypothesis has been presented by the current author. Furthermore, even though the numerical simulations of fluid dynamics and particle impact were not performed by the author, it supports the hypothesis that it would be extremely difficult to design and optimise FJP systems by purely experimental means.

The author provided the consortium led by *OpTIC* with the surface designs for seven E-ELT primary mirror prototype segment. The consortium has used these subsequently to polishing three E-ELT prototype segments. These have been, in contrast to their main (and only) competitor, certified by *ESO* to comply with the E-ELT primary mirror specifications. The author's contribution has been instrumental to meeting these demanding requirements.

Conformal tools adapt to the local surface form and are therefore not hindered by tool mismatch. However, they are ill-suited to correct surface errors with dimensions smaller than

the contact area between tool and workpiece. A method with considerable potential is developed to analyse the spatial frequency content of surface misfigure data. The result of this analysis is used to change the size of the contact area during a process run dynamically, as opposed to the constant-sized contact area that is state-of-the-art. This allows the automated optimisation of two process parameters along the tool-path, without having to resort to the use of supercomputers to overcome the computational constraints, as outlined in the first paragraph of this conclusion. A proof-of-concept has been presented of a two staged optimisation of both spot sizes and dwell times, which can be performed on standard personal computer hardware.

Some suggestions are offered to further improve the method of spatial frequency analysis and further research is recommended. Although the two staged approach shows ample promise, the software routines for supercomputers could be further developed to perform the optimisation of interacting process parameters or could be applied to cases requiring large datasets. Further research is also suggested to better understand the different effects of rigid tools. Specifically to understand their behaviour when hanging over the edge of a workpiece or when a mismatch exists between the surface of the tool and that of the workpiece. A new area of research, using numerical methods to aid optical manufacturing, could be the integration of optical design aberration analysis in the final surface figuring loop.

High demand for large optical surfaces with challenging specifications is anticipated in the coming years. The primary mirror of the E-ELT, including spares, will require 931 segments to be produced within a few years. Laser fusion energy projects, such as the High Power Laser Energy Research (HiPER), if funded, are also expected to require enormous quantities of optical surfaces, which will need to be replaced periodically, due to laser damage. This demand can be met only by automating the optical fabrication process. The work outlined in this thesis represents a significant piece of the jigsaw towards this ultimate vision, by applying numerical methods to a wide range of case-studies related to the use of sub-aperture tools in Computer Controlled Optical Surfacing, specifically for the manufacture of challenging optics for future astronomical instruments, and in particular segmented mirrors. The manufacturing process is only one facet of the technological challenge to meet the demand for these large optical surfaces. Gifted engineers and scientists take on problems in the fields of optical design, automated metrology, material science, structural engineering, machine design and coating. These disciplines will have to cooperate intimately to meet the challenging specifications of a telescope that is capable of directly imaging a planet in the habitable zone of another star.

Appendices

A

Source code for the calculation of mismatch

A.1 Source code of `calc_mismatch.m`

```
function [ pv, zernikes, terms ] = calc_mismatch( R, k, M1_dia, sa_dia, sa_trans,
    resolution, mask, show_misfit )
% CALC_MISMATCH calculates the mismatch betwen tool and workpiece
%
% function [ pv, zernikes, terms ] = calc_mismatch( R, k, M1_dia, sa_dia,
%                                     sa_trans, resolution, mask, show_misfit )
%
% Copyright (c) 2011, Pim Messelink
% All rights reserved.
%
% Redistribution and use in source and binary forms, with or without
% modification, are permitted provided that the following conditions are
% met:
%
%     * Redistributions of source code must retain the above copyright
%       notice, this list of conditions and the following disclaimer.
%     * Redistributions in binary form must reproduce the above copyright
%       notice, this list of conditions and the following disclaimer in
%       the documentation and/or other materials provided with the distribution
%
% THIS SOFTWARE IS PROVIDED BY THE COPYRIGHT HOLDERS AND CONTRIBUTORS "AS IS"
% AND ANY EXPRESS OR IMPLIED WARRANTIES, INCLUDING, BUT NOT LIMITED TO, THE
% IMPLIED WARRANTIES OF MERCHANTABILITY AND FITNESS FOR A PARTICULAR PURPOSE
% ARE DISCLAIMED. IN NO EVENT SHALL THE COPYRIGHT OWNER OR CONTRIBUTORS BE
% LIABLE FOR ANY DIRECT, INDIRECT, INCIDENTAL, SPECIAL, EXEMPLARY, OR
% CONSEQUENTIAL DAMAGES (INCLUDING, BUT NOT LIMITED TO, PROCUREMENT OF
% SUBSTITUTE GOODS OR SERVICES; LOSS OF USE, DATA, OR PROFITS; OR BUSINESS
% INTERRUPTION) HOWEVER CAUSED AND ON ANY THEORY OF LIABILITY, WHETHER IN
% CONTRACT, STRICT LIABILITY, OR TORT (INCLUDING NEGLIGENCE OR OTHERWISE)
% ARISING IN ANY WAY OUT OF THE USE OF THIS SOFTWARE, EVEN IF ADVISED OF THE
% POSSIBILITY OF SUCH DAMAGE.
```

```
31
32 %% Parameters
33 if ~( exist('R', 'var') && isscalar(R) )
34     R = 84000;
35 end
36 if ~( exist('k', 'var') && isscalar(k) )
37     k = -0.993295;
38 end
39 if ~( exist('M1_dia', 'var') && isscalar(M1_dia) )
40     M1_dia = 42000;
41 end
42 if ~( exist('sa_dia', 'var') && isscalar(sa_dia) )
43     sa_dia = 1500; %1500
44 end
45 if ~( exist('sa_trans', 'var') && isscalar(sa_trans) )
46     sa_trans = 20250; %20250
47 end
48 if ~( exist('resolution', 'var') && isscalar(resolution) )
49     resolution = 1/20000; %20000
50 end
51 if ~( exist('mask', 'var') && isvector(mask) )
52     mask = [ 0, 0, 0, 1, 0, 1, 1, 1, 1, 1, 1, 1, 1, 1, 1 ]; % Zernike terms mask,
         removes piston, tilt and power
53 %     mask = [ 0, 0, 0, 0, 1, 0, 0, 0, 0, 0, 0, 0, 0, 0, 0 ]; % Zernike terms mask,
      power
54 end
55 if ~( exist('show_misfit', 'var') && isscalar(show_misfit) )
56     show_misfit = false;
57 end
58
59 %% Create M1 mirror
60 [ x, y ] = meshgrid( -round( ( M1_dia + sa_dia ) / 2 ) : ( M1_dia + sa_dia ) *
      resolution : round( ( M1_dia + sa_dia ) / 2 ), ...
61     -round( ( sa_dia ) / 1 ) : ( M1_dia + sa_dia ) * resolution : round( ( sa_dia )
         / 1 ) );
62 z = gen_asphere_3D( x, y, R, k );
63 z( x.^2 + y.^2 >= (M1_dia + sa_dia) ^ 2 / 4 ) = NaN;
64 % light_surf( x, y, z );
65
66 %% Find position and normal of sub-aperture centre
67 [ sa_centre, d_sa_centre ] = gen_asphere_3D( sa_trans, 0, R, k );
68
69 %% Translate M1 so sub-aperture is centred at origin
70 x = x - sa_trans;
71 z = z - sa_centre;
72
73 %% Rotate M1 so normal is pointing up
74 theta = atan( d_sa_centre );
75 new_coors = [ cos( theta ), sin( theta ); -sin( theta ), cos( theta ) ] * [ x(:)'; z
      (:)' ];
76 x(:) = new_coors( 1, : );
77 z(:) = new_coors( 2, : );
78 clear('new_coors');
79
80 %% Removing all points outside the sub-aperture
81 z( x.^2 + y.^2 >= sa_dia ^ 2 / 4 ) = NaN;
82
83 % Cropping the data to a square matrix
84 [ subscript1, subscript2 ] = ind2sub( size(x), find( x >= -sa_dia / 2 & x <= sa_dia /
       2 & y >= -sa_dia / 2 & y <= sa_dia / 2 ) );
```

```
85
86  sa_size = [ max( subscript1 ) - min( subscript1), max( subscript2 ) - min( subscript2
        ) ];
87
88  new_x = x( min( subscript1 ) - ( sa_size(1) < sa_size(2) ) * ceil( ( sa_size(2) -
        sa_size(1) ) / 2 ) : max( subscript1 ) + ( sa_size(1) < sa_size(2) ) * floor( (
        sa_size(2) - sa_size(1) ) / 2 ), ...
89      min( subscript2 ) - ( sa_size(2) < sa_size(1) ) * ceil( ( sa_size(1) - sa_size(2)
            ) / 2 ) : max( subscript2 ) + ( sa_size(2) < sa_size(1) ) * floor( ( sa_size
           (1) - sa_size(2) ) / 2 ) );
90
91  new_y = y( min( subscript1 ) - ( sa_size(1) < sa_size(2) ) * ceil( ( sa_size(2) -
        sa_size(1) ) / 2 ) : max( subscript1 ) + ( sa_size(1) < sa_size(2) ) * floor( (
        sa_size(2) - sa_size(1) ) / 2 ), ...
92      min( subscript2 ) - ( sa_size(2) < sa_size(1) ) * ceil( ( sa_size(1) - sa_size(2)
            ) / 2 ) : max( subscript2 ) + ( sa_size(2) < sa_size(1) ) * floor( ( sa_size
           (1) - sa_size(2) ) / 2 ) );
93
94  new_z = z( min( subscript1 ) - ( sa_size(1) < sa_size(2) ) * ceil( ( sa_size(2) -
        sa_size(1) ) / 2 ) : max( subscript1 ) + ( sa_size(1) < sa_size(2) ) * floor( (
        sa_size(2) - sa_size(1) ) / 2 ), ...
95      min( subscript2 ) - ( sa_size(2) < sa_size(1) ) * ceil( ( sa_size(1) - sa_size(2)
            ) / 2 ) : max( subscript2 ) + ( sa_size(2) < sa_size(1) ) * floor( ( sa_size
           (1) - sa_size(2) ) / 2 ) );
96
97  clear( 'subscript1', 'subscript2', 'x', 'y', 'z' );
98
99  %% Extract sub-aperure
100 [ x, y ] = meshgrid( -round( sa_dia / 2 ) : ( M1_dia + sa_dia ) * resolution : round(
        sa_dia / 2 ) );
101 F = TriScatteredInterp( new_x(:), new_y(:), new_z(:) );
102 z = zeros( size( x ) );
103 z(:) = F( x(:) , y(:) ) ;
104 clear( 'new_x', 'new_y', 'new_z' );
105
106 %% Computing the Zernike coefficients of the sub-aperture
107 valid = ~isnan(z);
108 terms = zernike_coeffs3( z, 1:length(mask), x / sa_dia * 2, y / sa_dia * 2, valid, '
        original');
109
110 %% Computing the Zernike base functions
111 zpf = zernike_fcn3( 1:length(mask), x(:) / sa_dia * 2, y(:) / sa_dia * 2, valid(:), '
        original');
112
113 %% Create surface from selected Zernike terms
114 zernikes = zeros( [ size(x), length(mask) ] );
115 tmp_zernike = zeros( size(x) );
116 tmp_zernike( ~valid ) = NaN;
117 for i = 1:length(mask)
118     tmp_zernike( valid ) = zpf( :, i ) .* terms( i ) .* mask( i );
119     zernikes( :, :, i ) = tmp_zernike;
120 end
121 clear('tmp_zernike');
122 zernikes = sum( zernikes, 3 );
123
124 %% Plot surface
125 if show_misfit
126     light_surf( x, y, zernikes );
127 end
128
```

```
129 %% Result
130 pv = max(zernikes(:)) - min(zernikes(:));
131 disp( ['PV: ', num2str( pv )] );
132 end
```

A.2 Source code of gen_asphere_3D.m

```
function [ z, dz, x_out, y_out ] = gen_asphere_3D( x, y, R, k )
%GEN_ASPHERE_3D creates sags and normals for points (x,y)
%
% [ z, dz, x_out, y_out ] = gen_asphere_3D( x, y, R, k )
%
% Copyright (c) 2011, Pim Messelink
% All rights reserved.
%
% Redistribution and use in source and binary forms, with or without
% modification, are permitted provided that the following conditions are
% met:
%
%     * Redistributions of source code must retain the above copyright
%       notice, this list of conditions and the following disclaimer.
%     * Redistributions in binary form must reproduce the above copyright
%       notice, this list of conditions and the following disclaimer in
%       the documentation and/or other materials provided with the distribution
%
% THIS SOFTWARE IS PROVIDED BY THE COPYRIGHT HOLDERS AND CONTRIBUTORS "AS IS"
% AND ANY EXPRESS OR IMPLIED WARRANTIES, INCLUDING, BUT NOT LIMITED TO, THE
% IMPLIED WARRANTIES OF MERCHANTABILITY AND FITNESS FOR A PARTICULAR PURPOSE
% ARE DISCLAIMED. IN NO EVENT SHALL THE COPYRIGHT OWNER OR CONTRIBUTORS BE
% LIABLE FOR ANY DIRECT, INDIRECT, INCIDENTAL, SPECIAL, EXEMPLARY, OR
% CONSEQUENTIAL DAMAGES (INCLUDING, BUT NOT LIMITED TO, PROCUREMENT OF
% SUBSTITUTE GOODS OR SERVICES; LOSS OF USE, DATA, OR PROFITS; OR BUSINESS
% INTERRUPTION) HOWEVER CAUSED AND ON ANY THEORY OF LIABILITY, WHETHER IN
% CONTRACT, STRICT LIABILITY, OR TORT (INCLUDING NEGLIGENCE OR OTHERWISE)
% ARISING IN ANY WAY OUT OF THE USE OF THIS SOFTWARE, EVEN IF ADVISED OF THE
% POSSIBILITY OF SUCH DAMAGE.

    %% Parameters
    if ~( exist('x', 'var') && ismatrix(x) && ~isempty(x) ) && ...
            ~( exist('y', 'var') && ismatrix(y)  && ~isempty(y) )
        [ x, y ] = meshgrid( -21000:100:21000 );
    end
    if ~( exist('R', 'var') && isscalar(R) )
        R = 84000;
    end
    if ~( exist('k', 'var') && isscalar(k) )
        k = -0.993295;
    end

    %% Program
    rhosqr = x.^2 + y.^2;
    rho = sqrt( rhosqr );
    c = 1/R;

    numerator = c * rhosqr;
    denominator = 1 + sqrt( 1 - (1+k) * c^2 .* rhosqr );

    deriv_numerator = 2 * c * rho;
    deriv_denominator = -( (1+k) * c^2 .* rho ) ./ sqrt( 1 - (1+k) * c^2 .* rhosqr )
        ;

    z = numerator ./ denominator;

    %% Additional output
```

```
57      switch nargout
58          case 1
59          case 2
60              dz = ( deriv_numerator .* denominator - numerator .* deriv_denominator )
                    ./ ( denominator .^ 2 );
61          otherwise
62              dz = ( deriv_numerator .* denominator - numerator .* deriv_denominator )
                    ./ ( denominator .^ 2 );
63              x_out = x;
64              y_out = y;
65      end
66
67  end
```

B

Zernike polynomials

Z_0^0
Z_1^{-1}
Z_1^1
Z_2^{-2}
Z_2^0
Z_2^2
Z_3^{-3}
Z_3^{-1}
Z_3^1
Z_3^3

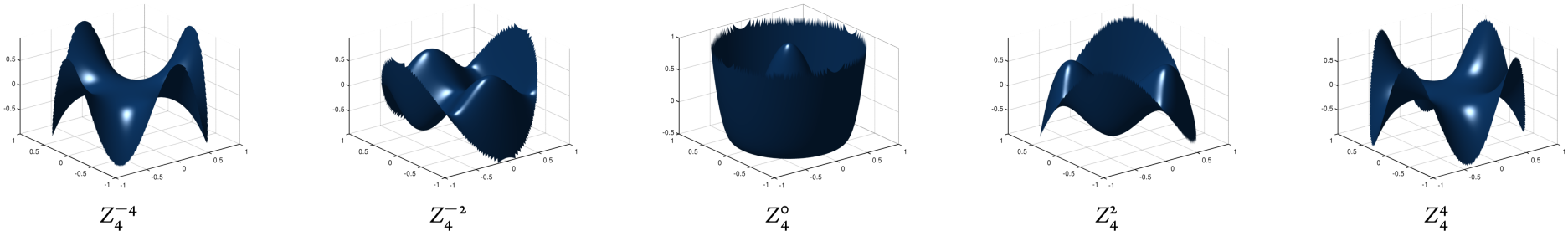

Figure B.1: Plots of the 15 lowest order Zernike polynomials.

C

Effect of resolution on mismatch analysis of sub-aperture rigid tools.

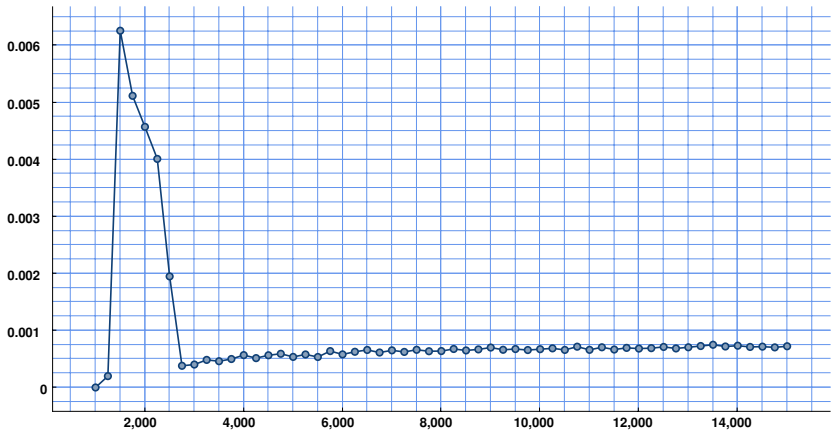

(a) 100 mm diameter tool

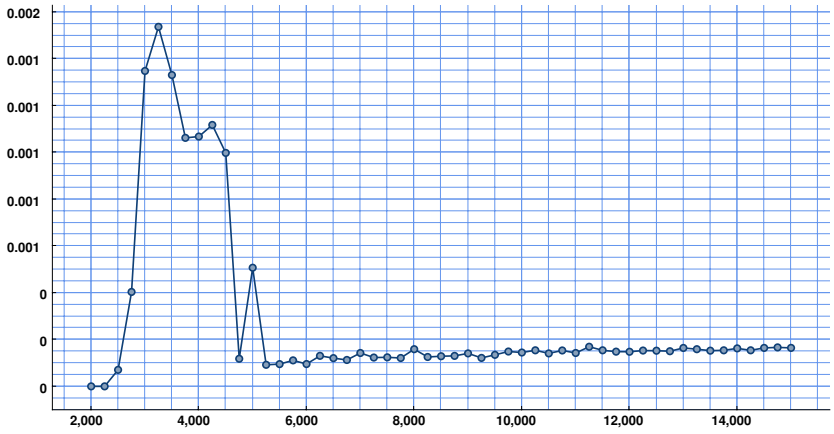

(b) 50 mm diameter tool

Figure C.1: Mismatch versus resolution for the sub-aperture rigid tools discussed in Chapter 2.

D

Source code for FEA modelling

D.1 Source code of GROLISHING.COMM

```
# GROLISHING.COMM is a command file for Code_Aster to simulate a Grolishing
# hanging over the edge of a workpiece by different amounts
#
# Copyright (c) 2014, Pim Messelink
# All rights reserved.
#
# Redistribution and use in source and binary forms, with or without
# modification, are permitted provided that the following conditions are
# met:
#
#     * Redistributions of source code must retain the above copyright
#       notice, this list of conditions and the following disclaimer.
#     * Redistributions in binary form must reproduce the above copyright
#       notice, this list of conditions and the following disclaimer in
#       the documentation and/or other materials provided with the distribution
#
# THIS SOFTWARE IS PROVIDED BY THE COPYRIGHT HOLDERS AND CONTRIBUTORS "AS IS"
# AND ANY EXPRESS OR IMPLIED WARRANTIES, INCLUDING, BUT NOT LIMITED TO, THE
# IMPLIED WARRANTIES OF MERCHANTABILITY AND FITNESS FOR A PARTICULAR PURPOSE
# ARE DISCLAIMED. IN NO EVENT SHALL THE COPYRIGHT OWNER OR CONTRIBUTORS BE
# LIABLE FOR ANY DIRECT, INDIRECT, INCIDENTAL, SPECIAL, EXEMPLARY, OR
# CONSEQUENTIAL DAMAGES (INCLUDING, BUT NOT LIMITED TO, PROCUREMENT OF
# SUBSTITUTE GOODS OR SERVICES; LOSS OF USE, DATA, OR PROFITS; OR BUSINESS
# INTERRUPTION) HOWEVER CAUSED AND ON ANY THEORY OF LIABILITY, WHETHER IN
# CONTRACT, STRICT LIABILITY, OR TORT (INCLUDING NEGLIGENCE OR OTHERWISE)
# ARISING IN ANY WAY OUT OF THE USE OF THIS SOFTWARE, EVEN IF ADVISED OF THE
# POSSIBILITY OF SUCH DAMAGE.

DEBUT();

```

```
mesh_g=LIRE_MAILLAGE(
  INFO=1,
  UNITE=20,
  FORMAT='MED',
);

mesh_t=LIRE_MAILLAGE(
  INFO=1,
  UNITE=21,
  FORMAT='MED',
);

iron=DEFI_MATERIAU(
  ELAS=(
    _F(
      E=66.1781e9,
      NU=0.27,
      RHO=7200.0,
    ),
  ),
);

alu=DEFI_MATERIAU(
  ELAS=(
    _F(
      E=69.0e9,
      NU=0.33,
      RHO=2700.0,
    ),
  ),
);

borosili=DEFI_MATERIAU(
  ELAS=(
    _F(
      E=64.0e9,
      NU=0.2,
      RHO=2230.0,
    ),
  ),
);

linst=DEFI_LIST_REEL(
  DEBUT=0.0,
  INTERVALLE=(
    _F(
      JUSQU_A=1.0,
      PAS=1.0,
    ),
#    _F(
#      JUSQU_A=2.0,
#      PAS=0.1,
#    ),
  ),
);

fun=DEFI_FONCTION(
  NOM_PARA='INST',
  VALE=(0.0,0.0,  1.0,1.0,)
);
```

```
91
92  noloops=9;
93  totaltrans=0.040;
94  step=totaltrans/(noloops-1);
95
96  for i in range(0,noloops):
97
98    if i>0:
99
100     mesh_g=MODI_MAILLAGE(
101       reuse=mesh_g,
102       MAILLAGE=mesh_g,
103       TRANSLATION=(-step, 0.0, 0.0),
104     );
105
106   #ENDIF if i>0:
107
108   mesh=ASSE_MAILLAGE(
109     OPERATION='SUPERPOSE',
110     MAILLAGE_1 = mesh_g,
111     MAILLAGE_2 = mesh_t,
112   );
113
114   mesh=MODI_MAILLAGE(
115     reuse=mesh,
116     MAILLAGE=mesh,
117     ORIE_PEAU_3D=(
118       _F(
119         GROUP_MA='bot_g',
120       ),
121       _F(
122         GROUP_MA='cir_g',
123       ),
124       _F(
125         GROUP_MA='top_g',
126       ),
127       _F(
128         GROUP_MA='bot_i',
129       ),
130       _F(
131         GROUP_MA='cir_h_i',
132       ),
133       _F(
134         GROUP_MA='top_h_i',
135       ),
136       _F(
137         GROUP_MA='cir_i',
138       ),
139       _F(
140         GROUP_MA='top_i',
141       ),
142       _F(
143         GROUP_MA='bot_f_a',
144       ),
145       _F(
146         GROUP_MA='cir_f_a',
147       ),
148       _F(
149         GROUP_MA='top_f_a',
150       ),
```

```
151         _F(
152           GROUP_MA='ocir_p_a',
153         ),
154         _F(
155           GROUP_MA='icir_p_a',
156         ),
157         _F(
158           GROUP_MA='side_p_a',
159         ),
160         _F(
161           GROUP_MA='top_f_a',
162         ),
163       ),
164     );
165
166     mesh=DEFI_GROUP(
167       MAILLAGE=mesh,
168       reuse=mesh,
169       CREA_GROUP_NO=(
170         _F(
171           GROUP_MA='bot_g',
172         ),
173         _F(
174           GROUP_MA='cir_g',
175         ),
176         _F(
177           GROUP_MA='top_g',
178         ),
179         _F(
180           GROUP_MA='bot_i',
181         ),
182         _F(
183           GROUP_MA='cir_h_i',
184         ),
185         _F(
186           GROUP_MA='top_h_i',
187         ),
188         _F(
189           GROUP_MA='cir_i',
190         ),
191         _F(
192           GROUP_MA='top_i',
193         ),
194         _F(
195           GROUP_MA='bot_f_a',
196         ),
197         _F(
198           GROUP_MA='cir_f_a',
199         ),
200         _F(
201           GROUP_MA='top_f_a',
202         ),
203         _F(
204           GROUP_MA='ocir_p_a',
205         ),
206         _F(
207           GROUP_MA='icir_p_a',
208         ),
209         _F(
210           GROUP_MA='side_p_a',
```

```
211         ),
212         _F(
213           GROUP_MA='top_p_a',
214         ),
215       ),
216     );
217
218     IMPR_RESU(
219       FORMAT='MED',
220       UNITE=70+i,
221       RESU=(
222         _F(
223           MAILLAGE=mesh,
224         ),
225       ),
226     );
227
228     model=AFFE_MODELE(
229       MAILLAGE=mesh,
230       AFFE=(
231         _F(
232           GROUP_MA=('alu','iron','glass','bot_g','cir_g','top_g','bot_i','cir_h_i','
                top_h_i','cir_i','top_i','bot_f_a','cir_f_a','top_f_a','ocir_p_a','
                icir_p_a','side_p_a','top_p_a',),
233           PHENOMENE='MECANIQUE',
234           MODELISATION='3D',
235         ),
236       ),
237     );
238
239     material=AFFE_MATERIAU(
240       MAILLAGE=mesh,
241       AFFE=(
242         _F(
243           GROUP_MA=('iron',),
244           MATER = iron
245         ),
246         _F(
247           GROUP_MA=('alu',),
248           MATER = alu,
249         ),
250         _F(
251           GROUP_MA=('glass'),
252           MATER = borosili,
253         ),
254       ),
255     );
256
257     fix=AFFE_CHAR_MECA(
258       MODELE=model,
259       DDL_IMPO=(
260         _F(
261           GROUP_NO='top_p_a',
262           DX=0.0,
263           DY=-0.00,
264         ),
265         _F(
266           GROUP_NO='bot_g',
267           DX=0.0,
268           DY=-0.00,
```

```
269             DZ=0.0,
270           ),
271         ),
272         LIAISON_MAIL=(
273           _F(
274             GROUP_MA_MAIT='alu',
275             GROUP_MA_ESCL='top_i',
276           ),
277         ),
278       );
279
280       selfwght=AFFE_CHAR_MECA(
281           MODELE=model,
282           PESANTEUR=_F(
283                GRAVITE=9.80665,DIRECTION=(0,0,-1),
284                GROUP_MA=('glass','iron','alu',),
285           ),
286       );
287
288       contact=DEFI_CONTACT(
289         MODELE=model,
290         FORMULATION='CONTINUE',
291         ALGO_RESO_CONT='POINT_FIXE',
292         ALGO_RESO_GEOM='POINT_FIXE',
293         ITER_GEOM_MAXI=4,
294         ITER_CONT_MAXI=30,
295         LISSAGE='NON',
296         INFO=2,
297         ZONE=(
298           _F(
299             GROUP_MA_ESCL='bot_i',
300             GROUP_MA_MAIT='top_g',
301             INTEGRATION='AUTO',
302             ALGO_CONT='STANDARD',
303             COEF_CONT=1000.0,
304           ),
305         )
306       );
307
308       result=STAT_NON_LINE(
309         MODELE=model,
310         CHAM_MATER=material,
311         INCREMENT=(
312           _F(
313             LIST_INST=linst,
314           ),
315         ),
316         EXCIT=(
317           _F(
318             CHARGE=fix,
319           ),
320           _F(
321             CHARGE=selfwght,
322             FONC_MULT=fun,
323           ),
324         ),
325         CONTACT=contact,
326         COMP_ELAS=(
327           _F(
328             RELATION='ELAS',
```

```
329         ),
330       ),
331       NEWTON=(
332         _F(
333           MATRICE='ELASTIQUE',
334           REAC_ITER=1,
335         ),
336       ),
337       CONVERGENCE=(
338         _F(
339           ARRET='OUI',
340           ITER_GLOB_MAXI=30,
341           RESI_GLOB_MAXI=1.E-8,
342         ),
343       ),
344     );
345
346     result=CALC_CHAMP(
347       reuse=result,
348       RESULTAT=result,
349       CRITERES='SIEQ_ELNO',
350       CONTRAINTE='SIGM_ELNO',
351       FORCE=('REAC_NODA'),
352     );
353
354     result=CALC_CHAMP(
355       reuse=result,
356       RESULTAT=result,
357       CRITERES='SIEQ_NOEU',
358       CONTRAINTE='SIGM_NOEU',
359     );
360
361     mass=POST_ELEM(
362         RESULTAT =result,
363         MODELE=model,
364         MASS_INER=_F(
365             GROUP_MA=('glass','iron','alu',),
366         ),
367         TITRE=  'Mass'
368     );
369
370     IMPR_TABLE(
371       TABLE=mass,
372       FORMAT_R='1PE12.3',
373     );
374
375     IMPR_RESU(
376       MODELE=model,
377       FORMAT='RESULTAT',
378       RESU=(
379         _F(
380           MAILLAGE=mesh,
381           GROUP_NO=('bot_i',),
382           RESULTAT=result,
383           NOM_CHAM='DEPL',
384           NOM_CMP=('LAGS_C',),
385         ),
386       ),
387     );
388
```

```
389   IMPR_RESU(
390     FORMAT='MED',
391     UNITE=80+i,
392     RESU=(
393       _F(
394         GROUP_MA=('alu','iron','glass','bot_g','cir_g','top_g','bot_i','cir_h_i','
                top_h_i','cir_i','top_i','bot_f_a','cir_f_a','top_f_a','ocir_p_a','
                icir_p_a','side_p_a','top_p_a',),
395         RESULTAT=result,
396         NOM_CHAM=('DEPL',),
397         LIST_INST=linst,
398       ),
399       _F(
400         GROUP_MA=('bot_i',),
401         RESULTAT=result,
402         NOM_CHAM=('DEPL',),
403         NOM_CMP='LAGS_C',
404         NOM_CHAM_MED='lags_c',
405         LIST_INST=linst,
406       ),
407       _F(
408         GROUP_MA=('bot_i','top_g',),
409         RESULTAT=result,
410         NOM_CHAM=('REAC_NODA',),
411         LIST_INST=linst,
412       ),
413     ),
414   );
415
416   DETRUIRE(
417     CONCEPT=(
418       _F(
419         NOM=mesh,
420       ),
421     ),
422     INFO=1,
423   );
424
425   DETRUIRE(
426     CONCEPT=(
427       _F(
428         NOM=model,
429       ),
430     ),
431     INFO=1,
432   );
433
434   DETRUIRE(
435     CONCEPT=(
436       _F(
437         NOM=material,
438       ),
439     ),
440     INFO=1,
441   );
442
443   DETRUIRE(
444     CONCEPT=(
445       _F(
446         NOM=fix,
```

```
447         ),
448       ),
449       INFO=1,
450     );
451
452     DETRUIRE(
453       CONCEPT=(
454         _F(
455           NOM=selfwght,
456         ),
457       ),
458       INFO=1,
459     );
460
461     DETRUIRE(
462       CONCEPT=(
463         _F(
464           NOM=contact,
465         ),
466       ),
467       INFO=1,
468     );
469
470     DETRUIRE(
471       CONCEPT=(
472         _F(
473           NOM=result,
474         ),
475       ),
476       INFO=1,
477     );
478
479     DETRUIRE(
480       CONCEPT=(
481         _F(
482           NOM=mass,
483         ),
484       ),
485       INFO=1,
486     );
487
488   #ENDFOR for i in range(0,noloops):
489
490   FIN();
```

D.2 Source code of parse_resu.m

```
function [ nodeCoors, faceNodes, faceCoors, results ] = parse_resu( filein, faceName
    )
% PARSE_RESU parses an output file from Code_Aster
%
% [ nodeCoors, faceNodes, faceCoors, results ] = parse_resu( filein, faceName )
%
% Copyright (c) 2014, Pim Messelink
% All rights reserved.
%
% Redistribution and use in source and binary forms, with or without
% modification, are permitted provided that the following conditions are
% met:
%
%     * Redistributions of source code must retain the above copyright
%       notice, this list of conditions and the following disclaimer.
%     * Redistributions in binary form must reproduce the above copyright
%       notice, this list of conditions and the following disclaimer in
%       the documentation and/or other materials provided with the distribution
%
% THIS SOFTWARE IS PROVIDED BY THE COPYRIGHT HOLDERS AND CONTRIBUTORS "AS IS"
% AND ANY EXPRESS OR IMPLIED WARRANTIES, INCLUDING, BUT NOT LIMITED TO, THE
% IMPLIED WARRANTIES OF MERCHANTABILITY AND FITNESS FOR A PARTICULAR PURPOSE
% ARE DISCLAIMED. IN NO EVENT SHALL THE COPYRIGHT OWNER OR CONTRIBUTORS BE
% LIABLE FOR ANY DIRECT, INDIRECT, INCIDENTAL, SPECIAL, EXEMPLARY, OR
% CONSEQUENTIAL DAMAGES (INCLUDING, BUT NOT LIMITED TO, PROCUREMENT OF
% SUBSTITUTE GOODS OR SERVICES; LOSS OF USE, DATA, OR PROFITS; OR BUSINESS
% INTERRUPTION) HOWEVER CAUSED AND ON ANY THEORY OF LIABILITY, WHETHER IN
% CONTRACT, STRICT LIABILITY, OR TORT (INCLUDING NEGLIGENCE OR OTHERWISE)
% ARISING IN ANY WAY OUT OF THE USE OF THIS SOFTWARE, EVEN IF ADVISED OF THE
% POSSIBILITY OF SUCH DAMAGE.

%% Sanity check input arguments
if ~( exist( 'filein', 'var') && ischar( filein ) )
    filein = '~/Desktop/example.resu';
end

if ~exist( filein, 'file')
    error( 'Input file not found' );
end

if ~( exist( 'faceName', 'var') && ischar( faceName ) )
    faceName = 'bot_b';
end

%% Open files
fidin = fopen( filein, 'r');

mode = 'CCOR_3D';
found = false;

%% Parse line by line

busy = Busy( 100 ); % Initialise busy indicator

while true

    cycle( busy ); % Update busy indicator
```

```
57
58      textline = fgetl( fidin );
59
60      if ~ischar( textline )
61          break
62      end
63
64      textelem = regexp( textline, ' ', 'split' );
65      textelem( cellfun( 'isempty', textelem ) ) = [];
66
67      if isempty( textelem )
68          continue
69      end
70
71      if ~found
72          switch mode
73              case 'COOR_3D'
74                  if strcmp( textelem{1,1}, 'COOR_3D' )
75                      found = true;
76                      continue
77                  end
78              case 'GROUP_NO'
79                  if strcmp( textelem{1,1}, 'GROUP_NO' )
80                      textline = fgetl( fidin );
81                      textelem = regexp( textline, ' ', 'split' );
82                      textelem( cellfun( 'isempty', textelem ) ) = [];
83                      if strcmp( textelem{1,1}, faceName )
84                          found = true;
85                          faceNodes = [];
86                          continue
87                      end
88                  end
89              case 'DEPL'
90                  if strcmp( textelem{1,1}, 'CHAMP' ) && strcmp( textelem{1,7}, 'DEPL'
                        )
91                      textline = fgetl( fidin );
92                      textelem = regexp( textline, ' ', 'split' );
93                      textelem( cellfun( 'isempty', textelem ) ) = [];
94                      if str2double( textelem{1,5} ) == 1
95                          found = true;
96                          fgetl( fidin );
97                          if ~( exist( 'results', 'var') )
98                              results = {};
99                          end
100                         numExp = length( results );
101                         results{ numExp + 1 } = [];
102                         continue
103                     end
104                 end
105             otherwise
106                 error( [ mode 'not supported yet!' ] );
107         end
108     else
109         switch mode
110             case 'COOR_3D'
111                 if strncmp( textelem{1,1}, 'FINSF', 5 )
112                     finalize( busy );
113                     disp( 'All node coordinates read.' );
114                     busy = Busy( 100 );
115                     found = false;
```

```
116                     mode = 'GROUP_NO';
117                 else
118                     nodeName = textelem{1,1};
119                     nodeIdx = str2double( nodeName(2:end) );
120                     nodeCoors( nodeIdx, 1 ) = str2double( textelem{1,2} );
121                     nodeCoors( nodeIdx, 2 ) = str2double( textelem{1,3} );
122                     nodeCoors( nodeIdx, 3 ) = str2double( textelem{1,4} );
123                 end
124             case 'GROUP_NO'
125                 if strncmp( textelem{1,1}, 'FINSF', 5 )
126                     finalize( busy );
127                     disp( [ 'All nodes read in ' faceName '.' ] );
128                     busy = Busy( 100 );
129                     found = false;
130                     mode = 'DEPL';
131                 else
132                     for i=1:length( textelem )
133                         nodeName = textelem{1,i};
134                         nodeIdx = str2double( nodeName(2:end) );
135                         faceNodes( end+1 ) = nodeIdx;
136                     end
137                 end
138             case 'DEPL'
139                 if isempty( textelem )
140                     finalize( busy );
141                     disp( [ 'Read results of experiment ' num2str( length( results )
                            ) '.' ] );
142                     busy = Busy( 100 );
143                     found = false;
144                     mode = 'DEPL';
145                 else
146                     numExp = length( results );
147                     resultIdx = length( results{numExp} ) + 1;
148                     nodeName = textelem{1,1};
149                     nodeIdx = str2double( nodeName(2:end) );
150                     if resultIdx > numel( faceNodes )
151                         finalize( busy );
152                         disp( [ 'Read results of experiment ' num2str( length(
                                results ) ) '.' ] );
153                         busy = Busy( 100 );
154                         found = false;
155                         mode = 'DEPL';
156                         continue
157                     end
158                     if faceNodes( resultIdx ) ~= nodeIdx
159                         error( 'Node index does not match the expected index.' );
160                     end
161                     results{numExp}(resultIdx) = str2double( textelem{1,2} );
162                 end
163             otherwise
164                 error( [ mode 'not supported yet!' ] );
165         end
166     end
167
168 end
169
170 finalize( busy ); % Delete busy indicator
171
172 %% Close files
173 fclose( fidin );
```

```
174
175 %% Calculate output
176  faceCoors = nodeCoors( faceNodes, :) ;
```

D.3 Source code of `create_profiles.m`

```
function [ xRanges, profiles, overhangs, calibFactors, interpData, RMSE ] =
    create_profiles( fileName, feaStep, centreRadius, meshStep )
% CREATE_PROFILES creates removal profiles for scans parallel to the edge
% based on data files created with PARSE_RESU.
%
% profiles = create_profiles( fileName, feaStep, centreRadius, meshStep )
%
% Copyright (c) 2014, Pim Messelink
% All rights reserved.
%
% Redistribution and use in source and binary forms, with or without
% modification, are permitted provided that the following conditions are
% met:
%
%     * Redistributions of source code must retain the above copyright
%       notice, this list of conditions and the following disclaimer.
%     * Redistributions in binary form must reproduce the above copyright
%       notice, this list of conditions and the following disclaimer in
%       the documentation and/or other materials provided with the distribution
%
% THIS SOFTWARE IS PROVIDED BY THE COPYRIGHT HOLDERS AND CONTRIBUTORS "AS IS"
% AND ANY EXPRESS OR IMPLIED WARRANTIES, INCLUDING, BUT NOT LIMITED TO, THE
% IMPLIED WARRANTIES OF MERCHANTABILITY AND FITNESS FOR A PARTICULAR PURPOSE
% ARE DISCLAIMED. IN NO EVENT SHALL THE COPYRIGHT OWNER OR CONTRIBUTORS BE
% LIABLE FOR ANY DIRECT, INDIRECT, INCIDENTAL, SPECIAL, EXEMPLARY, OR
% CONSEQUENTIAL DAMAGES (INCLUDING, BUT NOT LIMITED TO, PROCUREMENT OF
% SUBSTITUTE GOODS OR SERVICES; LOSS OF USE, DATA, OR PROFITS; OR BUSINESS
% INTERRUPTION) HOWEVER CAUSED AND ON ANY THEORY OF LIABILITY, WHETHER IN
% CONTRACT, STRICT LIABILITY, OR TORT (INCLUDING NEGLIGENCE OR OTHERWISE)
% ARISING IN ANY WAY OUT OF THE USE OF THIS SOFTWARE, EVEN IF ADVISED OF THE
% POSSIBILITY OF SUCH DAMAGE.

if ~( exist( 'fileName', 'var') && ischar( fileName ) )
    fileName = 'GrolishingBrass.mat';
end

if ~exist( fileName, 'file')
    error( 'Input file not found' );
end

if ~( exist( 'feaStep', 'var') && isscalar( feaStep ) )
    feaStep = 0.012;
end

if ~( exist( 'centreRadius', 'var') && isscalar( centreRadius ) )
    centreRadius = 0.009;
end

if ~( exist( 'meshStep', 'var') && isscalar( meshStep ) )
    meshStep = 0.001;
end

load( fileName, 'faceCoors' );
load( fileName, 'results' );

[x, y] = meshgrid( -0.05:meshStep:0.05 );

```

```
profiles = {};
extremes = [ 0, 0 ];
colours = { 'b', 'r', 'g', 'k', 'y', 'c', 'm', ...
    'b-.', 'r-.', 'g-.', 'k-.', 'y-.', 'c-.', 'm-.' };
numExp = length(results);

for i=1:numExp

    F = scatteredInterpolant( faceCoors(:,1), faceCoors(:,2), ...
        results{i}', 'linear', 'none' );
    p = F( x, y );
    p( x.^2 + y.^2 < centreRadius^2 ) = NaN;

    v = sqrt( x.^2 + y.^2 );
    r = v.*p;
    r( isnan(r) ) = 0;
    profiles{i} = sum(r);

    extremes(1) = min( extremes(1), min(profiles{i}) );
    extremes(2) = max( extremes(2), max(profiles{i}) );

end

% figure, hold on;

xRanges = {};
overhangs = {};

for i=1:numExp

    profiles{i} = -profiles{i}./extremes(1);
    overhangs{i} = feaStep * (i-1);

    if feaStep > 0
        xRanges{i} = ( 0:meshStep:0.1 ) - overhangs{i};
    else
        xRanges{i} = ( -0.1:meshStep:0 ) - overhangs{i};
    end

end

if feaStep > 0
    xRangesSum = -feaStep * (numExp-1) : meshStep : 0.1;
else
    xRangesSum = -0.1 : meshStep : -feaStep * (numExp-1);
end

extremes = [ 0, 0 ];

profilesSum = {};
profilesSum{1} = xRangesSum .* 0;

blkxRanges = xRanges{1};
blkProfile = profiles{1};

while true

    blkxRanges = blkxRanges + feaStep;

    if feaStep > 0
```

```
117
118         if max( xRangesSum ) < min( blkxRanges )
119             break
120         end
121
122         [ ~, lo ] = min( abs( xRangesSum - min( blkxRanges ) ) );
123         [ ~, hi ] = min( abs( blkxRanges - max( xRangesSum ) ) );
124
125         profilesSum{1}( lo:end ) = profilesSum{1}( lo:end ) + blkProfile( 1:hi );
126
127     else
128
129         if min( xRangesSum ) > max( blkxRanges )
130             break
131         end
132
133         [ ~, lo ] = min( abs( blkxRanges - min( xRangesSum ) ) );
134         [ ~, hi ] = min( abs( xRangesSum - max( blkxRanges ) ) );
135
136         profilesSum{1}( 1:hi ) = profilesSum{1}( 1:hi ) + blkProfile( lo:end );
137
138     end
139
140 end
141
142 for i=1:numExp
143
144     if i > 1
145         profilesSum{i} = profilesSum{i-1};
146     end
147
148     [ ~, lo ] = min( abs( xRangesSum - min( xRanges{i} ) ) );
149     [ ~, hi ] = min( abs( xRangesSum - max( xRanges{i} ) ) );
150
151     profilesSum{i}( lo:hi ) = profilesSum{i}( lo:hi ) + profiles{i};
152
153     extremes(1) = min( extremes(1), min(profilesSum{i}) );
154     extremes(2) = max( extremes(2), max(profilesSum{i}) );
155
156 end
157
158     function result = calc_dwell_profile( d )
159
160         d( d<0 ) = 0;
161         result = profilesSum{1} .* blkDwell;
162
163         for i=2:numExp
164             [ ~, lo ] = min( abs( xRangesSum - min( xRanges{i} ) ) );
165             [ ~, hi ] = min( abs( xRangesSum - max( xRanges{i} ) ) );
166             result( lo:hi ) = result( lo:hi ) + profiles{i} .* d(i-1);
167         end
168
169     end
170
171     function sos = calc_sum_of_squares( profile, indices )
172         sos = norm( profile( indices ) + 1 )^2;
173     end
174
175 if feaStep > 0
176     indices = ( xRangesSum >= 0 & xRangesSum <= 0.1 );
```

```
177 else
178     indices = ( xRangesSum <= 0 & xRangesSum >= -0.1 );
179 end
180
181 blkDwell = fminsearch( @(c) ( min( profilesSum{ 1 } .* c ) + 1 )^2, 1 );
182
183 dwells = fmincon( @(d) ...
184     calc_sum_of_squares( calc_dwell_profile( d ), indices ), ...
185     ones( 1, numExp-1 ), [], [], [], [], zeros( 1, numExp-1 ) );
186
187 sosConst = calc_sum_of_squares( profilesSum{ numExp } .* blkDwell, indices );
188 sosDwells = calc_sum_of_squares( calc_dwell_profile( dwells ), indices );
189 disp( [ 'RSS: ' num2str( sosConst ) ' ' num2str( sosDwells ) ] );
190
191 figure, hold on;
192
193 plot( -xRangesSum, -profilesSum{ numExp } .* blkDwell, 'b', 'LineWidth', 2 );
194 plot( -xRangesSum, -calc_dwell_profile( dwells ), 'r', 'LineWidth', 2 );
195
196 xlabel('Distance from edge (m)')
197 ylabel('Removal (\mum)')
198
199 xlim( [ 0 0.1 ] )
200 ylim( [ 0.5 1.5 ] )
201
202 grid on
203 legend( { 'constant feeds', 'optimised feeds' } );
204
205     function pv = calc_pv( profile, indices )
206         pv = abs( max( profile( indices ) ) - min( profile( indices ) ) );
207     end
208
209 dwells = fmincon( @(d) ...
210     calc_pv( calc_dwell_profile( d ), indices ), ...
211     ones( 1, numExp-1 ), [], [], [], [], zeros( 1, numExp-1 ) );
212
213 pvConst = calc_pv( profilesSum{ numExp } .* blkDwell, indices );
214 pvDwells = calc_pv( calc_dwell_profile( dwells ), indices );
215 disp( [ 'PV: ' num2str( pvConst ) ' ' num2str( pvDwells ) ] );
216
217 figure, hold on;
218
219 plot( -xRangesSum, -profilesSum{ numExp } .* blkDwell, 'b', 'LineWidth', 2 );
220 plot( -xRangesSum, -calc_dwell_profile( dwells ), 'r', 'LineWidth', 2 );
221
222 xlabel('Distance from edge (m)')
223 ylabel('Removal (\mum)')
224
225 xlim( [ 0 0.1 ] )
226 ylim( [ 0.5 1.5 ] )
227
228 grid on
229 legend( { 'constant feeds', 'optimised feeds' } );
230
231 baseFileName = 'overhang ';
232 colorIdx = 0;
233 feaStepSign = sign( feaStep );
234 legendText = {};
235
236 figure, hold on;
```

```
237
238 for i=1:numExp
239
240     overhangText = num2str( abs( overhangs{i} * 1000 ) );
241     fileName = [ baseFileName overhangText '.ascii' ];
242     if ~exist( fileName , 'file' )
243         continue
244     end
245
246     experiment{i} = importdata( fileName );
247
248     interpData{i} = interp1( experiment{i}(:,1) * 0.001, ...
249         experiment{i}(:,2), xRanges{i} * feaStepSign );
250
251     valid = ~isnan( interpData{i} );
252
253     a = fminsearch( @(a) norm( interpData{i}( valid ) - ...
254         a * profiles{i}(valid) )^2, -1 );
255     calibFactors{i} = a;
256
257     RMSE{i} = sqrt( mean( ( interpData{i}( valid ) - ...
258         a * profiles{i}(valid) ) .^ 2 ) );
259     disp( [ overhangText ': ' num2str( RMSE{i} ) ] );
260
261     colorIdx = colorIdx + 1;
262     plot( xRanges{i} * feaStepSign, a * profiles{i}, ...
263         [ colours{ colorIdx } '--' ], 'LineWidth', 2 )
264     plot( xRanges{i} * feaStepSign, interpData{i}, ...
265         colours{ colorIdx }, 'LineWidth', 2 )
266
267     legendText{ end + 1 } = [ overhangText ' mm (model)' ];
268     legendText{ end + 1 } = [ overhangText ' mm (experiment)' ];
269
270 end
271
272 xlabel('Distance from edge (m)')
273 ylabel('Removal (mm)')
274
275 xlim( [ -0.005 0.105 ] )
276 ylim( [ -0.0005 0.0055 ] )
277
278 grid on
279 legend( legendText );
280
281 figure, hold on;
282
283 plot( xRanges{1} * feaStepSign, calibFactors{1} * profiles{1}, ...
284     'b', 'LineWidth', 2 )
285 plot( xRanges{1} * feaStepSign, interpData{1}, ...
286     'r', 'LineWidth', 2 )
287
288 middle = importdata( 'middle.ascii' );
289 middleInterp = interp1( middle(:,1) * 0.001 - 0.1, ...
290     middle(:,2), xRanges{1} * feaStepSign );
291 valid = ~( isnan( middleInterp ) | isnan( interpData{1} ) );
292 middleRMSE = sqrt( mean( ( interpData{1}( valid ) - ...
293         middleInterp(valid) ) .^ 2 ) );
294 plot( xRanges{1} * feaStepSign, middleInterp, ...
295     'g', 'LineWidth', 2 )
296
```

```
297 repeat = importdata( 'middle (repeat experiment).ascii' );
298 repeatInterp = interp1( repeat(:,1) * 0.001 - 0.1, ...
299     repeat(:,2), xRanges{1} * feaStepSign );
300 valid = ~( isnan( repeatInterp ) | isnan( interpData{1} ) );
301 repeatRMSE = sqrt( mean( ( interpData{1}( valid ) - ...
302         repeatInterp(valid) ) .^ 2 ) );
303 plot( xRanges{1} * feaStepSign, repeatInterp, ...
304     'g--', 'LineWidth', 2 )
305
306 measRMSE = sqrt( mean( ( middleInterp(valid) - ...
307         repeatInterp(valid) ) .^ 2 ) );
308 disp( [ 'RMSEs: ' num2str( middleRMSE ) ' ' num2str( repeatRMSE ) ' ' ...
309     num2str( measRMSE ) ] );
310
311 xlabel('Distance from edge (m)')
312 ylabel('Removal (mm)')
313
314 xlim( [ -0.005 0.105 ] )
315 ylim( [ -0.0005 0.0025 ] )
316
317 grid on
318 legend( { 'model', 'experiment', 'repeat experiment', ...
319     'repeat measurement' } );
320
321 end
```

E

Risk analysis of local edge correction

E.1 Input quality

The process has to be able to cope with the output quality of the process that proceeds it in the process chain. This criteria could be further divided in different aspects of quality (e.g. surface roughness/texture and form errors, including edge characteristic). A reasonable input quality to expect after polishing with a 20 mm spot size would show an error in the bulk area area of less than 60 nm rms and an up-stand smaller than 1 µm in the edge zone. It needs to be verified that this is indeed achievable when a part runs through the whole process chain. Larger errors would be challenging for this process because of the blending in to the bulk area and total process time respectively. The mitigation strategy is to improve the output quality of the preceding steps in the process chain.

`Validation: 50% / Moderate Risk`

E.2 Output quality

The process has to provide an output quality that the following process in the process chain is able to deal with. As before, this could be further divided in different aspects of quality (e.g. surface roughness/texture and form errors, including edge characteristic). This would also include process specific requirements (e.g. minimum DC-removal for a smoothing process). All experiments until now have been done on single edges. These initial experiments on the IRP600 have shown that within one correction run/iteration the P-V of the error in the corrected area is predominantly determined by the 90 nm "ripple" effect of this specific machine (probable cause: lacking HSPC module). Experiments on part ZH3000-002 show the need to control the "step

function" between the bulk area an the corrected area. Initial results on part ZH3000-003 indicate this is now under control (there is no step between the bulk and the corrected edge), but this needs to be repeated. The same part also showed the importance to remove the right amount of power and tilt from the measurement data. The mitigation strategy is to improve metrology accuracy and improve process stability (higher resolution non-linear correction of machine axes inaccuracies and improved control of the slurry's specific density)

`Validation: 70% / Moderate Risk`

E.3 Asphere

The process has to be applied on an aspherical surface. Since all development is done on spherical surfaces (due to practicality) the process needs to be shown to have similar results on an aspherical surface. Over the complete area of the seven prototype segments at the edge of the primary mirror the local radius of curvature changes from 88 875 mm to 91 942 mm. The spot size therefore changes from 4.8892 mm to 4.8893 mm, which has an insignificant impact on the polishing result. The mitigation strategy is to use a more compliant bonnet.

`Validation: 90% / Low Risk`

E.4 Hexagonality

The fact that the segments are approximately hexagonal introduces some challenges regarding symmetry and corners due to the orthogonality of most polishing rasters. However, since most development work is done on hexagons this criteria shouldn't present any problems. A further challenge is to control six edges using a hex-to-hex "spiral". Changes to the CNC generating software are required and need to be evaluated. The mitigation strategy is to blend in six separate corrections of individual edges defining different polishing parameters along the contour of each edge zone.

`Validation: 50% / Moderate Risk`

E.5 Shallowness

Due to practical constraints, the development samples are much steeper in curvature than the E-ELT segments. This might lead to changes in the process (e.g. polishing spot size when using bonnets; or, possible, edge polishing behaviour). From the test samples with a radius of 3000 mm to the first segment, which has a highest radius of curvature of 91 942 mm the spot size changes from 4.8737 mm to 4.8893 mm, which is negligible: results from larger bonnets have been transposed from test samples to the 1.5 m hexagonal Master Spherical Segment (polished before the first prototype segment on the same machine). The mitigation strategy is to fine-tune the process parameters on witness parts with similar base RoC as E-ELT segments.

`Validation: 90% / Low Risk`

E.6 Repeatability

Not a separate criterion as such, but something that applies to all here mentioned criteria. A process should not only work once, but all the time. A minimum number of re-runs should be defined in each case to give confidence about the repeatability. Actual flatness within the corrected area seems very repeatable, as shown on sample ZH3000-003. Repeatability tests of other aspects is still ongoing. The mitigation strategy is to target a more conservative correction lowering the risk of over-correction but increasing the number of corrections needed.

`Validation: 50% / Moderate Risk`

E.7 Durability/Stability

A segment (approximately 1.5 m across corners hexagon) has six edges, so the total edge area is approximately $6 \times 750 \times 10$ mm^2, a factor of 45 times the area of a single edge of a 200 mm across corners test sample. For an even correction the removal rate of the process must be stable to within a few percent (as shown by the run logs kept by *OpTIC* during the polishing of the first E-ELT prototype segment). Likely causes of instability are tool wear, slurry concentration and environmental variations (temperature, humidity). Most of these are prone to larger variations if a larger surface area is processed. No work has yet been done to estimate the stability of the process while polishing a surface area of the size of the edge area of a prototype segment. As a first test the run-out of the bonnet will be measured using the non-linear correction tool after the cloth shows noticeable wear. The mitigation strategy is to use a more durable polishing cloth and implement finer control of the specific gravity of the slurry.

`Validation: Unknown / High Risk`

E.8 Practicality

The segments will be processed on a different machine (IRP1600), on a different mount and will be measured with a different interferometer (measurement tower) than those used for the development work. These differences might introduce limitations that prevent a one-to-one implementation (e.g. zero-zero-one condition due to the axis configuration on the IRP1600 and IRP1200 machine; tilt in the work piece, larger misalignment). The alignment is critical because of the small (150 µm) Tool Offset. The mitigation strategy is to accurately characterise the machines axis and workpiece alignment.

Lastly, it needs to be verified that the measurement data that will be available is of high enough resolution, quoted by *OpTIC* to be 5 mm per pixel. If it is not enough to qualify the expected error the mitigation strategy is to measure the complete edge zone by sub-aperture, on-machine, stitching interferometer.

`Validation: Unknown / High Risk`

F

Source code for creating surface designs

F.1 Source code of `gen_zeekotpg_input.m`

```
function gen_zeekotpg_input( R, k, CoordinateFilename, OutputFilename )
%GEN_ZEEKOTPG_INPUT creates an input file for ZeekoTPG
%
% gen_zeekotpg_input( R, k, CoordinateFilename, OutputFilename )
%
% Copyright (c) 2012, Pim Messelink
% All rights reserved.
%
% Redistribution and use in source and binary forms, with or without
% modification, are permitted provided that the following conditions are
% met:
%
%     * Redistributions of source code must retain the above copyright
%       notice, this list of conditions and the following disclaimer.
%     * Redistributions in binary form must reproduce the above copyright
%       notice, this list of conditions and the following disclaimer in
%       the documentation and/or other materials provided with the distribution
%
% THIS SOFTWARE IS PROVIDED BY THE COPYRIGHT HOLDERS AND CONTRIBUTORS "AS IS"
% AND ANY EXPRESS OR IMPLIED WARRANTIES, INCLUDING, BUT NOT LIMITED TO, THE
% IMPLIED WARRANTIES OF MERCHANTABILITY AND FITNESS FOR A PARTICULAR PURPOSE
% ARE DISCLAIMED. IN NO EVENT SHALL THE COPYRIGHT OWNER OR CONTRIBUTORS BE
% LIABLE FOR ANY DIRECT, INDIRECT, INCIDENTAL, SPECIAL, EXEMPLARY, OR
% CONSEQUENTIAL DAMAGES (INCLUDING, BUT NOT LIMITED TO, PROCUREMENT OF
% SUBSTITUTE GOODS OR SERVICES; LOSS OF USE, DATA, OR PROFITS; OR BUSINESS
% INTERRUPTION) HOWEVER CAUSED AND ON ANY THEORY OF LIABILITY, WHETHER IN
% CONTRACT, STRICT LIABILITY, OR TORT (INCLUDING NEGLIGENCE OR OTHERWISE)
% ARISING IN ANY WAY OUT OF THE USE OF THIS SOFTWARE, EVEN IF ADVISED OF THE
% POSSIBILITY OF SUCH DAMAGE.

```

```
%% Parameters

if ~( exist('R', 'var') && isscalar( R ) )
    R = 84000;
end
if ~( exist('k', 'var') && isscalar( k ) )
    k = -0.993295;
end
if ~( exist('CoordinateFilename', 'var') && ischar( CoordinateFilename ) )
    CoordinateFilename = 'Seg4CXYZ.csv';
end

if ~( exist('OutputFilename', 'var') && ischar( OutputFilename ) )
    [pathstr, name, ext] = fileparts( CoordinateFilename );
    if ( strcmp( ext, '.csv') && length( name ) == 8 && ...
            strcmp( name(1:3), 'Seg') && strcmp( name(5:8), 'CXYZ') )
        OutputFilename = [ pathstr, 'DesRot' name(4) '.csv' ];
    else
        error( 'Need output filename' );
    end
end

%% Load coordinates
CornerCoordinatesInM1 = load( CoordinateFilename );

%% Extract centre
C0_in_M1_x = CornerCoordinatesInM1( 1, 1 );
C0_in_M1_y = CornerCoordinatesInM1( 1, 2 );
C0_in_M1_z = CornerCoordinatesInM1( 1, 3 );

% radial in cylindrical coordinate system
C0_in_M1_r = norm( [ C0_in_M1_x C0_in_M1_y ] );

%% Calculate cylindrical tangentials
[ ~, dz, ~, ~ ] = gen_asphere_3D( C0_in_M1_x, C0_in_M1_y, R, k );
dx = C0_in_M1_x / C0_in_M1_r;
dy = C0_in_M1_y / C0_in_M1_r;

tangentials.radial = [ dx, dy, dz ];
tangentials.radial = tangentials.radial / norm( tangentials.radial );

tangentials.azimuthal = cross( [ dx, dy, 0 ], tangentials.radial );
tangentials.azimuthal = tangentials.azimuthal / norm( tangentials.azimuthal );

%% Calculate normal vector
normal = cross( tangentials.azimuthal, tangentials.radial );
normal = normal / norm( normal );

%% Calculate angles
angle_x = atan2( normal(2), normal(3) );
angle_y = -atan2( normal(1), norm( [ normal(2), normal(3) ] ) );

%% Calculate corner positions in segment coordinate system
transformationMatrix = makehgtform( ...
    'yrotate', angle_y, 'xrotate', angle_x, ...
    'translate', [ -C0_in_M1_x, -C0_in_M1_y, -C0_in_M1_z ] );

CornerCoordinatesInSN = transformationMatrix * ...
    [ CornerCoordinatesInM1'; ones( 1, size( CornerCoordinatesInM1 ,1 ) ) ];
CornerCoordinatesInSN = CornerCoordinatesInSN( 1:3, : )';
```

```
91
92  %% Calculate domain
93  max_domain = max( CornerCoordinatesInSN );
94  min_domain = min( CornerCoordinatesInSN );
95  max_domain = max_domain * 1.1;
96  min_domain = min_domain * 1.1;
97  max_domain = max_domain +  [ C0_in_M1_x, C0_in_M1_y, C0_in_M1_z ];
98  min_domain = min_domain +  [ C0_in_M1_x, C0_in_M1_y, C0_in_M1_z ];
99
100 %% Write file
101 fid = fopen( OutputFilename, 'w');
102
103 fprintf( fid, '% 15d % 15.9f % 15.9f\n', 1, R, k );
104
105 fprintf( fid, '% 15d % 15d % 15d\n', min_domain(1), min_domain(2), min_domain(3) );
106 fprintf( fid, '% 15d % 15d % 15d\n', max_domain(1), max_domain(2), max_domain(3) );
107
108 fprintf( fid, '% 15.9f % 15.9f % 15.9f\n', -C0_in_M1_x, -C0_in_M1_y, -C0_in_M1_z );
109 fprintf( fid, '% 15.9f % 15.9f % 15.9f\n', -angle_y * 180 / pi, angle_x * 180 / pi,
        0 );
110
111 for Row = 2:7;
112     fprintf( fid, '% 15.9f % 15.9f % 15.9f\n', CornerCoordinatesInSN( Row, 1 ),
          CornerCoordinatesInSN( Row, 2 ), CornerCoordinatesInSN( Row, 3 ) );
113 end
114
115 fclose( fid);
```

F.2 Source code of `gen_parabola.m`

```
function data = gen_parabola( alpha, beta, angle, datum, width, ap_centre, ap_width,
    extrap, step, filename, surf )
% GEN_PARABOLA creates a 3D point cloud that can be imported into ZeekoTPG
%
% function data = gen_parabola( alpha, beta, angle, datum, width, ap_centre,
%                               ap_width, extrap, step, filename, surf )
%
% Copyright (c) 2012, Pim Messelink
% All rights reserved.
%
% Redistribution and use in source and binary forms, with or without
% modification, are permitted provided that the following conditions are
% met:
%
%     * Redistributions of source code must retain the above copyright
%       notice, this list of conditions and the following disclaimer.
%     * Redistributions in binary form must reproduce the above copyright
%       notice, this list of conditions and the following disclaimer in
%       the documentation and/or other materials provided with the distribution
%
% THIS SOFTWARE IS PROVIDED BY THE COPYRIGHT HOLDERS AND CONTRIBUTORS "AS IS"
% AND ANY EXPRESS OR IMPLIED WARRANTIES, INCLUDING, BUT NOT LIMITED TO, THE
% IMPLIED WARRANTIES OF MERCHANTABILITY AND FITNESS FOR A PARTICULAR PURPOSE
% ARE DISCLAIMED. IN NO EVENT SHALL THE COPYRIGHT OWNER OR CONTRIBUTORS BE
% LIABLE FOR ANY DIRECT, INDIRECT, INCIDENTAL, SPECIAL, EXEMPLARY, OR
% CONSEQUENTIAL DAMAGES (INCLUDING, BUT NOT LIMITED TO, PROCUREMENT OF
% SUBSTITUTE GOODS OR SERVICES; LOSS OF USE, DATA, OR PROFITS; OR BUSINESS
% INTERRUPTION) HOWEVER CAUSED AND ON ANY THEORY OF LIABILITY, WHETHER IN
% CONTRACT, STRICT LIABILITY, OR TORT (INCLUDING NEGLIGENCE OR OTHERWISE)
% ARISING IN ANY WAY OUT OF THE USE OF THIS SOFTWARE, EVEN IF ADVISED OF THE
% POSSIBILITY OF SUCH DAMAGE.

if ~( exist('alpha', 'var') && isscalar( alpha ) )
    alpha = 24.9804968;
end
if ~( exist('beta', 'var') && isscalar( beta ) )
    beta = 20031.2295;
end
if ~( exist('angle', 'var') && isscalar( angle ) )
    angle = 0.7144877;
end
if ~( exist('datum', 'var') && isscalar( datum ) )
    datum = 20000;
end
if ~( exist('width', 'var') && isscalar( width ) )
    width = 250;
end
if ~( exist('ap_centre', 'var') && isscalar( ap_centre ) )
    ap_centre = 110;
end
if ~( exist('ap_width', 'var') && isscalar( ap_width ) )
    ap_width = 204;
end
if ~( exist('extrap', 'var') && isscalar( extrap ) )
    extrap = 50;
end
if ~( exist('step', 'var') && isscalar( step ) )
```

```
57          step = 1;
58  end
59  if ~( exist('filename', 'var') && ischar(filename) )
60      filename = 'parabola.csv';
61  end
62  if ~( exist('surf', 'var') && isscalar( surf ) )
63          surf = 0;
64  end
65
66  x_min = datum - extrap * cosd( angle );
67  x_width = width * cosd( angle );
68  x_max = x_min + x_width + extrap * cosd( angle ) + 50;
69
70  y_width = width;
71  y_max = y_width / 2 + extrap;
72  y_min = -y_width / 2 - extrap;
73
74  [ x, y ] = meshgrid( x_min:step:x_max, y_min:step:y_max );
75  z_xzplane = parabola( alpha, beta, x );
76  delta_z = z_xzplane - sqrt( z_xzplane .^ 2 - y .^ 2 );
77  z = z_xzplane - delta_z;
78
79  ap_centre_x = datum + ap_centre * cosd( angle );
80  ap_centre_z = parabola( alpha, beta, ap_centre_x );
81
82  x = x - ap_centre_x;
83  z = z - ap_centre_z;
84
85  theta = angle * pi / 180;
86  new_coors = [ cos( theta), sin( theta ); -sin( theta ), cos( theta ) ] * [ x(:)'; z
        (:)' ];
87  x(:) = new_coors( 1, :);
88  z(:) = new_coors( 2, :);
89  clear('new_coors');
90
91  [ x_new, y_new ] = meshgrid( -round( ap_width / 2 + extrap ) : step : round( ap_width
        / 2 + extrap ) );
92  F = TriScatteredInterp( x(:), y(:), z(:) );
93  z = zeros( size( x_new ) );
94  z_new = F( x_new, y_new );
95
96  data = zeros( size(z_new) + 1 );
97  data( 2:end, 2:end ) = z_new;
98  data( 1, 2:end ) = x_new( 1, : );
99  data( 2:end, 1 ) = y_new( :, 1 );
100 dlmwrite( filename, data, 'delimiter', ',' );
101
102 if ( surf )
103     lightSurf( x_new, y_new, z_new );
104 end
105
106     function z_values = parabola( alpha, beta, x_values )
107         z_values = sqrt( alpha .* ( x_values + beta ) );
108     end
109
110 end
```

F.3 Source code of `GEN_HYPERBOLA.M`

```
function data = gen_hyperbola( alpha, beta, angle, datum, width, ap_centre, ap_width,
    extrap, step, filename, surf )
% GEN_HYPERBOLA creates a 3D point cloud that can be imported into ZeekoTPG
%
% function data = gen_hyperbola( alpha, beta, angle, datum, width, ap_centre,
%                                ap_width, extrap, step, filename, surf )
%
% Copyright (c) 2012, Pim Messelink
% All rights reserved.
%
% Redistribution and use in source and binary forms, with or without
% modification, are permitted provided that the following conditions are
% met:
%
%     * Redistributions of source code must retain the above copyright
%       notice, this list of conditions and the following disclaimer.
%     * Redistributions in binary form must reproduce the above copyright
%       notice, this list of conditions and the following disclaimer in
%       the documentation and/or other materials provided with the distribution
%
% THIS SOFTWARE IS PROVIDED BY THE COPYRIGHT HOLDERS AND CONTRIBUTORS "AS IS"
% AND ANY EXPRESS OR IMPLIED WARRANTIES, INCLUDING, BUT NOT LIMITED TO, THE
% IMPLIED WARRANTIES OF MERCHANTABILITY AND FITNESS FOR A PARTICULAR PURPOSE
% ARE DISCLAIMED. IN NO EVENT SHALL THE COPYRIGHT OWNER OR CONTRIBUTORS BE
% LIABLE FOR ANY DIRECT, INDIRECT, INCIDENTAL, SPECIAL, EXEMPLARY, OR
% CONSEQUENTIAL DAMAGES (INCLUDING, BUT NOT LIMITED TO, PROCUREMENT OF
% SUBSTITUTE GOODS OR SERVICES; LOSS OF USE, DATA, OR PROFITS; OR BUSINESS
% INTERRUPTION) HOWEVER CAUSED AND ON ANY THEORY OF LIABILITY, WHETHER IN
% CONTRACT, STRICT LIABILITY, OR TORT (INCLUDING NEGLIGENCE OR OTHERWISE)
% ARISING IN ANY WAY OUT OF THE USE OF THIS SOFTWARE, EVEN IF ADVISED OF THE
% POSSIBILITY OF SUCH DAMAGE.

if ~( exist('alpha', 'var') && isscalar( alpha ) )
    alpha = 1.001249025;
end
if ~( exist('beta', 'var') && isscalar( beta ) )
    beta = 12.49024839;
end
if ~( exist('angle', 'var') && isscalar( angle ) )
    angle = 2.1479307;
end
if ~( exist('datum', 'var') && isscalar( datum ) )
    datum = 19997.5;
end
if ~( exist('width', 'var') && isscalar( width ) )
    width = 250;
end
if ~( exist('ap_centre', 'var') && isscalar( ap_centre ) )
    ap_centre = 107.5;
end
if ~( exist('ap_width', 'var') && isscalar( ap_width ) )
    ap_width = 204;
end
if ~( exist('extrap', 'var') && isscalar( extrap ) )
    extrap = 50;
end
if ~( exist('step', 'var') && isscalar( step ) )
```

```
57          step = 1;
58  end
59  if ~( exist('filename', 'var') && ischar(filename) )
60      filename = 'hyperbola.csv';
61  end
62  if ~( exist('surf', 'var') && isscalar( surf ) )
63          surf = 0;
64  end
65
66  x_max = datum + extrap * cosd( angle );
67  x_width = width * cosd( angle );
68  x_min = x_max - x_width - extrap * cosd( angle ) + 50;
69
70  y_width = width;
71  y_max = y_width / 2 + extrap;
72  y_min = -y_width / 2 - extrap;
73
74  [ x, y ] = meshgrid( x_min:step:x_max, y_min:step:y_max );
75  z_xzplane = hyperbola( alpha, beta, x );
76  delta_z = z_xzplane - sqrt( z_xzplane .^ 2 - y .^ 2 );
77  z = z_xzplane - delta_z;
78
79  ap_centre_x = datum - ap_centre * cosd( angle );
80  ap_centre_z = hyperbola( alpha, beta, ap_centre_x );
81
82  x = x - ap_centre_x;
83  z = z - ap_centre_z;
84
85  theta = angle * pi / 180;
86  new_coors = [ cos( theta), sin( theta ); -sin( theta ), cos( theta ) ] * [ x(:)'; z
        (:)' ];
87  x(:) = new_coors( 1, :);
88  z(:) = new_coors( 2, :);
89  clear('new_coors');
90
91  [ x_new, y_new ] = meshgrid( -round( ap_width / 2 + extrap ) : step : round( ap_width
        / 2 + extrap ) );
92  F = TriScatteredInterp( x(:), y(:), z(:) );
93  z = zeros( size( x_new ) );
94  z_new = F( x_new, y_new );
95
96  data = zeros( size(z_new) + 1 );
97  data( 2:end, 2:end ) = z_new;
98  data( 1, 2:end ) = x_new( 1, : );
99  data( 2:end, 1 ) = y_new( :, 1 );
100 dlmwrite( filename, data, 'delimiter', ',' );
101
102 if ( surf )
103     lightSurf( x_new, y_new, z_new );
104 end
105
106     function z_values = hyperbola( alpha, beta, x_values )
107         z_values = sqrt( alpha .* ( beta + x_values ) .^2 - x_values.^2 );
108     end
109 end
```

Bibliography

[1] G. Ifrah. *A universal history of computing: from the abacus to the quantum computer*. John Wiley, 2001.

[2] A. Spector and D. Gifford. The space shuttle primary computer system. *Communications of the ACM*, 27, 1984.

[3] Brain Marshall. Inside a cell phone. http://electronics.howstuffworks.com/inside-cell-phone.htm, April 2000. Accessed: 17 November 2014.

[4] G. E. Moore. Cramming More Components onto Integrated Circuits. *Electronics*, 38(8):114–117, April 1965.

[5] Harro van Lente and Arie Rip. Chapter 7 Expectations in Technological Developments: An Example of Prospective Structures to be Filled in by Agency. In C. Disco and B. van der Meulen, editors, *Getting New Technologies Together: Studies in Making Sociotechnical Order*, de Gruyter Studies in Organization. De Gruyter, 1998.

[6] David R. S. Cumming, Stephen B. Furber, and Douglas J. Paul. Beyond moore's law. *Philosophical Transactions of the Royal Society of London A: Mathematical, Physical and Engineering Sciences*, 372(2012), 2014.

[7] U.S. Naval Historical Center. Photo #: NH 96566-KN picture data. http://www.history.navy.mil/photos/images/h96000/h96566kc.htm, August 24 1999. Accessed: 17 November 2014.

[8] John von Neumann. First draft of a report on the EDVAC. *IEEE Annals of the History of Computing*, 15(4):28–75, October/December 1993. Edited and corrected by Michael D. Godfrey.

[9] A. M. Turing. On computable numbers, with an application to the entscheidungsproblem. *Proceedings of the London Mathematical Society*, s2-42(1):230–265, 1937.

[10] A. M. Turing. Proposed electronic calculator. Report, National Physical Laboratory, 1946.

[11] William Pease. An automatic machine tool. *Scientific American*, 187(3):101–112, September 1952.

[12] Alfred K. Susskind and James O. McDonough. Numerically controlled milling machine. *Managing Requirements Knowledge, International Workshop on*, 0:133, 1952.

[13] Richard O. Maschmeyer, Chester A. Andrysick, Thomas W. Geyer, Helmuth E. Meissner, Charles J. Parker, and L. Michael Sanford. Precision molded-glass optics. *Appl. Opt.*, 22(16):2410–2412, August 1983.

[14] Robert O. Woods. Clear as glass. *Mechanical Engineering*, 128(10):38 – 41, 2006.

[15] Isaac Newton. *Opticks : or, a treatise of the reflexions, refractions, inflexions and colours of light. Also two treatises of the species and magnitude of curvilinear figures*. printed for Sam. Smith, and Benj. Walford London, 1704.

[16] Robert E. Parks. Traditions of optical fabrication. In Malcolm R. Howells, editor, *Reflecting Optics for Synchrotron Radiation*, volume 0315 of *Proc. SPIE*, pages 56–64. SPIE, 1982.

[17] Ray Williamson. *Field Guide to Optical Fabrication*, volume FG20 of *Field Guide*. SPIE, August 2011.

[18] F. W. Preston. The Theory and Design of Plate Glass Polishing Machines. *Journal of the Society of Glass Technology*, 11:214–256, 1927.

[19] G. Beilby. *Aggregation and Flow of Solids*. MacMillan & Company, 1921.

[20] Frank Philip Bowden and David Tabor. *The friction and lubrication of solids*. Clarendon Press Oxford, 1950.

[21] E. Brüche and H. Poppa. Das Polieren von Glas. Teil I: Optische Politur. *Glastechnische Berichte*, 28:232–242, 1955.

[22] E. Brüche and H. Poppa. Das Polieren von Glas. Teil II: Technische Politur des Flachglases. *Glastechnische Berichte*, 29:183–192, 1956.

[23] E. Brüche and H. Poppa. Das Polieren von Glas. Teil III: Oberflachenschichten beim Polierprozess. *Glastechnische Berichte*, 30:163–175, 1957.

[24] H. Poppa. Das Polieren von Glas. Teil IV: Ausfullung und Verwalkung beim Polierprozess. *Glastechnische Berichte*, 30:387–393, 1957.

[25] E. Brüche, K. Peter, and H. Poppa. Das Polieren von Glas. Teil V: Kompression und Plastizität von Glas. *Glastechnische Berichte*, 31:341– 348, 1958.

[26] Adolf Keller. Vorgänge beim polieren des glases. In Prof. Dr. Paul Görlich, editor, *Janaer Jahrbuch 1959*, volume 1, pages 181–210. VEB Gustav Fischer, 1959.

[27] E. Brüche, K. Peter, and H. Poppa. Das Polieren von Glas. Teil VI: Oberflächenfehler bei technischem glas. *Glastechnische Berichte*, 33:37–45, 1958.

[28] Tetsuro Izumitani. Polishing, Lapping and Diamond Grinding of Optical Glasses. In H. Herman, M. Tomozawa, and R.H. Doremus, editors, *Treatise on Materials Science and Technology: Glass II*, volume 17 of *Treatise on Materials Science and Technology*, page 115. Academic Press, 1977.

[29] Lee M. Cook. Chemical processes in glass polishing. *Journal of Non-Crystalline Solids*, 120(1–3):152 – 171, 1990.

[30] C.J. Evans, E. Paul, D. Dornfeld, D.A. Lucca, G. Byrne, M. Tricard, F. Klocke, O. Dambon, and B.A. Mullany. Material removal mechanisms in lapping and polishing. *CIRP Annals - Manufacturing Technology*, 52(2):611 – 633, 2003.

[31] Torsten Wons. private communication, 2005.

[32] Ronald Aspden, Ralph McDonough, and Francis R. Nitchie. Computer assisted optical surfacing. *Appl. Opt.*, 11(12):2739–2747, December 1972.

[33] R. E. Wagner and R. R. Shannon. Fabrication of aspherics using a mathematical model for material removal. *Appl. Opt.*, 13(7):1683–1689, July 1974.

[34] Daniel J. Bajuk. Computer controlled generation of rotationally symmetric aspheric surfaces. *Optical Engineering*, 15(5):155401–155401–, 1976.

[35] Robert A. Jones. Optimization of computer controlled polishing. *Appl. Opt.*, 16(1):218–224, January 1977.

[36] Y. Hagiuda, K. Karikomi, T. Nakagawa, and T. Sata. Manufacturing of a sintered cast iron lapping plate with fixed abrasives and its lapping abilities. *CIRP Annals - Manufacturing Technology*, 30(1):227 – 231, 1981.

[37] Theodore T. Saito. Diamond turning of optics: The past, the present, and the exciting future. *Optical Engineering*, 17(6):176570–176570–, 1978.

[38] R.L. Rhorer and C.J. Evans. Fabrication of optics by diamond turning. In Michael Bass, Casimer DeCusatis, Jay Enoch, Vasudevan Lakshminarayanan, Guifang Li, Carolyn Macdonald, Virendra Mahajan, and Eric Van Stryland, editors, *Handbook of Optics, Third Edition Volume II: Design, Fabrication and Testing, Sources and Detectors, Radiometry and Photometry*. McGraw-Hill, Inc., New York, NY, USA, 3 edition, 2010.

[39] W.S. Blackley and R.O. Scattergood. Ductile-regime machining model for diamond turning of brittle materials. *Precision Engineering*, 13(2):95 – 103, 1991.

[40] L. Chouanine, H. Eda, and J. Shimizu. Analytical study on ductile-regime scratching of glasses using sharply pointed tip diamond indenter. *International Journal of the Japan Society for Precision Engineering*, 31(2):109–114, 1997.

[41] F.Z. Fang, X.D. Liu, and L.C. Lee. Micro-machining of optical glasses - a review of diamond-cutting glasses. *Sadhana - Academy Proceedings in Engineering Sciences*, 28(5):945–955, 2003.

[42] J. Gan, X. Wang, M. Zhou, B. Ngoi, and Z. Zhong. Ultraprecision diamond turning of glass with ultrasonic vibration. *The International Journal of Advanced Manufacturing Technology*, 21(12):952–955, 2003.

[43] M. Zhou, P. Jia, and M. Li. Research on the influence of cutting fluids on the critical depth of cut in diamond cutting of optical glass BK7. *Key Engineering Materials*, 431-432:126–129, 2010.

[44] S. Zafran, K. A. Kaufman, and M. M. Silver. Ion polishing of optical surfaces. *Optical Engineering*, 21(6):216002–216002–, 1982.

[45] S. R. Wilson and J. R. McNeil. Neutral ion beam figuring of large optical surfaces. In Robert E. Fischer and Warren J. Smith, editors, *Current Developments in Optical Engineering II*, volume 0818 of *Proc. SPIE*, pages 320–324. SPIE, 1987.

[46] Y. Mori, K. Yamauchi, and K. Endo. Elastic emission machining. *Precision Engineering*, 9(3):123 – 128, 1987.

[47] Takahiro Hirata, Yoshinori Takei, and Hidekazu Mimura. Machining property in smoothing of steeply curved surfaces by elastic emission machining. *Procedia CIRP*, 13(0):198 – 202, 2014. 2nd CIRP Conference on Surface Integrity (CSI).

[48] L. D. Bollinger and Charles B. Zarowin. Rapid, nonmechanical, damage-free figuring of optical surfaces using plasma-assisted chemical etching (pace): Part i experimental results. In Jones B. Arnold and Robert E. Parks, editors, *Advances in Fabrication and Metrology for Optics and Large Optics*, volume 0966 of *Proc. SPIE*, pages 82–90. SPIE, 1989.

[49] C . B. Zarowin and L. D. Bollinger. Rapid, non-mechanical, damage free figuring of optical surfaces using plasma assisted chemical etching (pace): Part II theory & process control. In Jones B. Arnold and Robert E. Parks, editors, *Advances in Fabrication and Metrology for Optics and Large Optics*, volume 0966 of *Proc. SPIE*, pages 91–97. SPIE, 1989.

[50] Carlo Fanara, Paul Shore, John R. Nicholls, Nicholas Lyford, Phil Sommer, and Peter Fiske. A new reactive atom plasma technology (rapt) for precision machining: the etching of ule optical surfaces. In Eli Atad-Ettedgui, Joseph Antebi, and Dietrich Lemke, editors, *Optomechanical Technologies for Astronomy*, volume 6273 of *Proc. SPIE*, pages 62730A–62730A–12. SPIE, 2006.

[51] Yuzo Mori, Kazuto Yamauchi, Kazuya Yamamura, and Yasuhisa Sano. Development of plasma chemical vaporization machining. *Review of Scientific Instruments*, 71(12):4627–4632, 2000.

[52] T.G. Bifano, T.A. Dow, and R.O. Scattergood. Ductile-regime grinding. a new technology for machining brittle materials. *Journal of engineering for industry*, 113(2):184–189, 1991.

[53] Stephen D. Jacobs, Donald Golini, Yuling Hsu, Birgit E. Puchebner, D. Strafford, Igor V. Prokhorov, Edward M. Fess, D. Pietrowski, and William I. Kordonski. Magnetorheological finishing: a deterministic process for optics manufacturing. In Toshio Kasai, editor, *International Conference on Optical Fabrication and Testing*, volume 2576 of *Proc. SPIE*, pages 372–382. SPIE, 1995.

[54] Oliver W. Fähnle, Hedser van Brug, and Hans J. Frankena. Fluid jet polishing of optical surfaces. *Appl. Opt.*, 37(28):6771–6773, October 1998.

[55] S.M. Booij. *Fluid Jet Polishing*. PhD thesis, Technische Universiteit Delft, 2003.

[56] Wilhelmus A. C. M. Messelink, Reto Waeger, Torsten Wons, Mark Meeder, Kurt C. Heiniger, and Oliver W. Faehnle. Prepolishing and finishing of optical surfaces using Fluid Jet Polishing. In H. Philip Stahl, editor, *Optical manufacturing and testing VI*, volume 5869 of *Proc. SPIE*, pages 38–43, 2005.

[57] O.D. Fähnle, T. Wons, and W. Messelink. Device for removing material, use of gas bubbles in an abrasive liquid and process for grinding and/or polishing surfaces, October 15 2008. EP Patent 1,618,993.

[58] O.D. Fähnle, T. Wons, and W. Messelink. Device and process for grinding and/or polishing surfaces, October 15 2008. EP Patent 1,618,992.

[59] Silvia M. Booij, Oliver W. Faehnle, Mark Meeder, Torsten Wons, and Joseph J. M. Braat. Jules verne: a new polishing technique related to fjp. In H. Philip Stahl, editor, *Optical Manufacturing and Testing V*, volume 5180 of *Proc. SPIE*, pages 89–100. SPIE, 2004.

[60] Wilhelmus A. C. M. Messelink, Reto Waeger, Mark Meeder, Herbert Looser, Torsten Wons, Kurt C. Heiniger, and Oliver W. Faehnle. Development and optimization of FJP tools and their practical verification. In H. Philip Stahl, editor, *Optical manufacturing and testing VI*, volume 5869 of *Proc. SPIE*, pages 58690A–58690A–8. SPIE, 2005.

[61] William Kordonski, Aric Shorey, and Marc Tricard. Jet-induced high-precision finishing of challenging optics. In H. Philip Stahl, editor, *Optical Manufacturing and Testing VI*, volume 5869 of *Proc. SPIE*, pages 586909–586909–8. SPIE, 2005.

[62] Jorge González-García, Alberto Cordero-Dávila, Esteban Luna, Manuel Nú nez, Elfego Ruiz, Luis Salas, Victor H. Cabrera-Peláez, Irene Cruz-González, and Erika Sohn. Static and dynamic removal rates of a new hydrodynamic polishing tool. *Appl. Opt.*, 43(18):3623–3631, June 2004.

[63] Thomas Arnold, Georg Boehm, Inga-Maria Eichentopf, Manuela Janietz, Johannes Meister, and Axel Schindler. Plasma jet machining. *Vakuum in Forschung und Praxis*, 22(4):10–16, 2010.

[64] David Walker, David Brooks, Andrew King, Richard Freeman, Roger Morton, Gerry McCavana, and Sug-Whan Kim. The 'Precessions' tooling for polishing and figuring flat, spherical and aspheric surfaces. *Opt. Express*, 11(8):958–964, April 2003.

[65] David Walker, David Brooks, Andrew King, Richard Freeman, Roger Morton, Gerry McCavana, and Sug-Whan Kim. The "Precessions" tooling for polishing and figuring flat, spherical and aspheric surfaces. *Opt. Express*, 11(8):958–964, April 2003.

[66] E. Fess, J. Schoen, M. Bechtold, and D. Mohring. Ultraform finishing. In Randal W. Tustison, editor, *Window and Dome Technologies and Materials IX*, volume 5786 of *Proc. SPIE*, pages 305–309. SPIE, 2005.

[67] D. D. Walker, A. T. H. Beaucamp, V. Doubrovski, C. Dunn, R. Evans, R. Freeman, J. Kelchner, G. McCavana, R. Morton, D. Riley, J. Simms, G. Yu, and X. Wei. Automated optical fabrication: first results from the new precessions 1.2m cnc polishing machine. In Eli Atad-Ettedgui, Joseph Antebi, and Dietrich Lemke, editors, *Optomechanical Technologies for Astronomy*, volume 6273 of *Proc. SPIE*, pages 627309–627309–8. SPIE, 2006.

[68] D. D. Walker, A. Baldwin, R. Evans, R. Freeman, S. Hamidi, P. Shore, X. Tonnellier, S. Wei, C. Williams, and G. Yu. A quantitative comparison of three grolishing techniques for the precessions process. In James H. Burge, Oliver W. Faehnle, and Ray Williamson, editors, *Optical manufacturing and testing VII*, volume 6671 of *Proc. SPIE*, pages 66711H–66711H–9. SPIE, 2007.

[69] G. Yu, H. Li, and D. Walker. Removal of mid spatial-frequency features in mirror segments. *Journal of the European Optical Society - Rapid publications*, 6(0), 2011.

[70] Dae Wook Kim and James H. Burge. Rigid conformal polishing tool using non-linear visco-elastic effect. *Opt. Express*, 18(3):2242–2257, February 2010.

[71] I. F. Stowers, R. Komanduri, and E. D. Baird. Review of precision surface generating processes and their potential application to the fabrication of large optical components. In Jones B. Arnold and Robert E. Parks, editors, *Advances in Fabrication and Metrology for Optics and Large Optics*, volume 0966 of *Proc. SPIE*, pages 62–73. SPIE, 1989.

[72] Christina R. Dunn and David D. Walker. Pseudo-random tool paths for CNC sub-aperture polishing and other applications. *Opt. Express*, 16(23):18942–18949, November 2008.

[73] Isobel M. Hook. *The science case for the European extremely large telescope: the next step in mankind's quest for the universe*. OPTICON, 2005.

[74] Isobel M. Hook. Summary of the science case for an ELT. *EAS Publications Series*, 25:111–118, January 2007.

[75] Gregory Bothun. Wide and Ultra-Wide Field CCD Imaging. *CCD Astronomy*.

[76] Isobel M. Hook. The science case for ELTs. In Arne L. Ardeberg and Torben Andersen, editors, *Second Backaskog Workshop on Extremely Large Telescopes*, volume 5382 of *Proc. SPIE*, pages 1–6, 2004.

[77] Jerry Nelson. Segmented mirror telescopes. In Renaud Foy and Françoise Claude Foy, editors, *Optics in Astrophysics*, volume 198 of *NATO Science Series II: Mathematics, Physics and Chemistry*, pages 61–72. Springer Netherlands, 2005.

[78] D. D. Walker, H. S. Yang, and D. Brooks. Interferometry applied to testing large optics. In K.T.V. Grattan, editor, *Applied optics and optoelectronics 1998*, pages 303–310. Institute of Physics, Institute of Physics Publishing, March 1998.

[79] D.D. Walker and R.G. Bingham. Unspecified. In J.P. Rozelot and W.C. Livingston, editors, *Proceedings of the International Workshop on Mirror Substrate Alternatives, Grasse, France*, pages 19–28. OCA/CERGA, October 1995.

[80] Jacob Lubliner and Jerry E. Nelson. Stressed mirror polishing. 1: A technique for producing nonaxisymmetric mirrors. *Appl. Opt.*, 19(14):2332–2340, July 1980.

[81] Jerry E. Nelson, George Gabor, Leslie K. Hunt, Jacob Lubliner, and Terry S. Mast. Stressed mirror polishing. 2: Fabrication of an off-axis section of a paraboloid. *Appl. Opt.*, 19(14):2341–2352, July 1980.

[82] A. Swat. Eso prototype segment specification. Technical report, European Southern Observatory, July 2009.

[83] P. Shore, P. Morantz, X. Luo, X. Tonnellier, R. Collins, A. Roberts, R. May-Miller, and R. Read. Big OptiX ultra precision grinding/measuring system. In Angela Duparréand Roland Geyl and Lingli Wang, editors, *Optical Fabrication, Testing, and Metrology II*, volume 5965 of *Proc. SPIE*, pages 59650Q–59650Q–8. SPIE, September 2005.

[84] X. Tonnellier, P. Shore, P. Morantz, A. Baldwin, D. Walker, G. Yu, and R. Evans. Sub-surface damage issues for effective fabrication of large optics. In Eli Atad-Ettedgui and Dietrich Lemke, editors, *Advanced Optical and Mechanical Technologies in Telescopes and Instrumentation*, volume 7018 of *Proc. SPIE*, pages 70180F–70180F–10, 2008.

[85] X. Tonnellier, P. Shore, P. Morantz, and D. Orton. Surface quality of a 1m zerodur part using an effective grinding mode. In Angela Duparré and Roland Geyl, editors, *Optical Fabrication, Testing, and Metrology III*, volume 7102 of *Proc. SPIE*, pages 71020B–71020B–9, 2008.

[86] David D. Walker, David Brooks, Richard Freeman, Andrew King, Gerry McCavana, Roger Morton, David Riley, and John Simms. First aspheric form and texture results from a production machine embodying the precession process. In H. Philip Stahl, editor, *Optical Manufacturing and Testing IV*, volume 4451 of *Proc. SPIE*, pages 267–276, 2001.

[87] David D. Walker, A. T. H. Beaucamp, Richard G. Bingham, David Brooks, Richard Freeman, Sowoon Kim, Andrew King, Gerry McCavana, Roger Morton, David Riley, and John Simms. Precessions process for efficient production of aspheric optics for large telescopes and their instrumentation. In Eli Atad-Ettedgui and Sandro D'Odorico, editors, *Specialized Optical Developments in Astronomy*, volume 4842 of *Proc. SPIE*, pages 73–84, 2002.

[88] David D. Walker, A. T. Beaucamp, David Brooks, Richard Freeman, Andrew King, Gerry McCavana, Roger Morton, David Riley, and John Simms. Novel CNC polishing process for control of form and texture on aspheric surfaces. In Robert E. Fischer, Warren J. Smith, and R. Barry Johnson, editors, *Current Developments in Lens Design and Optical Engineering III*, volume 4767 of *Proc. SPIE*, pages 99–105, 2002.

[89] Caroline Gray, Ian Baker, Gary Davies, Rob Evans, Nathan Field, Tony Fox-Leonard, Wilhelmus Messelink, John Mitchell, Paul Rees, Steve Waine, David D. Walker, and Guoyu Yu. Fast manufacturing of E-ELT mirror segments using CNC polishing. In Oliver W. Fähnle, Ray Williamson, and Dae Wook Kim, editors, *Optical Manufacturing and Testing X*, volume 8838 of *Proc. SPIE*, pages 88380K–88380K–12. SPIE, September 2013.

[90] E. Brinksmeier, Y. Mutlugünes, F. Klocke, J.C. Aurich, P. Shore, and H. Ohmori. Ultra-precision grinding. *CIRP Annals - Manufacturing Technology*, 59(2):652 – 671, 2010.

[91] Ci Song, David Walker, and Guoyu Yu. Misfit of rigid tools and interferometer subapertures on off-axis aspheric mirror segments. *Optical Engineering*, 50(7):073401–073401–6, 2011.

[92] Fritz Zernike. Beugungstheorie des schneidenver-fahrens und seiner verbesserten form, der phasenkontrastmethode. *Physica*, 1:689–704, May 1934.

[93] M. Born and E. Wolf. *Principles of Optics*. Cambridge University Press, October 1999.

[94] Daniel Malacara. *Optical Shop Testing (Wiley Series in Pure and Applied Optics)*. Wiley-Interscience, 2007.

[95] Victor L. Genberg. Optical surface evaluation. In Lester M. Cohen, editor, *Structural mechanics of optical systems I*, volume 450 of *Proc. SPIE*, pages 81–87. SPIE, 1984.

[96] H. Nyquist. Certain topics in telegraph transmission theory. *Proceedings of the IEEE*, 90(2):280–305, February 2002.

[97] James C. Wyant. Advances in interferometric metrology. In Zhicheng Weng, Jose M. Sasian, and Yongtian Wang, editors, *Optical Design and Testing*, volume 4927 of *Proc. SPIE*, pages 154–162. SPIE, 2002.

[98] John Hayes. Dynamic interferometry handles vibration. *Laser Focus World*, 38(3):109, 2002.

[99] James C. Wyant. Dynamic interferometry. *Opt. Photon. News*, 14(4):36–41, April 2003.

[100] Natalia Yaitskova and Mitchell Troy. Rolled edges and phasing of segmented telescopes. *Appl. Opt.*, 50(4):542–553, February 2011.

[101] Glenn W. Zeiders, Jr. and Edward E. Montgomery IV. Diffraction effects with segmented apertures. In Pierre Y. Bely; James B. Breckinridge, editor, *Space Telescopes and Instruments V*, volume 3356 of *Proc. SPIE*, pages 799–809. SPIE, 1998.

[102] Natalia Yaitskova, Kjetil Dohlen, and Philippe Dierickx. Analytical study of diffraction effects in extremely large segmented telescopes. *J. Opt. Soc. Am. A*, 20(8):1563–1575, August 2003.

[103] Mitchell Troy and Gary Chanan. Diffraction effects from giant segmented-mirror telescopes. *Appl. Opt.*, 42(19):3745–3753, July 2003.

[104] Silvia M. Booij, Hedser van Brug, Joseph J. M. Braat, and Oliver W. Fa¨hnle. Nanometer deep shaping with fluid jet polishing. *Optical Engineering*, 41(8):1926–1931, 2002.

[105] Wilhelmus A. C. M. Messelink, Oliver W. Faehnle, and Martin Forrer. Deterministic shape correction with Fluid Jet Polishing using a sub-aperture footprint. In James H. Burge, Oliver W. Faehnle, and Ray Williamson, editors, *Optical manufacturing and testing VII*, volume 6671 of *Proc. SPIE*, 2007. Presentation only.

[106] Peiji Guo, Hui Fang, and Jingchi Yu. Edge effect in fluid jet polishing. *Appl. Opt.*, 45(26):6729–6735, September 2006.

[107] Jay Daniel, Ulrich Mueller, Tracy Peters, Stephen F. Sporer, and Tony Hull. Tinsley progress on stress mirror polishing (SMP) for the thirty meter telescope (TMT) primary mirror segments ii. In Larry M. Stepp, Roberto Gilmozzi, and Helen J. Hall, editors, *Ground-based and Airborne Telescopes III*, volume 7733 of *Proc. SPIE*, pages 773328–773328–9. SPIE, 2010.

[108] Scott R. Runnels and L.Michael Eyman. Tribology analysis of chemical-mechanical polishing. *Journal of the Electrochemical Society*, 141(6):1698–1701, 1994.

[109] Scott R. Runnels. Feature-scale fluid-based erosion modeling for chemical-mechanical polishing. *Journal of the Electrochemical Society*, 141(7):1900–1904, 1994.

[110] C. Rogers, J. Coppeta, L. Racz, A. Philipossian, F.B. Kaufman, and D. Bramono. Analysis of flow between a wafer and pad during cmp processes. *Journal of Electronic Materials*, 27(10):1082–1087, 1998.

[111] J. Lu, J. Coppeta, C. Rogers, V.P. Manno, L. Racz, A. Philipossian, M. Moinpour, and F. Kaufman. The effect of wafer shape on slurry film thickness and friction coefficients in chemical mechanical planarization. In *Materials Research Society Symposium*, volume 613, pages E1.2.1 – E1.2.6, San Francisco, CA, United states, 2000. Chemical mechanical planarization;Dual emission laser;Fluid film thickness;Friction coefficients;.

[112] H Li. *Research on manufacturing mirror segments for an extremely large telescope*. PhD thesis, University College London, 2012.

[113] David Walker. private communication, 2013.

[114] Jan-Claas Kupfer, Marcel Achtsnick, and Elisabeth Becker. Model-based polishing of meter size optics. In Julie L. Bentley and Matthias Pfaff, editors, *Optifab 2013*, volume 8884 of *Proc. SPIE*, pages 88841P–88841P–6. SPIE, 2013.

[115] Robert Hooke, James Young, Denis Pappins, G. T., and Samuel Sturmy. *Lectures de potentia restitutiva, or, Of spring [microform] : explaining the power of springing bodies : to which are added some collections viz. a description of Dr. Pappins wind-fountain and force-pump, Mr. Young's observation concerning natural fountains, some other considerations concerning that subject, Captain Sturmy's remarks of a subterraneous cave and cistern, Mr. G.T. observations made on the Pike of Teneriff, 1674, some reflections and conjectures occasioned thereupon, a relation of a late eruption in the Isle of Palma / by Robert Hooke*. Printed for John Martyn London, 1678.

[116] Albert E. Moyer. Robert Hooke's ambiguous presentation of "Hooke's Law". *j-ISIS*, 68(2):266–275, June 1977.

[117] Robert A. Jones. Computer-controlled optical surfacing with orbital tool motion. *Optical Engineering*, 25(6):256785–256785–, 1986.

[118] Esteban Luna-Aguilar, Alberto Cordero-Davila, Jorge Gonzalez, Manuel Nunez-Alfonso, Victor Cabrera, Carlos I. Robledo-Sanchez, Jorge Cuautle-Cortez, and Maria H. Pedrayes. Edge effects with preston equation. In J. Roger, P. Angel, and Roberto Gilmozzi, editors, *Future Giant Telescopes*, volume 4840 of *Proc. SPIE*, pages 598–603. SPIE, 2003.

[119] Alberto Cordero-Dávila, Jorge González-García, María Pedrayes-López, Luis Alberto Aguilar-Chiu, Jorge Cuautle-Cortés, and Carlos Robledo-Sánchez. Edge effects with the preston equation for a circular tool and workpiece. *Appl. Opt.*, 43(6):1250–1254, February 2004.

[120] Dae Wook Kim, Won Hyun Park, Sug-Whan Kim, and James H Burge. Parametric modeling of edge effects for polishing tool influence functions. *Optics Express*, 17:5656–5665, 2009.

[121] Dae Wook Kim, Won Hyun Park, Sug-Whan Kim, and James H Burge. Edge tool influence function library using the parametric edge model for computer controlled optical surfacing. In James H. Burge, Oliver W. Faehnle, and Ray Williamson, editors, *Optical manufacturing and testing VIII*, volume 7426 of *Proc. SPIE*, 2009.

[122] David Walker, Guoyu Yu, Hongyu Li, Wilhelmus Messelink, Rob Evans, and Anthony Beaucamp. Edges in CNC polishing: from mirror-segments towards semiconductors, paper 1: edges on processing the global surface. *Opt. Express*, 20(18):19787–19798, August 2012.

[123] Robert D. Cook, David S. Malkus, Michael E. Plesha, and Robert J. Witt. *Concepts and Applications of Finite Element Analysis*. John Wiley & Sons, 1989.

[124] D. D. Walker, A. T. Beaucamp, D. Brooks, V. Doubrovski, M. D. Cassie, C. Dunn, R. R. Freeman, A. King, M. Libert, G. McCavana, R. Morton, D. Riley, and J. Simms. Recent developments of precessions polishing for larger components and free-form surfaces. In P. Z. Mouroulis, W. J. Smith, and R. B. Johnson, editors, *Current Developments in Lens Design and Optical Engineering V*, volume 5523 of *Proc. SPIE*, pages 281–289, 2004.

[125] J.-F. Chatelain, R. Roy, and R. Mayer. Development of a spiral trajectory for high speed roughing of light alloy aerospace components. *WSEAS Transactions on Applied and Theoretical Mechanics*, 3(3):83–93, 2008.

[126] S.S. Makhanov and S.A. Ivanenko. Grid generation as applied to optimize cutting operations of the five-axis milling machine. *Applied Numerical Mathematics*, 46(3–4):331–351, 2003. Applied Numerical Computing: Grid Generation and Solution Methods for Advanced Simulations.

[127] Guoyu Yu, David D. Walker, and Hongyu Li. Research on fabrication of mirror segments for E-ELT. In Li Yang, Eric Ruch, and Shengyi Li, editors, *6th International Symposium on Advanced Optical Manufacturing and Testing Technologies: Advanced Optical Manufacturing Technologies*, volume 8416 of *Proc. SPIE*, pages 841602–841602–6. SPIE, 2012.

[128] Oliver W. Faehnle, Hedser van Brug, and Hans J. Frankena. Fluid Jet Polishing of optical surfaces. *Applied Optics*, 37(28):6771–6773, 1998.

[129] Wilhelmus A. C. M. Messelink, Richard Freeman, and Oliver W. Faehnle. FJP: edge sharp finishing of optical surfaces. In Yang Li, Yaolong Chen, Ernst-Bernhard Kley, and Rongbin Li, editors, *Advanced Optical Manufacturing Technologies*, volume 6722 of *Proc. AOMATT*. SPIE, 2007. Presentation only.

[130] Anthony Beaucamp and Yoshiharu Namba. Super-smooth finishing of diamond turned hard X-ray molding dies by combined fluid jet and bonnet polishing. *CIRP Annals - Manufacturing Technology*, 62(1):315 – 318, 2013.

[131] Larry Stepp. Silicon carbide tertiary mirror for tmt. Technical report, Thirty-Meter Telescope International Observatory LLC, May 17 2010.

[132] L Yin, E Y J Vancoille, K Ramesh, H Huang, J P Pickering, and A C Spowage. Ultraprecision grinding of tungsten carbide for spherical mirrors. *Proceedings of the Institution of Mechanical Engineers, Part B: Journal of Engineering Manufacture*, 218(4):419–429, 2004.

[133] Siddharth Choudhary, Shobhit Singhal, Ujjawal Mayank Srivastava, Pratik Jain, and Vikrant Yadav. Tungsten-carbide composite: A review. *International Journal of Scientific & Engineering Research*, 3(9), September 2012. ISSN 2229-5518.

[134] Seung I. Cha and Soon H. Hong. Microstructures of binderless tungsten carbides sintered by spark plasma sintering process. *Materials Science and Engineering: A*, 356(1–2):381 – 389, 2003.

[135] Dmytro Demirskyi, Andrey Ragulya, and Dinesh Agrawal. Initial stage sintering of binderless tungsten carbide powder under microwave radiation. *Ceramics International*, 37(2):505 – 512, 2011.

[136] H. Engqvist, N. Axén, and S. Hogmark. Resistance of a binderless cemented carbide to abrasion and particle erosion. *Tribology Letters*, 4:251–258, 1998.

[137] Håkan Engqvist, Gianluigi A. Botton, Niklas Axén, and Sture Hogmark. Microstructure and Abrasive Wear of Binderless Carbides. *Journal of the American Ceramic Society*, 83(10):2491–2496, 2000.

[138] Anthony Beaucamp, Yoshiharu Namba, Wilhelmus Messelink, David Walker, Phillip Charlton, and Richard Freeman. Surface integrity of fluid jet polished tungsten carbide. *Procedia CIRP*, 13(0):377 – 381, 2014. 2nd CIRP Conference on Surface Integrity (CSI).

[139] H. Vahedi Tafreshi and B. Pourdeyhimi. Cavitation and hydraulic flip. *Fluent News*, 13(1):38, 2004.

[140] F. G. Hammitt. Observations on cavitation damage in a flowing system. *Journal of Basic Engineering*, 85(3):347, 1963.

[141] P.J. McNulty and I.S. Pearsall. Cavitation inception in pumps. *Digest of Papers - IEEE Computer Society International Conference*, pages 163 – 170, 1979. CAVITATION INCEPTION;.

[142] H. Chaves, M. Knapp, A. Kubitzek, F. Obermeier, and T. Schneider. Experimental study of cavitation in the nozzle hole of diesel injectors using transparent nozzles. *SAE Technical Papers*, 1995.

[143] E. Lassner and W.D. Schubert. *Tungsten: Properties, Chemistry, Technology of the Elements, Alloys, and Chemical Compounds*. Springer US, 1999.

[144] SCHOTT North America, Inc. - Advanced Optics, 400 York Avenue, Duryea, PA 18642, USA. *Optical Glass - Data Sheets*.

[145] A.J. Gant and M.G. Gee. Structure–property relationships in liquid jet erosion of tungsten carbide hardmetals. *International Journal of Refractory Metals and Hard Materials*, 27(2):332 – 343, 2009. International Conference on the Science of Hard Materials - 9.

[146] J Brillo, H Kuhlenbeck, and H.-J Freund. Interaction of O2 with wc(0001). *Surface Science*, 409(2):199 – 206, 1998.

[147] Feng-Che Tsai, Biing-Hwa Yan, Chun-Yu Kuan, Rong-Tzong Hsu, and Jung-Chou Hung. An investigation into superficial embedment in mirror-like machining using abrasive jet polishing. *The International Journal of Advanced Manufacturing Technology*, 43(5-6):500–512, 2009.

[148] K. L. Johnson, K. Kendall, and A. D. Roberts. Surface energy and the contact of elastic solids. *Proceedings of the Royal Society of London A: Mathematical, Physical and Engineering Sciences*, 324(1558):301–313, 1971.

[149] H. Vahedi Tafreshi and B. Pourdeyhimi. The effects of nozzle geometry on waterjet breakup at high reynolds numbers. *Experiments in Fluids*, 35(4):364–371, 2003.

[150] J.P. Franc and J.M. Michel. *Fundamentals of Cavitation*. Fluid Mechanics and Its Applications. Kluwer Academic Publishers, 2006.

[151] G. Kuiper. *Cavitation in Ship Propulsion*, chapter Chapter 3 Physics of cavitation: GAS CONTENT AND NUCLEI. Delft University of Technology, January 15 2010.

[152] Chun Yan Shi, Jia Hu Yuan, Fan Wu, Yong Jian Wan, and Yu Han. Analysis of parameters in fluid jet polishing by cfd. In Li Yang, John M. Schoen, Yoshiharu Namba, and Shengyi Li, editors, *4th International Symposium on Advanced Optical Manufacturing and Testing Technologies: Advanced Optical Manufacturing Technologies*, volume 7282 of *Proc. SPIE*, pages 72821Y–72821Y–5. SPIE, 2009.

[153] Anthony Beaucamp, Yoshiharu Namba, and Richard Freeman. Dynamic multiphase modeling and optimization of fluid jet polishing process. *CIRP Annals - Manufacturing Technology*, 61(1):315 – 318, 2012.

[154] A.T. Beaucamp, A. Matsumoto, and Y. Namba. Ultra-precision fluid jet and bonnet polishing for next generation hard X-ray telescope application. In *Proceedings - ASPE 2010 Annual Meeting*, volume 50, pages 57–60, 2010.

[155] L. Proserpio, M. Ghigo, S. Basso, P. Conconi, O. Citterio, M. Civitani, R. Negri, G. Pagano, G. Pareschi, B. Salmaso, D. Spiga, G. Tagliaferri, L. Terzi, A. Zambra, G. Parodi, F. Martelli, M. Bavdaz, and E. Wille. Production of the IXO glass segmented mirrors by hot slumping with pressure assistance: tests and results. In Stephen L. O'Dell and Giovanni Pareschi, editors, *Optics for EUV, X-Ray, and Gamma-Ray Astronomy V*, volume 8147, pages 81470M–81470M–11, 2011.

[156] David Aikens, Jessica E. DeGroote, and Richard N. Youngworth. Specification and control of mid-spatial frequency wavefront errors in optical systems. In *Frontiers in Optics 2008/Laser Science XXIV/Plasmonics and Metamaterials/Optical Fabrication and Testing*, page OTuA1. Optical Society of America, 2008.

[157] James J. Kumler and J. Brian Caldwell. Measuring surface slope error on precision aspheres. In James H. Burge, Oliver W. Faehnle, and Ray Williamson, editors, *Optical manufacturing and testing VII*, volume 6671 of *Proc. SPIE*, pages 66710U–66710U–9. SPIE, 2007.

[158] David M. Aikens, C. Robert Wolfe, and Janice K. Lawson. Use of power spectral density (psd) functions in specifying optics for the national ignition facility. In Toshio Kasai, editor, *International Conference on Optical Fabrication and Testing*, volume 2576 of *Proc. SPIE*, pages 281–292. SPIE, 1995.

[159] Ross Zhelem. Specification of optical surface accuracy using the structure function. In Bernd Bodermann, editor, *Modeling Aspects in Optical Metrology III*, volume 8083 of *Proc. SPIE*, pages 808310–808310–10. SPIE, 2011.

[160] Erkin Sidick. Power spectral density specification and analysis of large optical surfaces. In Harald Bosse, Bernd Bodermann, and Richard M. Silver, editors, *Modeling Aspects in Optical Metrology II*, volume 7390 of *Proc. SPIE*, pages 73900L–73900L–12. SPIE, 2009.

[161] P.Z. Takacs, S. Barber, E.L. Church, K. Kaznatcheev, W.R. McKinney, and V.Y. Yashchuk. 2d spatial frequency considerations in comparing 1d power spectral density measurements. In *Optical Fabrication and Testing (OF&T) Topical Meeting*, June 2010.

[162] Oliver Fähnle, Safer Mourad, Karin Hauser, and Mark Meeder. Detection and removal of spatial mid-frequencies in sub-aperture finishing. In *International Optical Design Conference and Optical Fabrication and Testing*, page OWE4. Optical Society of America, June 2010.

[163] D. Gabor. Theory of communication. part 1: The analysis of information. *Journal of the Institution of Electrical Engineers - Part III: Radio and Communication Engineering*, 93:429–441(12), November 1946.

[164] Ingrid Daubechies. *Ten Lectures on Wavelets*. Society for Industrial and Applied Mathematics, Philadelphia, PA, USA, 1992.

[165] Alfred Haar. Zur theorie der orthogonalen funktionensysteme. *Mathematische Annalen*, 69(3):331–371, 1910.

[166] Albert Cohen. *Ondelettes, analyses multiresolutions et traitement numerique du signal*. PhD thesis, Université Paris, 1990. Thèse de doctorat dirigée par Meyer, Yves Sciences appliquées Paris 9 1990.

[167] Anthony Teolis. *Computational Signal Processing with Wavelets (Applied and Numerical Harmonic Analysis)*. Birkhäuser, 1998.

[168] Stephane G. Mallat. A theory for multiresolution signal decomposition: The wavelet representation. *IEEE Transactions on Pattern Analysis and Machine Intelligen*, 11(7), 1989.

[169] Andrew P. Bradley. Shift invariance in the discrete wavelet transform. In *VIIth Digit. Image Comp*, pages 29–38, 2003.

List of Publications

[1] Detailed Modelling of Edge-Features in CNC Polishing. Technical report, Optic Glyndŵr Ltd., November 2014. Report delivered to Welsh Government under the A4B (Academic Expertise for Business) scheme. Joint work with David D. Walker (ed.).

[2] Surface integrity of fluid jet polished tungsten carbide. *Procedia CIRP*, 13(0):377 – 381, 2014. 2nd CIRP Conference on Surface Integrity (CSI). Joint work with Anthony Beaucamp, Yoshiharu Namba, David Walker, Phillip Charlton and Richard Freeman.

[3] Edge control in CNC polishing, paper 2: simulation and validation of tool influence functions on edges. *Optics Express*, 21:370, January 2013. Joint work with H. Li, D. Walker, G. Yu, A. Sayle, R. Evans and A. Beaucamp.

[4] Fast manufacturing of E-ELT mirror segments using CNC polishing. In Fähnle, Oliver W., Ray Williamson, and Dae Wook Kim, editors, *Optical Manufacturing and Testing X*, volume 8838 of *Proc. SPIE*, pages 88380K–88380K–12. SPIE, September 2013. Joint work with Caroline Gray, Ian Baker, Gary Davies, Rob Evans, Nathan Field, Tony Fox-Leonard, John Mitchell, Paul Rees, Steve Waine, David D. Walker and Guoyu Yu.

[5] Edge-control and surface-smoothness in sub-aperture polishing of mirror segments. In Prieto, Ramón Navarro; Colin R. Cunningham; Eric, editor, *Modern Technologies in Space- and Ground-based Telescopes and Instrumentation II*, volume 8450 of *Proc. SPIE*, pages 84502A–84502A–9. SPIE, 2012. Joint work with D. Walker, A. Beaucamp, R. Evans, T. Fox-Leonard, N. Fairhurst, C. Gray, S. Hamidi, H. Li, J. Mitchell, P. Rees and G. Yu.

[6] Edges in CNC polishing: from mirror-segments towards semiconductors, paper 1: edges on processing the global surface. *Opt. Express*, 20(18):19787–19798, August 2012. Joint work with David Walker, Guoyu Yu, Hongyu Li, Rob Evans and Anthony Beaucamp.

[7] Technologies for producing segments for extremely large telescopes. In Burge, James H., Oliver W. Fähnle, and Ray Williamson, editors, *Optical Manufacturing and Testing IX*, volume 8126 of *Proc. SPIE*, pages 812604–812604–9. SPIE, 2011. Joint work with D. Walker, C. Atkins, I. Baker, R. Evans, S. Hamidi, P. Harris, H. Li, J. Mitchell, M. Parry-Jones, P. Rees and G. Yu.

[8] Device and method for manufacturing optical elements, December 15 2010. EP Patent 1,977,860. Joint work with O. Fähnle and M. Meeder.

[9] Device and process for grinding and/or polishing surfaces, October 15 2008. EP Patent 1,618,992. Joint work with O.D. Fähnle and T. Wons.

[10] Device for removing material, use of gas bubbles in an abrasive liquid and process for grinding and/or polishing surfaces, October 15 2008. EP Patent 1,618,993. Joint work with O.D. Fähnle and T. Wons.

[11] Exploiting the process stability of fluid jet polishing. In *Frontiers in Optics 2008/Laser Science XXIV/Plasmonics and Metamaterials/Optical Fabrication and Testing*, page OThD3. Optical Society of America, 2008. Joint work with Oliver W. Faehnle.

[12] Deterministic shape correction with Fluid Jet Polishing using a sub-aperture footprint. In Burge, James H., Oliver W. Faehnle, and Ray Williamson, editors, *Optical manufacturing and testing VII*, volume 6671 of *Proc. SPIE*, 2007. Presentation only. Joint work with Oliver W. Faehnle and Martin Forrer.

[13] FJP: edge sharp finishing of optical surfaces. In Li, Yang, Yaolong Chen, Ernst-Bernhard Kley, and Rongbin Li, editors, *Advanced Optical Manufacturing Technologies*, volume 6722 of *Proc. AOMATT*. SPIE, 2007. Presentation only. Joint work with Richard Freeman and Oliver W. Faehnle.

[14] Analysis of the ductile-brittle mode transition in loose abrasive grinding. In Stahl, H. Philip, editor, *Optical Manufacturing and Testing VI*, volume 5869 of *Proc. SPIE*, pages 58690M–58690M–6. SPIE, 2005. Joint work with Mark Meeder and Oliver W. Faehnle.

[15] Development and optimization of FJP tools and their practical verification. In Stahl, H. Philip, editor, *Optical manufacturing and testing VI*, volume 5869 of *Proc. SPIE*, pages 58690A–58690A–8. SPIE, 2005. Joint work with Reto Waeger, Mark Meeder, Herbert Looser, Torsten Wons, Kurt C. Heiniger and Oliver W. Faehnle.

[16] Prepolishing and finishing of optical surfaces using Fluid Jet Polishing. In Stahl, H. Philip, editor, *Optical manufacturing and testing VI*, volume 5869 of *Proc. SPIE*, pages 38–43, 2005. Joint work with Reto Waeger, Torsten Wons, Mark Meeder, Kurt C. Heiniger and Oliver W. Faehnle.

[17] Feature-based detection of land mines in infrared images. In Broach, J. Thomas, Russell S. Harmon, and Gerald J. Dobeck, editors, *Detection and Remediation Technologies for Mines and Minelike Targets VII*, volume 4742 of *Proc. SPIE*, pages 108–119. SPIE, 2002. Joint work with Klamer Schutte, Albert M. Vossepoel, Frank Cremer, John G. M. Schavemaker and Eric den Breejen.

Colophon

This thesis was typeset using LaTeX, originally developed by Leslie Lamport and based on Donald Knuth's TeX. The body text is set in 11 point Arno Pro, designed by Robert Slimbach in the style of book types from the Aldine Press in Venice, and issued by Adobe in 2007. A template, based on the excellent Harvard template by Jordan Suchow and Andrew Leifer, which can be used to format a PhD thesis with this look and feel, has been released under the permissive MIT (X11) license, and can be found online at: https://github.com/pimmesselinkucl/ or from the author at: pim.messelink.10@ucl.ac.uk.